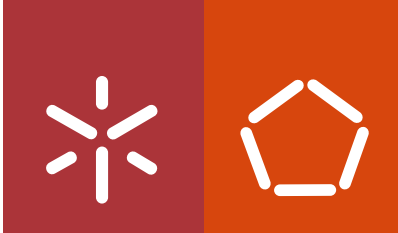**Universidade do Minho**

Escola de Engenharia

Iman Ferdosian

Material Development and Self-healing Capacity of Eco-Efficient Ultra-High Performance Concrete (EEUHPC)

April, 2016

Universidade do Minho
Escola de Engenharia

Iman Ferdosian

Material Development and Self-healing Capacity of Eco-Efficient Ultra-High Performance Concrete (EEUHPC)

Doctoral Thesis for PhD degree in
Civil Engineering

Supervisor:
Professor Dr. Aires Camões

April, 2016

DECLARAÇÃO

Nome: Iman Ferdosian

Endereço electrónico: ferdosian.i@gmail.com

Título : Material Development and Self-healing Capacity of Eco-Efficient Ultra-High Performance Concrete (EEUHPC)

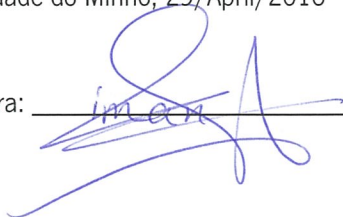Orientador: Professor Dr. Aires Camões

Ano de conclusão: 2016

Designação do Doutoramento: Civil Engineering

É AUTORIZADA A REPRODUÇÃO INTEGRAL DESTA TESE/TRABALHO APENAS PARA EFEITOS DE INVESTIGAÇÃO, MEDIANTE DECLARAÇÃO ESCRITA DO INTERESSADO, QUE A TAL SE COMPROMETE;

Universidade do Minho, 29/April/2016

Assinatura: _____
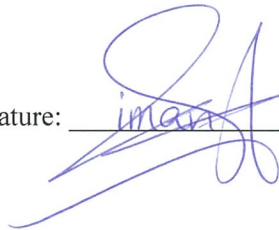
Statement of integrity

I hereby declare having conducted my thesis with integrity. I confirm that I have not used plagiarism or any form of falsification of results during the thesis elaboration.
I further declare that I have fully acknowledged the Code of Ethical Conduct of the University of Minho.

University of Minho, _____

Full name: Iman Ferdosian

Signature: _____

ACKNOWLEDGMENTS

I would like to express my sincere appreciation to my advisor, Professor Doctor Aires Camões for his wonderful mentorship, support, guidance and patience during this research.

I acknowledge the University of Minho and all its governing bodies for being a host institution throughout this PhD work.

I would like to thank the laboratory technicians for all their help to perform the experimental tests.

Special thanks go to all my dear friends in Portugal. Your delighted friendship was such a wonderful honor and pleasure particularly during the most challenging and hopeless moments.

I am profoundly grateful to my dearly beloved wife, Nava Naeimi. You are always the endless source of love, encouragement and support in my life. Your companionship would be the utmost blessing during my lifetime.

A deep-felt appreciation to my wife's family. I am sincerely grateful to my parents-in-law for all their support and loving-kindness. The mainspring of the decision for pursuing my education was not else but your extremely valuable suggestion, consultations and companionship.

Last, but certainly not least, I would like to express my heartfelt gratitude to my family. My parents are the heroes of my life. I am grateful of all your invaluable efforts and thank you for inspiring me since childhood for the love of science.

ABSTRACT

Ultra-high performance concrete (UHPC) is a promising type of self-compacting steel fiber-reinforced concrete, which exhibits extraordinary performances in its fresh and hardened states. It not only demonstrates ultra-high strength in compression, but also exhibits ultra-high durability characteristics. Since sustainability-related issues have become major priorities in the world ahead in recent years, therefore, a special attention to any product and service, particularly those used with an increasing pace and embrace considerable carbon footprint and substantial economic impacts, such as UHPC with high content of cement and silica fume, would be of great significance.

In this scope, this research aimed to develop an eco-efficient type of UHPC as an innovative and high-tech material through partially substitution of cement and silica fume by other pozzolanic industrial-waste materials. Response surface methodology (RSM), as a statistical mixture design tool, was applied in order to create a scientific basis for developing the optimum composition with higher environmental and economic efficiency. The performance of the optimum composition, nominated as eco-efficient UHPC (EEUHPC), was evaluated through standard test methods in its fresh and hardened states. Furthermore, an effective low-energy mixing procedure, with the aim of improved flowability, was introduced.

Finally, the autogenic self-healing ability of the material was studied as an important issue regarding the life cycle of the material and its capacity for structural recovery. The tests were carried out in short and long-term life of the material. Effect of different crack widths on self-healing capacity of cracked specimens was investigated as well as influence of steel fibers on energy absorption of samples in post-cracking stage.

Keywords

Ultra-high Performance Concrete; Eco-efficient UHPC; Silica fume; Fly ash; Mixture design; Response surface methodology; Autogenic self-healing; Sustainability; Durability; Energy absorption; Post cracking; Crack width.

RESUMO

O betão de ultra elevado desempenho (BUED) é um tipo de betão autocompactável reforçado com fibras bastante promissor e que é dotado de um desempenho extraordinário tanto no estado fresco como no estado endurecido. Este tipo de betão não só apresenta ultra elevada resistência à compressão como, também, é caracterizado por ultra elevada durabilidade. Nos últimos anos as questões relacionadas com a sustentabilidade passaram a ser consideradas prioritárias em todo o mundo. Portanto, passou a ser de importância acrescida garantir especial atenção a qualquer produto ou serviço, em particular os de utilização crescente compreendendo uma considerável da pegada de carbono e impacto económico substancial, tal como o BUED, fabricado geralmente com um teor de cimento e sílica de fumo elevados.

Neste âmbito, este trabalho teve como objetivo desenvolver um material inovador e de alta tecnologia, um BUED eco-eficiente, produzido com recurso à substituição parcial de cimento e sílica de fumo por subprodutos industriais com características pozolânicas. A definição das composições foi efetuada recorrendo à metodologia de superfície de resposta (MSR), uma ferramenta estatística que permitiu determinar, com base científica, as composições ótimas, com maior eficiência ambiental e económica. O desempenho da composição ótima, designada BUED eco-eficiente (BUEDEE), foi avaliado por intermédio de ensaios laboratoriais, realizados tanto no estado fresco como no estado endurecido. Além disso, foi também desenvolvido um processo de mistura eficaz e de baixa energia, concebido com o objetivo de melhorar a fluidez.

Finalmente, a capacidade de autorreparação autogénea do material foi estudada como uma questão importante relacionada com o ciclo de vida do material e com a sua capacidade de recuperação estrutural. Os testes foram realizados tanto em idades iniciais como a longo prazo. O efeito da abertura de fenda na capacidade de autorreparação dos provetes fendilhados foi avaliado, assim como a influência da presença das fibras metálicas na capacidade de absorção de energia de provetes em estado pós-fendilhado.

Palavras chave

Betão de ultra elevado desempenho; BUED eco-eficiente; Sílica de fumo; Cinza volante; Método de composição; Metodologia de superfície de resposta; Autorreparação autogénea; Sustentabilidade; Durabilidade; Absorção de energia; Pós-fendilhado; Abertura de fenda.

TABLE OF CONTENTS

LIST OF FIGURES

LIST OF TABLES

LIST OF ABBREVIATIONS

Abbreviation	Description
A.H.	After healing
AAI	Absorption after immersion
AAIB	Absorption after immersion and boiling
Al_2O_3	Aluminum oxide
ANOVA	Analysis of variance
B.H.	Before healing
BDAI	Bulk density after immersion
BDAIB	Bulk density after immersion and boiling
C.S.	Compressive strength
C_2S	Dicalcium Silicate
C_3A	Tricalcium Alluminate
C_3S	Tricalcium Silicate
C_4AF	Tetracalcium alumino ferrite
CaO	Calcium oxide
CCD	Central composite design
CEM	Portland cement
C-H	Calcium Hydroxide
Cl^-	Chloride ion
CMOD	Crack-mouth-opening displacement
C-S-H	Calcium silicate hydrate
DEF	Delayed ettringite formation
df	Degree of freedom
DOE	Design of experiments
EEUHPC	Eco-efficient ultra-high performance concrete
EPM	Elastic-Plastic Material
F.D.	Flow diameter
FA	Fly ash
FA D-30	Dry-milled fly ash for 30 minutes
FA W-240	Wet-milled fly ash for 240 minutes
FA W-360	Wet-milled fly ash for 60 minutes
FA W-60	Wet-milled fly ash for 360 minutes
f-CaO	Free lime

Fe_2O_3	Ferric oxide
FPW	First-part water
FRC	Fiber-reinforced concrete
H.S2	Healed step 2
LOP	Limit of proportionality
LVDT	Linear variable differential transformers, linear variable displacement transducers
MgO	Magnesium oxide
MK	Metakaolin
N.H.S2	Non-healed step 2
NC	Normal cured
O-FA	Original fly ash
PRESS	Predicted Residual Sum of Squares
RPC	Reactive powder concrete
RPM	Rotations per minute
RSM	Response Surface Methodology
SCC	Self-compacting concrete
SF	Silica fume
SFF	silica fume-free
SFRC	Steel-fiber-reinforced concrete
SH	Self-healing
SiO_2	Silicon Dioxide
SMD	Statistical mixture design
SO_3	Sulfur trioxide
SP	Superplasticizer
SSD	Saturated-surface-dry
SSM	Solid Suspension Model
St.F	Steel fiber
Std. Dev.	Standard deviation
StdErr	Standard error
TWC	Tempered-water cured
UFFA	Ultra-fine fly ash
UHPC	Ultra-high performance concrete
V.Lq.SP/V.P	Volume of liquid SP/ volume of powder
V_f	Volume fraction
VIF	Variance Inflation Factors
W/B	Water/binder
Wt	Weight fraction
W_t.S.SP/V.P	Weight of solid particles in SP/volume of binder

Chapter 1

Introduction

1.1 Introduction

Ultra-high performance concrete (UHPC) is a high-tech construction composite material with extraordinary mechanical and durability characteristics such as self-compactness, compressive strength higher than 150 MPa, and sustained post-cracking tensile and flexural strength as a function of internal fiber reinforcement (Graybeal, 2011). This material also demonstrates extraordinary resistance to aggressive environments due to its discontinuous pore structure. Another characteristic of UHPC is its very low water/binder content, less than 0.2 w_t., with respect to its sufficient workability, through using high-range water reducing admixtures as well as high packing density of its granular ingredients. Nevertheless, due to the high cost and environmental impacts of UHPC its application has been scarce so far and it is not expected to be a top-consumed type of concrete in near future. Therefore, in order to widespread its application, reduction of its cost and environmental impacts would be a

mandatory task to obtain a sustainable type of UHPC. In recent years, this material has been applied in several real-scale structural and architectural projects including bridges, highways, high-rise buildings and other infrastructures. In this regard, many researches have been fulfilled in order to study the structural and environmental behavior of UHPC in various applications and conditions. Besides, many attempts have been done in order to produce UHPC with conventional materials and technologies aiming at reduction of environmental impacts of this new material. With respect to presented similarities and differences existed in reports, an undeniable fact is the high potentiality of UHPC for any application that has been far beyond our ability so far. Nevertheless, more works is needed in order to reduce the environmental impact of UHPC, due to its high cement content, as well as studying its durability-related characteristics such as chloride and carbonation resistance.

The research presented herein, aimed at optimizing UHPC mixture in order to minimize its cement content, resulting in lower embodied CO_2, through cement substitution with other pozzolanic materials particularly fly ash with very low embodies CO_2. Finally studying self-healing ability of UHPC helps for better understanding of its durability characteristics, which is a useful criterion regarding service life of the material.

1.2 Motivation

Based on the current focus on sustainability and due to ever-increasing anthropogenic CO_2 emissions, leading to global warming phenomena, and with respect to the fact that cement industry contributes to almost 5% of anthropogenic CO_2 emissions, studying UHPC with high cement content and as one of the most durable types of concrete would be of great importance. In other words, UHPC plays two

simultaneous significant role from both economic and environmental point of view, which in turn brings more social value to humanity.

From another perspective, UHPC brings many advantages to construction industry, which motivates any researcher to study its characteristic profoundly from either material or structural point of view. These advantages include:

- Possibility of slim section design resulting in lower cement consumption and less quantity of material in structural members, which all mitigate the final price and improve the sustainability of the projects as well.

- Longer service life and durability with low permeability against aggressive environments and agents, compared to conventional or even high-performance concretes as well as structural steel, which also leads to save long-term service and maintenance costs which finally defines UHPC as a more sustainable material and gives the possibility of using UHPC for many applications (Voo & Foster, 2010).

- Immediate project costs and time saving through:

   1. Elimination of a significant part of the reinforcement bars and secondary shear reinforcement, due to improved tensile behavior of UHPC (Voo & Foster, 2010; Voo, et al., 2006);

   2. Decreased considerable human labors, supervision tasks and quality control activities as result of ease of installation process of lightweight slim UHPC members including handling and transportation, which would be also more convenient and safer as well as self-compactness of UHPC without any vibration.

- More aesthetical value through enabling architects to design buildings more

freely and more flexible;

- Low creep and shrinkage, concerning structural design and long-term behavior,

UHPC would be one of the best choices to be used in a) aggressive environments such as many bridge structures; b) when the dead loads are an important issue during the construction phase; c) in special cases with high fatigue and impact loads; and d) in particular architectural cases for instance very thin balconies (**Figure 1.1**).

Figure 1.1: Balconies by Hi-Con® (HiCON, 2016).

The third reason, which gives motivation for this research study, is attached to fly ash consumption as a supplementary pozzolanic material for cement replacement. Fly ash is available in huge quantities worldwide as an industrial waste material from thermal power plants. It bears very low cost and environmental impacts particularly with respect to the fact that its application prevents the massive landfills used by this waste material (see **Figure 1.2**). It was reported that 100 and 136 million tons of coal ash per year feeds landfills and ponds in Europe and USA respectively (Kaufman, 2011). In addition, UHPC is usually made with high quality materials turning its cost a great hindrance to its widespread usage compared to conventional or even high-performance concretes. Therefore, developing an UHPC with lower cost and environmental impacts, which is capable to contribute to its worldwide application, would be of great significance.

Figure 1.2:   Typical fly ash landfills (Girard, 2011; Lester Lefkowitz, 2006).

1.3   Objectives

The main research objectives include:

- Investigating optimum, namely cost-efficient and eco-efficient, UHPC mixtures with the help of Response Surface Methodology;

- Application of fly ash with the aim of silica fume and cement substitution in UHPC to meet two key indicators of sustainability, those are economy and environmental criteria, through cost and CO_2 footprint mitigation;

- Studying self-healing ability of EEUHPC as a criteria for durability assessment and evaluation of EEUHPC;

1.4   Summary of Approach

This research project includes three experimental and two numerical phases. The first experimental phase is related to the mix design of EEUHPC. It consists of 4 steps: a) studying the effect of FA particle size on paste fluidity; b) studying the saturation dosage of superplasticizer and its interaction with different cementitious materials namely cement, silica-fume and fly ash; c) investigating a proper mixing procedure to develop high-fluidity cementitious pastes; and d) preparing 5x5x5 cm^3 sample cubes

for optimization process of UHPC.

The second experimental phase is related to material characterization of developed EEUHPC including compressive strength, modulus of elasticity, direct tensile test, 3-point bending test, 4-point bending test, water absorption through capillary and immersion, chloride ion diffusion, and carbonation test.

The third experimental phase includes studying self-healing ability of EEUHPC. For this aim, the absorbed energy of 4x4x16 cm^3 notched prisms under 3-point flexural test in their early age and long age before and after healing period of the samples were measured. The samples were cracked with different crack mouth opening sizes and their energy-absorption ability during the elastic phase, before and after healing period, were assessed as a criterion for self-healing ability of EEUHPC.

The first analytical phase was performed through Response Surface Methodology (RSM) with the help of Design-Expert® software in order to statistically analyze the experimental results, elaborate mathematical models regarding our goals, and finally optimize UHPC to meet this research goal, that was to find out an eco-efficient mixture.

The second numerical phase as mentioned before was performed in order to study the self-healing ability of EEUHPC in early age as well as long term age through analyzing the energy absorption of cracked prisms under 3-point-flexure test.

1.5   Outline of Thesis

This thesis is divided in 8 chapters. Chapter 1 presents a brief introduction to the UHPC, its advantages and the goals of current study as well as an overall view to the methods and tools that have been applied herein. Chapter 2 is a state-of-the-art one and presents relevant background information in the area of UHPC and its self-healing ability. In chapter 3 the materials applied in this study particularly fly ash, with respect

to its particle size and its enhancement method, were discussed. In addition, this chapter

includes detailed study on saturation dosage of SP and the best mixing procedure to

develop UHPC with respect to its self-compacting ability. Chapter 4 includes the

detailed explanation of RSM and the way it was employed to optimize UHPC. At the

end of this chapter, two solutions as cost-efficient and eco-efficient mixtures are

proposed. Chapter 5 explains the characterization of proposed eco-efficient

composition, obtained in the previous chapter as EEUHPC, including mechanical and

durability related test results as well as fiber distribution. Chapter 6 presents

self-healing ability of EEUHPC. Both experimental and analytical phases related to this

issue are fully described in this chapter. In chapter 7, the main conclusions of the current

research program beside proposed topics for future researches are presented. Finally,

the last chapter includes bibliography and references used in this thesis. Three annexes

also can be found at the end of the thesis indicating the individual test results and

detailed information related to each chapter.

Chapter 2

Background and

Overview to UHPC

This chapter tries to provide a complete review to UHPC. This review includes definition of UHPC, its first development methodology and the common materials and constituents that could be applied. The approaches to develop UHPC are studied as well. The chapter is continued by explanation of some characteristics of the material in fresh and hardened state. Some of the known applications of UHPC are mentioned in the following part and finally the significant advantages of UHPC in construction industry are enumerated. The chapter is followed by a review about statistical techniques regarding mixture design and its application in concrete production. Finally, it describes the characteristics concerned with self-healing of UHPC and the methods used to heal the cracked material and techniques for

self-healing verification.

2.1   Definition

By definition, UHPC, also designated as reactive powder concrete (RPC), is a composite material composed of cementitious materials plus an optimized particle size of granular ingredients with eliminated coarser aggregates, a water/binder ratio less than 0.25 ($w_t.\%$), and a high content of internal fibers plus high-range water-reducing admixtures. The compositions of first UHPC mixtures, introduced under the titles of RPC 200 (compressive strength: 170-230 MPa) and RPC 800 (compressive strength: 410-890 MPa), are depicted in **Table 2-1** (Richard & Cheyrezy, 1995).

Table 2-1: The first composition of UHPC.

	RPC 200				RPC 800	
	Non fibered		Fibered		Silica aggregates	Steel aggregates
Portland Cement	1	1	1	1	1	1
Silica fume	0.25	0.23	0.25	0.23	0.23	0.23
Sand 150 – 600 µm	1.1	1.1	1.1	1.1	0.5	-
Crushed quartz d_{50} = 10 µm	-	0.39	-	0.39	0.39	0.39
Superplasticizer (Polyacrylate)	0.016	0.019	0.016	0.019	0.019	0.019
Steel fiber L=12 mm	-	-	0.175	0.175	-	-
Steel fiber L=3 mm	-	-	-	-	0.63	0.63
Steel aggregates <800 µm	-	-	-	-	-	1.49
Water	0.15	0.17	0.17	0.19	0.19	0.19
Compacting pressure	-	-	-	-	50 MPa	50 MPa
Heat treatment temperature	20°C	90°C	20°C	90°C	250-400°C	250-400°C

Based on definition of mortar existed in "The European Guidelines for Self-Compacting Concrete" (BIBM, et al., 2005), UHPC can also be defined as a high-tech mortar with improved characteristics. However there is not yet a consensus on the range of mechanical properties of UHPC, it is supposed to have compressive

strength greater than 120 MPa in normal curing conditions (Graybeal, 2011) and greater

than 150 MPa (Voo & Foster, 2010), even feasible reaching 250 and 800 MPa, after

special curing regimes (Resplendino, 2004; AFGC, 2002; Richard & Cheyrezy, 1995).

In addition, its sustained post-cracking tensile strength is greater than 5.0 MPa. Besides,

due to discontinuous pore structure of UHPC in its hardened state, it demonstrates

enhanced durability characteristics, resulted from reduced liquid permeation, compared

to conventional and high-performance concretes (Aïtcin, 1998). This ultra-high

performance material offers a variety of interesting applications since as mentioned in

preceding chapter it allows sustainable and economic construction with slim and

flexible design. Furthermore, due to its high strength and post-cracking behavior as well

as enhance durability characteristics it would be an ideal material for bridge industry,

shell structures, high-load bearing columns and aggressive environments. As reported

by (Schachinger, et al., 2008), UHPC has also the ability to get more strength even after

6 years as a result of continuous but slow pozzolanic reaction of pozzolans producing

more C-S-H products which makes UHPC a unique material.

Since another characteristics of UHPC is its self-compacting or self-consolidating,

first a precise definition of self-compacting concrete (SCC) would be necessary. As

Association Française de Génie Civil (AFGC) defines, a type of concrete with enough

fluidity, homogeneity and stability enabling casting just with gravity and without any

compaction would be defined as SCC (AFGC, 2000). As this recommendation states,

minimum 55 cm slump-flow diameter is required. For this aim, optimizing particle size

and using high-range water reducing admixtures are of great importance.

2.2 Background of Ultra-High Performance Concrete

According to (Resplendino, 2004), the first investigations on UHPC were carried out by Bouygues from 1990 to 1995. However, it was reported by (Blais & Couture, 1999) that Densit® (Densit, 2016) had developed a kind of UHPC in 1960's. Nevertheless, the first composition of UHPC, designated as reactive powder concrete, has been reported in 1995 (Richard & Cheyrezy, 1995). Since 1994 research on Ductal® started as a collaborative result of three companies, Lafarge, Bouygues and Rhodia (Acker & Behloul, 2004).The first reactive powder concrete structure, made of Ductal®, is the 60 m span Sherbrooke footbridge in Quebec, built in 1997 with a compressive strength of 200 MPa (Blais & Couture, 1999).

In parallel to the three mentioned companies, it was in 1996 that the Eiffage company started to manufacture a type of UHPC, designated as Béton Spécial Industriel (BSI), followed by French and European patents registered by this company in 1998 and 1999. Their product was used in the world first road bridge in France. Then after and since 2000, Sika started a partnership with Eiffage and developed a similar material called it Ceracem® without requiring any post-heat curing beside using aggregate size ranged between 0 and 7 mm (Maeder, et al., 2004; Hajar, et al., 2004).

The firs French recommendations for UHPC was published in 2002 in three chapters including characterization of UHPC such as mechanical performance, design and analysis of UHPC structures and durability of UHPC (AFGC, 2002).

2.2.1 UHPC constituent materials

The main constituent materials existing in most of UHPC compositions include cement, silica fume, filler such as glass powder or silica powder, fine sand, superplasticizer, steel fiber, water and other cementitious materials such as fly ash or

ground granulated blast-furnace slag. Some known compositions of UHPC are depicted

in **Table 2-2**.

Table 2-2: Typical UHPC compositions and its constituent materials (w_t.%).

Cement	Silica fume	Fine Sand	Filler	Glass Powder	SP	Steel fiber	Water	Reference
1	0.25	1.1	-	-	0.016	0.175	0.17	(Richard & Cheyrezy, 1995)
1	0.32	1.42	0.3	-	0.027	0.27	0.28	(Blais & Couture, 1999)
1	0.324	1.43	0.3	-	0.043	0.21	0.15	(Graybeal, 2006)
1	0.25	0.92	-	0.25	0.0108	0.22-0.31	0.18-0.2	(Wille, et al., 2011)
1	0.16	1.17	0.25	-	0.041	-	0.23	(Mazanec & Schießl, 2008)
1	0.32	1.43	0.3	-	0.025	-	.265	(Tam & Tam, 2012)
1	0.25	1.1	0.3	-	0.012	0.02 *	0.25	(Yoo, et al., 2013)
1	0.32	1.43	0.3	-	0.02	-	0.32	(Ng, et al., 2010)
1	0.25	1.1	0.4	-	0.035	0.02 *	0.23	(Murthy, et al., 2013)
1	0.25	1.48	-	-	0.052	0.2	0.188	(Tayeh, et al., 2012)
1	0.27	1.25	0.5	-	0.01(s)	0.29	0.28	(Voit & Kirnbauer, 2014)
1	0.2	1.38	0.42	-	0.049	0.134	0.28	(Ghafari, et al., 2015)
1	0.2	0.81	0.34	-	0.02	-	0.24	(ZDEB, 2013)
1	0.32	1.43	0.3	-	0.024	0.27	0.276	(Dallaire, et al., 1998)

∗ Volume fraction

2.2.1.1   Cement

Cement plays the most significant role, with respect to sustainability, in UHPC. In

this regard and to minimize the negative impacts of cement its type as well as its content

should be studied very carefully regarding strength, workability, cost and its

environmental impacts on UHPC.

According to the following studies, cement 42.5R shows its efficiency for

developing UHPC. Scheydt, et al., (2008) investigated that cement 42.5R in the mortar

exhibits lower plastic viscosity leading to 18% higher flowability while it reveals 5%

lower compressive strength after 7 days of heat curing at 90°C compared to cement

52.5R with higher Blaine specific surface value (Scheydt, et al., 2008). Furthermore,

the spread flow diameter and flow time of mortar including cement 42.5R is hardly affected by the time of adding the superplasticizer. On the other hand, cement 52.5R is highly sensitive to the addition method of superplasticizer (Tue, et al., 2008).

With respect to cement substitution by other pozzolanic or even non-pozzolanic materials, Wang (2014) indicated that with water/binder ratios of 0.18, 0.25 and 0.4, the highest degree of cement hydration is 40%, 60% and 90% respectively. Furthermore, in UHPC with water/binder and silica fume/cement ratios of 0.18 and 0.3 respectively, just around 15% of silica fume, as an expensive material, reacts in pozzolanic activity and the rest remain as filler. The proposed model by author for compressive strength of UHPC with 0.18 and 0.3 water/binder and silica fume/cement respectively, showed that the strength evolves very fast up to 28 days however, the 90-days compressive strength is around 21% higher than the 28-days compressive strength and after that the changes are negligible (Wang, 2014). These results conforms to other researches. For instance, it was studied that in a plain cement paste, with 0.19-0.24 W/B ratio, just 50-60% of cement is hydrated at the age of 90 days and the rest of cement remain as filler in the matrix (Poon, et al., 2000). As a result, application of other pozzolanic and non-pozzolanic materials, known as fillers, not only do not deteriorate the fresh and hardened properties of UHPC but also can add environmental and economic value to UHPC. As an example, quartz powder, as filler, with a mean particle diameter of 16 μm has proved its efficiency to be applied in UHPC (Cwirzen, et al., 2008; Lee & Chisholm, 2005). In addition, some pozzolanic reactivity of the quartz powder after 48 hours of heat treatment at temperatures higher than 200°C has been observed (Cwirzen, et al., 2008). The other cementitious and non-cementitious powders can be seen in **Table 2-2**. Recently four optimum mixture regarding compressive strength, fluidity, steel fiber and cement content have been introduced.

The best eco-efficient composition has a cement and steel fiber content of 669 and

90 kg/m³ and a compressive strength and table flow of 151 MPa and 200 mm

respectively without heat curing. It was also showed that quartz flour with particle size

lower that 10 μm could enhance both compressive strength and flowability (Ghafari, et

al., 2015).

2.2.1.2   Supplementary cementitious materials

As mentioned in the previous sections supplementary cementitious materials can

play two distinct roles simultaneously. First, they contribute to the cement hydration to

react with C-H products and build new C-S-H gels those improving the mechanical

properties of concrete based on following reactions:

$$2C_3S + 6H \rightarrow C_3S_2H_3 + 3CH \tag{1}$$

$$2C_2S + 4H \rightarrow C_3S_2H_3 + CH \tag{2}$$

$$Pozzolan + CH \rightarrow C\text{-}S\text{-}H \tag{3}$$

Second, they work as filler and fill the gaps between coarser particles such as

aggregates and even cement. Regarding their first role, the degree of pozzolanic

reaction of supplementary cementitious materials is highly dependent on their mean

diameter. In other words, the finer the pozzolans, the higher the degree of hydration

(Niu, et al., 2002). The authors showed that with increasing the surface area of the

pozzolans, 3 and 28 days compressive strength increase. On the other hand, by the

increase in the pozzolan content by more than an optimum level, in the mortar of cement

and pozzolan, the compressive strength will decrease.

The most famous pozzolans, widely used in concrete industry, are silica fume, fly

ash, rice hush ash, ground granulated blast-furnace slag and metakaolin.

2.2.1.2.1 Metakaolin (MK)

Metakaolin ($Al_2Si_2O_7$) is a highly reactive pozzolanic material. It is formed after dehydroxilization or thermal activation of kaolin clay at a temperature between 500°C and 800°C. Kaolin itself is a fine and white clay that traditionally has been used in porcelain production. Kaolinit, chemically known as hydrated aluminum disilicate, is the main constituent of kaolin (Siddique, 2007).

UHPC containing MK demonstrates low workability rather than other ultra-fine pozzolanic materials with the same SP dosage and water to binder ratio. However, as Li & Ding (2003) explain, by incorporating 20%-30% ultra-fine slag in a paste containing 10% MK, not only the fluidity improves, but also the compressive strength of the blend increases. The reason why MK degrades the concrete fluidity is that it tends to absorb water to turn to deactivate kaolin (Li & Ding, 2003). On the other hand, concrete incorporating MK in a ratio of 10% cement replacement, has the best compressive strength compared to plain cement concrete (Li & Ding, 2003; Zhang & Malhotra, 1995; Balogh, 1995). In addition, concrete incorporating MK shows faster strength at early ages rather than silica fume concrete however, it falls behind after 28 days. Furthermore, concrete incorporating MK shows lower drying shrinkage in 28 days rather than plain cement concrete and silica fume concrete as well. It also reveals outstanding results in the freezing and thawing test (Zhang & Malhotra, 1995).

2.2.1.2.2 Silica fume

Silica fume is another pozzolanic material with very high reactivity due to its fine particles, large surface area, and high SiO_2 content in vitreous phase. It is a byproduct of silicon metal or ferrosilicon alloys which remains like a smoke after furnace operation and combustion of quartz, coal, and woodchip. Rather than being landfilled,

it plays an important role in high-strength concrete as a mineral admixture (SFA, 2014).

Silica fume plays three basic roles in concrete: a) as filler, to fill the gaps between coarser particles such as cement b) as rheology enhancer, through lubrication effects of its spherical particles, and c) C-S-H producer, by pozzolanic reaction with $Ca(OH)_2$ produced from cement hydration (Richard & Cheyrezy, 1995).

Generally, silica fume to cement ratio in weight for UHPC is about 0.25 corresponding to its filling-ability function and its contribution to pozzolanic reaction however, it is more than enough for pozzolanic activity (Richard & Cheyrezy, 1995). It was investigated that silica fume in suspension state causes more fluidity and compressive strength since it prohibits the agglomeration of silica fume. In other word, silica fume could be dispersed better resulting better interaction in the cement hydration process to make C-S-H gel (Terzijski, 2004).

Replacement of cement with silica fume increases the strength of mortars and concretes with any w/c ratio as a result of improved bond between paste and aggregates as the result of non-porous interfacial zone which interlocks the paste and aggregate matrix (Toutanji & El-Korchi, 1995). On the other hand, as authors stated, it does not improve the paste strength, particularly in the cases of w/c ratio less than 0.22, resulting self-desiccation due to lack of water. According to this research and with respect to workability, the silica fume/cement mortars demonstrate higher workability compared with silica fume/cement paste.

2.2.1.2.3 Fly ash

Pozzolanic reaction in hydration process of fly ash/cement concrete is mainly influenced by the fly ash content and water to binder ratio (Poon, et al., 2000). Nevertheless, it has been observed that in a concrete where 45% to 55% w_t. of its

cement has been replaced by fly ash, around 20% of fly ash could react with hydration products during 90days of curing and the rest (80%) remains unreacted and just works as micro aggregate (Lam, et al., 2000; Poon, et al., 2000). Experiments also have shown that fly ash in concretes with low water/binder ratio has higher contribution in strengthening rather than concretes with higher water/binder ratio (Poon, et al., 2000). Other findings (Hashimoto, et al., 2011) confirms that by replacement of 15% of cement with classified fine fly ash the water content could be reduced by 5 to 10 kg/m^3 producing a concrete with almost equal compressive strength compared with conventional concrete. Furthermore, by limiting fly ash average particle size from 20 μm to 8 μm both physical and chemical properties of fly ash increases due to their higher quality, sphericity and uniformity of particles compared with normal particles containing internal voids (Hashimoto, et al., 2011). Fly ash can react as well as silica fume when UHPC is heat or autoclave treated (Müller, et al., 2008).

As Paya, et al. (1995) studied, cement substitution by fly ash up to 60% reduces required water for the same mortar flow table particularly for finer fly ash. Based on this fact, increase of very fine fly ash dose not reduce the compressive and flexural strength of concrete significantly. They also studied that the particles finer than 10 μm are responsible for enhancement of strength. In other words, a good correlation between particle fineness and strength could be found. Furthermore, in higher curing temperature the pozzolanic reactivity of fly ash is higher resulting in enhancement of compressive and flexural strength (Paya, et al., 1995).

It should not be overlooked that the extra usage of pozzolanic materials in conventional concrete may cause self-neutralization as a consequence of C-H consumption. It causes a reduction in pH level, which can results in dissolution of other hydration products that finally leads to deterioration of concrete matrix (Groves &

Richardson, 1994).

2.2.1.3 High-range water reducer

In general, two generation of superplasticizer (SP) exist: a) the traditional ones, such as naphthalenesulfonate, vinyl copolymers or melamine sulfonate, including long chains carrying negative charges to produce electrostatic repulsion and preventing cement particle to stick to each other, and b) new generation of SPs having ionic function. They separate cement particles with steric repulsion through their polyether chains, (Maeder, et al., 2004).

For better understanding of the chemical process of dispersion of cementitious minerals by polycarboxylate-based superplasticizers, it was demonstrated that the plasticizing effect is attributed to the adsorption of anionic SP particles to cement particles, confined by Ca^{2+} as a positive layer from the cement dissolution in water (Yu, et al., 2013). According to this study, as time elapses, the C_3S and C_2S are consumed, C-S-H gels are gradually formed and the number of positive particles, adsorbing the SP chains, reduces. In this regard, the addition time of SP with respect to highest fluidity is during the first 15 minutes after adding water to cement and particularly between first 2 and 3 minutes (Hsu, et al., 1999). Another recent experiment also confirms that stepwise and particularly delayed addition of SP, which mean adding SP in two stages and also not adding all the SP with water at the beginning, could improve the flowability of UHPC by more than 25% compared to direct addition of SP with or immediately after water addition (Tue, et al., 2008). Despite these studies, some experiments have been carried out just using stepwise addition of SP (Rougeau & Borys, 2004; Schachinger, et al., 2004) and some with direct addition method (Ewert, et al., 2008). However, SP in general reduces the heat of hydration in early stage due to the delayed

reaction of C_2A and C_3S, but the reaction is compensated by passing the time (Šiler, et al., 2014).

Super-retarding poly carboxylic acid water reducing agents could be more preferable in some cases such as high-volume concrete constructions in which the time of fluidity as well as heat of hydration are considerable. In other words, this type of SP can retain good slump for longer time and retard the setting time for more than 20 hours. Moreover, the maximum heat of hydration could be mitigated by 20% at around 50 hours after mixing compared with 10 hours of plain mixtures with a broaden hydration peak. Besides, they remain more fluid in any temperature compared to other SP (Li, et al., 2013).

2.2.1.4   Steel fibers

The role of fibers is to improve the post-cracking toughness and enhance the energy absorption capacity as well (Ferrara, et al., 2007). Incorporation of steel fibers reduces the flowability of concrete while increases its strength (El-Dieb, 2009). Fiber content, aspect ratio and their type are three main parameters influencing the hardened and fresh properties of SCC. In this regard, fiber content plays the most important role while aspect ratio and type are in the next level of importance (Johnston & Zemp, 1991). Findings of the research by Johnstone & Zemp also indicate that, the minimum applicable percentage of steel fiber, in volume fraction (V_f.), and its corresponding aspect ratio regarding flexural fatigue loading are 1% and 70 respectively. By this content of steel fiber, it has also been observed that the permeability of cracked concrete is reduced compared to lower steel fiber content (Rapoport, et al., 2002). As Aïtcin (2011) explains, high and ultra-high performance concretes are highly sensitive to fibers' length, diameter and ultimate stress compared to usual concretes. In fact, due to

very strong bond between the matrix and the fibers in high performance concretes, the resisting bond strength exceeds the ultimate tensile strength of fibers. Therefore, before occurring the pull-out phenomenon the fibers break resulting in slightly stronger but yet brittle material. To overcome this deficiency and to enhance the toughness of the material, two ways have been suggested namely increasing the tensile strength of the fibers as well as applying shorter fibers with smaller diameter (Aïtcin, 2011). As the author clarifies, the first solution prevents the fibers failure before their debonding from the matrix and the second way decreases the bond strength so that the ultimate tensile strength of the fibers remain higher than the bonding stress. In addition, by applying the second method, including smaller fibers, more fibers will exist per unit volume of concrete resulting in a more uniform reinforced matrix compared to conventional steel fiber-reinforced concretes. Accordingly, although micro steel fibers seems beneficial for developing UHPC, more investigations are required with respect to their cost and particularly their negative impact on workability. In this regard, based on a statistical model, using response surface methodology (RSM), it has been shown that the best percentage of steel fiber, to meet self-compactness criteria in UHPC, is 1.75% (V_f.) of hybrid steel micro-fibers with diameter of 0.15 and 0.2 mm and length of 10 and 13 mm respectively, (Ghafari, et al., 2014). According to the concluding remarks of this research, to meet three objectives namely self-compactness, highest flexural strength, and lowest micro-steel fiber content simultaneously, hybrid micro-steel fiber with length of 10 mm and 13 mm and diameter of 0.15 mm and 0.2 mm in a ratio of 1% for shorter one and 1.1% for longer one, are required. For the same reason, however by increasing the volume fraction of steel fiber from 1% to 4%, compressive and flexural strength increase 20% and 82% respectively, flow-spread value decreases significantly (Xiao, et al., 2014). Another study also shows that 1% (V_f.) of steel fiber would be an

efficient quantity with respect to the load-carrying capacity of the specimens under four-point flexure test (Naghibdehi, et al., 2014).

2.2.2   UHPC characteristics and performance criteria

The general properties of UHPC in its fresh and hardened states are depicted in **Table 2-3**. Beside the values reported by authors in this table, slump-flow diameters ranging from 600 mm to 800 mm have been also reported (Ferrara, et al., 2007; Brouwers & Radix, 2005; Felekoglu, et al., 2007). As Voo (2010) has stated a flow-table diameter in range of 170 mm-190 mm generates the same values regarding slump-flow diameter. However, with increasing the flow diameter from 130 mm to 230 mm the compressive strength decrease linearly (Voo & Foster, 2010). These findings are in perfect conformity with values reported by Graybeal (2005). As he had also stated, flow-table diameter between 150-185 mm for initial flow and between 180-210 mm after 20 drops in 20 seconds fulfils the self-compacting ability of UHPC (Graybeal, 2005).

Table 2-3: Some performance criteria for UHPC.

Flow (mm)	Compressive strength (MPa)	Elasticity Modulus (GPa)	Poisson's ratio	Tensile strength (MPa)	Flexural strength (MPa)	Reference
170-190	150	45	0.19	5.5	22.5	(Voo & Foster, 2010)**
-	170	50	-	-	30	(Richard & Cheyrezy, 1995)
-	199	-	-	-	30	(Maeder, et al., 2004)
-	175	64	-	8	-	(Hajar, et al., 2004)*
	189	-	-	-	30.1	(Yiğiter, et al., 2012)
-	150.6	45.6	-	9.07	-	(Hassan, et al., 2012)**
	165.6				18.3	(Allena & Newtson, 2011)***

*   Steel fiber 3% V_f
**   Steel fiber 2% V_f
*** Steel fiber 1.5% V_f

2.2.3   Approaches to Obtain Ultra-High Performance Concrete

2.2.3.1   Elimination of coarse aggregates

According to research performed by Richard & Cheyrezy (1995) and due to the fact that reaching high compressive strength is a prerequisite for UHPC, one of the first and most important principles to develop UHPC is elimination of the coarse aggregates. Obviously coarser aggregates due to their higher hardness and Young's modulus compared to the paste lead to ununiformed stress distribution in the material resulting in heterogeneousity and lower strength. Coarser aggregates removal also leads to higher compacted density, which would be beneficial for strength, durability and self-compacting ability of UHPC. In this regard, coarse aggregate elimination and replacing them with finer sand with a maximum size of 600 μm, improves mechanical characteristics of the paste and finally reduces the aggregate/paste ratio as a key parameter to overcome this heterogeneity (Richard & Cheyrezy, 1995). To eliminate or improve this deficiency, the size of coarse aggregate should be limited or stronger types should be selected (Aïtcin, 1998) because in some cases, the aggregate strength governs the compressive strength of concrete and not the quality of cement paste.

Elimination of coarser aggregates also facilitates the rolling down and sliding effect of particles during casting. In other words, friction between coarser aggregates reduces the slump-flow and the filling-ability of concrete in general. To overcome this problem a high volume of paste including cement, pozzolanic materials, admixtures, water and air is required to surround and separate the aggregates, which results in lower friction between aggregates (AFGC, 2000). However, such a high paste content can deteriorates other concrete properties such as its strength, cost and eco-efficiency. Therefore, another way to ensure high workability without further consumption of just paste and

its related negative impacts, is using higher fine particles (smaller than 125 µm) including cement, pozzolanic materials and particularly aggregates (Wang, et al., 2012; Martirena, et al., 2004).

2.2.3.2 Application of pressure

The other principle reported by Richard & Cheyrezy (1995), is using pressure or autoclaving during and after setting time, which improves the compacted density of concrete. Beside higher density, the application of pressure has also other advantages such as entrapped air bubbles reduction and excess water removal as well which reduces the water to binder ratio resulting a denser and more durable concrete.

2.2.3.3 Microstructure enhancement by heat curing (HC)

The microstructure and the mechanical performance of UHPC could be improved by heat curing at 90°C and ambient pressure as a consequence of accelerated pozzolanic reactions (Richard & Cheyrezy, 1995). According to scientific recommendations of AFGC (2002), by heat treatments the UHPC can reach to its final maturity without waiting for long periods of normal curing, which is of great importance for prefabrication industry beside the minimum amount of autogenous shrinkage and creep (AFGC, 2002). The reason for this early maturation is that by increasing temperature, in heat curing method, the cement hydration and also the pozzolanic activity increases (Cheyrezy, et al., 1995). For instance, the pozzolanic ratio of heat curing in temperatures of 20, 50, 100, 200 and 250°C would be around 72%, 80%, 92%, 92% and 97% respectively. The authors also, through thermo-gravimetric analysis, showed that just 40% to 60% of cement in reactive powder concrete remains un-hydrated. Besides, it was investigated that in a curing temperature higher than 90°C, water starts to be extracted from concrete, which results in a more compacted matrix. Furthermore,

it has been observed some pozzolanic reactivity of the quartz powder after 48 hours of

heat treatment at temperatures higher than 200°C (Cwirzen, et al., 2008).

2.2.3.4   High packing density through granular matrix optimization

It is clear that special heat and pressure curing methods carrying environmental and

economic impacts as a result of their high cost and energy consumption. Besides that,

application of these methods is infeasible in most of real-scale or in-situ projects. To

overcome these problems as well as improving mechanical properties of UHPC with

simple heat-curing conditions, which would be feasible in any pre-fabrication plants or

even on-site applications, one way is to optimize the granular skeleton of UHPC. This

optimized matrix results in highest packing density of the ingredients as a whole, which

in turn demands lower water and causes denser matrix as well, which all finally result

in advanced workability, strength and durability. In other words, low packing density

produces low workability, resulting in higher water demand and consequently higher

cement content. Similarly, filling the gaps between cement particles also plays an

important role for making UHPC (Geisenhanslüke & Schmidt, 2004).
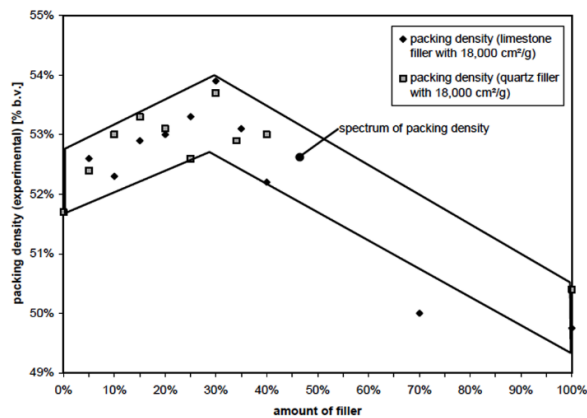
Figure 2.1:   The impacts of fillers on packing density of cement-filler mix (Geisenhanslüke & Schmidt, 2004).

As demonstrated in **Figure 2.1**, the highest packing density for cement and limestone filler blend could be achieved with a cement/filler ratio of 0.7/0.3. Furthermore, the higher amount of filler worsens the packing density compared with pure cement content. It was also monitored by Geisenhanslüke & Schmidt (2004) that packing density is well correlated with concrete viscosity in its fresh state. As depicted in **Figure 2.2**, the maximum packing density results in a lower viscosity, which means better flowability.
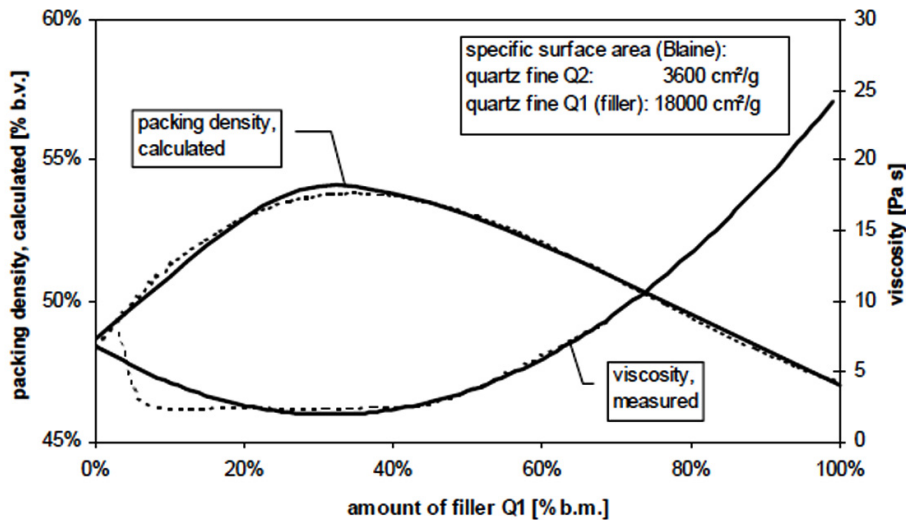
Figure 2.2:   Correlation between packing density of two kinds of filler for cement and the mortar viscosity (Geisenhanslüke & Schmidt, 2004).

Since cement is the coarser constituent of paste with a mean particle size (d_0) around 20 μm, based on Horsfield model (Fayed & Otten, 1997), addition of particles with a mean diameter less than $0.414d_0 = 8.28$ μm and $0.225d_0 = 4.5$ μm may fill the tetragonal and triangular voids among the cement particles respectively and produce a denser matrix as well. One of the models, showed its efficiency regarding packing density, was Solid Suspension Model (SSM) resulted in a homogeneous UHPC with compressive strength of 236 MPa (de Larrard & Sedran, 1994). Another compacting method widely

used with respect to self-compactness of ordinary concrete, is based on the model

proposed first by Fuller and Thompson (Fuller & Thompson, 1907) and then Andreasen

and Andersen (Andreasen & Andersen, 1930). Based on the proposed model, the

highest packing density as well as minimum porosity could be achieved by an optimal

particle size distribution for all granular ingredients as shown in **Equation 1.1**:

$$P(D) = \left(\frac{D}{D_{max}}\right)^q \qquad \text{Eq.(1.1)}$$

where P(D) is a fraction of the total solid ingredients smaller than particle size of D

(μm), D_{max} is the maximum particle size (μm), and q is the distribution modulus. It can

be seen that the minimum particle size was not incorporated in the proposed model. It

was then in 1994 that Funk and Dinger (Funk & Dinger, 2013) modified this model,

known as modified Andreasen and Andersen model, considering the minimum particle

size in their proposed equation (**Equation 1.2**) as follows:

$$P(D) = \frac{D^q - D_{min}^q}{D_{max}^q - D_{min}^q} \qquad \text{Eq.(1.2)}$$

where D_{min} is the minimum particle size (μm). This model has already proved its

efficiency in optimization of granular skeleton of normal and self-compacting concretes

by applying different q values. In this regard, higher q values (q>0.5) result in coarser

mixtures while the lower quantities (q<0.25) lead to compositions containing finer

matrix (Hüsken & Brouwers, 2008). Brouwers (2006) also investigated that to obtain

the optimum packing density of concrete skeleton, the q should have a value in range

of 0.2-0.37 (Brouwers & Radix, 2005; Brouwers, 2006). Afterwards, Hunger (2010)

recommended q values in range of 0.22-0.25 to develop self-compacting concrete

(Hunger, 2010). Recently, Yu, et al. (2014) used a fixed q-value of 0.23 to develop

UHPC (Yu, et al., 2014).

2.2.3.5   Mixing of Ultra-High Performance Concrete

Several mixing procedure with mixing time between 10 to 18 minutes have been practiced up to now to develop UHPC however, there is not any consensus on the time and method of mixing particularly with respect to addition time of water and SP. For instance Wille et al. (2012) applied a 15 minutes mixing method including 5 minutes sand and silica fume, 5 minutes cement and glass powder and more 5 minutes after adding water and SP (Wille, et al., 2012). It should be reminded that they added water and SP separately and fibers were added during this last 5 minutes. It is obvious that by increasing the mixer speed it is possible to reduce the mixing time. For instance an optimum UHPC, regarding both fresh and hardened state, was achieved by 40 seconds mixing in high speed of 6.1 m/s followed by 70 seconds of lower speed of 1.4 m/s (Mazanec & Schießl, 2008).

It was also mentioned that 2 minutes of mixing with high speed after adding the steel fibers would be important to distribute the fibers evenly thorough the concrete (Xiao, et al., 2014) .

2.2.3.6   Curing of UHPC

Since the water/binder is very low in UHPC, another major step in any project is to prevent waterscape from the exposed surface. Otherwise, early-age cracking in dehydrated surface and its degradation-related issues would be uncontrollable (Graybeal, 2011). In addition to this matter and as a result of simultaneous hydration of cement particles, resulting in autogenous shrinkage of UHPC, access to external water through one of the water curing methods, such as fogging or water pounding,

immediately after casting and finishing the concrete, particularly during the age of 12 hours to 7 days, would be critical (Aïtcin, 1998). Steam curing also immunes UHPC to durability-related issues such as freeze-thaw and chloride ion penetration (Graybeal, 2006).

Thermal curing is one of the known methods for UHPC development particularly in pre-casting. However, as mentioned in the last paragraph, it should be accompanied with water or steam. The advantage of heat or steam curing is that it could increase the 28-day compressive strength for instance from 165 MPa of air-cured samples to greater than 200 MPa. The modulus of elasticity and Poisson's ratio are not highly affected by different curing regimes (Ahlborn, et al., 2008). As another instance to approve the positive effect of thermal curing, it was observed that heat treatment at 90°C is highly effective before the age of 7 days since it accelerates the pozzolanic activity. In this regard, a two-day heat treatment improves the compressive strength equal to 3.5 years of curing in water with 20°C (Schachinger, et al., 2008). On the other hand, UHPC samples cured in water at 20°C without any heat curing reveal less damage in the freeze-thaw durability test (Cwirzen, et al., 2008). In addition, decreased strength at later age was reported as a negative result of increased curing temperature (Turkel & Alabas, 2005).

The first research to investigate the influence of curing on mechanical properties and microstructure of UHPC demonstrated that by increasing the temperature and the duration of heat curing, the length of C-S-H chains increases as a result of enhancement of cement hydration, higher activity of pozzolanic materials and even crushed quartz (Zanni, et al., 1996). The curing temperature plays a significant role in the process of curing. In fact, curing temperature is a compromise between final strength and the rate of strength. In other words, as mentioned before, the higher the curing temperature is,

the lower the final strength and higher the rate of strength. Furthermore, the strength after steam curing, depending on the curing time, temperature and concrete composition, is between 60% and 94% of the 28-day compressive strength of normal cured concrete. (Turkel & Alabas, 2005). As an example, it has been showed that high-volume fly ash concrete, with 70% of cement substitution and steam cured at 65°C, just for 5 hours in maximum temperature and after that in water bath, results in almost the same compressive strength compared with normal-cured specimens at 28 and 90 days (Yazici, et al., 2005). Since the duration of steam curing was short in that study, the specimens got around 10% more strength when they cured in saturated lime water at 20±2°C, after their steam curing, rather than air cured ones. The other positive effect of steam curing is the higher volume stability of concrete when the high-calcium fly ash replacement increases to 60% and 70% due to faster consumption of free CaO in higher temperatures and lower expansion of concrete before gaining enough strength. Furthermore, as fly ash/cement substitution increases to 50% and 60%, the initial and final set is retarded by approximately 1 hour and 2.5 hours respectively.

The other important issue regarding thermal curing is the time interval between the time of mixing and starting the thermal curing process, known as delay time. For more clarification, by saying delay period, we mean the period between the time of wetting of cement by water and the time of starting the steam or heat curing of the concrete. If the temperature rises more rapidly to 50°C during the first two hours and 100°C during the first 6 hours after the time of mixing, not only the concrete does not obey the rule of maturity of concrete, considering temperature and time, but also adversely affects the later-age strength of concrete (Saul, 1951). With respect to this fact, before any heat curing of concrete, to avoid detrimental effects of curing on strength and durability of concrete, a delay interval based on initial setting time of concrete is beneficial

(Erdem, et al., 2003). In this regard, it has been concluded that applying steam curing

in the range of 60-80°C and for a period of 2-5 hours with a delay period less than one

hour is detrimental to long-term compressive strength (Soroka, et al., 1978).

Furthermore, a delay interval of 2-6 hours prior to steam curing improves the 24h

strength 15% to 40%, depending on the steam temperature, compared to samples with

immediate steam curing of fresh concrete (Shideler & Chamberlin, 1949). In fact, as

delay period increased from 1 hour to 5 hours, an enhancement in strengths of all ages

was observed (Hanson, 1963). To prevent the deteriorative effects of steam curing, the

delay time should be defined in such a way that the temperature could not be able to

expand the fresh concrete. This time interval corresponds to the time required for

concrete to gain a compressive strength of 0.7-0.8 MPa (Mironov, 1966). To overcome

the negative impacts of concrete expansion due to steam curing, depending on the

water/cement ratio, 4-7 hours of delay interval results in no strength loss at late ages

(Alexanderson, 1972). As Alexanderson (1972) explains, generally there are two causes

for the loss of strength during the 28 days. The first cause, dominating the second one,

is physical including porosity and cracking while the second cause is chemical as a

result of different chemical compositions, micro-structure and degree of hydration. He

suggest that to neutralize the pore pressure which produces cracks in early age, a

minimum tensile strength must be attained by concrete before heat curing, enabling it

to overcome the stress produced by expansion of concrete. It was shown that first-day

compressive strength of all specimens with different delay periods cured with steam

curing method, are higher than the normal cured specimens while, the later-age (3, 7,

28, 90 days) compressive strength of specimens with a delay period less than setting

time reduces by reduction of delay interval (Erdem, et al., 2003). On the other hand, no

strength loss was observed when the specimens were cured after a delay period equal

to setting time of the concrete. Furthermore, 3-day compressive strength of samples, cured after a delay time equal to setting time of the concrete, is higher than 7, 28 and 90-day compressive strength of other specimens with delay period of less than setting time. In general, the strength trend increases with increasing the delay interval from zero to setting time. This strength enhancement is due to the fact that during the temperature rise in the surface of the concrete, if the delay time is less than setting time, the surface gets strength while the core of the specimens are still in plastic form. After this and when the temperature of the inner part of the concrete tend to increase, by heat of steam, this part tends to expand while the outer part is rigid enough to withstand this expansion resulting in a damage in the interface of exterior and interior of concrete. For more clarification, this enhancement in strength is also attributed to the reduction of cracks due to higher tensile strength of concrete as a result of increased delay interval before tempered curing (Alexanderson, 1972). As Alexanderson (1972) explains, different thermal expansion coefficients of concrete ingredients may cause micro-cracks as well as higher porosity during the heat curing. To eliminate this deteriorative effect it is suggested that the steam curing should be postponed after the initial setting time when no plastic concrete will remain inside the specimens. Otherwise, it causes micro-cracks, since the concrete has not enough tensile strength to overcome all these thermal stresses (Erdem, et al., 2003). Consequently, setting time of UHPC plays a significant role in starting time of curing. Generally, the initial and final setting time of UHPC occurs between 12 to 24 hours after mixing the material and in some cases even 28 hours has been reported (Graybeal, 2005).

The temperature under which steam curing is performed, has also an indispensable role in strength development of the concrete. With respect to chemical deterioration, secondary ettringite formation play a significant role in deterioration of steam-cured

concretes in temperatures higher than 75°C (Heinz & Ludwig, 1987). If an inappropriate curing temperature or even improper heating and cooling rates or delay periods are chosen, micro-cracks can be generated as a result of thermal stress. This results in direct lower strength beside the potentiality to be deteriorated by other damaging processes such as delayed ettringite formation which again causes strength reduction resulted from the weakening of the aggregate-paste bond due to facilitated water penetration into the concrete (Taylora, et al., 2001). They also reported that delayed ettringite formation (DEF), which generally starts after hardening of the concrete and with the help of sulfates inside the concrete paste, is a result of concrete temperature higher than 70°C because of heat curing as well as heat of hydration in mass concretes. DEF finally affect the mechanical properties of concrete (Taylor, et al., 2001). Furthermore, the higher temperatures also have negative effects on surface resistivity and durability of concrete as the result of coarser pores structure of the material beside the higher water absorption for longer steam cured specimens (Ramezanianpour, et al., 2013). In addition, when the treatment duration at maximum temperature in a range of 60°C to 80°C increases, the compressive strength tends to increase more while the highest strength happens at 70°C (Bingöl & Tohumcu, 2013).

Regarding the rate of heating from starting the heat-curing to its maximum temperature, some studies propose a very low temperature rise trend such as 5°C/h to a maximum temperature of 65°C (Hanson, 1963). Nevertheless, considering all these experiments and related results a satisfactory curing cycle as shown in **Figure 2.3** is suggested (ACI, 1992). This cycle includes a delay period, heating with rate of 22-44°C/h to maximum temperature, and finally a cooling period with the same rate of heating.
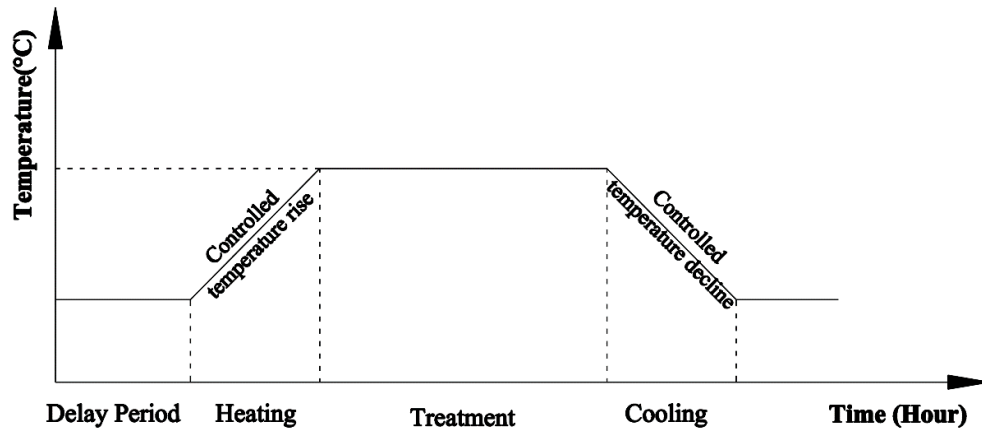
Figure 2.3: A schematic heat-curing cycle (ACI, 1992).

2.2.4 Applications

The first applications of UHPC in the world are presented in **Table 2-4**. As can be seen the first UHPC was applied in 1997 in Canada as a footbridge. Then one year later, it arrived in power plant industry and continued its way to highway in 2007. Some of these applications are shown in **Figure 2.4** to **Figure 2.7**.

Table 2-4: First applications of UHPC.

Project	year	Location	Reference
Sherbrooke Pedestrian Overpass, Quebec, Precast, post-tensioned space truss, 60 meter span	1997	Canada	(Blais & Couture, 1999)
World first industrial applications, Cattenom and Civaux power plants beams by BSI® and Ductal®	1998	France	(Resplendino, 2004)
world first UHPC road bridges on the Bourg-lès-Valence bypass in France's Drôme region	2001	France	(Hajar, et al., 2004)
Sunyudo (Peace) Footbridge on Han river in Seoul.	2002	South Korea	(Behloul, et al., 2002)
Akakura (Yamagata) footbridge box girder	2004	Japan	(Rebentrost & Wight, 2008)
Tahara (Aichi) Footbridge	2004	Japan	(Rebentrost & Wight, 2008)
Mars Hill Bridge, Wapello County, IA Three 1.1- m deep bulb-tee beams with 33.5 m Span	2006	United States	(Bierwagen & Abu-Hawash, 2005)
Highway 11 over CN Railway at Rainy Lake, Ontario, Joints between precast panels and shear connector panels	2006	Canada	(Perry, et al., 2007)

Project	year	Location	Reference
Glenmore/Legsby Pedestrian Bridge, Calgary, Precast, post-tensioned tee-section	2007	Canada	(Perry & Seibert, 2008)
Highway 11/17, Sunshine Creek, Ontario, Joint fill between adjacent box beams and between precast curbs	2007	Canada	(Graybeal, 2009)

Figure 2.4:   Sherbrooke Pedestrian Overpass, Canada (Ductal®, 1997).

Figure 2.5:   Sunyudo (Peace) Footbridge on Han River in Seoul (Ductal®, 2002).

Figure 2.6: Mars Hill Bridge, Iowa, Canada.

Figure 2.7: Joints between precast panels and shear connector panels, Rainy Lake, Ontario.

2.3   Advantages

The main advantages of applying this ideal material in construction industry, as briefly described in Chapter 1, include:

- Supporting the concept of sustainable development with respect to lower embodied energy and CO_2 emissions in long-term as well as enhanced durability, which results in longer service life (Voo & Foster, 2010; Prisco,

et al., 2014).

- Improved tensile behavior compared to other types of concrete resulted from internal fibers (Voo, et al., 2006).

- UHPC will lead to save long-term service costs (Nematollahi, et al., 2012)

- Installation process of lightweight UHPC members, including handling and transportation, would be more convenient and safer.

- By elimination of a significant part of the reinforcement bars and stirrups, considerable human labors, supervision tasks and quality control activities could be decreased beside reduction of permanent load resulting in lighter structures (Richard & Cheyrezy, 1995).

- Low creep and shrinkage. In addition, it demonstrates other excellent characteristics such as durability with low permeability against aggressive environments and agents, provides durable protection of steel to provide resistance to corrosion, abrasion and impact loads.

- Less cement and aggregate are needed for bearing a definite load (Aïtcin, 1998; Staquet & Espion, 2004; Voo & Foster, 2010).

- Due to its higher strength rather than normal concretes, UHPC could be recycled one or two times more than conventional concretes (Aïtcin, 1998).

- Extraordinary slim designs as the result of high strength and ductility (Acker & Behloul, 2004).

- The ability for repair and strengthening of normal concrete substrates due to strong bonding strength in composites and long-term serviceability and durability (Tayeh, et al., 2012; Tayeh, et al., 2013; Freytag, et al., 2004).

- Ability to be recycled at the end of their life-cycle as high-quality aggregates

for new generation of concretes resulting in lower extraction of natural

resources (Voo & Foster, 2010).

2.4 UHPC development by means of response surface methodology (RSM)

With respect to the fact that developing a sustainable and eco-efficient UHPC is of

great importance to meet two indicators of material sustainability those are

environmental and economic impacts of material, minimization of cement and silica

fume plays an important role in this way. In other words, by cement reduction both cost

and embodied CO_2 can be reduced. In the same way, by silica fume reduction the cost

factor will be reduced as well. Nevertheless, it cannot be neglected that these materials

have significant influence on fresh and hardened properties of UHPC and respectively

their reduction should be studied very carefully. In this regard and due to the fact that

this process is a multi-variable and multi-objective optimization as well, it seems

necessary to apply an appropriate tool in order to study this process. Design of

experiment (DOE) or experimental design is a systematic procedure of analyzing the

process of experiments in order to evaluate the impacts of input variables, also known

as predictors, on the process outputs or outcomes. In other words, DOE helps to

investigate the target level of inputs to achieve the desired output. Statistical mixture

design (SMD) is an efficient type of DOE in which the design region is investigated

statistically in order to find the most probable solutions, for instant the optimum ones,

in the feasible region of possibilities (Anderson & Whitcomb, 1998) or study the effect

of input variables on outputs simultaneously (Eriksson, et al., 1998). With respect to

definition of SMD, Response surface methodology (RSM) is a statistical based

technique to investigate the best response in an applicable region of possibilities or at

least better understanding of any response affected by multiple variables without requiring a definite total sum of ingredients, which is required in mixture design. It was first in 1950th that this technique introduced to find the complex relationships in the case of multi-variable and multi-objective optimizations with the aim of finding the desired output (Box & Wilson, 1951). The advantages of this experimental design approach include the possibility of evaluation of factors interaction within the experimental region, recognition of the optimal response based on different priorities, and finally developing a generalized model of the data with minimum experimental labor (Upasani & Banga, 2004).

However, various applications of RSM could be found in process optimization in industry, it is somehow a new field in concrete technology and particularly UHPC development. It was in 2000 that the effect of W/C ratio, binder and coarse aggregate content, as variables, were studied on fresh behavior and compressive strength of one type of self-compacting concrete (SCC) and relevant models were proposed (Khayat, et al., 2000). Afterwards in 2004, a three-level full factorial experimental design and response surface method were used to study the interaction of volume fraction of steel fiber and their aspect ratio, as two variables, on mechanical properties of steel-fiber reinforced concrete particularly its fracture energy (Bayramov, et al., 2004). Finally, it was in 2014 that this method was applied for developing a type of UHPC with already known materials and not any other supplementary cementitious materials (Ghafari, et al., 2014; Ghafari, et al., 2015). This method eliminates the sophisticated procedure of packing density of dry skeleton particularly with respect to the fact that there is no consensus on the q factor introduced in modified Anderson model. It gives the opportunity to study all the factor and response variables all together and simultaneously.

2.5   Self-healing

It was first in 1994 that the International Council for Research and Innovation in Building and Construction, *Conseil International du Batiment* (CIB) indicated seven principles of sustainable construction (Kibert, 2012) including:

1) Reducing consumption of resources;

2) Reusing the resources;

3) Using the recyclable resources;

4) Protecting the nature;

5) Elimination of toxins;

6) Applying life cycle cost;

7) Improving the quality.

One of the most efficient way to study the sustainability of any material since now is to analyze its life cycle from cradle to grave. In other words, with this method one can quantify the environmental impact of any product or service during the entire life of that project or service. For this aim, several methods and analytical software tools have been developed so far by quantifying the embodied CO_2 or embodied energy of various materials from their early production phases, known as cradle, to their end life, known as grave. The whole process span from extraction of the material to the time it could not be recycled or reused anymore. A useful indicator related to the life cycle of any material, is obviously its durability under various aggressive conditions namely chloride ions or carbonation. The other point which helps us to estimate the service life or life cycle of any material, in our case UHPC, is to know if the material is capable of being repaired with the aim of prolonged life cycle or not? Answering to this question may shed more light on the concept of durability, service life or life cycle of UHPC.

With respect to these facts, studying the self-healing of UHPC has two main advantages. First, it shows the ability and possibility of using the material in aggressive environments in which repair and rehabilitation of structures are beyond the labor access. Second, it helps us to estimate the whole service life of the material more accurately and realistically even after some limited damage such as cracks. This phenomenon is closely linked with the concept of damage management introduced for the first time in 2008 (Zwaag, 2008). In this context, the damage is not considered problematic as long as it can be recovered or healed. In other words and with respect to notion of service life, the end life of material depends on the rate of damage formation versus the rate of healing (de Rooij, et al., 2013). This phenomenon is of great importance particularly in brittle material such as cement-based materials and most importantly, UHPC since any damage formation or cracking is translated to fracture or failure. Since 2007, Japan Concrete Institute (JCI) has started a research on self-healing of concrete. They have classified the concept of self-healing/repairing in different categories as depicted in **Table 2-5**, **Table 2-6** and **Figure 2.8** (Igarashi, et al., 2009). According to this report (JCI-TC075B) the general term of recovery in **Figure 2.8** refers to "*an event in general in which at least one function of concrete recovers by whatever means*". In this regard, conventional repair/strengthening as well as self-healing/repairing are both considered as recovery. However, the later one implies to the recovery as an inherent mechanism existing in the concrete itself without any imposed repair or strengthening from outside. For more clarification, the notions of healing and repairing should also be differentiated. Healing refers to any crack clogging phenomena due to innate chemical reactions, which could be found inside the conventional concretes, such as hydration of excess un-hydrated cement or $CaCO_3$ formation and deposition. In this regard, Rouse (2011) attributes the healing to closure

of micro-cracks when the un-hydrated cement starts to react again with the penetrated

water through micro-cracks and seals the defects automatically (Rouse, et al., 2011).

Besides that, it includes addition of any supplementary cementitious materials those are

all related to the natural reactions in ordinary cementitious materials and concretes. On

the other hand, repairing entails addition of any external artificial devices such as

embedded microcapsules and heat-generating devices those are beyond the

conventional and ordinary reactions of supplementary cementitious materials and

concretes (Igarashi, et al., 2009).

Table 2-5: Mechanisms and classification of healing/repairing (Igarashi, et al., 2009).

Natural healing	A phenomenon in which cracks in concrete are naturally clogged in an environment involving moisture , for instance , without any special arrangement in the material design, etc.
Autonomic healing	A phenomenon in which cracks are clogged in concrete made with special material design, such as the use of an appropriate supplementary cementing material in expectation of its effect of clogging or accelerating the clogging of cracks in the concrete in an environment involving moisture, etc.
Activated repairing	A phenomenon in which cracks are clogged in concrete by a mechanism of devices embedded in the concrete beforehand for the purpose of autonomically repairing cracks.
Autogenous healing	A concept encompassing natural healing and autonomic healing; the whole phenomenon of cracks in concrete being clogged in an environment involving moisture, etc.
Engineered healing/repairing	A concept encompassing autonomic healing and activated repairing; a phenomenon in which cracks in concrete are clogged by the use of the concrete made with special material design to clog/repair cracks
Self-healing/repairing	The whole phenomenon of clogging of cracks in concrete not by human hand.
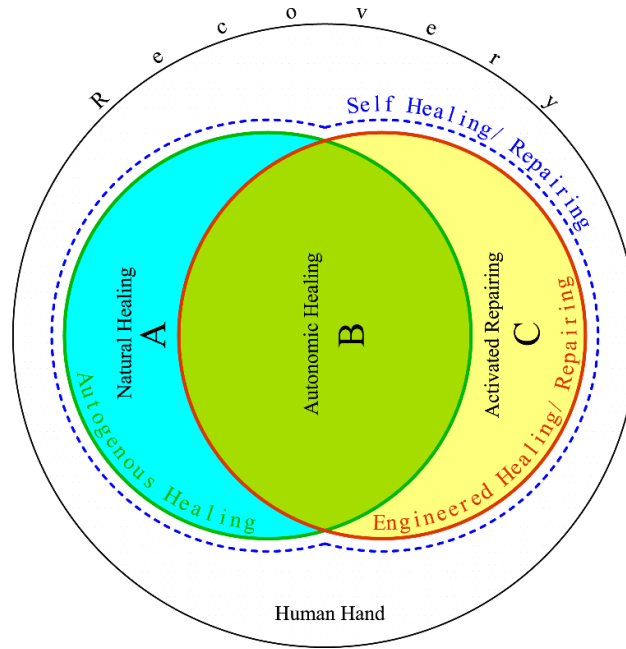
Figure 2.8: Visual terminology of recovery based on JCI TC-075B.

Table 2-6: Examples corresponding to type of Healing/Repairing according to JCI TC-075B.

Type	Examples	Healing/ Repairing	Inherent/ Engineered
A: Natural healing	• Rehydration of residual unhydrated cement in low W/C concrete • Rehydration of cracks found in hydraulic structures	Healing	Inherent
B: Autonomic healing	• Use of fly ash • Cementitious composites containing fly ash • Use of special additive (expansive additive) • Use of bacteria		Engineered
C: Activated repairing	• Inclusion of microcapsules, etc. • Use of brittle pipe network • Use of heat-generating devices • Use of shape-memory alloys • Fusion with monitoring techniques	Repairing	

Later RILEM (2013) developed the terminology of self-healing as follows (RILEM

Technical Committee 221-SHC, 2013):

• Self-healing: Any process by the material itself, which improves the earlier

declined performance.

- Autogenic healing: the process of self-healing when the material components, required for the recovery process, are all present in the material itself and the material has not been designed previously and specifically for self-healing. As **Figure 2.9** illustrates, there are different mechanisms by which the material could be healed autogenically.

- Autonomic healing: is the process of self-healing when the required components for recovery do not exist in the material itself and should be provided and embedded in the material earlier from outside in order to be activated if damage occurs. This external components include glues, resins, expansive agents, nanoparticles, etc (Lee, et al., 2004).
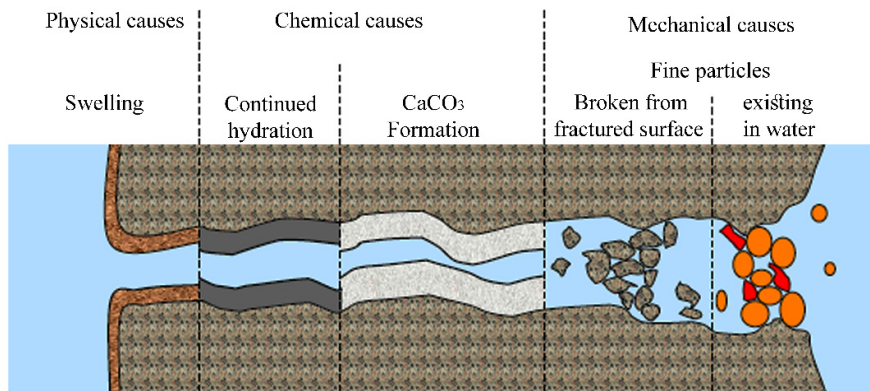
Figure 2.9:   Causes of autogenic self-healing (Reinhardt, et al., 2013).

As mentioned above, RILEM categorized self-healing in two sub categories while JCI has divided it into three divisions. As an example of differences in these two terminologies, the RILEM consider the addition of cement or supplementary cementitious materials as autogenous while JCI considers it as autonomous. Besides

that, JCI considers the autonomic as a part of autogenous while in RILEM definition,
they are basically different. Similarly, RILEM has integrated the autonomic and natural
self-healing existing in JCI to just autogenous and changed the activated repairing to
autonomic healing.

There is also another classification in the area of material since based on their level
of intelligence as can be seen in

Figure 2.10 (Mihashi, et al., 2001; Sharp & Clemena, 2004).
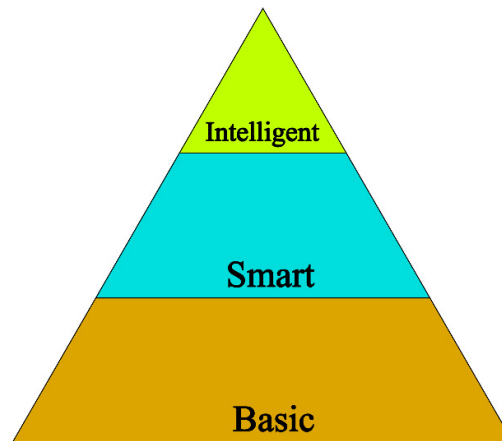
Figure 2.10: Classes of materials based on their level of intelligence.

According to this classification, the basic materials are those without any response
characteristics. This category includes most of known materials. The smart level are
those providing just a unique response in case of a particular change such as smart
polymeric materials those are sensitive to temperature. Their color is changed as a
response to temperature change. The highest level allocates to intelligent materials,
which receive information, combine and process them and finally react to the stimuli.
This behavior is highly similar to the behavior of living organs such as skin, or bone.
Schmets (2003) explains that however manmade materials demonstrate high efficiency

in some of their performances, they are deficient in some other aspects (Schmets, 2003). In this regard, we need to learn from biological systems. The natural materials are intelligence in the sense that they are inherently adaptable to their surrounding environment. Another prominent feature of biological materials is that they can autonomously repair their own damages. In other words, they have the ability of self-healing such as recovery of fractured bones. Accordingly, attributing intelligent to any kind of concrete seems yet and exaggeration. In this regard, normal concretes just with autogenous-healing ability can be considered as basic materials while concretes containing encapsulated healing agents, capable of autonomic healing, fall in the category of smart material. If some sensors are embedded into the material and the feedbacks sent by sensors are being processed for any response such as starting the healing/repairing, this material could be considered as an intelligent one (de Rooij, et al., 2013).

In general, self-healing, more precisely autogenous healing, of UHPC is mainly attributed to new C-S-H gel formation of unreacted cement with penetrated water inside the cracks (Granger, et al., 2007; Jacobsen, et al., 1995). Nevertheless, some research pointed out that the formation of calcium hydroxide or calcium carbonate is responsible for crack bridging (Neville, 2002). The research performed by Granger (2007), studied the effect of curing age of UHPC with cracks of around 15 μm to provide some information related to the effect of self-healing on mechanical properties of UHPC. The hydration process was accelerated in their test by two days of normal water curing and two days of heat treatment in 90°C and 100% RH to accelerate the process of hydration. Their aim was to cease the strength evolution of concrete itself during the water curing after cracking aiming at studying the mechanical properties enhancement just as result of self-healing (Granger, et al., 2007). They showed that presence of water is vital for

healing but the air curing after cracking does not improve the mechanical properties

substantially. It is also possible that self-healing is a consequence of blocking cracks by

the formation of $CaCO_3$ because of penetrated CO_2 inside the cracks (**Figure 2.11**).

With respect to this phenomenon, some researches include the self-healing of concrete

through water permeability test.
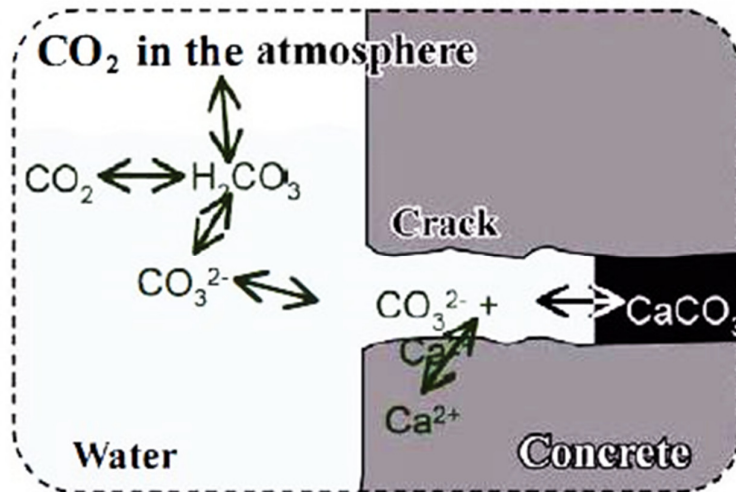
Figure 2.11: Mechanism of natural healing in hydraulic structures (Edvardsen, 1999).

Anyhow, different methods and techniques exist in order to evaluate the damage

after and before healing/repairing such as microscope, water permeability, ultrasonic

pulse velocity, capillary absorption, depth of chloride ion penetration, flexural strength,

absorbed energy, rigidity, and relative dynamic modulus (Igarashi, et al., 2009).

Today, one of the extensively used techniques is microscopy. This method provides

deep understanding of efficiency and quality of self-healing method beside

characterization of damage and finally visual assessment of the degree of recovery

(Çopuroglu, et al., 2013). However, it is not efficient to provide a precise quantification

on the degree of healing and if the recovery is just on the surface or in deep.

The second group of techniques are those to assess the recovery of material against

environmental actions. One of these tests is air permeability by test setup displayed in

Figure 2.12 (Kunieda, et al., 2012).
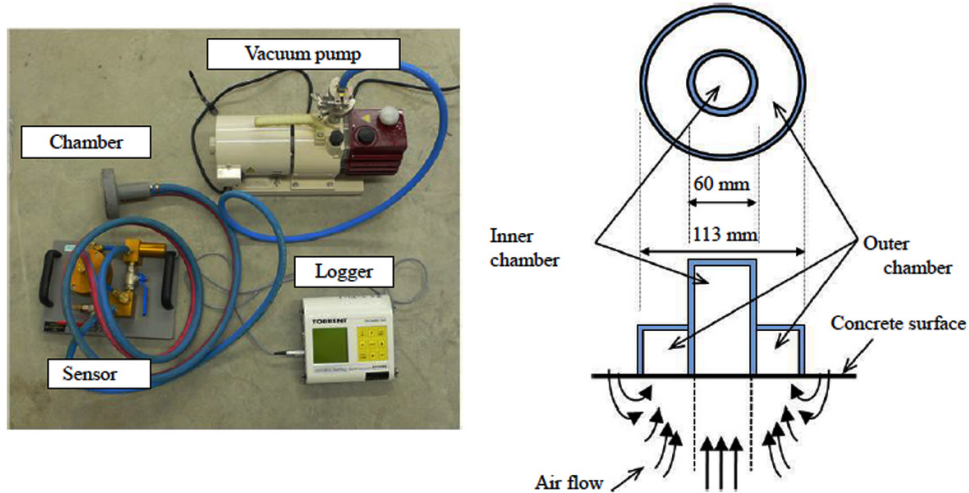
Figure 2.12: Air permeability test setup (Torrent, 1992).

The other known test verifying environmental recovery of concrete is water permeability by means of controlled cracks in specimens such as test setup illustrated in **Figure 2.13** followed by healing and permeability test (Rapoport, et al., 2002; Jang, et al., 2011; Wang, et al., 1997; Reinhardt & Jooss, 2003).
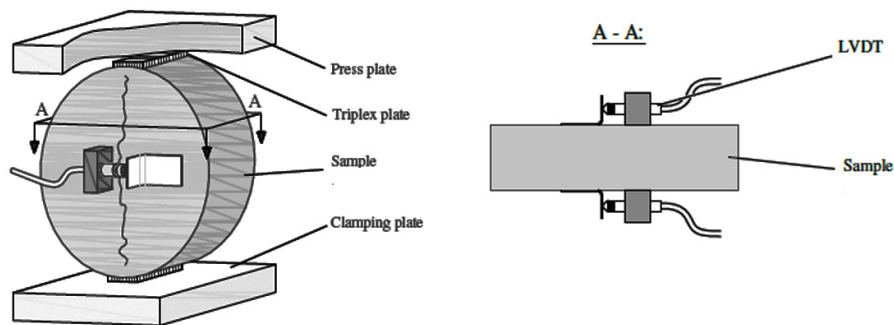
Figure 2.13: Test setup for crack generating of samples for permeability test.

The third test used to verify the self-healing facing environmental actions is capillary water absorption and the related comparison between plain, cracked and healed samples (Tittelboom, et al., 2012). Other techniques include resonant frequency analysis (Aldea, et al., 2000), ultrasonic measurements (Abdel-Jawad & Dehn, 2005), electrochemical impedance measurements (Yang, et al., 2010), computed tomography (Mihashi, et al., 2001), resistance against corrosion (Pelletier, et al., 2011) and Fourier-transform infrared spectroscopy which shows the chemical composition of precipitated material in surface of the crack (Wiktor & Jonkers, 2011).

The third class of tests in the context of self-healing, evaluate the mechanical properties of material before and after healing process through regain in properties such as strength or stiffness. In general, these type of tests can demonstrate less error in verifying the self-healing ability of material with respect to the fact that the two former techniques have not the ability to evaluate cracks in depth precisely. Besides that, they may conclude that a material is recovered while it has been just sealed due to some superficial chemical reactions in its surface. In this regard, mechanical based techniques are of pivotal significance particularly in this research work.

The first common test in this category is three-point-bending test. The commonly used test setup can be seen in **Figure 2.14**.
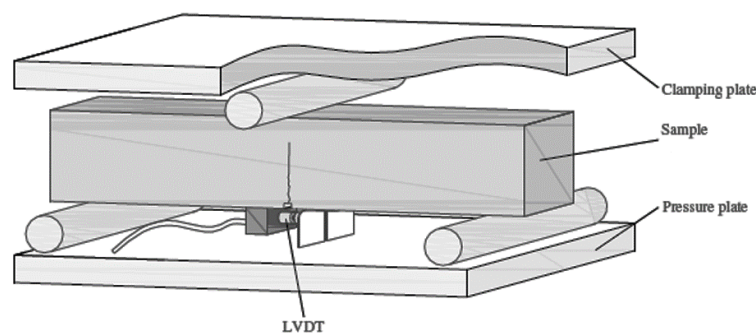
Figure 2.14: 3-point-bending test setup (Çopuroglu, et al., 2013).

The deformation in this method is measured by means of vertical linear variable differential transformers (LVDT) giving the vertical strain at the middle span of prism. In addition, the crack-mouth-opening displacement (CMOD) is measured through another LVDT shown in **Figure 2.14**. The tests is stopped when the pre-defined CMOD is obtained. Then the samples recover with pre-determined methods and again the 3-point-bending test is performed in order to evaluate the degree of self-healing. To quantify the degree of self-healing, different quantities could be compared such as maximum flexural load/strength, first-cracking strength, modulus of elasticity, the ultimate strength, stiffness and finally multiple-cracking behavior (Snoeck, et al., 2014; Snoeck & Belie, 2012). Granger et al. (2005) used a 3-point-bending test with a notch (Granger, et al., 2005). The other mechanical-based techniques include fatigue resistant test (Yang, et al., 2011) and acoustic emission analysis (Granger, et al., 2007).

Some of these techniques are suitable to verify just the self-sealing ability of the material, which is defined as its recovery against environmental related aggressive agents, such as water permeability, capillary absorption or depth of chloride ion penetration. On the other hand, some techniques has the ability of evaluation of self-healing ability of the material which encompass the sealing-ability as well such as flexural strength, absorbed energy, rigidity, and relative dynamic modulus.

As depicted in **Figure 2.15**, some performance criteria, such as durability-related indicators, could be recovered totally, while the recovery of structural performance indicators just have the ability being recovered to some extent (de Rooij, et al., 2013).
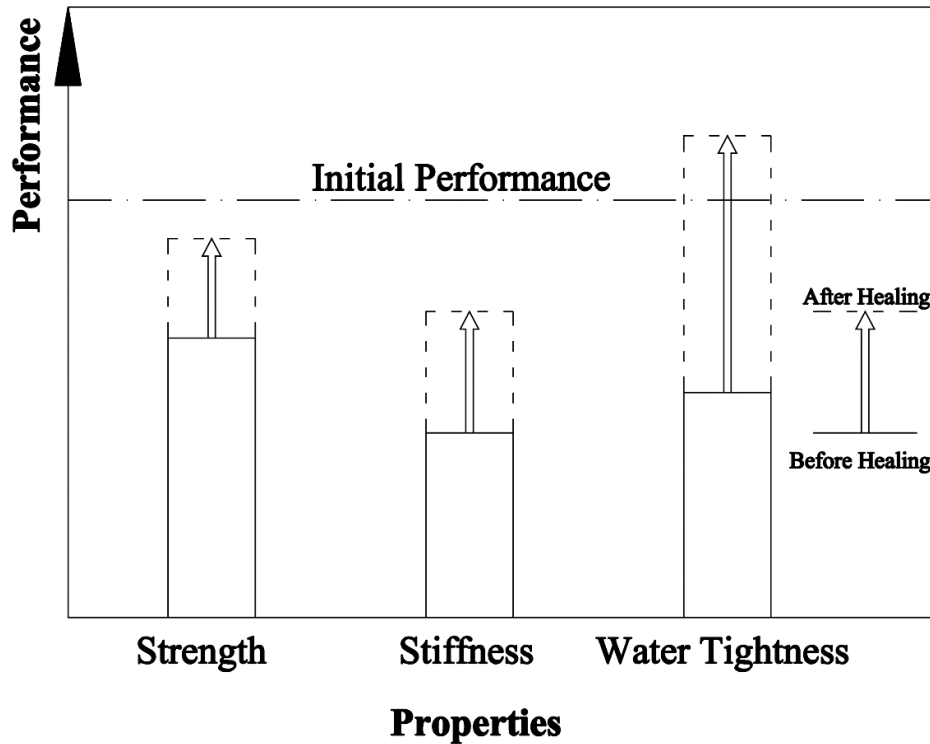
Figure 2.15: Effect of Self-healing on different performances.

Li and Yang (2007) showed that the permeability of samples having cracks wider than 150 μm could not be improved after 10 wet/dry cycles (Li & Yang, 2007). Yang, et al. (2009) also found the same results. While the cracks thinner than 50 μm width were recovered 100%, no recovery could be verified for the crack width above 150 μm (Yang, et al., 2009).

According to this overview, studying UHPC, including its constituent materials, mixture design and finally its self-healing capacity, would be a crucial step in developing a new generation of sustainable and durable cementitious composite materials.

Chapter 3

Constituent Materials and developing paste for UHPC

T his chapter deals with the main properties of constituent materials applied for developing EEUHPC and the reason why they have been selected. These materials include cement, silica fume, fly ash, high-range water reducer admixtures, sand and finally water. Their relevant physical and chemical properties are being discussed in following sections.

In the second part of this chapter, an effective low-energy mixing procedure is introduced with the aim of highest fluidity. It should be noticed that this chapter has

been published in the journal of "*Materia-Rio de Janeiro*" (Ferdosian & Camões, 2016) and also presented in "*VII International Materials Symposium"* in Portugal.

In the third part of this chapter, different pozzolans were studied with respect to their effect on fluidity and strength of paste. The aim was to understand the limits of each of pozzolans particularly fly ash to be applied in UHPC with lowest negative impacts on the paste.

Finally, the chapter ends with a study on optimum dosage of SP and its interaction with the most important pozzolans those could be applied toward realization of our goals.

3.1 Constituent Materials

This subsection describes the main characteristics of all materials used in this study beside their related positive effects or negative impacts. To measure the density of all powders used in current study and depicted in **Table 3-2**, the standard test method conforming to test method for density of hydraulic cement (ASTM, 1995) was performed.

3.1.1 Cement

Cement is the first and most important material in all types of concrete. It plays a crucial role in strength gaining of material. As explained in the previous chapter, however cement 52.5R in mortar results in higher compressive strength in early age, compared to cement 42.5R, no difference in their final strength is expected (Scheydt, et al., 2008). Furthermore, cement 42.5R reveals higher fluidity compared with cement 52.5R (Scheydt, et al., 2008). Nevertheless, for more assurance and to examine their effect on fluidity of cement paste, SECIL® type I Portland cement 42.5R and 52.5R

from Portugal according to BS EN 197-1 (BS EN 197-1, 2000) were studied in the

preliminary stage. Their physical properties and chemical analysis are given in

Table 3-1 based on the information delivered by factory as well as Bogue's

expressions.

Table 3-1: Chemical and physical compositions of cement.

Components	$w_t\%$	
	CEM I 42.5R	CEM I 52.5R
SiO$_2$	19.79	20.61
Al$_2$O$_3$	4.37	4.89
Fe$_2$O$_3$	3.52	3.15
CaO	63.09	63.52
MgO	1.67	2.17
SO$_3$	2.82	3.47
Cl$^-$	0.04	0.04
f-CaO	1.18	1.30
C$_3$S	65.9	58.84
C$_2$S	4.56	11.19
C$_3$A	5.63	7.64
C$_4$AF	10.7	9.58
loss of Ignition	3.01	1.19
Blaine surface area (cm^2/g)	4228	4463
Specific gravity (g/cm^3)	3.11	3.15

3.1.2   Silica fume (SF)

Silica fume is the most famous pozzolanic material particularly for developing

UHPC generally with a content of 25% to 32% (w_t.%) of cement (Wille, et al., 2011;

Graybeal, 2006). This material plays three important roles in UHPC: a) as micro-filler,

with a mean particle size less than 1 μm, to fill the gaps between coarser particles such

as cement, b) rheology modifier, due to its glassy and spherical particles and finally c)

C-S-H producer through reaction with Ca(OH)$_2$ from the cement hydration (Cheyrezy,

et al., 1995). Despite of these benefits and particularly highest reactivity of SF compared with other pozzolanic materials, having around 90% of vitreous SiO_2, its high price makes it as a non-desired material in a sustainable context. In this study Elkem Microsilica®, MS 940-U, with an average particle size of 0.15 μm was used.

3.1.3 Metakaolin (MK)

The other pozzolanic material is metakaolin (MK) which develops high pozzolanic activity while it degrades the workability due to its high propensity to absorb water (Loeb, et al., 2008). The other disadvantage of MK is its high embodied CO_2 generated for the production of one ton of MK, normally around 330 kg/ton compared to values of 14 and 4 kg/ton for silica fume and fly ash respectively (Leese & Casey, 2012; Jones, et al., 2011). The MK used in this research was obtained from Barqueiros mine in Portugal with calcination temperature of 700°C. Some physical and chemical characteristics of MK are also provided in **Table 3-2**.

3.1.4 Fly ash (FA)

The other pozzolanic material which is of great interest is fly ash (FA), available in huge quantities worldwide as a waste material with very low cost and environmental impacts since its application prevents the massive landfills use by this waste material from the thermal power plants (Kaufman, 2011). It was found that in a concrete with 45%-55% cement replacement by fly ash, just 20% of it react in pozzolanic reaction and the rest remain as filler (Poon, et al., 2000; Lam, et al., 2000). It was also studied that by restraining the mean particle size of fly ash from 20 μm to 8 μm, its activity increases leading to higher compressive strength (Hashimoto, et al., n.d.). This chapter aims at development of an eco-efficient UHPC paste with high content of ultra-fine fly ash, as partial replacement of cement and silica fume. The original fly ash (O-FA), used

in this research was provided from Pego thermal power plant in Portugal as Class F fly ash. Pego Power Station is situated 150 km to the northeast of Lisbon, on the left bank of the river Tejo, in the administrative parishes of Pego and Concavada and at a distance approximately 8 km from the city of Abrantes, the center of the Municipality and the location of the region's Circuit Court (**Figure 3.1**).

Figure 3.1: A view of Pego power station (Lopes, 2010).

Some physical properties and chemical analysis of the materials mentioned in this chapter are reported in **Table 3-2.**

Table 3-2: Chemical and physical compositions of cement, SF, MK and O-FA.

Components	w_t%		
	MS 940-U	MK	FA
SiO$_2$	> 90	50.50	48.02
Al$_2$O$_3$	-	42.60	29.59
Fe$_2$O$_3$	-	2.28	4.48
CaO	-	0.16	4.65
MgO	-	0.22	1.44
SO$_3$	-	0.04	0.49
Cl$^-$	-	-	-
loss of ignition	< 3	-	3.0
Blaine surface area (cm^2/g)	150000-300000	-	3848
Specific gravity (g/cm^3)	2.2-2.3	2.3	2.4

3.1.5   Superplasticizer (SP)

Two types of commercial superplasticizer (SP), Glenium SKY 617® and MasterGlenium SKY 526® were studied. The SPs are carboxylic ether polymer based, as a brown liquid, with properties according the definitions and requirements of Standard EN 934-2, established for European concrete admixtures (BS EN 934-2, 2009). Since these SPs are a suspension of solid particles in water, before starting any test it would be necessary to measure the quantity of solids and water in the suspensions. The reason is that we require the water quantity in order to consider it as a part of water in water/cement or water/binder ratios. For this aim, two samples of each SP were selected. They were weighted and then placed in oven at 110°C. Their weight was measured until no weight change was observed. After 48 hours, they reached to a constant weight and the percentage of solid content for each of SPs was calculated as shown in **Table 3-3**. As mentioned, the rest of the SP weight is related to water content which should be considered as a part of water in all paste or concrete mixtures.

Table 3-3: Technical characteristics of Superplasticizer Glenium Sky 617®.

	Glenium Sky 617®	MasterGlenium SKY 526®
Relative density (20°C)	1.05±0.02 g/cm^3	1.07±0.02 g/cm^3
pH:	7.3±1.5	6.0±1.0
Chloride ion content	< 0.1%	≤ 0.1%
Solid content	18%	30%

3.1.6   Sand

A siliceous natural sand with commercial name of S40/45, delivered from Rio Maior in Portugal, was applied during current research (**Figure 3.2**, **Figure 3.3**). The technical information regarding this natural sand is available in the technical sheet provided in **Figure 3.5**. The reason why this sand was selected was its particle size distribution

conforming to requirements explained in **Chapter 2**, namely its particle size less than

1 mm with white color (**Figure 3.4**). Since the sand will be used in saturated surface

dry (SSD) state, its water absorption capacity to be SSD was measured according to

procedure explained in ASTM (ASTM C128–04a, 2004). It showed 0.32% water

absorption in SSD compared to its oven-dried state.

Figure 3.2:   Raw material mines, Rio Mior, Portugal (http://www.parapedra.pt/en/sifucel.php).

Figure 3.3:   Parapedra Group job site situated in Rio Mior, Portugal (http://www.parapedra.pt/en/sifucel.php).

Figure 3.4: Sand 40/45 texture.

CARACTERÍSTICAS FÍSICAS / Physical Specifications / Caractéristiques Physiques		
PH	**7**	ISO 787/9
DUREZA MOHS / Mohs Hardness / Dureté Mohs	**7**	—
BRANCURA / Whiteness / Blancheur	**L* 82,5**	Minolta CR300
DENSIDADE APARENTE / Non Compacted Bulk Density / D.A. Non Tassée	**1,58 g/ml**	EN 12902
MASSA VOLÚMICA / Particle Density / Masse Volumique	**2,62 Mg/m³**	EN 1097-6
INDICE de REFRACÇÃO / Refractive index / Indice de Réfraction	**1,55**	—
HUMIDADE[1] / Moisture / Humidité	**3 - 5 %**	DIN 53198
CORTE SUPERIOR / Top Cut / Coupure	**1 mm**	—

[1] Disponível em seco / Available without Moisture / Disponibles sans Humidité

CARACTERISTICAS QUÍMICAS[2] / Chemical Specifications / Caractéristiques Chimiches									
SiO_2	Al_2O_3	Fe_2O_3	CaO	MgO	Na_2O	K_2O	TiO_2	P_2O_5	MnO
99,4	**0,05**	**< 0,025**	**0,02**	**0,06**	**0,20**	**0,02**	**0,02**	**0,01**	**0,00**

[2] F.R.X. / X-Ray Fluorescence / Fluorescence des Rayons-X

ANÁLISE GRANULOMÉTRICA[3] / Particle Size Distribution / Analyse Granulométrique					
Peneiros Sieves Tamis (mm)	**Retido** Retained Conserveid (%)	**Acumulado** Cumulated Cumulé (%)	**Passa** Passing Passant (%)	**Limite** Limits Limites (%)	
1,40	**0,0**	0,0	100	100	
1,00	**0,0**	0,0	100	95 - 100	
0,500	**16,2**	16,2	84	—	
0,250	**77,9**	94,1	6	0 - 35	
0,125	**5,9**	100,0	0	—	
0,063	**0,0**	100,0	0	0 - 3	
<0,063	**0,0**	100,0	—	—	

[3] EN 933-1

Figure 3.5: Characteristics of Sand 40/45 (Grupo Parapedra, 2016).

3.1.7 Steel fiber

The steel fiber used in this research is a type of Dramix® steel fiber with commercial name of OL 13/.20 representing the length and diameter of 13 mm and 0.2 mm respectively. They also exhibit a tensile strength and modulus of elasticity equal to 2600 MPa and 200 GPa respectively as reported by the factory (BEKAERT, 2015). These characteristics conform to the needs and requirements explained by Aïtcin (2011).

3.2   Effective low-energy mixing procedure to develop high-fluidity cementitious pastes

The first step for performing this research was to obtain the most effective mixing procedure to apply it during this research with the same consistency and procedure. In this regard and with respect to the fact that by that time just SP Glenium Sky 617® was accessible, this SP was selected for this preliminary study in order to find its optimum dosage when it is mixed with cement 42.5R and 52.5R. Again, it should be noticed that this phase just was performed to find out the most efficient mixing procedure without any comparison between two SP regarding their dispersing-ability. Even, the interaction of the most efficient SP with different pozzolans was postponed to a proper time when the most effective SP, mixing method and best pozzolans are selected.

As UHPC has very low water to cement and binder ratio, as a prerequisite for obtaining ultra-high strength, enough fluidity would not be accessible without superplasticizer agents. In this regard, an efficient application of SP including its optimum dosage, the proper addition time to the materials and finally the mixing time of all ingredients can play an important role to maximize the SP effects on concrete paste resulting highest fluidity. Consequently, the water content for a definite target value of fluidity could be reduced which results in higher compressive strength and durability as well. For better understanding of the chemical process of cementitious minerals' dispersion by polycarboxylate-based superplasticizers, it was demonstrated that the plasticizing effect is attributed to the adsorption of anionic SP particles to cement particles, confined by Ca^{2+} as a positive layer from the cement dissolution in water (Yu, et al., 2013). According to this study, as time elapses, C_3S and C_2S are consumed and C-S-H gels are gradually formed and the number of positive particles, adsorbing the SP chains, reduces. In this regard, the addition time of SP with respect to

highest fluidity is during the first 15 minutes after adding water to cement and particularly between first 2 and 3 minutes (Hsu, et al., 1999). Another recent experiment also confirms that stepwise and particularly delayed addition of SP, which mean adding SP in two stages and also not adding all the SP with water at the beginning, could improve the flowability of UHPC by more than 25% compared to direct addition of SP with or immediately after water addition (Tue, et al., 2008). Despite these studies, some experiments have been carried out just using stepwise addition of SP (Rougeau & Borys, 2004; Schachinger, et al., 2004) and some with direct addition method (Ewert, et al., 2008).

Although it is right to say that the rheological behavior of UHPC is different from its cement paste, since it contains other pozzolans and micro-sand, its fresh rheology is highly dependent on the cement dispersion in the paste by SP since the cement content in UHPC is around 3 times more than silica fume in weight fraction (Graybeal, 2006). It means that dispersion of cement particles is of great importance. However, as mentioned above, stepwise and delayed addition of SP may improve the flowability but the addition method of water has not been studied yet. The findings of this section help to improve the short and long-term performance of any concrete containing SP and low water/binder ratio, particularly UHPC, through enhancing the fluidizing effects of SP. In other words, the objective of this section is to promote the limited accessible knowledge regarding the mixing time after adding the water reducing agents and stepwise water addition, which both result in lower water content, higher workability, advanced strength and possibility of using higher aggregate content. These factors lead to a more eco-efficient UHPC and pave the way towards sustainable construction.

According to the fact that the liquid SP is a solution of solid particles in water, which should be taken into account as a part of water to cement or binder ratio, first an

appropriate quantity of SP was placed in oven at a temperature of 110°C for 72 hours.

The samples were weighted until a constant weight was reached and the solid and water

content of the SP could be calculated. Afterwards, the saturation dosage of SP, in which

the flowing time is minimum, was investigated for Portland cement I class 42.5R and

52.5R as the first phase of this research. This test method conforms to standard test

method known as Marsh funnel test for viscosity of slurries (ASTM D6910-04, 2004;

Ferraris, et al., 2001). In order to prepare the slurry, in laboratory condition of 22°C and

50% RH, first the cement was poured in the mixer. The SP in different percentages of

cement weight was mixed with the whole water, 35% w/c, and added to the cement.

Then all the constituents were mixed for 10 minutes. This test demonstrates that, the

longer the time of flow the more viscose the slurry and less effective the SP.
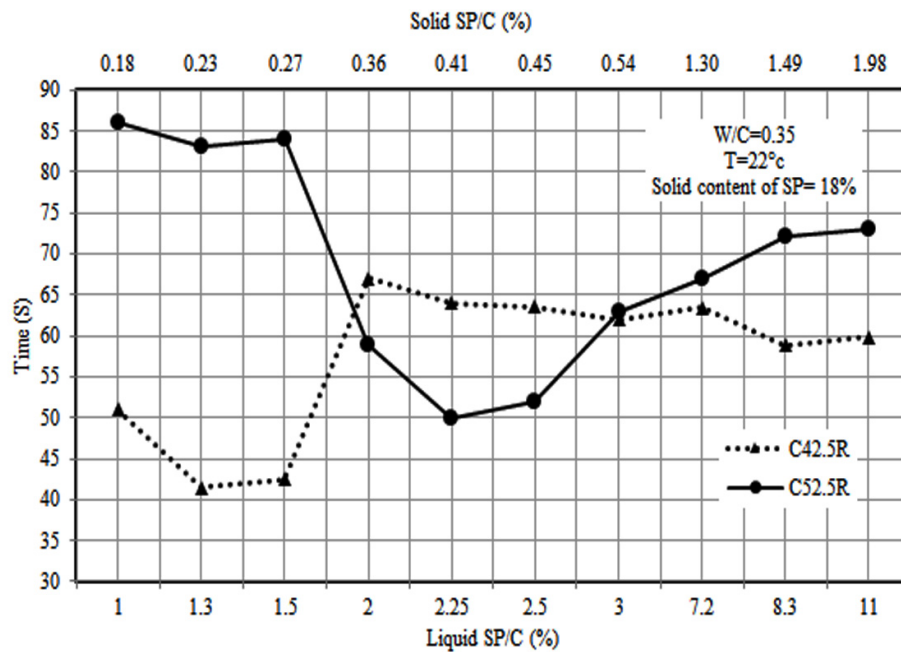
Figure 3.6:   Effect of SP dosage on Marsh funnel time.

The optimum SP dosage was obtained for cement 42.5R and 52.5R as well. The

outflow time for 300mL of the paste and the SP dosage relationship are depicted in

Figure 3.6. The optimum dosage of liquid SP for cement 42.5R and 52.5R are 1.3%

and 2.25% of the cement weight respectively corresponding to 0.23% and 0.41% solid

particles in SP as well. It can clearly be seen that, the general trend for both cements

are the same. In other words, the viscosity deceases to the optimum dosage and after

this point again increases and levels out with negligible fluctuations. Moreover, the

viscosity of C 52.5R is generally higher than that of C 42.5R except the liquid SP dosage

interval between 2% to 3%. The higher viscosity of paste of cement 52.5R even with

higher dosage of SP could be attributed to its finer particles and higher surface area.

Due to the fact that the liquid SP is more viscous than the pure water, by passing the

optimum dosage, in which most of cement particles are dispersed, and adding higher

amount of liquid SP, with respect to its 82% of solvent water, the portion of pure water

contributing in 35% w/c is reduced. This leads to higher viscosity and longer outflow

time. As a result, in both cases by passing the optimum SP content the viscosity

increases sharply.

As can be seen from the results, the preferred cement would be cement 42.5R since

it results lower viscosity with a lower SP content. Nevertheless, as we did not apply the

other pozzolans for the next phase, since we do not know their right proportions, cement

52.5R was used to compensate the effect of fineness of other pozzolans during mixing

procedure investigation.

In the second phase, three general methods were studied. The first method includes

watering the cement with 100% of the 0.35w/c content, mixing for 3 minutes, adding

SP and finally mixing for an extra 10 minutes. The second method is watering the

cement with a fraction of the whole required water, in this case 60%, mixing for 3

minutes, adding SP and mixing for another 4 minutes and finally adding the rest of 40%

water and continuing the mixing for another 6 minutes. In the third general method, first 60% of water was poured in mixer containing cement, mixed for 3 minutes, SP was solved in the 40% of the rest of water and added to the mixture and the process continued for another 10 minutes. The all three methods are similar in such a way that the SP is mixed for 10 minutes after its introduction to the mix to reach a steady-state consistency. Moreover, in all the three methods based on the findings for highest SP efficiency (Hsu, et al., 1999; Tue, et al., 2008), in which the effective time of SP addition is around 150 seconds after watering the cement, water and cement mixed for 3 minutes and then the SP was introduced.

In the third phase, to fulfill the process of adding water and SP to the mix, 50%, 60%, 70% and 80% of the 0.35 w/c was introduced to cement as first-part water (FPW) and mixed for 3 minutes. Afterwards, with the same method for all the samples, SP was introduced and mixed for another 4 minutes and finally the rest of remained water poured in the mixer and mixed for another 6 minutes. Then, the Marsh cone test was performed to compare the outflow time of the pastes and find the best FPW with respect to outflow time.

After finding the best mixing procedure of watering and adding the SP to cement, the optimum required mixing time after adding SP to cement was investigated with the aim of highest fluidity. This time interval has been fixed in the last tests in 4 minutes. This step fulfilled by altering the mixing time of SP, after its addition to the mix, from 2 minutes to 9 minutes. It should be noted that, the mixer used in this research is a mortar mixer according to EN 196-1 (BS EN 196-1, 1995). In addition, the low speed with planetary movement of 60 r/min was adopted.
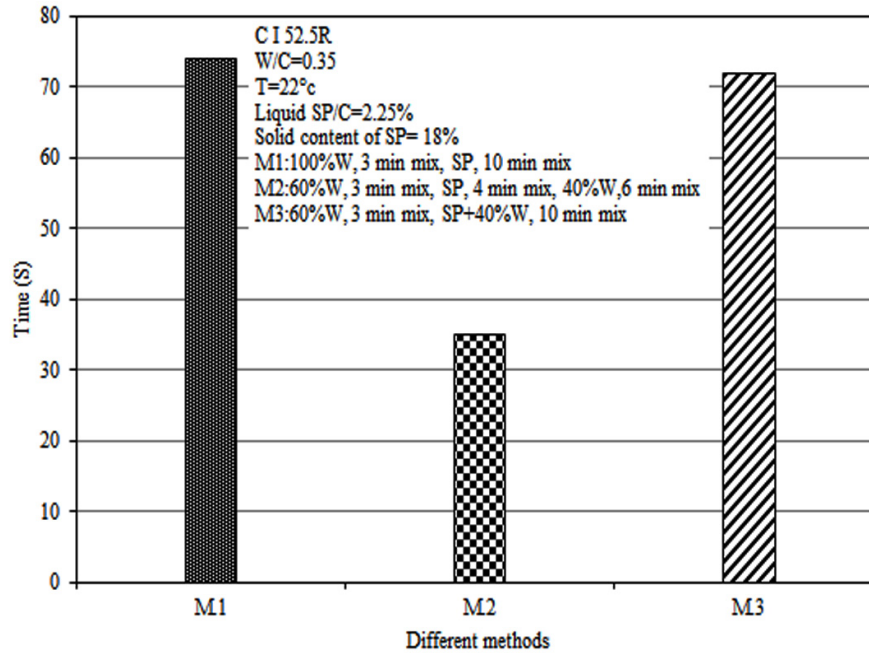
Figure 3.7: Effect of water and SP addition method on Marsh funnel time.

As described above, the second phase was to investigate the best method of watering the cement and adding the SP. It could be clearly seen in **Figure 3.7** that, the test method M.2 reveals a huge difference in outflow time and fluidity. In fact, as soon as a percentage of water introduces to the cement, cement particles dissolve in water and get ready to adsorb the anionic SP particles as a result of adsorption force between opposite charges which is a kind of chemical adsorption and goes beyond the aim of this research. Anyway, the SP disperses the cement particles and releases water. By now, all these 3 methods are the same particularly the first and the third methods which show almost the same results but in M.2 after the dispersion process of cement particles a percentage of water seems do not engaged in reaction with cement entirely. This part of water remains as free water resulting a higher fluidizing effect and consequently lower outflow time thus proving the superiority of M.2 among the other methods. These findings also are in agreement with the results reported in previous studies (Hsu, et al.,

1999; Tue, et al., 2008) demonstrating the effectiveness of delayed addition time of SP
to cement. Furthermore, it can be understood that the stepwise and delayed water
addition is also an efficient method with respect to higher fluidity as studied in this
research work.

The next phase as mentioned in previous section was to optimize the detected
method of watering the cement among different ratio of first-part water. As illustrated
in **Figure 3.8**, by increasing the amount of water, being mixed with cement to solve it
and release the Ca^{2+} ions, from 50% to 70% the fluidizing effect of SP increases
drastically. By passing the 70% of the whole water, i.e. 0.35w/c, the outflow time
increases again. The reason of higher viscosity for water quantities lower than 70%
could be attributed to the lack of appropriate water to solve the cement particles and
release Ca^{2+} ions which adsorb the SP's chains. In other words, although enough SP
content is accessible, the cement particles cannot be charged positively being confined
sufficiently with Ca^{2+} ions due to lack of water and consequently dispersed by SP. On
the other hand, for the first-part water fraction higher than 70%, the lower efficiency of
paste could be attributed to the lack of second-part water which could be remain free
after the fluidizing effect of SP to improve its fluidity and accordingly reduce the
outflow time.

The final phase was to find out the minimum mixing time after SP addition to the
wet cement. According to the obtained results in this part, these mixtures are all
composed of 0.35w/c and 2.25% SP/c. First 70% of water was introduced to the cement
and mixed for 3 minutes. Consequently, SP was added to the wet cement and mixed for
2, 4, 7 and 9 minutes. Finally, the 30% of remained water poured in mixer and mixed
for an extra 6 minutes. Based on **Figure 3.9**, the results show that at least 4 minutes of
mixing is obligatory after SP addition to the mix to be able to disperse the cement

particles and release water. Nevertheless, according to the improved apparent features of the paste such as less air bubbles, through visual observation, 6 minutes of mixing is suggested.
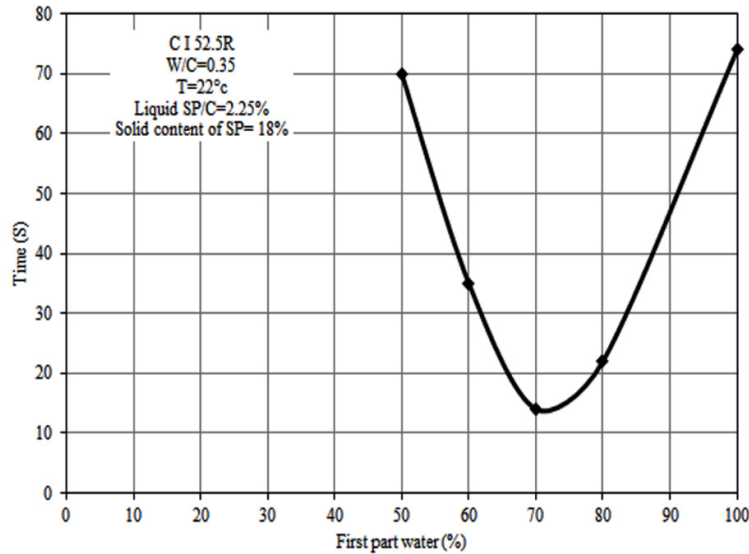
Figure 3.8: Relationship between the first-part water and Marsh funnel time.
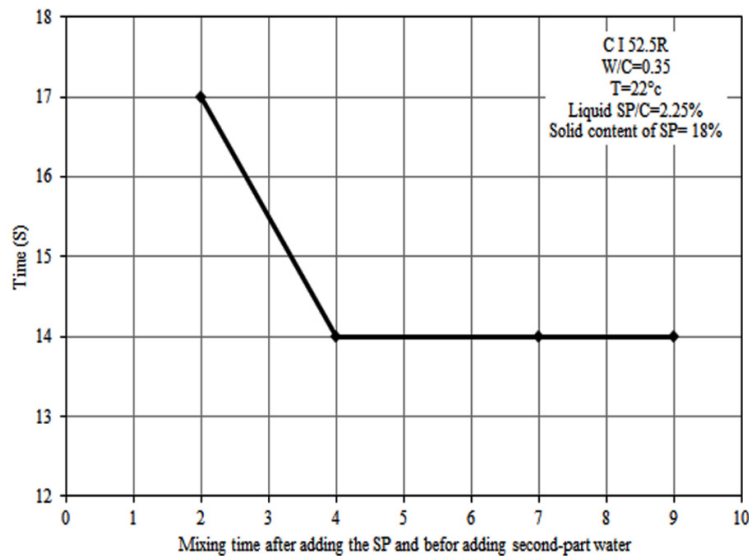
Figure 3.9: Effect of mixing time after adding SP on Marsh funnel time.

3.3 High-volume fly ash paste for developing UHPC

As explained before, the goal of this part of research is to develop a more eco-efficient UHPC paste, compared to known commercially available UHPCs. In this regard, it would be of great importance to replace cement and silica fume, as two main constituents of the prevalent UHPC compositions and particularly with high cost and environmental impacts, by other pozzolans to a maximum extent. Besides, since a part of cement and silica fume remain unreacted and remains just as filler, the other pozzolans could be replaced to play all these roles at the same time. In addition, as silica fume is very expensive and MK is responsible for high-embodied CO_2, fly ash seems to be the main priority for cement and silica fume substitution. FA is available in huge quantities worldwide as a waste material with very low cost and environmental impacts since its application prevents the massive landfills used by this waste material from the thermal power plants. It was found that in a concrete with 45%-55% cement replacement by fly ash, just 20% of it react in pozzolanic reaction and the rest remain as filler (Poon, et al., 2000; Lam, et al., 2000). It also was studied that by restraining the mean particle size of fly ash from 20 μm to 8 μm, its activity increases leading to higher compressive strength (Hashimoto, et al., n.d.). In this regard, the presented chapter aims at development of an eco-efficient UHPC paste with high content of fly ash in different average particle size, as partial replacement of cement and silica fume, to study its effect on fresh and hardened properties of paste.

3.3.1 Fly ash preparation

Two different methods were applied to decrease the grain size of the original fly ash (O-FA): dry milling and wet milling. The first one includes milling the fly ash for 30 minutes (FA D-30) in a container with 15 ceramic balls of 2 cm in diameter

(**Figure 3.10**) which results in an ultra-fine fly ash with 4.48 μm of average particle size, determined by particle size analyzer (**Figure 3.12**).

Figure 3.10: Dry-milling machine.

The second method includes fly ash milling as a suspension in water with 1.4 g/cm^3 of density. In this process almost 30% of the milling container volume was filled with round balls with diameters of 2 to 3.5 cm (**Figure 3.11**) and the mill was operated in different time steps: 60, 240 and 360 minutes, named as FA W-60, FA W-240 and FA W-360, respectively.

Figure 3.11: Wet-milling machine and its ceramic balls.

The particle size of cement and fly ash with different grinding time were also analysed by CILAS EcoSizer 920L® (**Figure 3.12**). This instrument easily performs analysis of particles in range of 0.3 to 400µm in a liquid dispersion mode.
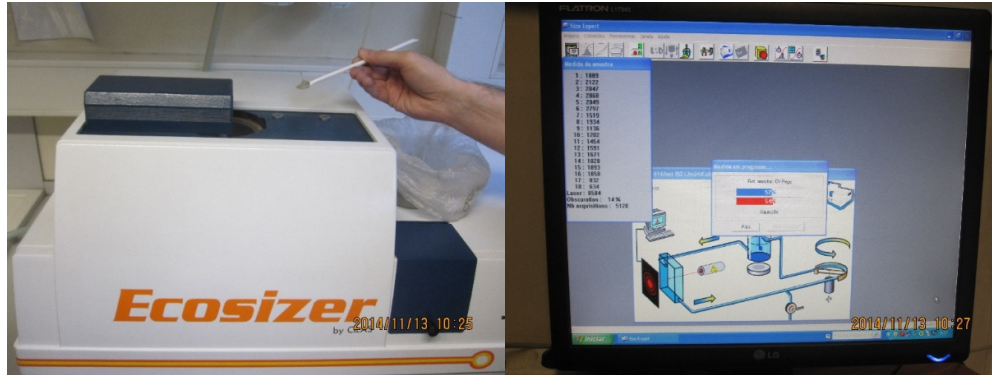
Figure 3.12: Particle size analyzer instrument.

The results of particle size analysis are presented in **Figure 3.13**.
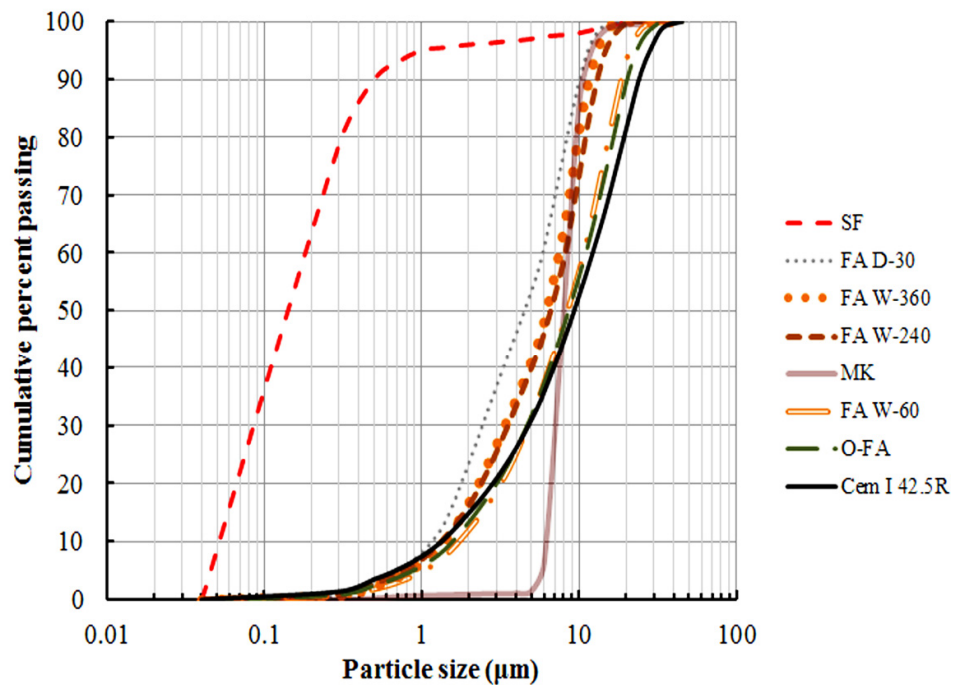
Figure 3.13: Cumulative particle size distribution; From left: SF, FA D-30, FA W-360, FA W-240, MK, FA W-60, O-FA and Cement I 42.5R with average particle size of 0.15, 4.48, 6.19, 6.61,8, 8.5, 8.55 and 9.3 µm respectively.

As can be seen, the wet grinding process is not as efficient as the dry one since the mean particle size remains around 6 μm after 360 minutes of milling. **Figure 3.14** and **Figure 3.15** were obtained by scanning electron microscopy (SEM – Hitachi SU1510) and show the particle shape of O-FA and FA D-30. It is also clear that the finer particles preserve their own original spherical shape and just the coarser particles were crashed into finer ones.
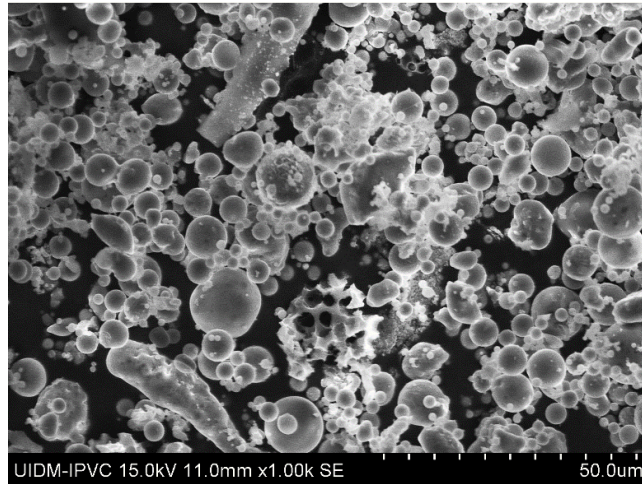
Figure 3.14: Low magnified SEM image of O-FA particles.
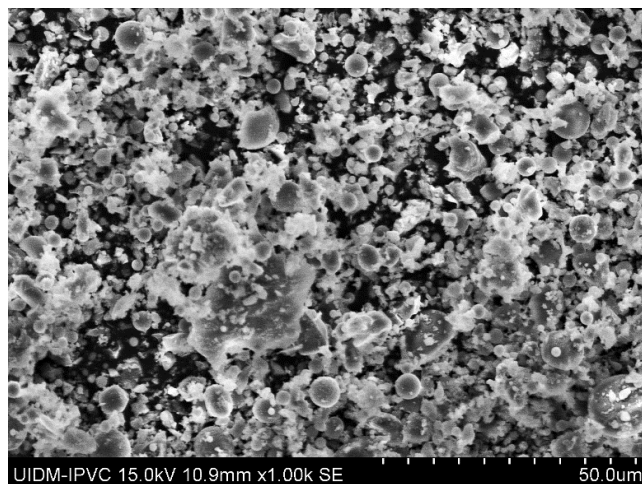
Figure 3.15: Low magnified SEM image of FA D-30 particles.

3.3.2 Paste preparation

The fluidity and compressive strength are two of the most important UHPC paste properties and its adjustment should be carefully developed. In this regard, the effects of O-FA, FA D-30, FA W-360, metakaolin and silica fume were studied based on the apparatus described in ASTM C 230/C230M–03 flow table test for Hydraulic Cement (ASTM C 230/C 230M – 03, 2007). Before starting the mixtures, the enhanced fly ash, FA W-360, was dried in oven at 110°C for 24 hours until a constant weight was obtained and after that, it was cooled during 24 hours at temperature of 20°C. It should be noticed that before this stage, MasterGlenium SKY 526® was compared with Glenium Sky 617® through a series of preliminary tests based on the procedure presented in **Section 3.2**. It was concluded that MasterGlenium SKY 526® provides higher fluidity for paste. With respect to this fact, the rest of this research was performed with MasterGlenium SKY 526®. In the first step, cement was mixed with 10%, 15%, 20%, 25%, 30% and 35% of its weight by O-FA. For all these pastes water to binder ratio of 18% (w_t.%) and SP to binder ratio of 2.5% (w_t.%) were used. After mixing the dry powders during 3 minutes, 70% of water was added and after 3 minutes of mixing, the SP was introduced to the wet powder and mixed during more 6 minutes. Afterwards, the rest of water was added and the mixture was continuously mixed for more 6 minutes. After the total mixing time (18 minutes), the flow table (**Figure 3.16)** was carefully wiped and the paste placed in the conical mold. Then the paste was cut to a plane surface and the mold was lifted up. When no diameter change was observed, the measurement of two perpendicular sides was made and the average of the two readings was registered as the paste final flow. After the final flow determination, the paste was replaced in the mixer, mixed by hand and molded in three cubes of 5x5x5 cm^3. To evaluate the compressive strength of the samples after 28 days, they were demolded after 24 hours

and were immersed in water at 20°C for more 27 days. With this method the optimum

percentage of O-FA regarding fluidity and compressive strength was obtained. This

test was also performed with FA W-360 and FA D-30 in order to study their effects on

the fresh paste consistency as well as its compressive strength at the hardened state.

Figure 3.16: Flow-table test procedure.

As can be seen (**Figure 3.17**), concerning the compressive strength, the best addition

percentage of the original fly ash (O-FA), with 8.55 μm of average particle size, related

to cement weight is 15% while 20% of it brings highest fluidity (143 MPa and 33 cm

respectively). Nevertheless, its fluidity is still 0.5 cm lower than the plain mixture

without any fly ash. The main reason regarding the fluidity improvement by increasing

FA content from 10% to 20%, could be attributed to its spherical-shape particles (see

Figure 3.14) with better sliding effect rather than angular cement particles. By

increasing the fly ash content to 35% (w_t.%) of cement, both strength and fluidity of

paste decrease by around 10% and 12% of their corresponding maximums to 128 MPa

and 29.1 cm respectively.

In the next step, FA W-360 with 6.19 μm of average particle size was used instead

of FA. It was interestingly observed that not only the compressive strength increased

(to around 5% compared to 20% FA), but also the fluidity was increased even more

than the best of FA (7.6% to a flow spread of 35.5 cm). This phenomenon can take great

importance in the UHPC workability when very low water/binder ratio is applied.

Fluidity and compressive strength were even more improved with replacement of FA

D-30 instead of FA and FA W-360 to a maximum of 153 MPa and 37.5 cm of strength

and fluidity respectively, for 25% of FA D-30 addition to cement which is equivalent

to 20% cement replacement.
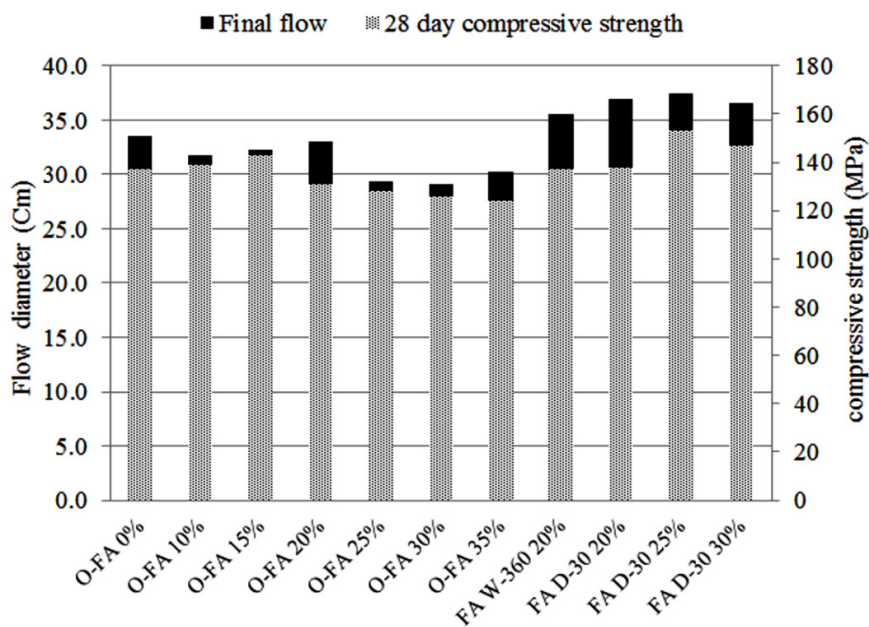
Figure 3.17: Comparison of strength and fluidity of pastes composed of O-FA, FA W-360 and FA D-30 in different
percentages.

The reason why fluidity is directly dependent on the fly ash particle size is the

sphericity of its fine particles and their glassy surface as well, even after crushing,

which offers easier particles sliding between each other when incorporated in cement

paste (see **Figure 3.14** and **Figure 3.15**). Compressive strength improvement could be

attributed to the higher reactivity of finer FA particles, which could promote a better

distribution in the paste and react with higher percentage of cement particles resulting

in higher C-S-H development. The other reason could be higher packing density of the

paste, since these finer particles are able to fill the voids between coarser cement particles, developing a uniform distribution of the compressive stress. As FA W-360 20% reveals strength and fluidity higher than O-FA but less than FA D-30, it was decided to continue the process of wet milling for more duration to obtain average particle size similar to FA D-30. In this regard, a regression analysis was performed according to the time and average particle size of wet-milled fly ash particles.

$y = 8.7051e^{-1E-03x}$
$R^2 = 0.9618$

Mean particle size of FA D-30
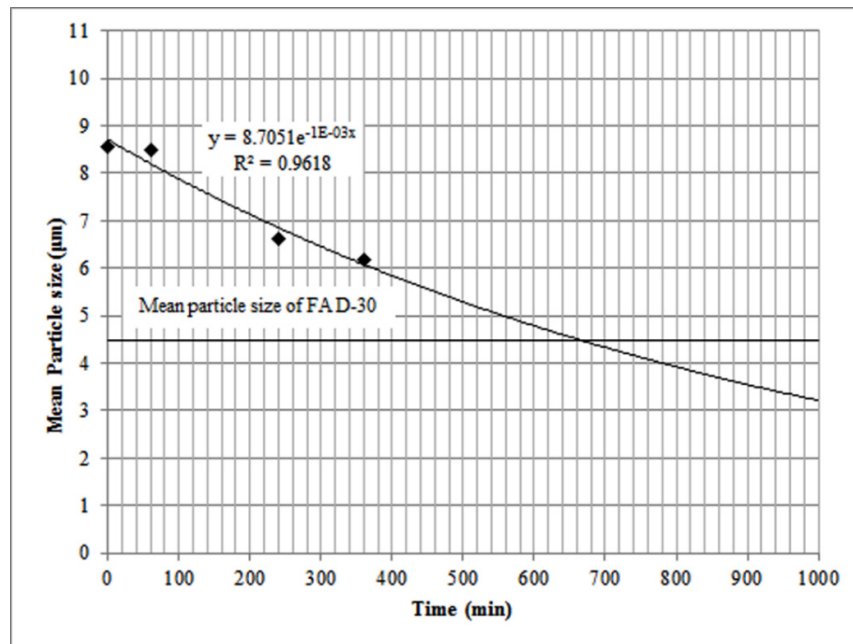
Figure 3.18: Estimated time for wet-milling process to obtain average particle size of 4.5 µm.

According to the fitted logarithmic curve, depicted in **Figure 3.18**, the minimum required time to obtain grinded fly ash with the same size of FA D-30 is 660 minutes. However, it was predicted that when the particles become finer the milling process would not be as efficient as coarser state. With respect to this fact, the time was adjusted for 48 hours to ensure enough particle fineness. In addition, the longer process would be preferable since if the average particle size reduces even lower than FA D-30, it is expected that they will improve fluidity as well as strength. Accordingly, with the same

procedure and density a larger wet-milling machine with capacity of 100 kg
(**Figure 3.19)** was loaded with water, fly ash and small ceramic balls, as shown in
Figure 3.11, and lunched for 48 hours. After finishing the process, a small sample of
material was taken and dried in oven (110°C) to be tested. Unfortunately, the paste
containing the new powder was not again as efficient as dry milled FA D-30 with
respect to its fluidity. The reason why fluidity of paste is of great importance for
developing UHPC is that it enables us to use more aggregate or pozzolans which all
reduce the cement content in 1 m^3 of concrete.

Figure 3.19: Wet-milling machine with 100 kg capacity

After this step, it was concluded that generally, wet-milling process would not be an efficient way of fly ash processing and our research was followed by FA D-30. The reason can be attributed to some chemical reactions of fly ash components during wetting and drying phases or even different particle size as result of different grinding mechanism. To investigate what the reason is, thermogravimetric analysis (TGA) as well as SEM were performed on two samples of FA D-30 and wet-grinded powder after 48 hours (FA W-48). As shown in **Figure 3.20** and **Figure 3.21**, the particles' sizes and shapes are very similar while the TGA results demonstrate a considerable difference particularly in temperatures between 100°C to 200°C.

a)   **b)**
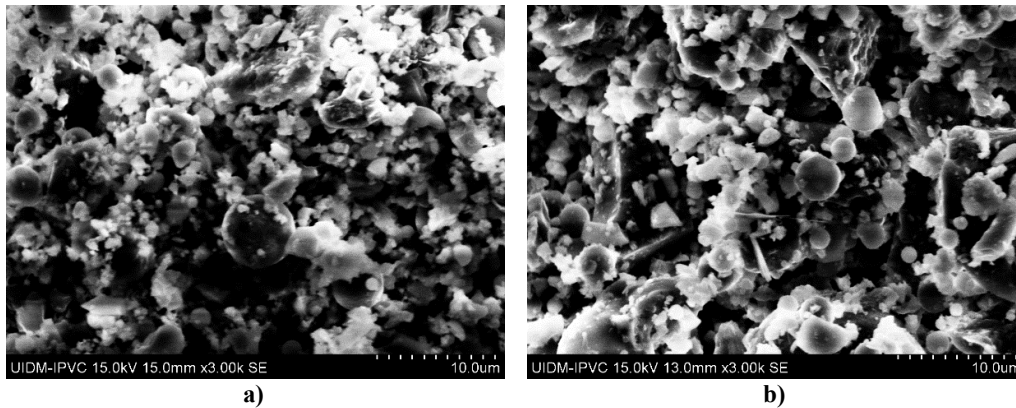
Figure 3.20: SEM image of FA W-48 (a) and FA D-30 (b).
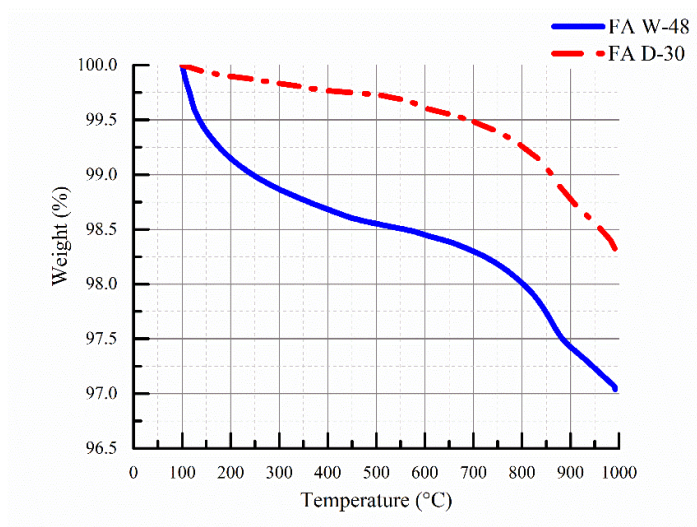
Figure 3.21: TGA curves for FA W-48 and FA D-30 (heating rate of 10°C/min in Argon).

The weight loss between 100°C and 200°C is mainly the result of decomposition of ettringite or dehydration of gypsum (Zhou & Glasser, 2001; Van der Merwe, et al., 1999). Besides, the weight loss between 450°C and 500°C corresponds to the decomposition of $Ca(OH)_2$ and finally the weight loss at 750°C is related to decarbonation of calcium carbonate existing in clinker or filler (Alarcon-Ruiz, et al., 2005). As can be seen in **Figure 3.21**, there is a steep decline in FA W-48 curve between 100°C and 200°C apparently demonstrating ettringite formation or gypsum hydration during the wet-milling process. In addition, by comparing two curves of FA D-30 and FA W-48 between 450°C and 500°C, some limited C-H products in FA W-48 can be distinguished based on the higher slope of the FA W-48 curve. The rest of the curves exhibit almost the same trend. Accordingly, the same particle size and shape could be acquired through both of the milling methods. However, the probable chemical reactions of fly ash with water during the wet-milling procedure makes it an inferior processing method. Therefore, it seems that jet-milling machines or air classifiers would be better technologies to prepare fly ash with very small and fine particle size without any chemical reactions and particularly very low energy consumption per 1 kg of powder due to their very high capacity.

Since the best amount of added fly ash is 25% (wt.%) of cement in the FA D-30 state, the next part of this chapter was performed with this fixed quantity of the enhanced FA and with incorporation of two other pozzolanic materials, metakaolin and silica fume, to study their effects on the paste rheology and compressive strength as well. As can be seen (**Figure 3.22**), by addition of MK, the fluidity reduces by 4% and 12.8% for 2.5% and 5% of added MK, respectively, compared to the mixture of cement with 25% FA D-30. On the other hand, the obtained results show that the compressive strength of the mixture containing 5% MK is 1.7% higher than FA D-30 25% which is

not considerable.
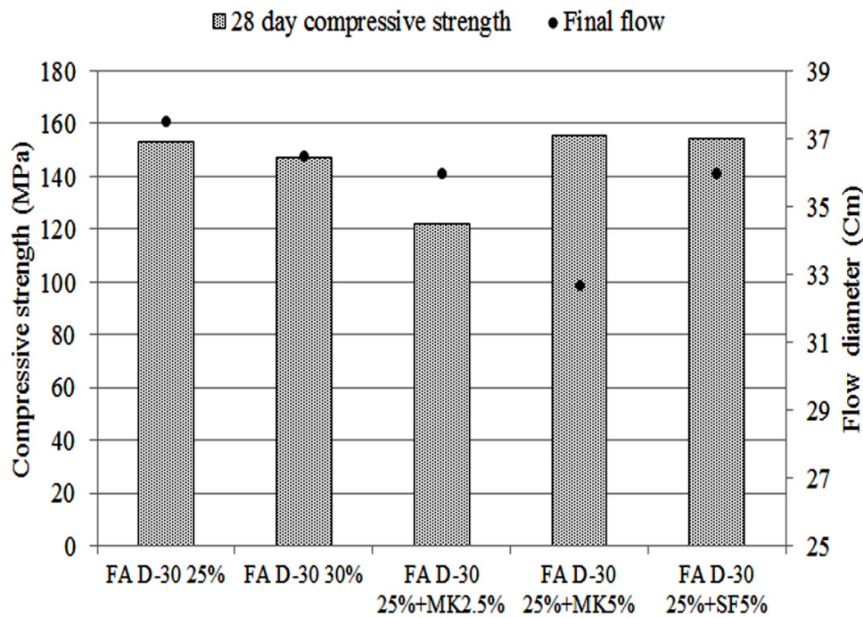
Figure 3.22: Comparison of different pastes including 25% FA D-30, 30% FA D-30, 2.5% MK+25% FA D-30, 5% MK+25% FA D-30 and 5% Basf® silica fume+25% FA D-30.

Two compositions could be selected regarding the highest cement replacement, fluidity and compressive strength at the same time. The first one is 25% of FA D-30 plus 5% of Elkem® micro silica which gives approximately 154.4 MPa of compressive strength and 36 cm fluidity. The second one is the mixture with 30% of FA D-30 with 147 MPa and 36.5 compressive strength and fluidity respectively. As expected the former one develops higher strength and the later one shows higher fluidity. On the other hand, the selected metakaolin seems to be an unsuitable material for self-compacting UHPC. Although the compressive strength of the mixture containing 5% MK is almost equal but slightly greater than the mixture having 5% silica fume, its fluidity is 9% less than that. This undesired effect of MK could be attributed to its gap-graded particle size distribution (**Figure 3.13**) and its angular particle shape as well (Li & Ding, 2003; Karahan, et al., 2012). In addition, MK bears high amount of

embodied CO_2 which makes it an undesirable pozzolan with the aim of our research to

develop an eco-efficient UHPC.

3.4 Interaction of SP with cement and pozzolans

In last section it was investigated that fly ash and silica fume would be two main

pozzolans for developing UHPC. In addition, it is obvious that water/cement ratio is a

very important factor regarding strength and self-compactness. Consequently, SP

quantity and its interaction with cement and pozzolans is a crucial factor influencing

water quantity, fluidity and finally strength. In other words, if the quantity of SP used

in concrete be less or more than its optimum dosage, it may causes some problems. In

the former situation, it cannot disperse all the particles existing in the paste and in the

latter case, it causes lower quantity of pure water when a fixed water/cement or

water/binder ratio should be used. In fact, when the SP exceeds its optimum dosage,

due to its higher viscosity compared to tap water, the amount of added pure water should

be reduced which finally leads to a more viscose and adhesive paste. In this regard,

finding the optimum dosage of SP for each of aforementioned materials both

individually and collectively would be of great importance. In this section two different

test method were performed to study the interaction of SP on cement, fly ash and silica

fume. From now on, ultra-fine fly ash (UFFA) is being used instead of FA D-30.

The first method of measuring the interaction of cement-Pozzolans-SP was

mini-slump test by means of mini-cone flow-table test. The top and bottom of this cone

have diameters of 19 mm and 38 mm and a height of 57 mm. Based on this test we can

measure the flow diameter of prepared paste to understand the optimum dosage of SP

and the way they interact with different pozzolans. **Figure 3.23** shows the cone used

for this test. The spread of the paste is attributed to paste viscosity and not the

flowability since the shear stress during rising the mold is greater than yield stress (Camões, 2002). In this regard, determination of spread of paste allows us to evaluate the optimum dosage of SP as well as its compatibility with cement and pozzolans (Mendes, 2013).
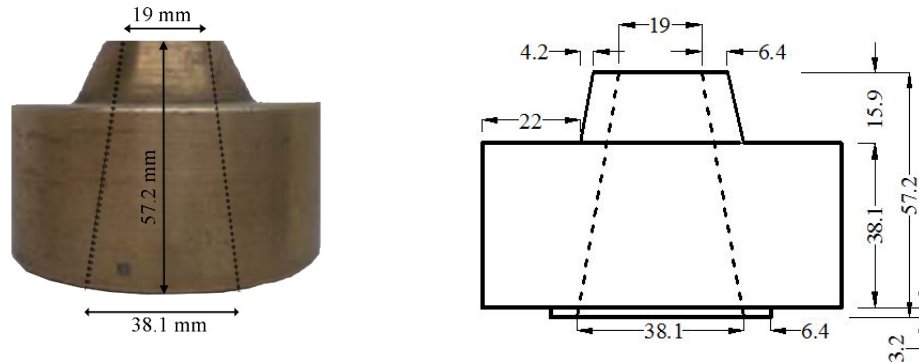
Figure 3.23: Mini-slump cone (dimensions in mm).

The second test is based on Brookfield instrument to measure and control the viscosity. This device measures fluid viscosity at given shear rates. By definition, viscosity is a principal parameter representing a fluid resistance to flow. In other words, it is a measure of friction of two layers of a liquid when they are moving in relation to each other with different velocities. The greater this friction is, the greater the force required for this movement. This force is called shear. Therefore, the higher the viscosity, the greater the shear force required for any movement. This is why viscosity is of great importance for any concrete particularly UHPC with supper-fine powders, very low water/binder ratio and particularly self-compactness ability.
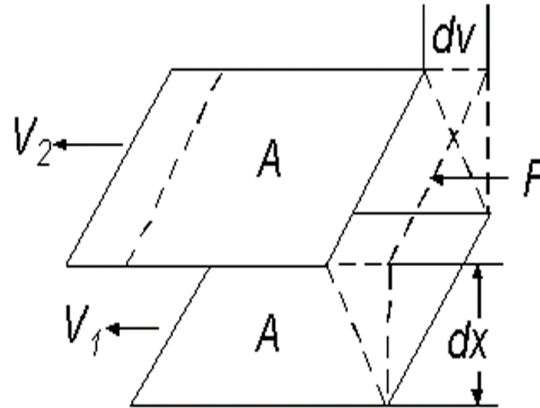
Figure 3.24: Schematic representation of concept of viscosity (Brookfield Engineering Laboratories, Inc. , 2015).

Newton described the concept of viscosity based on **Figure 3.24**. According to his theory, viscosity is defined mathematically as **Equation 3.2**:

$$\eta = Shear\ stress\Big/Shear\ rate = \frac{F/A}{dV/dX}$$

Eq.(3.2)

where η is viscosity, A is the area of two parallel planes of liquid, dx is the distance between planes, V_1 and V_2 are the velocity of planes movement in the same direction, F is the force required to maintain the velocities constant and dV/dX is called velocity gradient or shear rate.

Brookfield instrument deals with liquids and semi-solids. To operate this test, a spindle is immersed in the test fluid. Then it is derived through a calibrated spring. The viscosity force of the fluid acts against the spindle and is measured by spring deflection which itself is measured by a rotary transducer. The measurements depend on the rotational speed of spindle, the size and shape of spindle, type of container in which spindle is rotating and finally the torque of calibrated spring (Brookfield Engineering Laboratories, Inc. , 2015).

Figure 3.25: Typical Brookfield viscometer and its spindles.

One advantage of this equipment is that, by suitably combining the angular speed of spindles, it is possible to cover a wide range of velocity gradients (shear rate), shear stress and thus viscosities. By varying the value of the angular velocity, it is possible to register the respective values of the apparent viscosities. For the aim of this research spindle N.5 was applied since it has shown its efficiency for this type of pastes (Mendes, 2013). The viscosity was registered for six different speeds namely 5, 15, 40, 60, 80 and 100 RPM in two upward and downward trends. After the apparent viscosities were obtained, the corresponding shear stress and shear rate for each angular velocity and apparent viscosity are calculated based on **Equation 3.3** (Camões, 2002).

$$\tau = \frac{\pi}{15}\eta_0 \overline{\omega_0} \qquad\qquad\qquad\qquad\qquad \text{Eq.(3.3.a)}$$

$$\dot{\gamma} = \frac{\tau}{\eta_0} \qquad\qquad\qquad\qquad\qquad\qquad \text{Eq.(3.3.b)}$$

where τ is shear stress (mPa), η_0 is apparent viscosity in (mPa.s), $\overline{\omega_0}$ is angular velocity (RPM) and $\dot{\gamma}$ is shear rate (s^{-1}). Based on the results of these equations the

relevant rheogram, such as one depicted in **Figure 3.26**, is drawn. Then the

corresponding regression analysis is performed based on Bingham equation (**Equation**

3.4), in order to estimate the viscosity and yield stress of the paste (Camões, 2002).
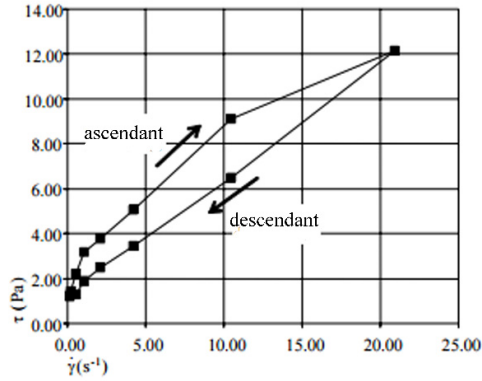
Figure 3.26: Typical rheogram (Camões, 2005).

$$\tau = \tau_0 + \eta\dot{\gamma}$$ Eq.(3.4)

where τ_0 is yield stress and η is the viscosity of the studied paste.

3.4.1   Slurry preparation

For development of slurries, a fixed volume of cement, 200 mL, was taken to

measure the viscosity and fluidity of the slurry through mini-slump test and Brookfield

viscometer as well. The water/powder ratio, SP ratio and pozzolans replacements are

all in terms of volume fraction. The reason why all these ratios are considered as volume

fractions is that the SP particles interact with each particle of powder. Therefore, the

fluidity and viscosity of slurry is highly dependent on fineness of particles and not just

their weight. Otherwise, if the fraction ratios of SP, water and other substituted

pozzolans being changed in terms of their weights, this study changes to a bi-variable

optimization since the water content should also be taken into account beside the

variation of SP. In other words, as the powders get finer, their volume, in terms of a definite weight, increases and their density decreases. Therefore, the required water for the same fluidity, without considering SP, should be increased in weight method while, the water/powder is fixed. To avoid this, it was preferred to substitute cement by pozzolans in terms of volume fraction and just change the SP content to study its sole effect. Based on this fact, SP contents, shown in **Figure 3.27**, are in terms of "weight of solid particles in SP/ volume of binder" (W_t.S.SP/V.P). If we translate this ratio to "volume of liquid SP/ volume of powder"(V.Lq.SP/V.P) the percentages are changed as depicted in **Figure 3.28**. Water was fixed to 80% V_f of powder volume. As can be seen in the following chart, first the interaction of cement-SP was studied. In this step, SP in different percentages was added to slurry to investigate its effect. In the next phase, 33.3 % (V_f.) of cement was substituted by SF. This combined binder was also studied with different percentages of SP. The same procedure was carried out for blend of cement and UFFA by 33.3% V_f. of cement replacement. The goal of this study was to investigate the interaction of SP with cement and other pozzolanic admixtures when used as a blend. It is worthy to remind that the percentage of solid particles inside SP is 30% (w_t.) of its liquid. For more clarification, all the compositions studied herein, in terms of both volume and weight of their constituents and their corresponding flow diameter and viscosity, are depicted in **Table 3-4** to **Table 3-7**. The mixture preparation includes 3 minutes of powder mixing in dry state, adding 70% of water to powder and mixing for another 3 minutes followed by adding SP and mixing for 5 minutes and finally adding the rest of water and mixing for more 4 minutes which totally last for 15 minutes. This procedure is derived from the main low-energy mixing method described in previous sections of this chapter.

Regarding the quantity of SP, one composition in the following tables is explained

here. For instance for C66.7-SF 33.3-SP 2.3, we have totally 200 mL of powder, 133.4

mL of that is cement and 66.6 mL is SF. As explained before, 2.3% is the fraction ratio

of weight of solid SP particles to volume of powder, equal to 4.6 gr of solid SP particles.

As 30% of weight of liquid SP is composed of solid particles, for having 4.6 gr of solid

particles, 15.33 gr liquid SP is required. With respect to density of 1.070 gr/cm^3 for

applied SP, this volume corresponds to 14.33 mL equal to 7.16% of volume of powder

as shown in **Figure 3.28**. By transforming these fraction ratios to weight of liquid

SP/ weight of powder (W_t.Lq.SP/W_t.P), **Figure 3.29** can be obtained.
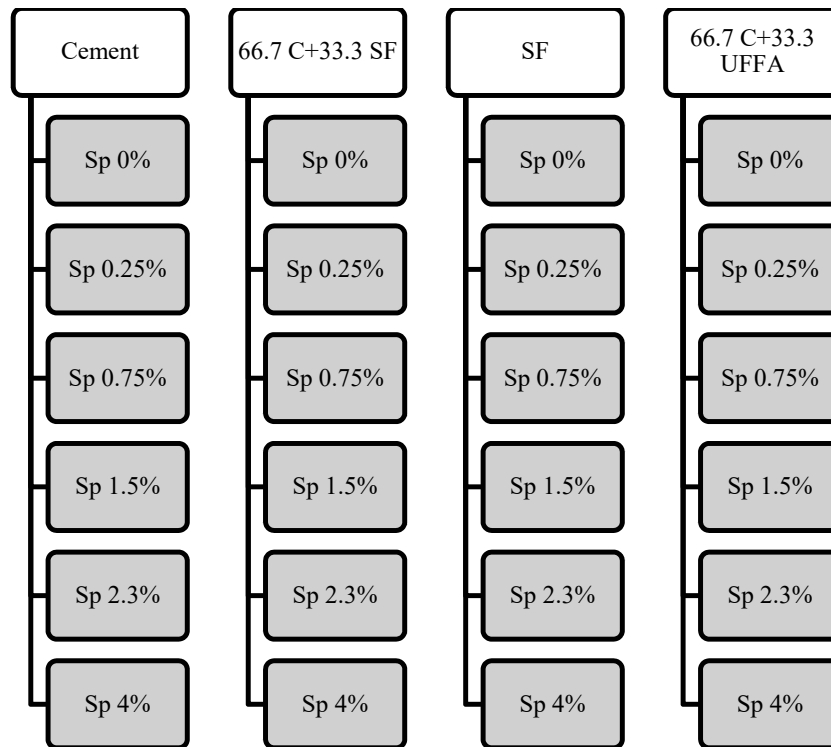
Figure 3.27: Schematic representation of test procedure based on W_t.S.SP/V.P.

Cement	66.7 C+33.3 SF	SF	66.7 C+33.3 UFFA
Sp 0%	Sp 0%	Sp 0%	Sp 0%
Sp 0.78%	Sp 0.78%	Sp 0.78%	Sp 0.78%
Sp 2.34%	Sp 2.34%	Sp 2.34%	Sp 2.34%
Sp 4.68%	Sp 4.68%	Sp 4.68%	Sp 4.68%
Sp 7.16%	Sp 7.16%	Sp 7.16%	Sp 7.16%
Sp 12.46%	Sp 12.46%	Sp 12.46%	Sp 12.46%
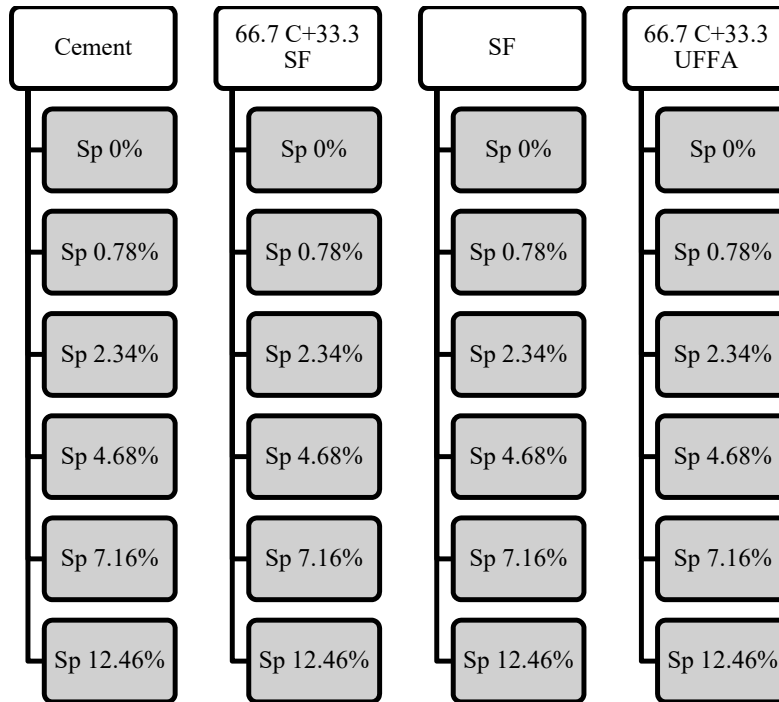
Figure 3.28: Schematic representation of test procedure based on V.Lq.SP/V.P.

Cement	66.7 C+33.3 SF	SF	66.7 C+33.3 UFFA
Sp 0%	Sp 0%	Sp 0%	Sp 0%
Sp 0.27%	Sp 0.3%	Sp 0.38%	Sp 0.29%
Sp 0.81%	Sp 0.89%	Sp 1.14%	Sp 0.87%
Sp 1.61%	Sp 1.79%	Sp 2.27%	Sp 1.74%
Sp 2.47%	Sp 2.74%	Sp 3.48%	Sp 2.67%
Sp 4.3%	Sp 4.76%	Sp 6.06%	Sp 4.65%
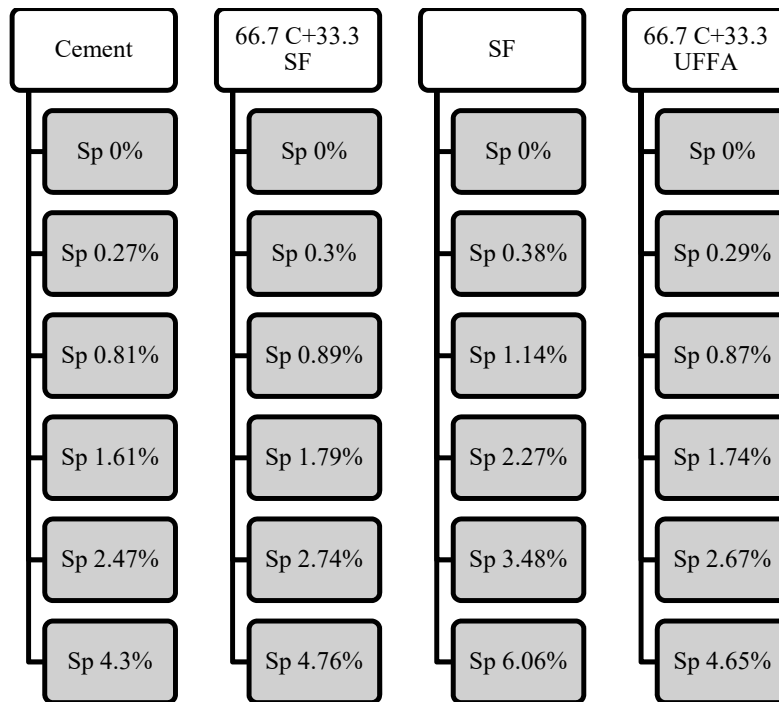
Figure 3.29: Schematic representation of test procedure based on W_t.Lq.SP/W_t.P.

As explained before, based on the obtained apparent viscosities and their relevant rotational speeds, from Brookfield test, the shear stress and shear rates were calculated based on **Equation 3.3** and their rheograms were plotted. As an example, a typical rheogram and the best-fitted line to its curve, representing the Bingham equation, for paste of C66.7- UFFA 33.3-SP 0.25 are depicted in **Figure 3.30**.
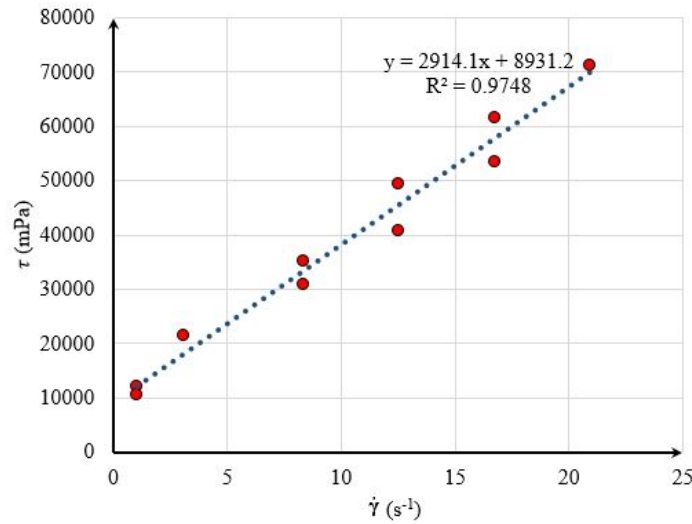
Figure 3.30: The rheogram and the best-fitted line for C66.7- UFFA 33.3-SP 0.25.

As can be seen from the fitted line, the viscosity and yield stress for this paste are 2914.1 mPa.s and 8931.2 mPa respectively. The results for other pastes are provided in **Table 3-4** to **Table 3-7**. In cases those yield stress showed a negative value, it was manually adjusted to zero.

Based on the results for fluidity of slurry and their corresponding obtained viscosities, as depicted in **Figure 3.31** and **Figure 3.32**, it can be seen that the both series of results could be used to verify the optimum percentage of SP for cement slurry. As shown, by increasing the SP dosage from 0% to 4%, the highest fluidity and lowest viscosity were attained with 1.5% of SP. Besides, both trends showed approximately the same behavior regarding the viscosity of slurry. Similarly, when flow diameter of slurry increases, the viscosity decreases.

Table 3-4: Cement slurry compositions.

Name		Cement	SF	UFFA	SP	Water	Flow (mm)	Viscosity (mPa.s)	Yield stress (mPa)
C-SP 0	Wt.	620	0	0	0	160	0	-	-
	Vol.	200	0	0	0	160			
C-SP 0.25	Wt.	620	0	0	1.67	158.8	0	3913.9	15995
	Vol.	200	0	0	1.56	158.8			
C-SP 0.75	Wt.	620	0	0	5	156.5	14.6	946.6	0
	Vol.	200	0	0	4.67	156.5			
C-SP 1.5	Wt.	620	0	0	10	153	15.2	456.5	0
	Vol.	200	0	0	9.35	153			
C-SP 2.3	Wt.	620	0	0	15.33	149.27	15.2	424.9	0
	Vol.	200	0	0	14.33	149.27			
C-SP 4.0	Wt.	620	0	0	26.67	141.33	15.1	463.7	0
	Vol.	200	0	0	24.92	141.33			
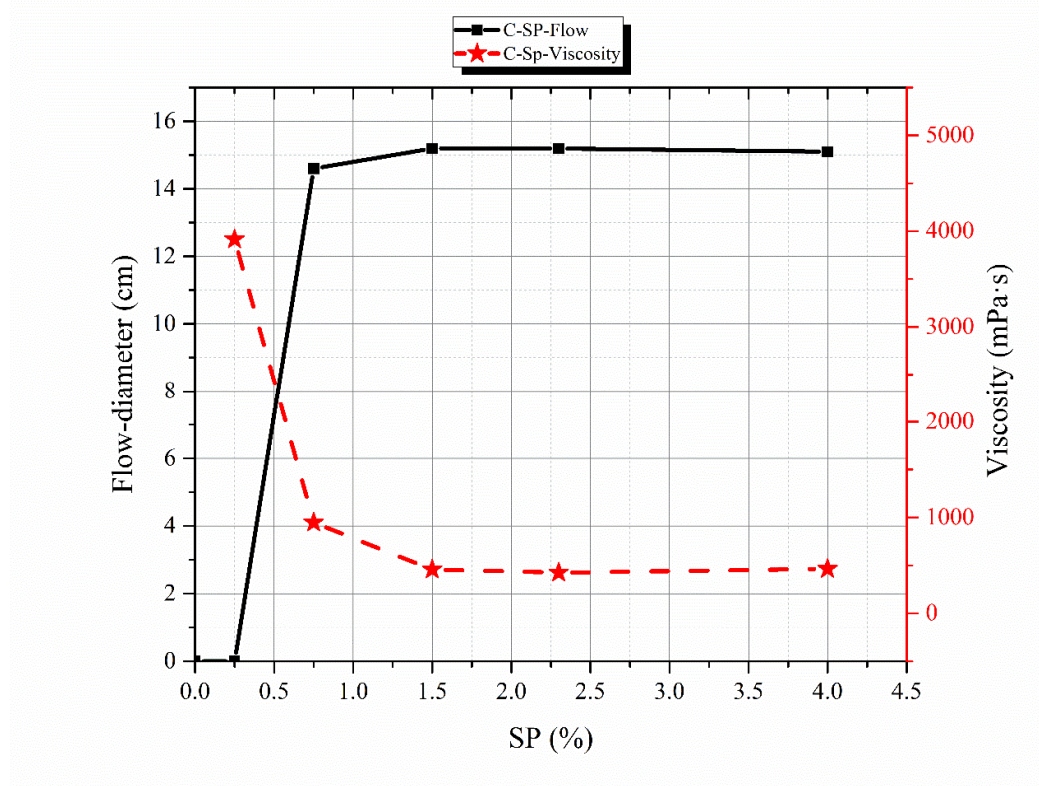
Figure 3.31: Flow diameter and viscosity of cement slurry with different percentage of SP (Wt.S.SP/V.P).

Figure 3.32: Slurry of cement with different percentages of SP.

It should be noticed that, however the results of Brookfield test demonstrated good

precision for slurry of cement and slurry of cement-UFFA (**Figure 3.36**), the results of

tests including SF were not reliable. In other words, during the test it was observed that in some cases, particularly in case of SF blends, as time elapses the slurry around the spindle was segregated and it caused inconsistency of test results. Furthermore, after finishing the test some sedimentation in the container was observed which means while the top part of the slurry becomes diluted, by passing the time, the bottom of it becomes more viscose resulting in some errors in the results. In addition, as mentioned above, even rotary movement of the spindle causes some segregation around itself, which changes the test results by passing the time as well as changing the rotary speed of the spindle. It means that however, we can use this method as a measure of viscosity it is not highly reliable for more precise and sensitive research studies. This problem could be diminished by utilizing a more proper spindle for cementitious pastes or by changing the spindle size and very detailed studying of its size effect on viscosity of slurries which is beyond the aim of current study. Based on the findings in this part of study, 1.5% $W_t.S.SP/V.P$ corresponding to 1.61% $W_t.Lq.SP/W_t.P$ is the confident SP content regarding highest fluidity and lowest viscosity of cement slurry.

In the next phase the slurry of cement-SF was studied. Generally, it was observed that all of the compositions of cement-SF slurry are much more adhesive than slurries without SF. This could be attributed to the very fine SF particles with their high tendency to water adsorption. Due to this fact, the Brookfield test results are non usable because the pastes are too stiffer for Brookfield viscometer operation, while, the flow diameters results reveals a strong basis for comparison. As shown in **Table 3-5**, **Figure 3.33** and **Figure 3.34**, the first two compositions, namely C66.7-SF 33.3-SP 0 and C66.7-SF 33.3-SP 0.25, do not show any fluid behavior. The third one, C66.7-SF 33.3-SP 0.75, however develops more, it is yet highly viscose being not able to flow. The rest of the mixtures show appropriate flowability and viscosity in flow-table and

Brookfield test. As depicted in **Figure 3.38**, even with 4% of SP, the flow-diameter is

lower than all other slurries not having SF. In other words, SF results in very high

viscosity, which is an undesirable property of SF for developing self-compacting

UHPPC beside its high price.

Table 3-5: Cement and SF slurry compositions.

Name		Cement	SF	UFFA	SP(Liq)	Water	Flow (mm)	Viscosity (mPa.s)	Yield stress (mPa)
C66.7-SF 33.3-SP 0	Wt.	413.54	146.52	0	0	160	0	-	-
	Vol.	133.4	66.6	0	0	160			
C66.7-SF 33.3-SP 0.25	Wt.	413.54	146.52	0	1.67	158.8	0	-	-
	Vol.	133.4	66.6	0	1.56	158.8			
C66.7-SF 33.3-SP 0.75	Wt.	413.54	146.52	0	5	156.5	0	3017.6	29509
	Vol.	133.4	66.6	0	4.67	156.5			
C66.7-SF 33.3-SP 1.5	Wt.	413.54	146.52	0	10	153	10	-	-
	Vol.	133.4	66.6	0	9.35	153			
C66.7-SF 33.3-SP 2.3	Wt.	413.54	146.52	0	15.33	149.27	12	4033.1	22608
	Vol.	133.4	66.6	0	14.33	149.27			
C66.7-SF 33.3-SP 4.0	Wt.	413.54	146.52	0	26.67	141.33	13	4500.8	11357
	Vol.	133.4	66.6	0	24.92	141.33			

Figure 3.33: Slurry of Cement-SF for two first compositions.
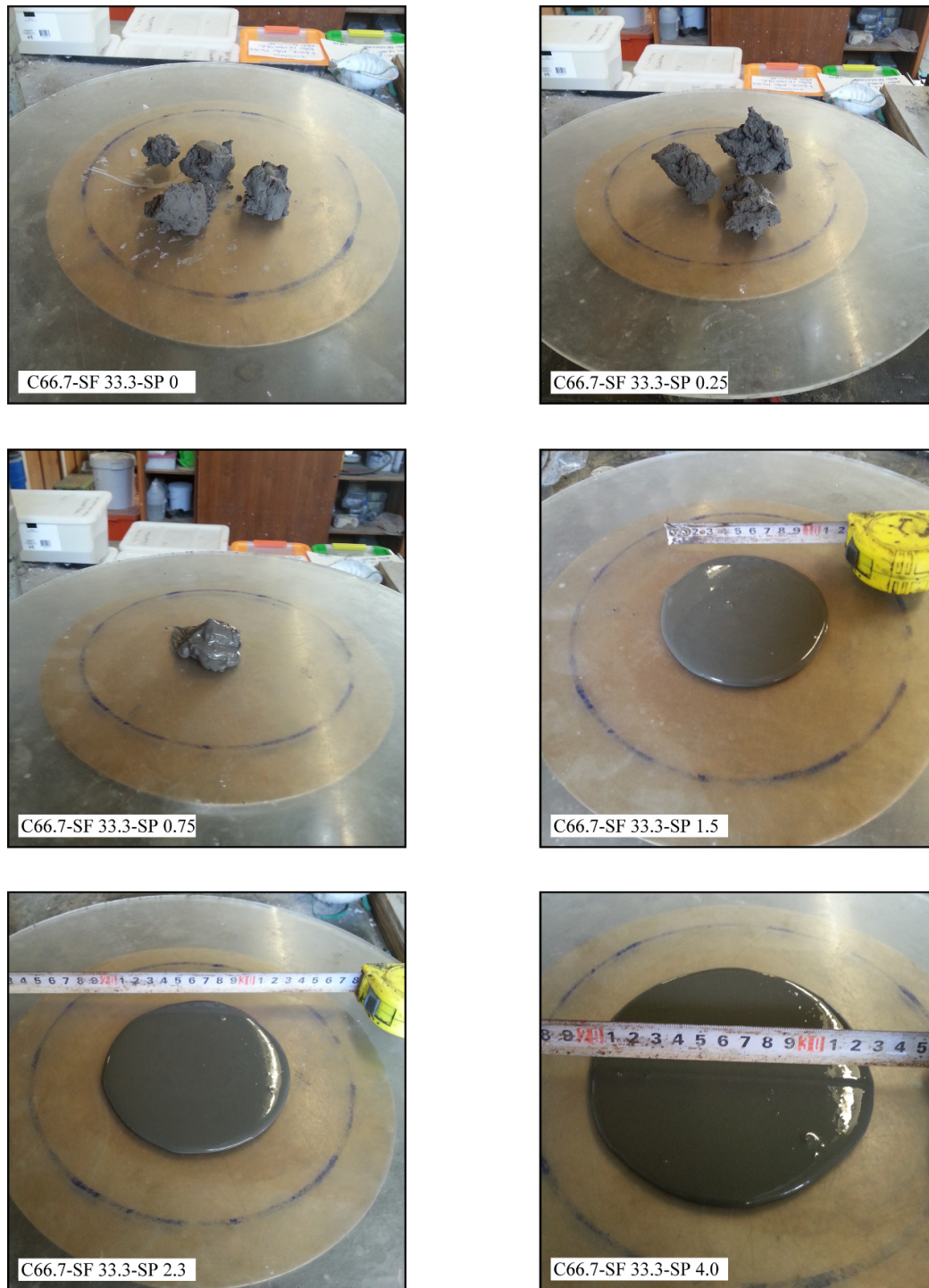
Figure 3.34: Slurry of cement-silica fume with different percentages of SP.

The next stage was to study the interaction of SP on a sole pozzolan without cement.

For this aim, SF was studied with various percentages of SP.
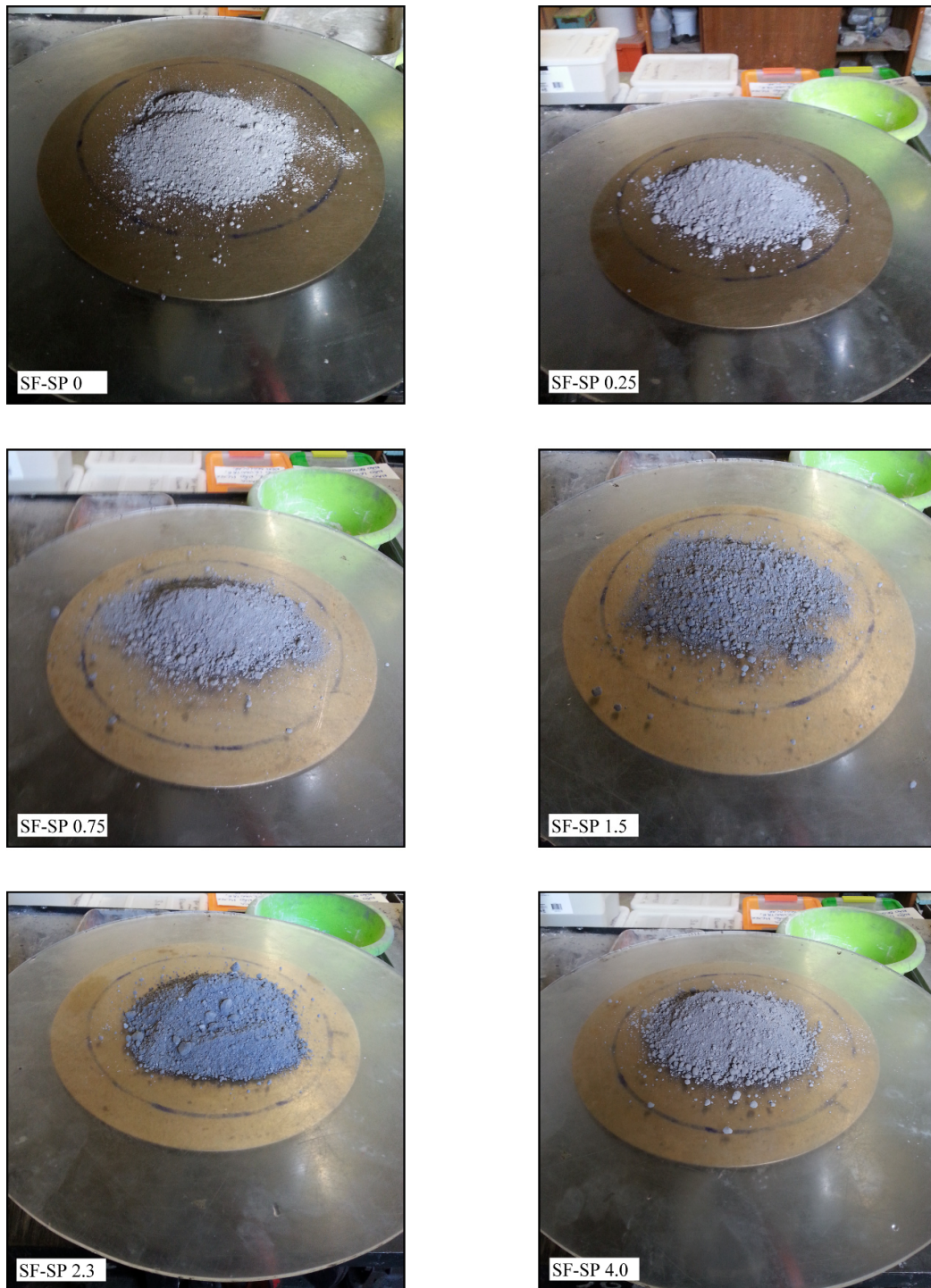
Figure 3.35: Slurry of silica fume with different percentages of SP.

As shown in **Figure 3.35**, SP cannot disperse the pozzolan particles when no cement

is included in the slurry. All of the mixtures remain in dry state however by increasing

the SP content, the texture of blend gets darker but without any sign regarding fluidity. As explained in **Chapter 2**, this phenomenon happens since there is no Ca^{2+} particles in blend of water-pozzolan to be surrounded by SP chains and be separated from water resulting in dispersion of particles.

Table 3-6: SF slurry compositions.

Name		Cement	SF	UFFA	SP(Liq)	Water	Flow (mm)	Viscosity (mPa.s)	Yield stress (mPa)
SF-SP 0	Wt.	0	440	0	0	160	0	-	-
	Vol.	0	200	0	0	160			
SF-SP 0.25	Wt.	0	440	0	1.67	158.8	0	-	-
	Vol.	0	200	0	1.56	158.8			
SF-SP 0.75	Wt.	0	440	0	5	156.5	0	-	-
	Vol.	0	200	0	4.67	156.5			
SF-SP 1.5	Wt.	0	440	0	10	153	0	-	-
	Vol.	0	200	0	9.35	153			
SF-SP 2.3	Wt.	0	440	0	15.33	149.27	0	-	-
	Vol.	0	200	0	14.33	149.27			
SF-SP 4.0	Wt.	0	440	0	26.67	141.33	0	-	-
	Vol.	0	200	0	24.92	141.33			

According to the results obtained from last series of test on SF, UFFA was not studied solely. Therefore, the final composition was blend of cement-UFFA in fraction ratio as explained before. The reason why the mixtures of higher quantity of SF or UFFA with cement were not examined is that the percentage of cement substitution normally would be in a range of 30% to 40% of volume of cement. As can be seen from **Figure 3.37**, the first composition of cement-UFFA blend, C66.7-UFFA 33.3-SP 0, regarding its fluidity is almost the same as third composition of cement-SF showing the higher fluidity of cement-UFFA slurries compared to cement-SF slurries. **Figure 3.38** and **Figure 3.39** also verifie the higher fluidity of cement-UFFA compared to other blends. As shown in **Figure 3.36**, the optimum percentage of SP for cement-UFFA slurry based on Brookfield and flow tests are 0.75% and 2% for viscosity and

flow-diameter respectively corresponding to 0.87% and 2.33% in scale of
$W_t.Lq.SP/W_t.P$. Accordingly, and for greater certainty, the flow test results are being
considered as basis to draw conclusions.

Table 3-7: Cement and UFFA slurry compositions.

Name		Cement	SF	UFFA	SP(Liq)	Water	Flow (mm)	Viscosity (mPa.s)	Yield stress (mPa)
C66.7-UFFA 33.3-SP 0	Wt.	413.54	0	159.84	0	160	0	2145.2	35251
	Vol.	133.4	0	66.6	0	160			
C66.7- UFFA 33.3-SP 0.25	Wt.	413.54	0	159.84	1.67	158.8	11	2914.1	8931.2
	Vol.	133.4	0	66.6	1.56	158.8			
C66.7- UFFA 33.3-SP 0.75	Wt.	413.54	0	159.84	5	156.5	14.8	226.7	0
	Vol.	133.4	0	66.6	4.67	156.5			
C66.7- UFFA 33.3-SP 1.5	Wt.	413.54	0	159.84	10	153	15	148.8	0
	Vol.	133.4	0	66.6	9.35	153			
C66.7- UFFA 33.3-SP 2.3	Wt.	413.54	0	159.84	15.33	149.27	16	173.3	0
	Vol.	133.4	0	66.6	14.33	149.27			
C66.7- UFFA 33.3-SP 4.0	Wt.	413.54	0	159.84	26.67	141.33	16.25	292.6	0
	Vol.	133.4	0	66.6	24.92	141.33			
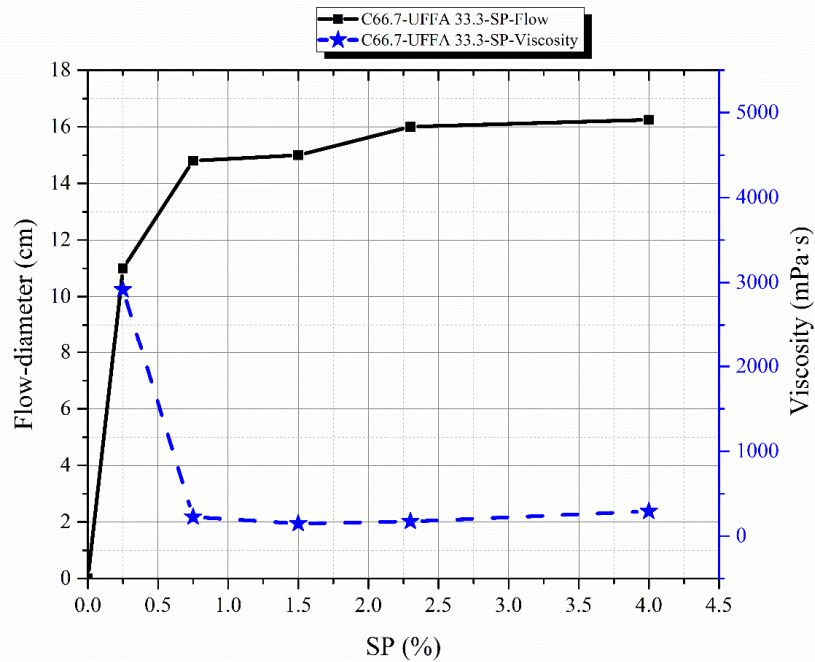
Figure 3.36: Flow diameter and viscosity of cement-UFFA slurry with different percentage of SP ($W_t.S.SP/V.P$).

C66.7-UFFA 33.3-SP 0

C66.7- UFFA 33.3-SP 0.25

C66.7- UFFA 33.3-SP 0.75

C66.7- UFFA 33.3-SP 1.5

C66.7- UFFA 33.3-SP 2.3

C66.7- UFFA 33.3-SP 4.0
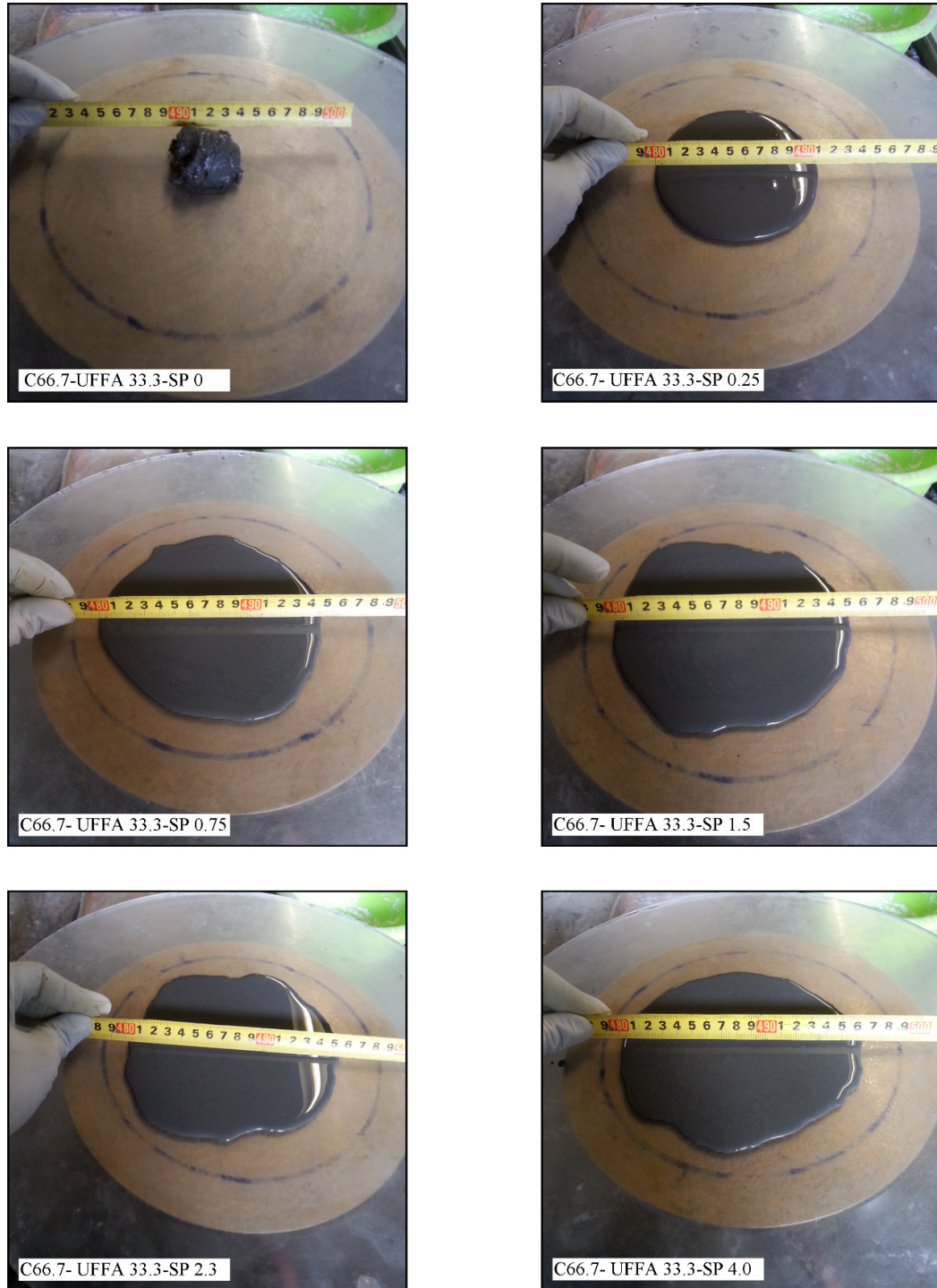
Figure 3.37: Slurry of cement-UFFA with different percentages of SP.
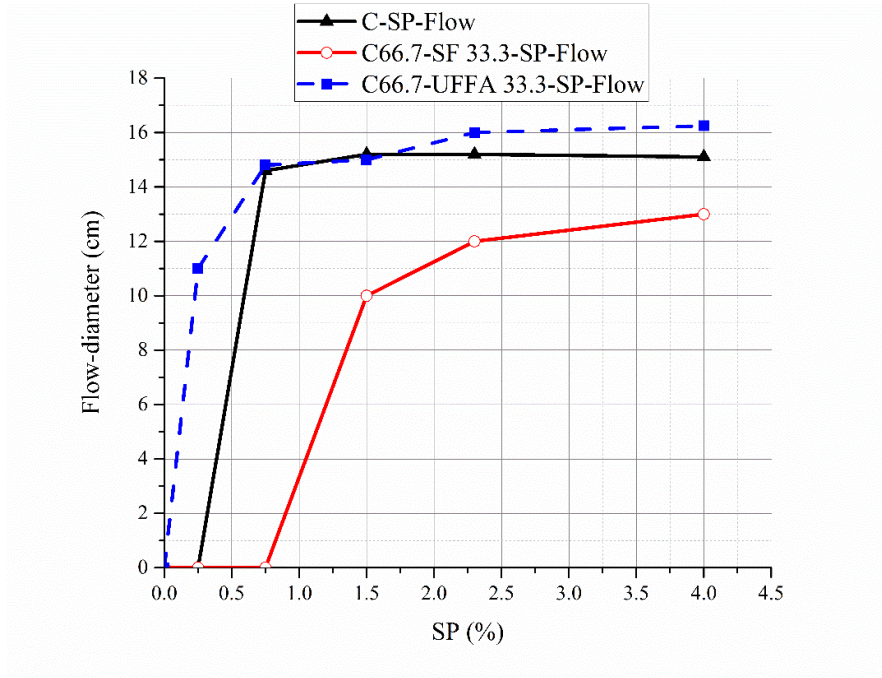
Figure 3.38: Flow diameter of C-SP, C-SF and C-UFFA slurries with different percentage of SP (Wt.S.SP/V.P).
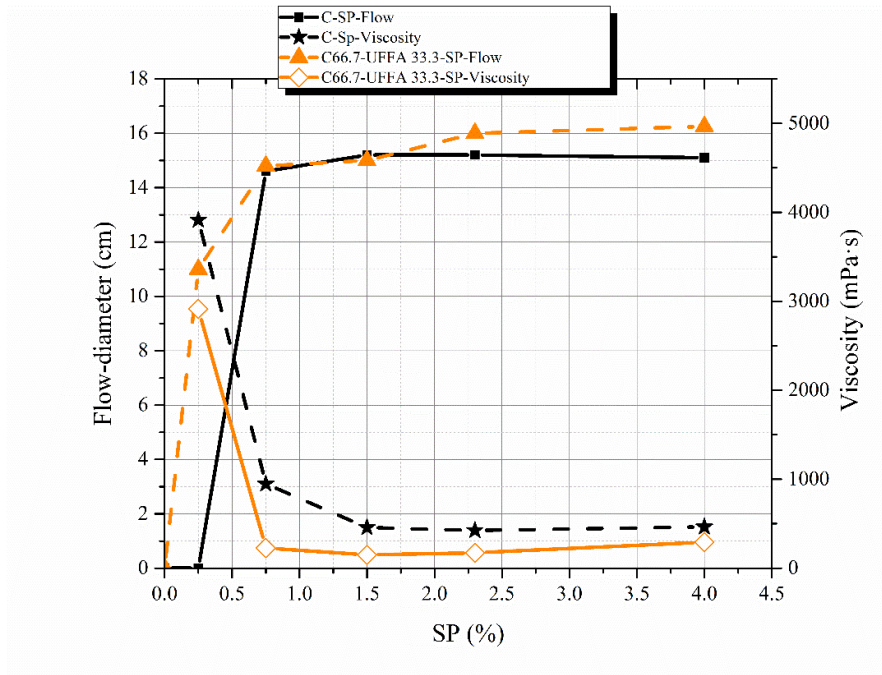
Figure 3.39: Flow diameter and viscosity of C-SP and C-UFFA slurries with different percentage of SP (Wt.S.SP/V.P).

3.5 Conclusion

Based on the preliminary studies in this chapter the constituent materials selected for the aim of this research include cement I 42.5R, silica fume, UFFA, SP MasterGlenium SKY 526®, and sand 40/45 with maximum particle size of 1 mm. MK showed its deficiency regarding its very low fluidity. Slurries containing UFFA exhibited higher fluidity and lower viscosity compared to slurries without UFFA. Moreover, it was shown that slurries having SF have lower fluidity and higher viscosity compared to slurries containing UFFA. So, it is recommended to use SF in its lowest applicable content and just to obtain enough mechanical performances. In this regard, incorporation of UFFA with average particle size of 4.48 μm seems beneficial in developing UHPC and is firmly suggested. UFFA consumption results in lower natural resources and respectively more waste landfills consumption resulting in cost and environmental efficiency. In addition, it was found that dry processing of FA would be a more effective way of its grinding to finer particle size rather than wet-milling process.

The best fluidizing effect was acquired after adding 70% of mixing water to the cementitious materials and mixing for 3 minutes followed by adding the optimum dosage of SP and mixing for 6 minutes and finally adding the remaining 30% of water and blending for an extra 6 minutes to reach a steady-state consistency.

The optimum dosage of SP in C, C-UFFA and C-SF blends found to be 1.5%, 2% and 2.3% ($W_t.S.SP/V.P$) respectively corresponding to 1.61%, 2.33% and 2.74% of $W_t.Lq.SP/W_t.P$ in each slurry. It was investigated that the quantity of SF should be limited as much as possible in UHPC regarding its week interaction with SP as well as its high price. Finally, 2.5% SP ($W_t.Lq.SP/W_t.P$) is suggested as an optimum dosage of SP with highest efficiency.

Chapter 4

Mixture Design of

EEUHPC

Mixture Design of fiber-reinforced ultra-high performance concrete, including its granular matrix, is presented and discussed in this chapter. The goal is to investigate if statistical mixture design method would be a proper method for developing UHPC or not and if yes which is the greenest UHPC composition which could be developed through this method and particularly with in-access materials and technologies.

4.1   Preliminary study

Based on composition introduced by Ductal®, as one of the most famous and commercially available ready-mix compositions, as well as the results obtained from

previous chapter, a set of preliminary experiments were carried out aiming at better

understanding of the behavior of UHPC. It should be noticed that according to previous

researches, reviewed in **Chapter 2** of this thesis, and the concluding remarks of Chapter

3, some parameters were fixed during the rest of this study. In this regard, SP was fixed

in 2.5 w_t.% (W_t.Lq.SP/W_t.P). In addition, the curing cycle of all specimens was selected

based on the tempered-water curing (TWC) cycle presented in **Figure 4.1**. As

illustrated, the maximum temperature is 67°C to avoid any negative impacts reported

in other studies. Besides that, the temperature rise of 22°C/H was applied conforming

to terms and conditions proposed by ACI (ACI, 1992). Furthermore, the aggregate used

in all the test was in saturated surface dry state. For the same consistency in all tests,

the aggregate were first oven dried and after that, addition water, equal to 0.32% of

their weight, was considered to be added in the mixture. This amount of water was

calculated in conformity with standard test method for density, relative density

(Specific Gravity), and Absorption of Fine Aggregate (ASTM C128–04a, 2004).
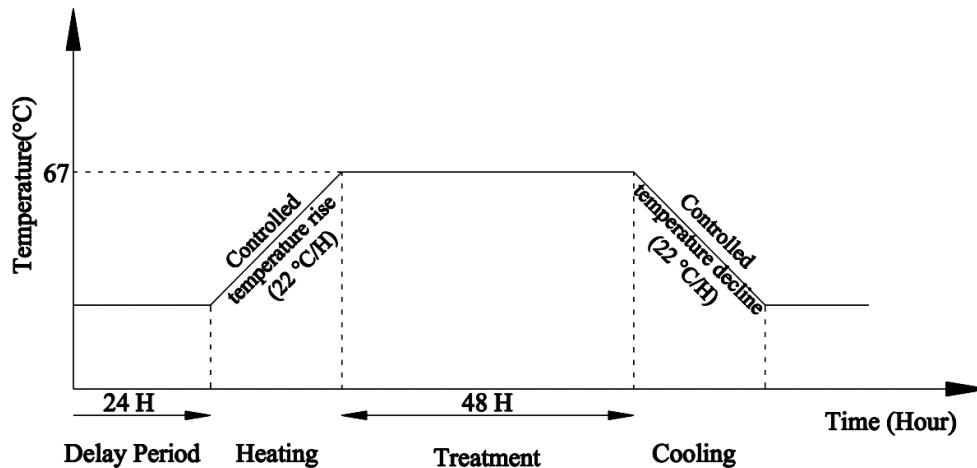
Figure 4.1: Applied tempered-water curing cycle for all specimens.

The Ductal® composition (Graybeal, 2006) and other developed mixtures including

UFFA are shown in the following table.

Table 4-1: Primary compositions for developing UHPC.

	Cement	SF	Fine Sand	Filler	UFFA	SP	Steel fiber (2% V_f)	Total water	Initial flow (cm)	Strength (MPa)
Ductal®*	1	0.324	1.43	0.3	-	0.043	0.21	0.15	18	171
C.N.1	1	0.05	1.43	-	0.55	0.04	0.221	0.25	17.5	159.4
C.N.2	1	0.05	1.43	-	0.55	0.04	0.226	0.278	25	158.9
C.N.3	1	0.05	1.43	-	0.55	0.04	0.223	0.264	23	165

* (Russell & Graybeal, 2013)

As can be seen, UFFA was applied as both pozzolan and filler in the tested mixtures. In other words, the accumulated content of SF and filler in Ductal® composition is equal to 0.624 of cement weight almost the same as three first compositions with sum of SF and UFFA equal to 0.6 of cement weight. In this preliminary study, the quantity of free water was considered to 0.222 and 0.25 of cement weight in Comp.N.1 and Comp.N.2 respectively correspond to 0.25 and 0.278 of total W/C ratio with considering water in SP. The reason was to introduce theoretical required water for complete hydration of cement particles. According to the fact that 70% of SP weight is composed of water, 9.8 gr, equal to 0.028 of cement weight in both cases was water of SP. Therefore, totally the W/C ratio would be 0.25 and 0.278 as written in the table. The mixing process was also fixed for the rest of this research based on the methodology introduced in **Chapter 3**. The first test after mixing all the ingredients was flow-table test. The flow diameter without dropping the table was 17.5 cm and 25 cm respectively for C.N.1 and C.N.2. As discussed in **Chapter 2**, a flow diameter of 19 cm is considered as accepted lower boundary for fresh UHPC. Therefore, the results for fluidity demonstrate the lack of water for the first composition while the second blend has appropriate water quantity with acceptable range of flowability. After this test, the mixture was poured in 5x5x5 cm^3 molds. Each mold was filled in two layers. Each layer was vibrated on vibration table for 20 seconds just for releasing the

entrapped air inside the concrete. Then the specimens were covered by a thin plastic

sheet to avoid water evaporation from the surface. Then, the molds were transferred to

humidity chamber with 20°C and 50% RH. After 24 hours, the specimens were

demolded and were placed in a heater for TWC based on the cycle explained before.

When the temperature reached to 67°C, the samples were transferred to another water

bath in an oven with fixed temperature of 67°C. After 48 hours, they again placed in

heater containing 67°C water and the inverse process of controlled cooling was started.

The temperature decline was performed by adding cold water to decrease the

temperature with a rate of 22°C/H. For this aim, the temperature was decreased

approximately 5.5°C in each 15 minutes. Then, samples were dried and tested for

compression test with a pace of 2.4 kN/s. The average of compressive strength for three

samples of each composition are 159.4 MPa and 158.9 MPa. In the third step the total

water content was reduced to 26.4% of cement weight in order to reduce the flow

diameter and avoid from strength reduction in next phase of the research that is

optimization of granular ingredients.

Figure 4.2:   Flow diameter of C.N.3 mixture.

As can be seen in **Table 4-1**, by reduction of water content by 1.4% compared to

C.N.2, the fluidity was reduced to 23 cm (**Figure 4.2**) in a range between C.N.1 and

C.N.2. In addition, a strength development to 165 MPa was observed. This could be as result of lower W/C compared to C.N.2 and lower viscosity in comparison with C.N.1 that facilitates escaping of entrapped air in the concrete. Because this percentage of water gives enough performance in fresh and hardened state and since our aim is to optimize the granular mixture of UHPC, this percentage of water was fixed during the rest of this project. The third mixture introduced here, has higher eco-efficiency compared to Ductal® because of substitution of almost 27% of its SF, with higher price and embodied CO_2, by UFFA as a cheap waste pozzolan with lower embodied CO_2. Although this composition is already a significant achievement of the current study, it has yet the potentiality of being studied more precisely to meet higher levels of eco-efficiency.

4.2   Response surface methodology

This section represents a statistical based model with the help of response surface methodology (RSM) aiming at studying the applicability of this method for UHPC mixture design and its optimization. Besides that, the effects of silica fume, UFFA and sand as three main variable constituents of UHPC on flow diameter (F.D.) and compressive strength (C.S.) as the main performance criteria and responses of this high-tech cementitious material were investigated. RSM is a statistical based technique to investigate the best response in an applicable region of possibilities or at least better understanding of any response affected by multiple variables. It was first in 1950th that this technique was introduced to find the complex relationships in the case of multi-variable and multi-objective optimizations with the aim of finding the desired output (Box & Wilson, 1951). The advantages of this experimental design approach include the possibility of evaluation of factors interaction within the experimental

region, recognition of the optimal response based on different priorities, and finally developing a generalized model of the data with minimum experimental labor (Upasani & Banga, 2004). The other advantage of RSM, as its name implies, is that it deals with continues input factors and response variables. In addition, RSM enables us to meet a set of specifications for various responses simultaneously.

In this research to perform data analysis and finally to carry out a multi-objective optimization, Design-Expert® software tool was utilized. Depending on the number of design factors, Design-Expert® offers variety of RSM design methods such as Central Composite Design (CCD), Box-Behnken and D-optimal design. Box-Behnken and D-optimal design methods have some disadvantages. The former one provides strong coefficient estimates when the optimum response is presumed to be near the center of design space and in the latter case, the points are not at any specific positions and are simply spread out in the design space. With respect to these disadvantages, CCD seems more preferable for the aim of this research since it is preferred to investigate all the design space of possibilities instead of focusing on center of design area making it necessary to have design point in all the space rather than simply distributed points in the design space in D-optimal design. So, in this research a central composite design (CCD) was utilized to determine the optimum combination of binders and aggregates aiming at obtaining acceptable range of workability and compressive strength in a region of interest with respect to lower cost and environmental impacts besides avoiding the sophisticated task of studying packing density of dry ingredients solely.

CCD includes three groups of design points (**Figure 4.3**): a) two level factorial or fractional factorial points representing the vertices of the cube as the possible combinations of all +1 and -1 coded values (2^k for a k-factor CCD); b) axial points renowned as star points situated in the center of each face of the cube with a distance

of ±α from the center giving the possibility of rotation in the feasible area of experiment

(2*k); c) and finally center points, in the center of the cube, with coded value of zero

for all the variables (Stat-Ease, 2014). In general, CCD offers 5 level for each variable

factor those are -α, -1, 0, +1 and +α.
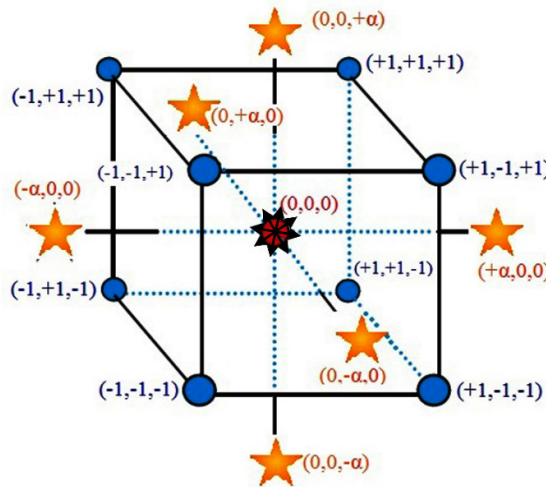
Figure 4.3:   Schematic representation of factorial, axial and center points in CCD.

Center points are usually repeated 4 to 6 times for better estimation of experimental

errors. The number of center points plays a vital role in statistical analysis of the design.

Since center points, including all their replications, are used to estimate pure errors in

lack of fit test, replication fewer than 5 or 6 results in a lack of fit test with very low

power. It should be noted that lack of fit test represents how the proposed model fits

the data. In fact, too few center points worsen the errors resulting in an inflation in

standard error plot. Finally, the more the number of replicates are, the more sound

would be the statistical analysis. Hence, the number of replicates for center point was

selected to 6 points as also suggested by software.

Regarding the value for α, a face-centered design, α=1, would be preferable for this

research since it causes a three-level design ensuring that axial points will not be

extreme values far from the feasible design space.

Based on these design points and their related experimental results a second order polynomial model for each response is calculated based on **Equation 4.1**:

$$y = \beta_0 + \sum \beta_i x_i + \sum \beta_{ii} x_i^2 + \sum \beta_{ij} x_i x_j \qquad \text{Eq.(4.1)}$$

where y is the predicted response value, β_0 is the intercept of the model, β_i represent the linear coefficients, β_{ii} correspond to quadratic coefficients, β_{ij} are coefficients of variables' interaction and x_i, x_j are the independent variables as shown in **Table 4-2**.

Table 4-2: Variables and their boundaries as ratio to cement weight.

Variables			Max & Min levels		
	Real	Coded	-1	0	+1
Silica fume	SF	A	0	0.05	0.1
UFFA	UFFA	B	0.3	0.475	0.65
Sand	Sand	C	1.3	1.55	1.8

A series of tests were performed to find out the applicable region of these variables those are the main focus point of this research with the aim of cement and silica fume substitution with UFFA and micro sand at their maximum possible level. The minimum and maximum range of each variable in terms of actual, as ratio to cement weight, and coded values are also represented in **Table 4-2**. As can be seen from the table, the highest level for silica fume is 0.1 of cement weight aiming at lowering the price and environmental impact as well as not affecting the flowability of paste and resulting ensured strength, as explained previously. UFFA and sand have a wider range with respect to their lower cost and environmental impact and up to the level that result almost no flowability. The maximum quantity of UFFA was considered as 0.65 just 0.1 higher than the quantity examined in C.N.1 to C.N.3 in the preliminary stage. This quantity ensures enough pozzolanic reactions as well as filling small gaps in the matrix

as a filler. Regarding highest quantity of sand, some mixtures were prepared with maximum level of SF and UFFA in ratios of 1.8, 1.85 and 1.9 Sand/cement up to a level that the mixture did not become fluid anymore and remained as a dry powder. As can be seen from **Figure 4.4**, the mixtures having 1.85 and 1.9 sand/cement remained as dry while the composition with 1.8 sand/cement showed a liquid state during mixing and hence 1.8 was selected as the upper boundary for sand.

Figure 4.4:   Tests to find the maximum level of sand.

Based on these boundaries, any further rotation in the region of interest is impractical leading to a center-faced central composite design with α=1 as noticed before. Totally 20 experimental points, designated as runs, are proposed for three numeric factors, 8 of them for factorial points without replication, 6 runs for axial points also with no replication and 1 point with 6 replications for the center point. For better fitting of the proposed models with the data points, 5 extra runs in the feasible region of interest were added manually to the proposed runs. Furthermore, 3 points proposed by software as solutions of analysis of the primary 25 design points, with respect to cost and eco-efficiency, were added at the final step to existing data in order to calibrate the proposed models with highest accuracy (see **Table 4-3**).

Table 4-3: Design points and corresponding responses.

Run	A:SF	B:UFFA	C:Sand	F.D.(cm)	C.S.(MPa)
1	0.1	0.3	1.8	14.5	157.04
2	0.1	0.3	1.3	27	162.9
3	0.1	0.65	1.8	18	156.8
4	0.1	0.475	1.55	22.75	168.1
5	0	0.65	1.8	10	128.2
6	0.05	0.3	1.55	23	151.4
7	0	0.3	1.8	11	130.1
8	0	0.475	1.55	21.5	142.6
9	0.05	0.475	1.55	24	155.7
10	0.05	0.475	1.55	23	153.1
11	0.05	0.475	1.8	17.5	145.5
12	0.05	0.475	1.55	23.5	156.6
13	0.05	0.65	1.55	18.5	152.2
14	0.05	0.475	1.3	26	156.3
15	0.05	0.475	1.55	24	154.7
16	0	0.65	1.3	20	134.6
17	0.05	0.475	1.55	24	156.4
18	0	0.3	1.3	26	142.6
19	0.05	0.475	1.55	24	156.6
20	0.1	0.65	1.3	21.5	167.4
21	0.1	0.65	1.7	17	158.8
22	0	0.3	1.7	12	135.1
23	0.1	0.3	1.7	19	162.3
24	0.05	0.47	1.5	23.5	155.3
25	0	0.65	1.7	11	139.5
26	0.09	0.57	1.76	19	160.3
27	0.083	0.626	1.713	18	159.7
28	0.081	0.569	1.779	18	158.6

4.2.1   Materials and samples preparation

It is worthy to remind that the UHPC, developed in this part, was composed of silica

fume (SF), ultra-fine fly ash (UFFA), Portland cement type CEM I 42.5 R conforming

to EN 197-1 (BS EN 197-1, 2000), and natural siliceous micro sand (sand 40/45) with

mean particles size of 0.15 μm, 4.48 μm, 9.3 μm, and 350 μm respectively (**Figure 4.5**).
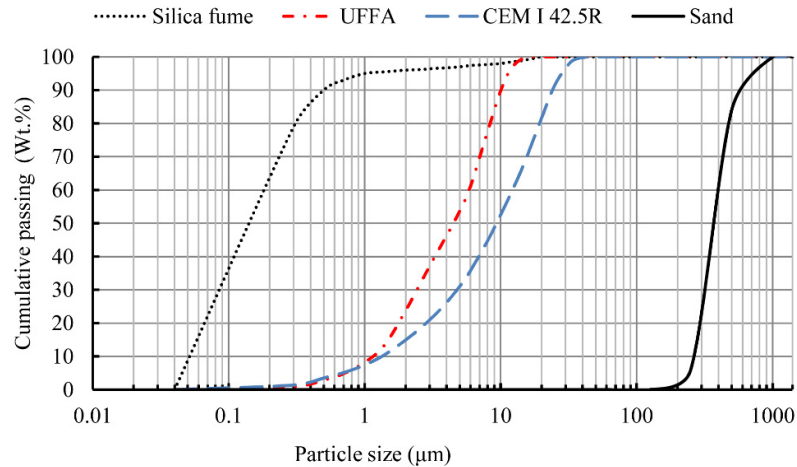
Figure 4.5: Particle size distribution of powders and aggregates.

The mixing procedure and specimens' preparation included the following steps as explained before: (1) cement, UFFA, SF and sand were mixed for 3 minutes in order to break any existing agglomerated particles and better distribution of fine materials; (2) 70% of required water was poured in the mixer for wetting the cementitious materials. After, they were mixed for 3 minutes in order to maximize the dispersion effect of SP added in the next step aiming at highest fluidity of UHPC; (3) SP was added and mixed for another 6 minutes which is the most efficient time regarding flowability; (4) rest of 30% required water was added and the mixing procedure was continued up to minute 18 in which the UHPC became completely fluid; (5) St.F was added and mixed for another 1 min; (6) the mixture was poured into the cubic molds of 50x50x50 mm^3 and sealed with a plastic sheet to prevent any evaporation from the external surface of the specimens. They were placed in ambient chamber with a temperature of 20°C and relative humidity of 65% for 24 hours as a delay time before TWC (Erdem, et al., 2003); (7) the samples were demolded and put in a water heater for temperature rise from 20°C to 67°C with a rate of 22°C/H followed by 48 hours of treatment in 67°C which finalized by a cooling period of 22°C/H for 2 hours and 15 minutes (**Figure 4.1**). The

reason why this temperature was adopted for TWC is to avoid any micro-structural

defects reported in other studies as a result of higher temperatures (Heinz & Ludwig,

1987; Taylor, et al., 2001; Hanson, 1963).

4.2.2   Testing UHPC compositions

After 19 minutes of mixing, the flowability of the fresh concrete was evaluated by

means of flow table test for mortars according to EN 1015-3 (BS EN 1015-3, 2004).

Once a steady state of flow was observed, after rising up the mini-slump cone, two

perpendicular dimensions of spreaded concrete were registered followed by jolting the

table for 15 times, approximately one per second, and again measuring the diameters in

two directions. Since self-compactness of UHPC is a prerequisite, the average of the

first measurements, before dropping the table, was registered as criteria for fluidity. The

pictures of fluidity tests for all 28 compositions are presented in **Annex I**. The

compression test was performed immediately after the cooling period. Three samples

of 50x50x50 mm^3 were allocated for compression test with a pace of 2.4 kN/s and their

average was considered as the compressive strength of each mixture. The test results

are depicted in **Table 4-3**.

4.2.3   Model fitting and its validation

For each response, before any transformation, a regression analysis was carried out

to fit all kind of the polynomial models to that specific response through comparing

their relevant statistics including p-value, lack of fit and R-squared results. Finally

based on the results, a highest order significant model, in this case a quadratic model

for both responses, having small P-value for the model, high P-value for the lack of fit

test and very close adjusted/predicted R-squared, within 20% of each other and with

the maximum values as well, were selected. In the next step based on analysis of

variance (ANOVA) for each of the models and through a backward process, the

insignificant model terms having P-value greater than 0.1 and not supporting the

hierarchy were eliminated from the model. Finally, through diagnostics it was found

that a power transformation with Lambda=2.74 regarding F.D. response was necessary.

No transformation was required for C.S. response. The final models are presented in

Table 4-4.

Table 4-4: Proposed model for flow diameter and compressive strength by ANOVA.

	F.D.$^{2.74}$	P-value	C.S.	P-value
Intercept	29997.00103	-	-23.6995	-
SF	40208.39989	< 0.0001	264.2937	< 0.0001
UFFA	-1067.665582	< 0.0001	105.7039	0.9701
Sand	-21478.13402	< 0.0001	197.7216	< 0.0001
SF*UFFA	-	-	-	-
SF*Sand	-	-	-	-
UFFA*Sand	24610.60021	< 0.0001	-	-
SF^2	-273565.3882	0.0097	-	-
UFFA^2	-44619.98881	< 0.0001	-111.136	0.0030
Sand^2	-	-	-68.8598	0.0007

As shown in **Table 4-5**, the F-values for both presented models demonstrate that

they are both significant. In addition, the Lack of Fit F-values for both models imply

that the Lack of Fits are not significant. Furthermore, the "Pred R-Squared" values for

both proposed models are in reasonable agreement with the "Adj R-Squared" values.

The graphical model prediction versus actual data as a diagnostic tool for both models

are also shown in **Figure 4.6** and **Figure 4.7**. As reflected in both graphs the actual

experimental values are well correlated to predicted values. More information regarding

this chapter and its statistical terms are provided in **Annex I**.

Table 4-5: ANOVA results for full regression models

Responses	Adj-R^2	Pre-R^2	Model		Lack of fit	
			F-Value	P-Value	F-Value	P-Value
F.D.	0.9596	0.9444	107.76	< 0.0001	3.0486	0.1113
C.S.	0.9568	0.9338	120.72	< 0.0001	3.03	0.1119
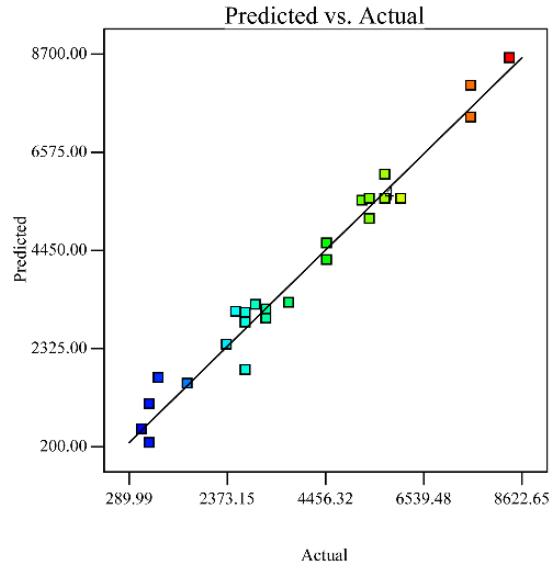
Figure 4.6: Predicted models vs actual data for F.D. model.
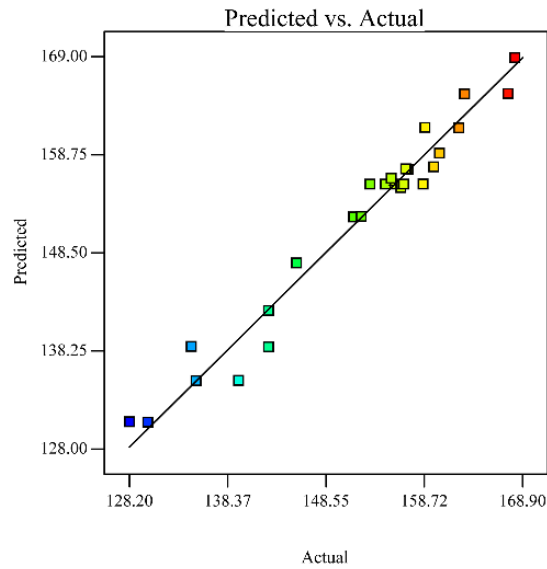
Figure 4.7: Predicted models vs actual data for C.S. model.

4.2.4   Effect of the components variation on responses

For better understanding of the effect of each constituent on flowability and compressive strength of the material **Figure 4.8** and **Figure 4.9** are presented. The curves display the sensitivity of the models to any variations of the variables those are SF, UFFA and sand. As can be seen, F.D. is highly affected by sand content. In other words, flowability decreases significantly with an increase of sand content. Besides that, C.S. also shows a reduction when the sand content overpass its 50% of its lower defined boundary. On the other hand, SF showed its ability to improve the compressive strength without any negative impact on flowability up to around 90% of its lower boundary. UFFA in a content above its reference point, which is in its middle range, affected both flowability and strength while its worst impact was related to flowability.
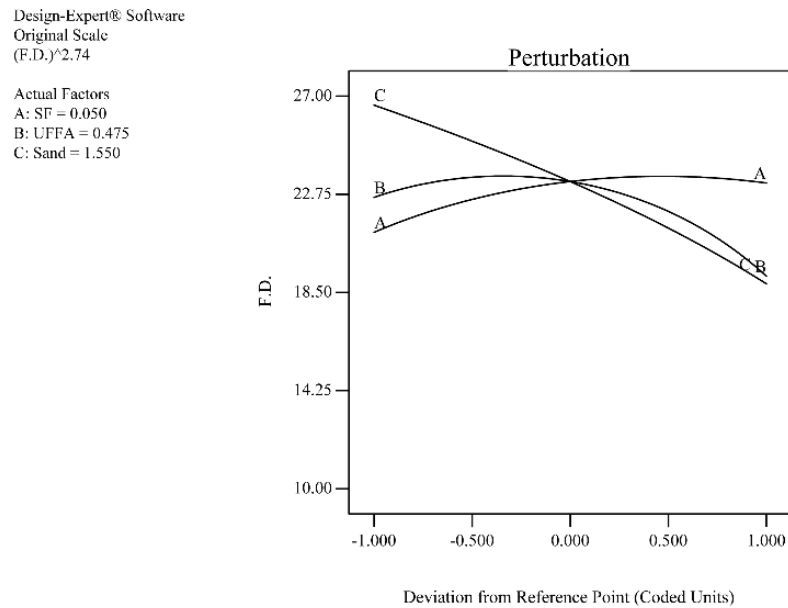
Figure 4.8:   The effect of constituents' variations on F.D.
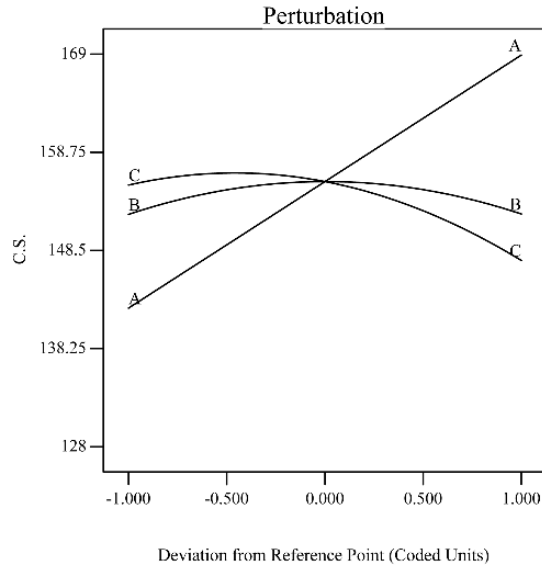
Figure 4.9:   The effect of constituents' variations on C.S.

In order to facilitate the assessment of constituents' interactions on the responses and to verify the discussion raised above, two 3D plots are also provided in **Figure 4.10** and **Figure 4.11**.
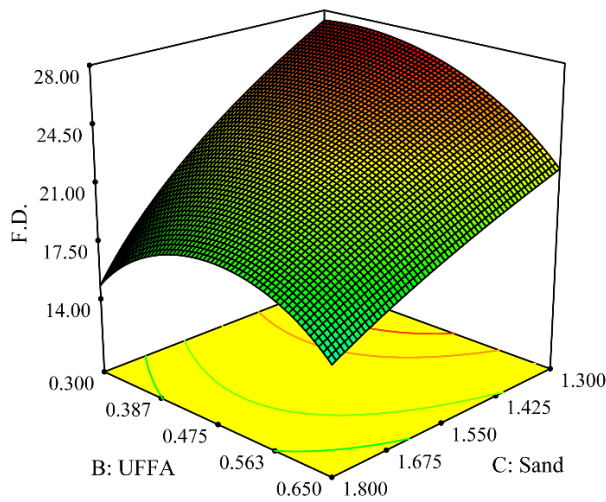
Figure 4.10: 3D representation of effect of sand and UFFA on F.D.
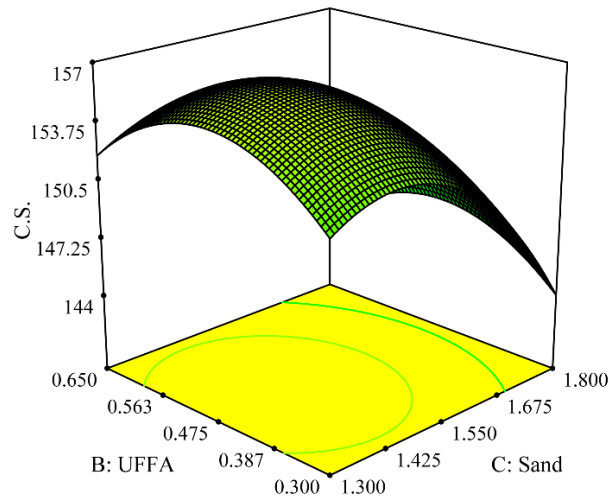
Figure 4.11: 3D representation of effect of sand and UFFA on C.S.

4.2.5 Optimization of UHPC

The aim of optimization is searching to find combinations of factor levels that simultaneously satisfy the requirements related to each of the responses and factors. There are two ways of performing optimization of one response or multiple responses simultaneously including graphical methods or numerical ones. In our case, we deal with a multi-objective optimization. The most significant objective is to minimize the cement content as much as possible. The second objective is to reduce the SF content in order to reduce the cost of UHPC. Other limitations are keeping the flow diameter and compressive strength in their accepted ranges those are 19 cm and 150 MPa respectively. In this regard, after developing a model for both responses, a multi-objective optimization performed in order to find out the eco-efficient UHPC composition as the main objective of the current study.

In general, through numerical optimization, the design space is explored to find out the best quantity of the variables or ingredients those meet the desirable defined goals

using the models fitted in the last analytical phase. The numerical optimization was

performed based on the global desirability function (**Equation 4.2**) (Derringer, 1980).

$$D = \left(d_1^{r_1} \times d_2^{r_2} \times d_3^{r_3} \times \ldots \times d_n^{r_n}\right)^{1/\Sigma r_i} = \left[\prod_{i=1}^{n} di^{r_i}\right]^{1/\Sigma r_i} \qquad \text{Eq.(4.2)}$$

where n is the number of variables and responses existing in the optimization, in our

case 5 corresponding to SF, UFFA, sand, F.D., and C.S.; r_i is the relative importance of

each variable or response which varies between 1+ to 5+ corresponding to lowest to

highest importance. In other words, the relative importance of one response over the

others can be specified through these 5 levels. Finally, d_i refers to individual desirability

of each variable and response by comparing its value by corresponding defined goal

with a quantity between 0 and 1 for a non-desired response to a desired one respectively.

Based on this equation, an optimum solution has a D value, as geometric mean of

individual desirability of variables and responses, close to 1 clarifying that the proposed

solution as well as its relevant individual variables and responses are all close to their

defined goals or targets. For each variable and response 5 different goals could be

assigned namely maximize, minimize, target, in range, equal to (just for variables), and

none (just for responses). Beside the importance and goal, a weight factor is also

defined ranged between 0.1 and 10 representing how the optimization tool searches for

the solutions. The lowest weights reveal more solutions that do not meet the defined

goals precisely whereas, the highest weights seek the solutions very close to the stated

goals. The meaning of the goal parameters used in this research are described as

follows:

$$\text{Maximum: d=} \begin{cases} 0 & y_i \leq L \\ \left[\dfrac{y_i - L}{U - L}\right]^{wt_i} & L \leq y_i \leq U \\ 1 & y_i \geq U \end{cases}$$

$$\text{Minimum: } d = \begin{cases} 0 & y_i \geq U \\ \left[\frac{U-y_i}{U-L}\right]^{wt_i} & L \leq y_i \leq U \\ 1 & y_i \leq L \end{cases}$$

$$\text{Range:} \quad d = \begin{cases} 0 & y_i \leq L \\ 1 & L \leq y_i \leq U \\ 0 & y_i \geq U \end{cases}$$

where U is upper limit, L is lower limit and wt_i is the weight factor ranging between 0.1 and 10 representing how the optimization tool searches for the solutions. In other words, the lowest weights reveal more solutions that do not meet the defined goals precisely while, the highest weights seek the solutions very close to the stated goals. A weight factor of 1 reveals a linear change of desirability function between 0 and 1 during minimization or maximization.

In this regard, two different scenarios were evaluated in current study. The first scenario included maximization of all the constituents, which indirectly means cement reduction as much as possible. In other words, SF, UFFA and sand were maximized with various importances to obtain the lower CO_2 content of the whole mixture. The second scenario included maximizing UFFA and sand and minimizing SF simultaneously which in turn leads to lower environmental impacts as well as cost reduction as a result of SF minimization since, SF plays an important role in the final price of UHPC. The goals for F.D. and C.S. in both scenarios were fixed, in range, with a minimum value of 19cm and 150MPa respectively.

To find out the relative importance of each variable over the other constituents, first cost and environmental impacts analysis of each variable was performed. The cost and embodied CO_2 for each of applied materials are depicted in **Table 4-6**. The prices were delivered by corresponding factories and companies and embodied CO_2 was reported by other researchers as well as Mineral Products Association (MPA) (Leese & Casey,

2012; Jones, et al., 2011; Hammond & Jones, 2011; Pacheco-Torgal, et al., 2013; Teixeira, et al., 2015). More information is provided in **Annex I**.

Table 4-6: Embodied CO_2 and Price related to 1 kg of materials.

	Cement	SF	UFFA	Sand 40/45
CO_2 (kg)	0.913	0.014	0.009	0.005
Price (€)	0.097	0.39	0.040	0.02492

According to these data, cement has the highest CO_2 content around 65, 101 and 182 times of SF, UFFA and sand respectively clarifying that for environmental impacts reduction of UHPC, cement should be reduced as much as possible through maximizing the other constituents. It also demonstrates that sand has the lowest CO_2 content around 55% of UFFA and 36% of SF, which means its importance weight, in the process of maximization of these three factors, should be considered almost 1.8 times of UFFA and 2.8 times of SF. In the same way, the importance weight of UFFA is approximately 1.5 times of SF. Since Design-Expert® just provides importance weights of +1 to +5, in the first step the importance weight for sand, UFFA and SF was considered as +5, +3 and +2 respectively. However, other importance weights, such as ones depicted in **Table 4-7**, were also examined to see their effects on the embodied CO_2 of material. It should be noted that as the other ingredients, those are SP, St.F and water, are almost fixed and do not play any significant role in CO_2 content variations of UHPC, the embodied CO_2 in **Table 4-7** is quantified based on the main 4 ingredients namely cement, SF, UFFA and sand. It should be reminded that to quantify the cost and embodied CO_2 of solutions, they were transformed from actual values to kg/m^3 of concrete.

Table 4-7: Different importance weights and their corresponding solutions for developing eco-efficient UHPC.

Alternatives	Variables	Goal	Importance weights	Solutions				CO_2 content*	Cost **
				CEM	SF	UFFA	Sand		
A.1	A:SF	Maximize	++	1	0.099	0.561	1.755	594.57	129.25
	B:UFFA		+++						
	C:Sand		+++++						
A.2	A:SF	Maximize	+	1	0.088	0.564	1.767	594.2	126.7
	B:UFFA		+++						
	C:Sand		+++++						
A.3	A:SF	Maximize	+++++	1	0.1	0.583	1.725	595.25	129.73
	B:UFFA		+++++						
	C:Sand		+++++						
A.4	A:SF	Maximize	+++++	1	0.1	0.561	1.753	594.68	129.49
	B:UFFA		+++						
	C:Sand		+++++						
A.5	A:SF	Maximize	+++++	1	0.1	0.631	1.624	602.29	130.88
	B:UFFA		+++						
	C:Sand		+						

∗ CO_2 content of CEM, SF, UFFA and sand (kg) per m^3 of UHPC.

∗∗Cost of CEM, SF, UFFA and sand (€) per m^3 of UHPC.

As can be seen from **Table 4-7**, the second alternative demonstrate lowest CO_2 content as well as price showing its desirability as an eco-efficient UHPC composition.

The next goal of this stage is to adjust the importance weights in such a way that result a cost-efficient composition besides eco-efficiency. In this regard, although we need to minimize cement through maximizing all the three variables again, SF also should be minimized with respect to its high price. According to **Table 4-6**, SF cost is 4, 10 and 15.7 times of cement, UFFA and sand respectively. In this regard, SF with different importance weight was minimized while sand and UFFA were maximized again. The results are summarized in **Table 4-8**.

Table 4-8: Different importance weights and their corresponding solutions for developing cost-efficient UHPC.

Alternatives	Variables	Goal	Importance weights	Solutions				CO_2 content*	Cost **
				CEM	SF	UFFA	Sand		
A.6	A:SF	Minimize	+++++	1	0.047	0.613	1.67	607.63	118.88
	B:UFFA	Maximize	+++++						
	C:Sand		+++++						
A.7	A:SF	Minimize	+	1	0.056	0.569	1.759	599.99	119.93
	B:UFFA	Maximize	+++						
	C:Sand		+++++						
A.8	A:SF	Minimize	+++	1	0.052	0.59	1.725	602.28	119.37
	B:UFFA	Maximize	+++						
	C:Sand		+++++						
A.9	A:SF	Minimize	+++++	1	0.048	0.599	1.69	606.72	118.92
	B:UFFA	Maximize	+++						
	C:Sand		+++++						
A.10	A:SF	Minimize	+++	1	0.045	0.622	1.644	610.43	118.74
	B:UFFA	Maximize	+++++						
	C:Sand		+++						

* CO_2 content of CEM, SF, UFFA and sand (kg) per m^3 of UHPC.

**Cost of CEM, SF, UFFA and sand (€) per m^3 of UHPC.

As depicted in both tables, CO_2 content and cost have a range between 594.2 kg/m^3 to 610.43 kg/m^3 and 118.74 €/m^3 to 130.88 €/m^3 respectively. The best composition regarding eco-efficiency is A.2 with lowest CO_2 content. This composition also has a cost value of 126.7 €/m^3 which is 34% lower than the maximum price in the table. It should be noted that due to the primary appropriate selection of upper limit for silica fume, maximum 10% of cement weight, even the eco-efficient composition could be considered as a cost-efficient mixture with a negligible higher price compared to cost-efficient one. According to above solutions, proposed by Design-Expert®, the following compositions known as cost-efficient and eco-efficient ones were tested to find their conformity to the predicted responses. As can be seen from **Table 4-9**, the predicted values of flow diameter for both solutions are perfectly identical to their experimental quantities. Also, the deviation of experimental from theoretical values for

compressive strength in both scenarios are very low representing the high efficiency of

RSM for UHPC mixture design.

Table 4-9: Criteria, optimum solutions and their relevant experimental results for developing cost and eco-efficient UHPC.

Variables and responses	Lower limit	Upper limit	Criteria					
			Cost-efficient			Eco-efficient		
			Importance	Goal	Solution	Importance	Goal	Solution
A:SF	0	0.1	3	minimize	0.045	1	maximize	0.088
B:UFFA	0.3	0.65	5	maximize	0.622	3	maximize	0.564
C:Sand	1.3	1.8	3	maximize	1.644	5	maximize	1.767
F.D. cm	19	27	-	In range	19	-	In range	19
C.S. MPa	150	168.1	-	In range	150	-	In range	158.2
Experimental F.D.			19 cm			19 cm		
Deviation from model			0%			0%		
Experimental C.S.			150.5 MPa			160.3 MPa		
Deviation from model			0.33%			1.32%		

The combined desirability of eco-efficient solution and the relevant desirability of

its variables and responses are shown in **Figure 4.12**. It could be seen that the proposed

model results in individual desirability values for F.D., C.S., sand, SF and UFFA

corresponding to 1, 1, 0.93, 0.88 and 0.76 respectively besides the combined

desirability function of 0.86 for the model.
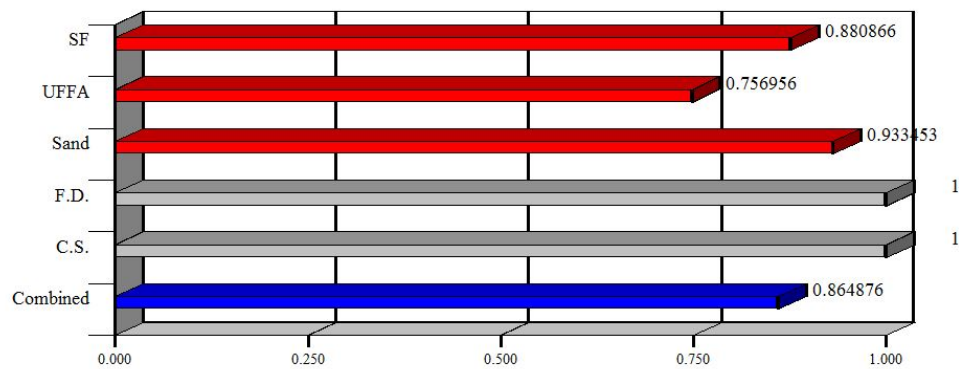
Figure 4.12: Desirability of proposed eco-efficient UHPC mixture for its individual variables and their combination.

As mentioned before, the aim of this research was finding an eco-efficient composition, which meets the minimum possible price as well. Nevertheless, it would be interesting to study an extra scenario, as silica fume-free (SFF) scenario, although far beyond the aim of this research, just to investigate its characteristics. As depicted in **Table 4-10**, just two solutions could be found as SFF compositions. No SFF solution with compressive strength greater than 150MPa was investigated in the design space indicating the possibility of developing a material just in the class of high-performance concretes (HPC) and not UHPCs. The first solution (SSF.1) is identical to Run 5, introduced in **Table 4-3** as a design point. It exhibited very sticky fresh behavior without self-compacting ability (see **Figure AI. 1**) as well as impossibility of using vibrator, which all make it as a useless solution. The second solution (SFF.2) is very close to Run 8. Although it demonstrated enough flowability, its compressive strength was 140.5 MPa, still lower than the minimum acceptable range for UHPC while interesting for HPC development.

Table 4-10: Different importance weights and their corresponding solutions for developing silica fume-free UHPC.

Variables and responses	Lower limit	Upper limit	Criteria					
			SFF.1			SFF.2		
			Importance	Goal	Solution	Importance	Goal	Solution
A:SF	0	0.1	-	=0	0	-	=0	0
B:UFFA	0.3	0.65	5	maximize	0.65	3	maximize	0.52
C:Sand	1.3	1.8	5	maximize	1.8	5	maximize	1.63
F.D. (cm)	10	27	-	In range	10.2	-	≥19	19
C.S. (MPa)	120	168.1	-	In range	130.8	-	In range	140.5

The constituents' quantities for all the solutions in terms of weight ratio in 1m^3 of concrete are also depicted in **Table 4-11**. As expected, cement quantity is lower in eco-efficient mixture by 18.2 kg/m^3 and 49.9 kg/m^3 compared with cost-efficient and SFF.2 respectively. On the other hand, SF content in cost-efficient mixture is near half

of that in eco-efficient composition and zero in SSF.2. In fact, cement and silica fume

directly affect the CO_2 content and price respectively while, UFFA does not play a

significant role in this regard. The other ingredients namely, steel fibers, water and SP

have almost the same quantities in all the compositions.

Table 4-11: Constituents weight ratio (kg/m^3) of UHPC.

	Cement	SF	UFFA	Sand*	St.F (1% V_f)	Total Water** (w/c=26.4%)	SP*** (sp/B=2.5%)
Eco-efficient	640.0	56.3	361.1	1131.2	78.7	167.1	25.61
Cost-efficient	658.2	29.6	409.4	1082.1	78.3	166.8	25.84
SFF.2	689.9	0	358.7	1124.5	78.6	166.8	26.22

*Sand is in saturated surface dry state.
**Water in SP has been taken into account as a part of total water.
***The SP is in liquid form.

To compare the cost and CO_2 content of the three compositions introduced here,

with commercially known UHPC compositions, such as Ductal®, the price and CO_2

content of ground quartz in Ductal® was estimated equal to UFFA. However, ground

quartz bears more environmental impacts as a natural material compared with UFFA as

an industrial waste material. In addition and as noticed before, the estimation was

performed based on the four main ingredients namely cement, SF, UFFA and sand

using **Table 4-6**. Based on these assumptions and according to the typical composition

of Ductal® (Russell & Graybeal, 2013), the estimated results are depicted in

Table 4-12. As can be seen, the cost and CO_2 content of two eco-efficient and cost

efficient compositions, developed in this research, are very close to each other and both

can be considered as eco-cost-efficient compositions due to proper selection of SF

interval during optimization. However, eco-efficient one consumes 18.2 kg/m^3 lower

cement resulting in 16.2 kg/m^3 lower CO_2 content and 7.96 €/m^3 higher cost compared

to cost-efficient one. Nevertheless, both of compositions, namely eco-efficient and

cost-efficient, demonstrate 10% and 7.6% lower CO_2 content and 34% and 38% lower price respectively compared to Ductal® as a promising achievement. The silica fume-free composition demonstrates the lowest price compared to all other compositions due its zero-silica fume content while it is responsible for higher cement and CO_2 content by 49.9 kg/m^3 and 44.5 kg/m^3 respectively compared to eco-efficient composition, which makes it an inferior choice particularly with 20MPa lower compressive strength. However, with respect to 84 €/m^3 of its lower price compared to Ductal®, it would be an appropriate composition where eco-efficiency and compressive strength of higher than 150MPa are not matters of concern. Accordingly, and due to the lower carbon footprint of eco-efficient composition, denoted as EEUHPC henceforth, besides its cost efficiency compared with known UHPCs, its characteristics will be investigated in the following chapters. However, based on its similar mix design close to cost-efficient one, it is predicted that they probably exhibit very similar mechanical and durability-related behavior.

Table 4-12: Cost and CO_2 content of different compositions.

	Eco-efficient	Cost-efficient	SFF.2	Ductal®	Conventional concrete (C20/25)
CO$_2$ content (kg/m^3)	594.2	610.43	638.7	660.3	240*
Cost (€/m^3)	126.7	118.74	109.3	193.0	65**

* (Hammond & Jones, 2011)

** (Preços de betão pronto, 2016)

The eco-efficient and cost-efficient compositions also exhibit around 2.5 times and 1.9 times of CO_2 content and price respectively compared to conventional concrete with compressive strength in range of 20-25 MPa. However, their compressive strength, which is at least 6 times of conventional concrete, their ultra-high durability, as will discussed later, and finally their other advantages, as explained in chapter 1 and chapter 2, justify their higher cost and environmental impacts particularly in long-term.

The interface of feasible region of responses and their relevant proposed solution, as well as 2D counter plots for eco-efficient composition are shown in **Figure 4.13** and **Figure 4.14**.
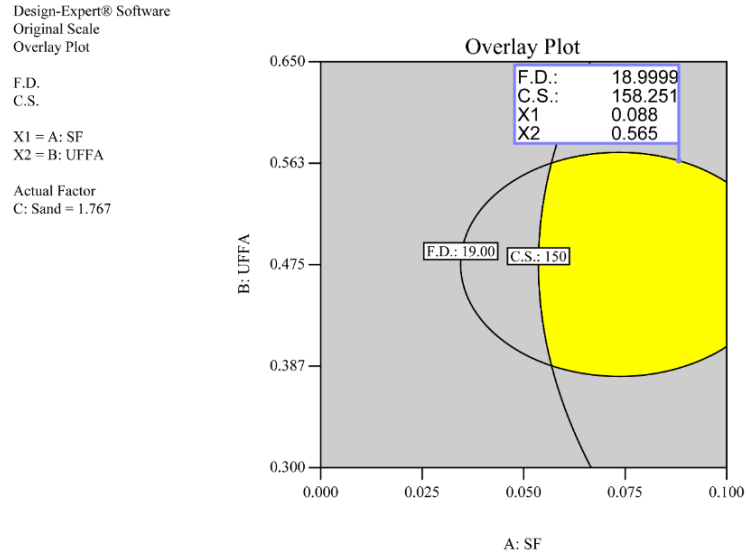
Figure 4.13: The overlay plot of feasible regions regarding optimum F.D. and C.S. for SF & UFFA
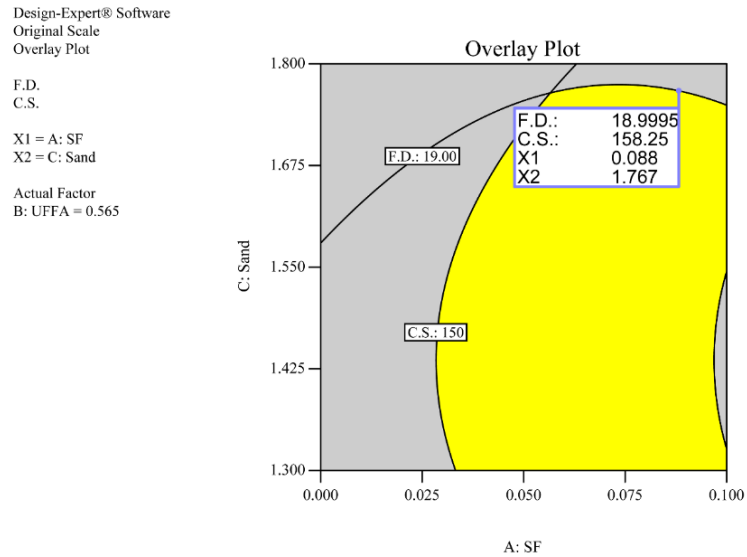
Figure 4.14: The overlay plot of feasible regions regarding optimum F.D. and C.S. for SF & sand.

2D counter plots for F.D. and C.S. are also provided in **Figure 4.15** to **Figure 4.18**.

They exhibit how the variables influence the two responses besides demonstrating position of the predicted solution on the graphs. **Figure 4.16** also demonstrates how flowability is highly dependent on sand variation as also observed in perturbation plots previously. In the same way, **Figure 4.17** and **Figure 4.18** demonstrate the effective contribution of SF on C.S.
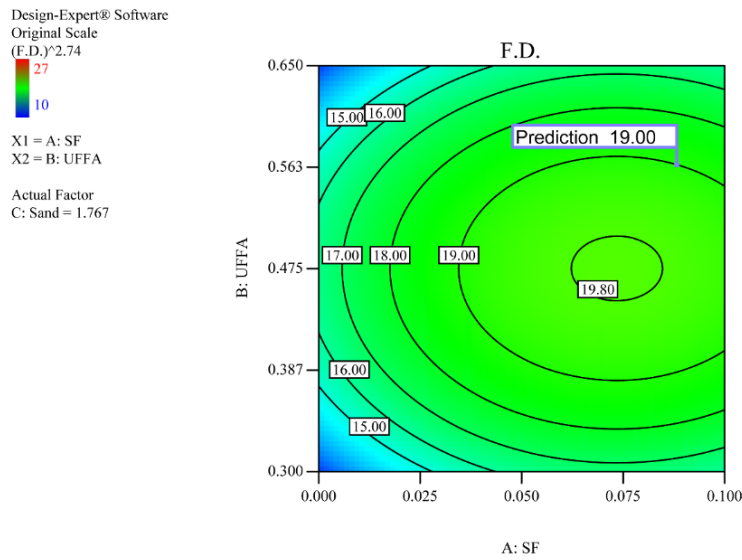
Figure 4.15: 2D effects of SF & UFFA on F.D. and the corresponding predicted point for eco-efficient UHPC.
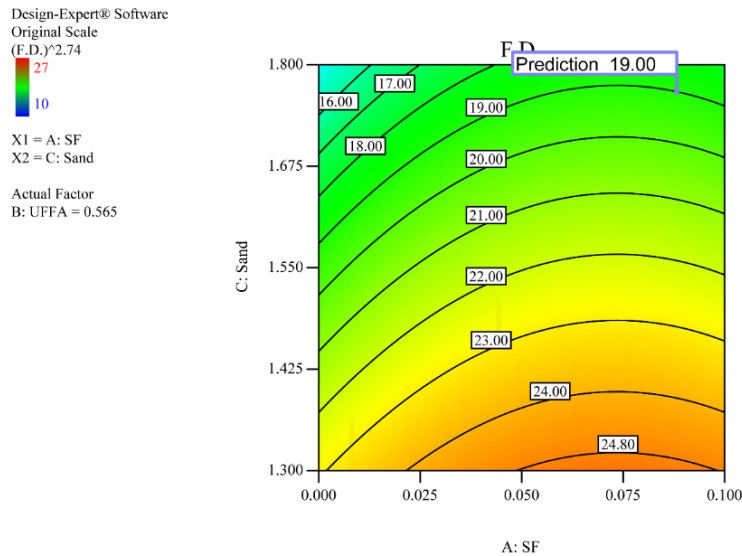
Figure 4.16: 2D effects of SF & sand on F.D. and the corresponding predicted point for eco-efficient UHPC.
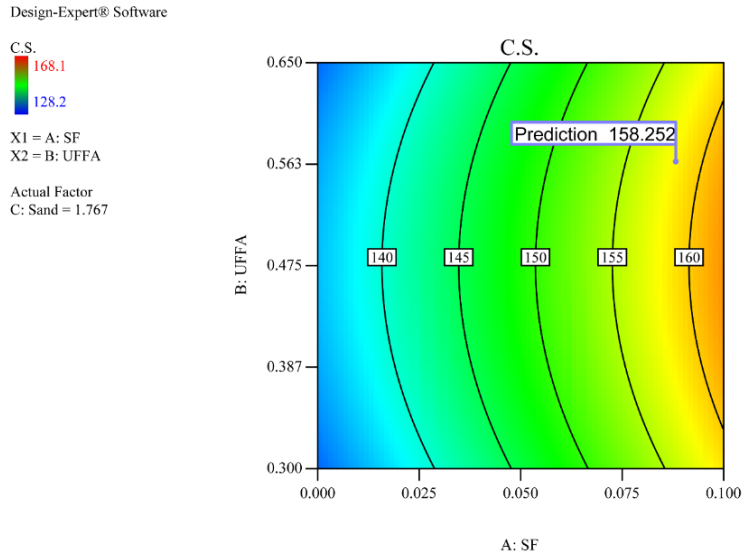
Figure 4.17: 2D effects of SF & UFFA on C.S. and the corresponding predicted point for eco-efficient UHPC.
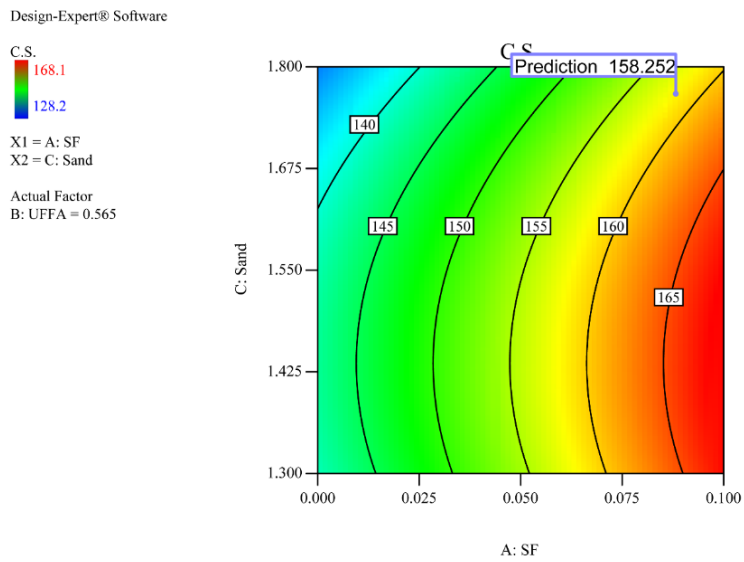
Figure 4.18: 2D effects of SF & sand on C.S. and the corresponding predicted point for eco-efficient UHPC.

4.3   Conclusions

A statistical mixture design method based on response surface methodology (RSM) aiming at developing eco-efficient UHPC was presented in this chapter. Two models regarding flow diameter and compressive strength with small P-value, insignificant lack of fit and very close adjusted/predicted R-squared were proposed. Sand was found

to have the greatest effect on flowability reduction while silica fume, up to 9% of cement weight, increased the flow diameter to some extent and then showed a slight negative impact. UFFA, up to 43% of cement weight, showed positive effect on both F.D. and C.S., but in higher percentage affected them marginally. Accordingly, UFFA as an industrial waste material, indicated its potential to be applied in UHPC as a substitute for CEM and SF. Regarding the compressive strength, SF plays an important role in strength development of UHPC. Sand exhibited a negative effect on compressive strength when exceeds 145% of cement weight.

A numerical optimization for two responses considering various scenarios and importance weights was also accomplished. The numerical solutions and their related experimental results demonstrated perfect conformity with high precision representing high efficiency of RSM for UHPC development. Based on the results, an eco-efficient UHPC containing low quantity of cement and silica fume with 640 kg/m^3 and 56.3 kg/m^3 respectively was developed. Compressive strength and flow diameter of the mixture were 160.3 MPa and 19 cm respectively. The total weight ratio of SF, UFFA and sand to cement in this mixture is almost 2.42, which is significantly high implying lower cement consumption compared to conventional UHPC compositions presented in **Table 2-2** with a powder/cement ratio in range of 1.3 to 2.05. In addition, the silica fume content of the developed mixture is at least 50% lower than the typical ones. Incorporation of ultra-fine fly ash with mean particle size of 4.48 μm, was found an effective way for cement and silica fume substitution particularly with respect to its positive effect on flowability and strength.

Chapter 5

Characteristics of

EEUHPC

This chapter deals with the main characteristics of EEUHPC developed in the previous chapter through RSM. The main tests fulfilled in this part include flow table, slump flow, compressive strength, modules of elasticity in compression, four-point and three-point flexure, direct tensile, chloride diffusion and carbonation tests.

5.1 Rheology of fresh EEUHPC

To study the fresh rheology of the developed mixture two tests were carried out. The first test is similar to flow table test described in last chapter for optimizing UHPC based on EN 1015-3 (BS EN 1015-3, 2004). The difference in both methods is just in

numbers of dropping the table. As we are dealing with SCC, our measurements were

performed without any table drop. To implement this test, the mini-slump cone was

filled with concrete. Then the conic mold was removed and once the concrete reached

a steady state, two perpendicular diameters were measured. The average of these two

reading was registered as flow diameter. As mentioned in the previous section the flow

table diameters for EFUHPPC was 19 cm. Besides that, this test was repeated for more

10 mixtures of the same composition to have the results with more accuracy. Finally, a

flow diameter with an average and Std. Dev. of 19.05 cm and 0.29 cm respectively was

obtained. In the next step in order to investigate the real slump-flow of the material, the

slump-flow test for SCC was completed according to EN 12350-8 (BS EN 12350-8,

2010) and based on recommendations for SCC (AFGC, 2000) as well. For this aim, a

baseplate with dimensions of 90 cm x 90 cm was moistened. Then the cone, with the

bottom diameter of 20 cm, was filled continuously up to the top of the cone. Then it

was lifted vertically and after the concrete spread was finished on the baseplate, the

final dimeters were measured. The average of two perpendicular slump-flow diameter

as can be seen in **Figure 5.1** is 60 cm indicating acceptable range of self-compactness.

Figure 5.1:   Slump-flow test.

5.2 Compressive strength

All compressive strength tests performed in this study were made according to standard test method for 50 mm cubic specimens (ASTM C109/C109M – 05, 2005). After the flow diameter of fresh concrete was measured, the reminded material on the table placed back to the mixing pan and were mixed by hand for 20 seconds. Since the concrete had enough fluidity, it directly was transferred from the mixing bowl to the molds without any tool such as scoop. Although this concrete is a SCC, to ensure a consistent approach, after casting of all the specimens the molds were vibrated on a vibration table for 20 seconds. Afterwards, their surface was smoothed with a trowel and covered with a thin plastic sheet to prevent any water loss from the exposed surface. Two different methods for curing the samples were applied in this part. The first method, known as tempered-water curing (TWC), was described in the previous chapter based on the introduced curing cycle. The second method was normal curing in 20°C water bath until the day of test. For compressive strength tests, a loading pace of 2.4 kN/s (Graybeal, 2006) equivalent to 1 MPa/s was selected for all the specimens during this research (**Figure 5.2**). It should be reminded that three samples were considered for each date. The results for second curing regime are presented in **Table 5-1** and **Figure 5.3**.
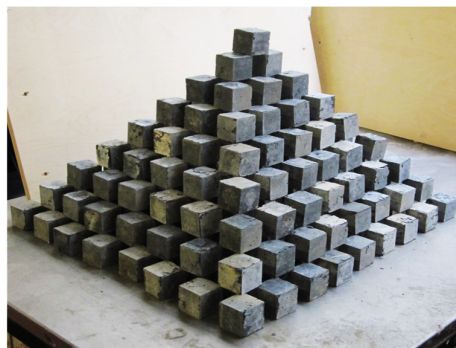
Figure 5.2: 5x5x5 cm^3 cubes for studying UHPC.

Table 5-1: Compressive strength of normal-cured samples.

Day	1	3	7	14	28	56	91	121
Compressive strength (MPa)	45.5	84.2	106.6	129.1	152.1	168.3	172.9	171.6

It is interesting to note that almost 26% of final strength is gained just 24 hours after mixing and around 50% of the maximum strength is achieved just after 3 days. Besides that, after 56 days of normal curing the concrete reaches close to its highest strength level, which is approximately 172 MPa. In addition, 28-day compressive strength is 88% of the final strength which could be used for any design purposes.
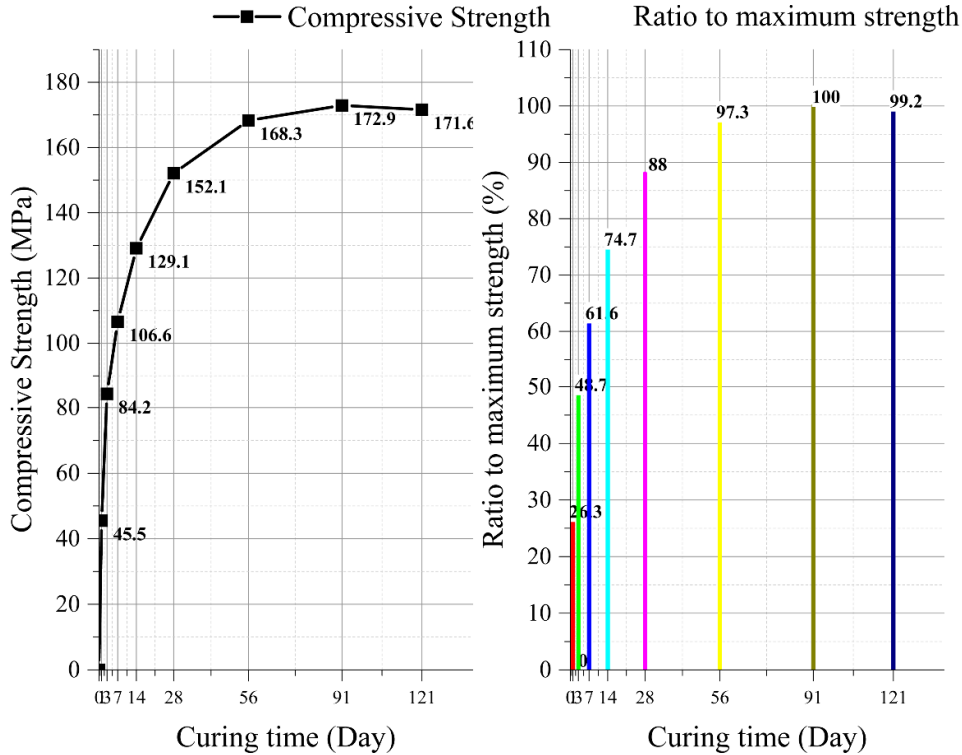
Figure 5.3: Compressive strength trend for normal-cured samples (left) and the ratios of each age to maximum strength in % (right).

The second group of samples, those cured with tempered water treatment method, were tested in different curing ages just to evaluate the final strength capacity of EEUHPC, which is useful for next step of this research work that is studying the

self-healing ability of the material. In this regard, 15 specimens were cured based on

the curing cycles explained in **Figure 4.1** and just with different treatment time intervals

from 24 hours to 168 hours (7 Days). As depicted in **Figure 5.4**, 48 hours of heat curing

in tempered water ensures an acceptable compressive strength around 96% of the final

capacity, which would be advisable for pre-fabrication industry. Nevertheless, 24 hours

would be also acceptable in cases where 85% of the finals strength is enough for

load-carrying purposes. After 48 hours, the increasing trend of strength-gain becomes

almost negligible.
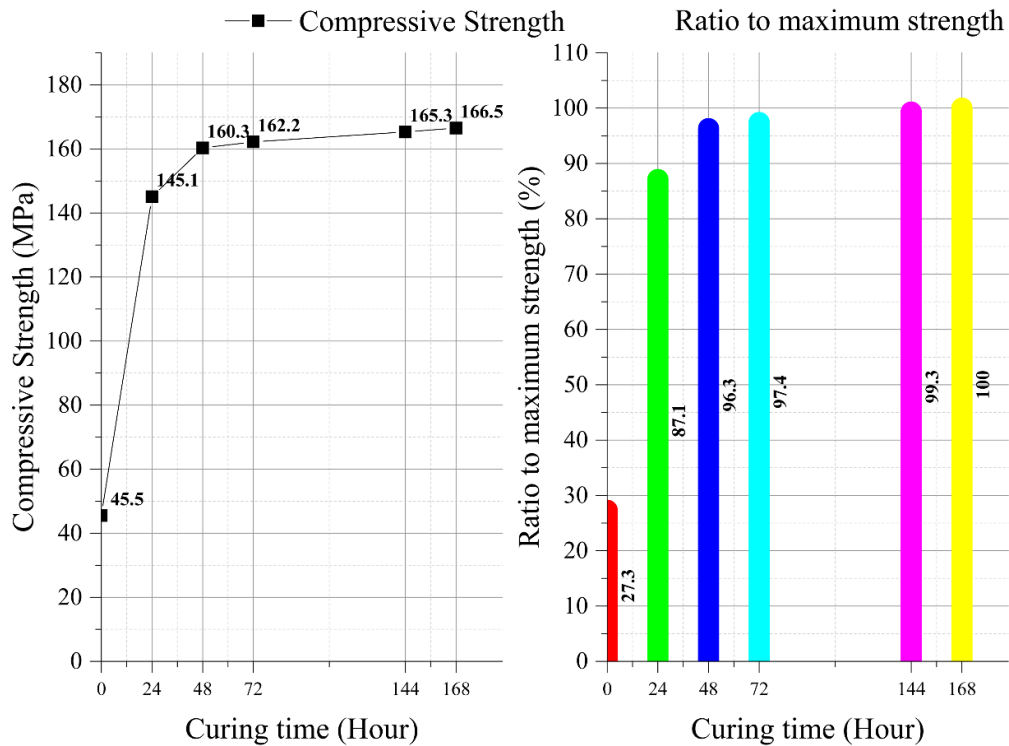
Figure 5.4:   Compressive strength trend for tempered water-cured samples (left) and the ratios of each age to
maximum strength in % (right).

Although with just 48 hours of curing in tempered water the compressive strength

goes slightly beyond the related value for 28 day in normal curing method, the final

strength of samples subjected to the adopted TWC was lower than NC.

5.3 Modulus of Elasticity

This test was performed in accordance with ASTM (ASTM-C469, 2010). Three cylindrical specimens with diameter and height of 10 cm and 20 cm respectively were casted and cured based on TWC and NC methods. After finishing the curing period, which was 48 hours of treatment in 67°C for TWC method and 28 days in water with 20°C for NC method, both sides of the specimens were rectified. The rectifier machine, test setup and one sample after compression are all shown in **Figure 5.5**.

a)   b)   c)
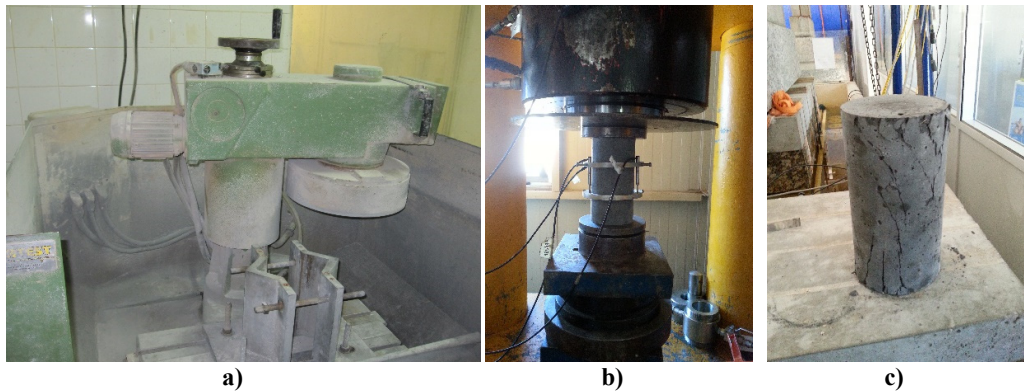
Figure 5.5:   Rectifying machine (a), Test setup for Modulus of Elasticity (b) and one sample after failure (c).

As indicated, the test setup included two parallel rings situated approximately in one third of the specimen height with a vertical distance between the centers of two rings equal to 7 cm. The rings were rigidly attached to the sample through three bolts. Finally, three linear variable displacement transducers (LVDT) were fixed to upper ring while their moving ends were placed on top of the lower ring to measure the axial deformation of the specimen from the beginning of the test to the failure. The machine was adjusted for 5 cycles of loading to a maximum load nearby 355 kN corresponding to 45.2 MPa which was almost 30% of predicted maximum load-carrying capacity of the specimens followed by reloading phase to ensure a validate modulus of elasticity. The axial strain for each cylinder was recorded from three LVDTs. If the results of 5 cycles are not in acceptable conformity to each other, the test should be rejected.

Otherwise, the average of best-fitted line for 5 cycles of 3 LVDTs in the stress-strain diagram is used to calculate the modulus of elasticity for each individual cylinder. A typical diagram for 5cycles of each LVDT for one sample is presented in **Figure 5.6**. The fitted line was calculated in the range of 10 MPa to 40 MPa in the Stress-Strain diagram for each recorded data series. All the corresponding results all presented in **Table 5-2**.
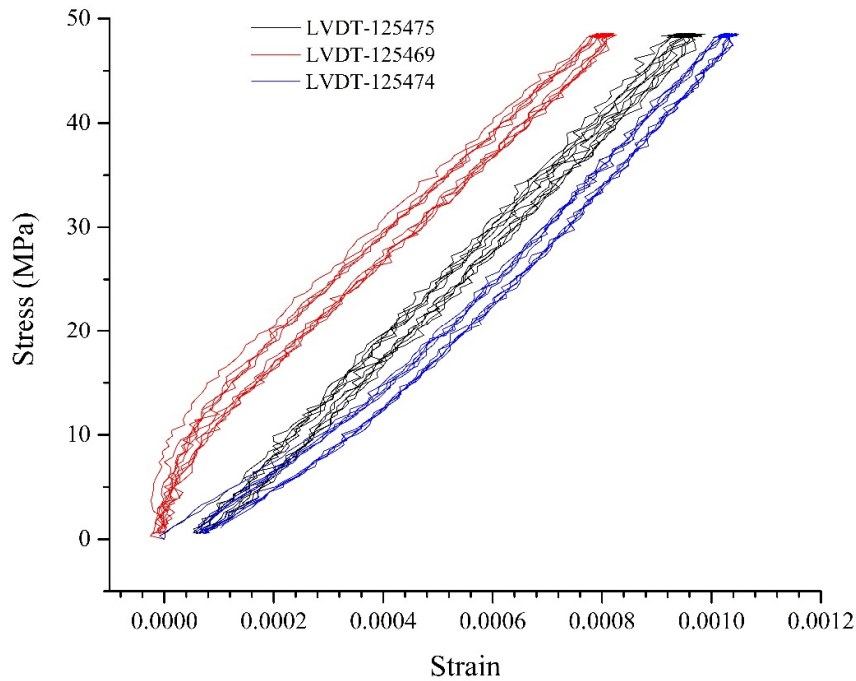
Figure 5.6: A typical axial Stress-Strain diagram representing 5 cycles of loading and reloading in each LVDTs in one of the NC samples.

Table 5-2: Results of Modulus of Elasticity in compression for TWC and NC samples.

Name of Series	Number of samples	Modulus of Elasticity in compression (MPa)		Density (kg/m³)	
		Ave.	St. Dev.	Ave.	St. Dev.
NC	3	50764.4	1711.6	2372.8	4.54
TWC	3	56494.5	1862.4	2380.0	1.63

As can be seen, the modulus of elasticity for TWC samples is around 11% higher

than 28-day NC samples. The density for all specimens were around 2380 kg/m^3.

5.4   Four-point bending test

This test procedure conforms to ASTM (ASTM-C78–02, 2002). Analyzing the flexural

strength and toughness indices of the developed material was also performed according

to ASTM (ASTM-C1018–97, 1998). The test setup of the performed test is depicted in

Figure 5.7. For this test, three 28-day samples of 4x4x16 cm^3 from NC series were

selected. The reason why NC specimens were selected was to monitor some

performance criteria of EEUHPC such as first-crack strength, toughness indices and

residual strength factors for comparison with different conventional, high performance

and ultra-high performance concretes. The selected dimensions for specimens and the

distances of load supports fulfil the requirements of ASTM C1018-97. For instance, the

width and depth of specimens, 4cm, are more than three times of fiber length, 1.3 cm.

In addition, the span length is three times of the specimen depth. The open surface of

the specimens were rectified before the test in order to remove any excess concrete on

the surface, remained after casting, which results in a smoother surface with required

dimensions. The vertical displacement rate of machine was adjusted to 3 μm/s. During

the test, the vertical deflection at mid-span as well as crack mouth opening displacement

(CMOD) were registered through two vertical and horizontal LVDTs. It should be

noted that, the specimens were tested without notch. The test results for EEUHPC are

depicted in **Figure 5.8**.
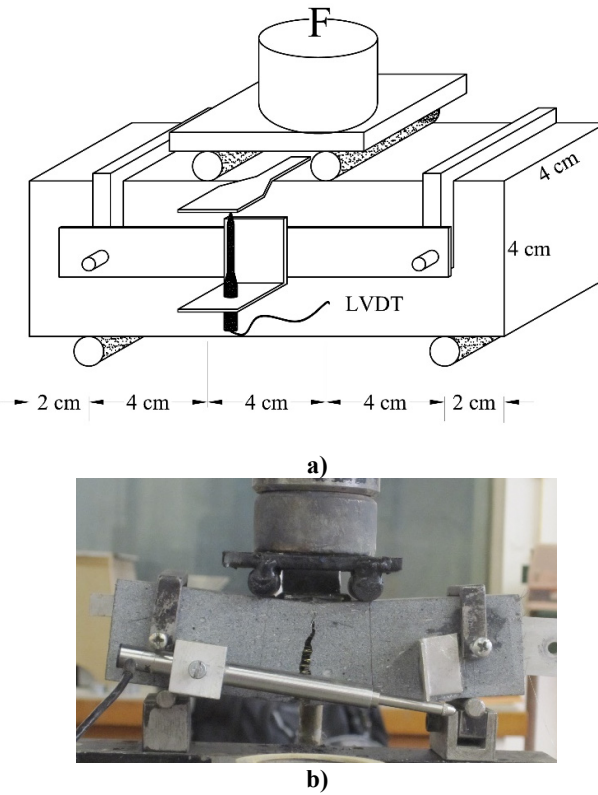
Figure 5.7: Schematic test setup, front view (a) and back view (b).

All fractures occurred inside the middle third of the span, as can be seen from **Figure 5.7**. In this regard, the modulus of rupture and flexural strength can be calculated using the following equation:

$$R = PL/bd^2 \qquad \text{Eq. (5.1)}$$

where R is the modulus of rupture in MPa, P is the maximum applied load in N, L is the span length in mm and b and d are average width and depth of specimen respectively in mm at the fracture point.

The load-deflection curve and its corresponding flexural strength-deflection curve are presented in **Figure 5.8**. Based on the average curves, the flexural strength at first-cracking point and the modulus of rupture are 12.071 MPa and 22.874 MPa with deflections of 0.02044 and 0.762 respectively.
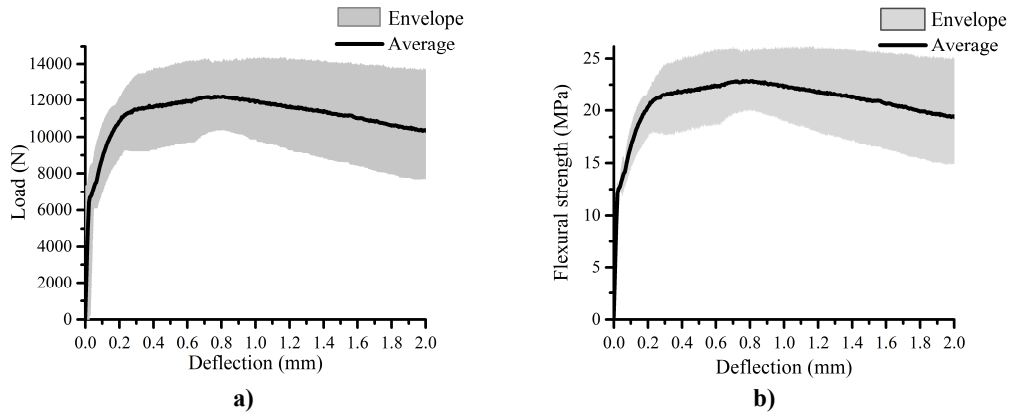
Figure 5.8: Load-deflection (a) and Flexural strength-deflection (b) curves in 4-point bending test of EEUHPC.

In addition to modulus of rupture, also referred to as bending strength, the maximum flexural strength of the concrete at its first-crack and the toughness indices are of great importance as well. They characterize the toughness after first-cracking up to a specific end-point deflection. Finally, the residual strength factors, indicated as a percentage of load at the first crack, are derived from toughness indices. They represent the retained strength after first crack through quantifying the average of post-crack load in a defined deflection interval.
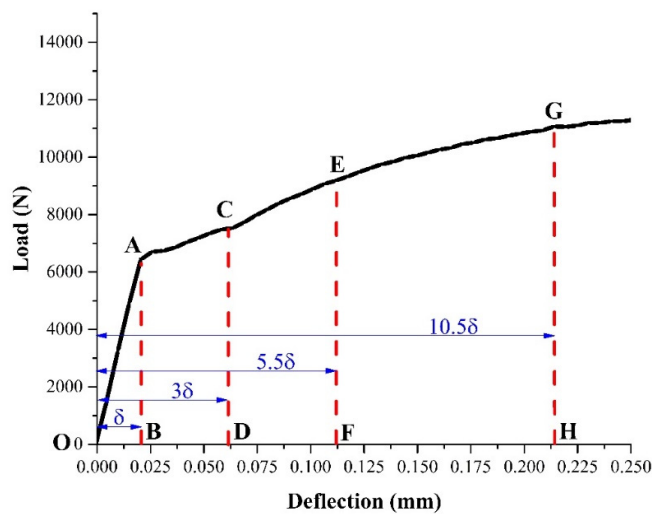
Figure 5.9: Load-deflections curve to calculate the toughness indices (adapted from (ASTM-C1018–97, 1998)).

According to ASTM C1018-97 (1998) and based on **Figure 5.9**, the toughness

indices of I_5, I_{10} and I_{20} are determined at δ, 3δ, 5.5δ and 10.5δ based on **Equation 5.2**

and **Equation 5.3** where δ is the deflection in first cracking.

I_5 = Area (OACD)/Area (OAB)   Eq. (5.2.a)
I_{10} = Area (OAEF)/Area (OAB)   Eq. (5.2.b)
I_{20} = Area (OAGH)/Area (OAB)   Eq. (5.2.c)

The residual strength factors of $R_{5,10}$ and $R_{10,20}$ are determined as follows when

required.

$R_{5,10}$ = 20 (I_{10} - I_5)   Eq. (5.3.a)
$R_{10,20}$ = 10 (I_{20} - I_{10})   Eq. (5.3.b)

All the results are provided in **Table 5-3**.

Table 5-3: Toughness indices and residual strength factors of EEUHPC.

δ	OAB	OACD	OAEF	OAGH	I_5	I_{10}	I_{20}	$R_{5,10}$	$R_{10,20}$
0.02044	68.8	355.6	784.7	1832.3	5.169	11.41	26.63	124.7	152.3

Since a material with linear elastic behavior before first cracking and perfect plastic

behavior after that reveals values of 5, 10 and 20 for its own toughness values at

deflections of 3δ, 5.5δ and 10.5δ, these indices provide a measure for undressing how

well a material behave in elastic or plastic phase before and after its first cracking. As

depicted in **Table 5-4**, plain concretes reveal a value of 1.0 for all these indices while

elastic-plastic materials as mentioned above demonstrate values of 5, 10 and 20. An

ideal fiber-reinforced concrete (FRC) should demonstrate values between 1 to 6, 1 to

12 and 1 to 25 for I_5, I_{10} and I_{20} respectively. In this regard, the developed EEUHPC in

this research exhibits perfect behavior. Even the I_{20} equal to 26.63 is higher than

corresponding value for other fibrous concretes in **Table 5-4**.

Table 5-4: Definition of toughness indices and related values for different materials (ASTM-C1018–97, 1998).

Index designation	Index definition	Deflection Criterion	Values of Toughness Indices		
			Plain Concrete	Elastic-Plastic Material	Observed Range for Fibrous Concrete
I_5	OACD/OAB	3δ	1.0	5.0	1-6
I_{10}	OAEF/OAB	5.5δ	1.0	10.0	1-12
I_{20}	OAGH/OAB	10.5δ	1.0	20.0	1-20

For better understanding of behavior of an elastic-plastic material and a fibrous concrete their load-deflection curves are presented in **Figure 5.10**. As can be seen, the elastic-plastic materials demonstrate a fixed load-carrying capacity while the fibrous concretes depending on the type and fiber quantity and even the concrete matrix exhibit different post-cracking behavior. The material developed in current study, revealed excellent post cracking behavior. Although there is no direct relationship between toughness and the energy-absorption capacity of the material, it can be estimated that after first cracking its energy absorption is much greater than an elastic-plastic material.
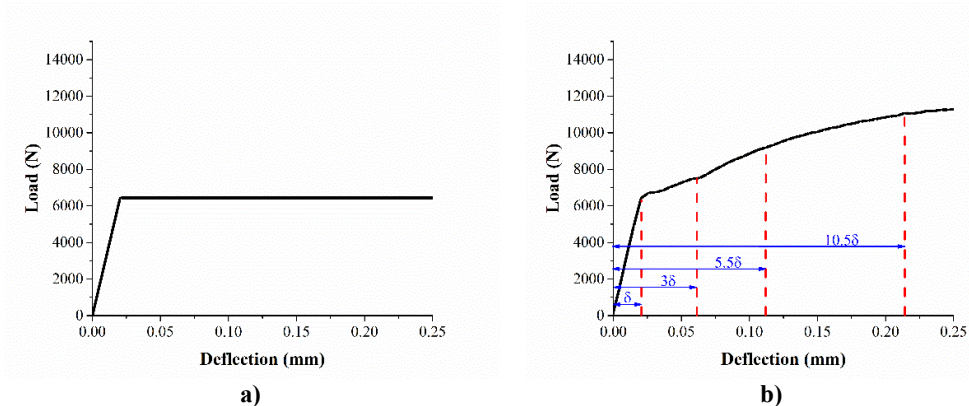
Figure 5.10: Elastic-Plastic material (a) and EEUHPC (b) behavior with identical first-crack deflection (δ).

If both diagrams for EEUHPC and an elastic-plastic material (EPM) with equal first cracking load and deflection drawn in one graph, **Figure 5.11**, it would be more obvious that the load-bearing capacity of EEUHPC developed here after first cracking is almost 90% of load in cracking point. This maximum load occurs at deflection of 0.76 mm. In

addition, two diagrams cross each other at deflection of around 3.5 mm demonstrating

the higher toughness of EEUHPC compared to an EPM.
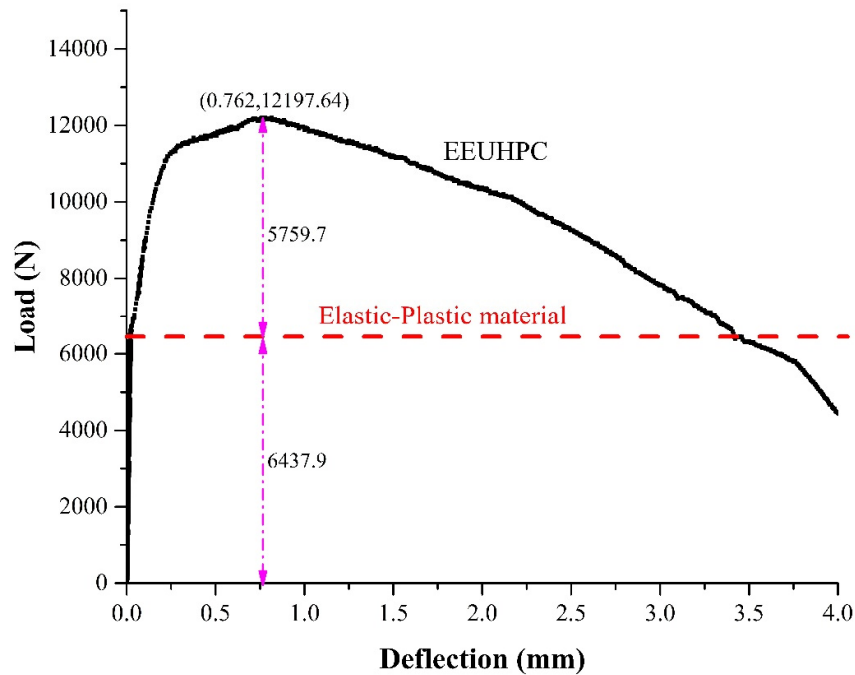
Figure 5.11: Graphical comparison of a perfect Elastic-Plastic material and EEUHPC.

If this comparison being continued to deflections higher than those in **Figure 5.9**,

interestingly it can be observed that the EEUHPC has an excellent plastic behavior even

in deflections of 200δ compared to EPMs. In this regard, by integrating the area under

the load-deflection curves, it can be seen that even close to the deflection of 230δ

corresponding to 4.7012 mm, the area under EEUHPC curve is bigger than the EPM's.

Figure 5.12 illustrates the relationship between different toughness indices for both

materials and their corresponding deflection as well as deflection ratio to first-crack

deflection (δ). This is shown that not only the toughness index curve for EEUHPC up

to a deflection close to 5 mm is on top of the EPM curve but also the gap between two

curves become wider, up to 0.2704 mm corresponding to 160δ, and after this point

again reduces however, it is still higher than the EPM diagram. For instance, I_{279}, I_{319}

and I_{359} for EEUHPC are greater than EPM's by a value of 162.8, 168.3 and 166.6

respectively. This exhibits perfect plastic behavior after first cracking, even better than

ideal EPMs. In addition, the toughness index of EEUHPC for peak load of 12199.6 N

and deflection of 0.76237 mm, corresponding to 37.3δ, is equal to 122.23, which is 1.63

times greater than the EPM's with a toughness index close to 73.6. **Figure 5.12** shows

the difference of the developed material in this research and a material with equal

load-deflection at cracking point and perfect plastic behavior.
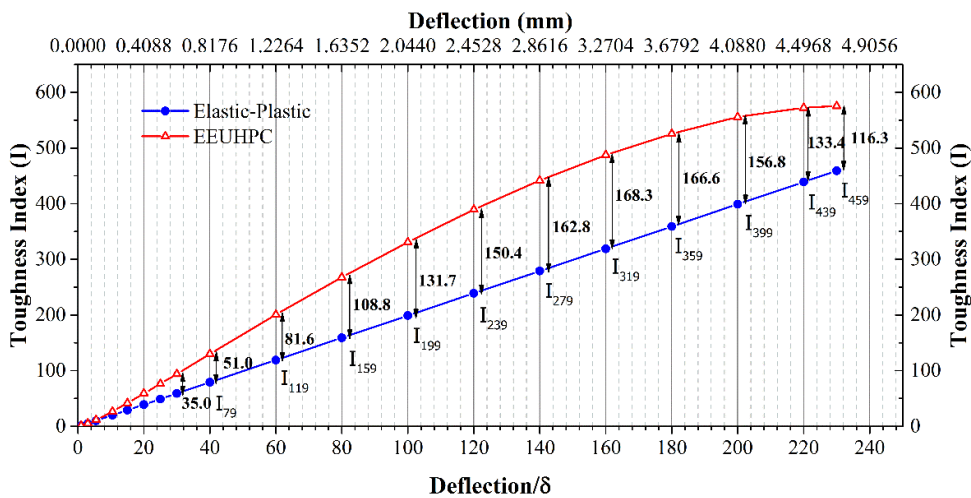
Figure 5.12: Comparison between toughness indices of an Elastic-Plastic material and EEUHPC.

5.5   Three-point bending test

The three-point bending test described here is in accordance with international code

proposed by RILEM (RILEM TC 162-TDF, 2002). The specimens were all from NC

series and tested at the age of 28 days. The specimens were notched before test at their

mid-span in order to avoid multiple cracking for more accurate determination of

energy-absorption capacity of the specimens exactly at the loading point. Generally this

test method is useful for determination of a) tensile behavior of steel-fiber-reinforced

concrete (SFRC), b) limit of proportionality (LOP) c) two equivalent flexural tensile

strength and d) four residual flexural tensile strengths as all will be explained in the

next part. The schematic and experimental test setups and configurations are presented

in **Figure 5.13** and **Figure 5.14**.
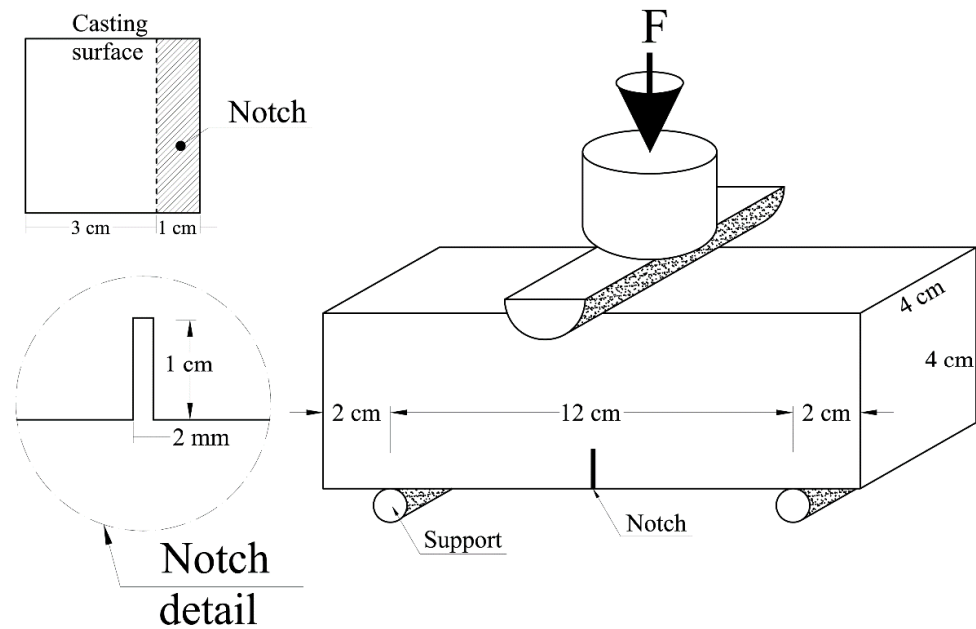
Figure 5.13: Specimen's size and details of notch.
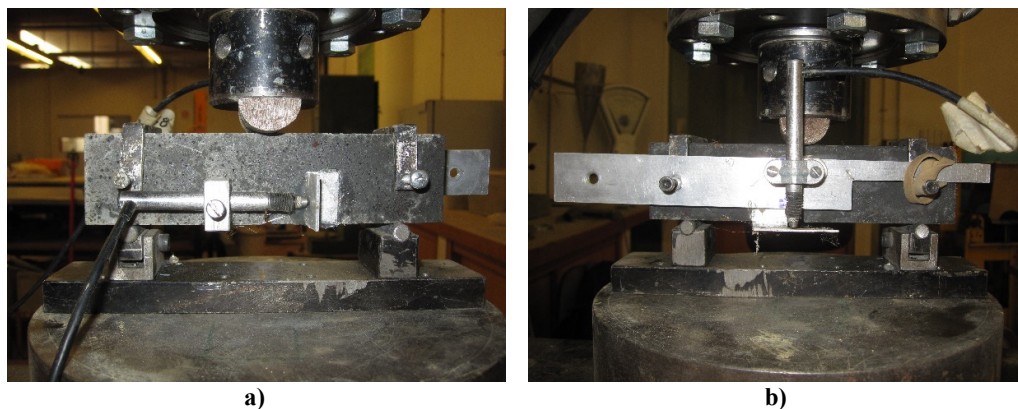
Figure 5.14: Place of two LVDTs in 3-point flexure test configuration for (a) CMOD and (b) deflection.

All the tests were performed with a loading rate of 3 μm/s equivalent to
0.18 mm/min. The test results in terms of Load-Deflection curves are presented in
Figure 5.15.
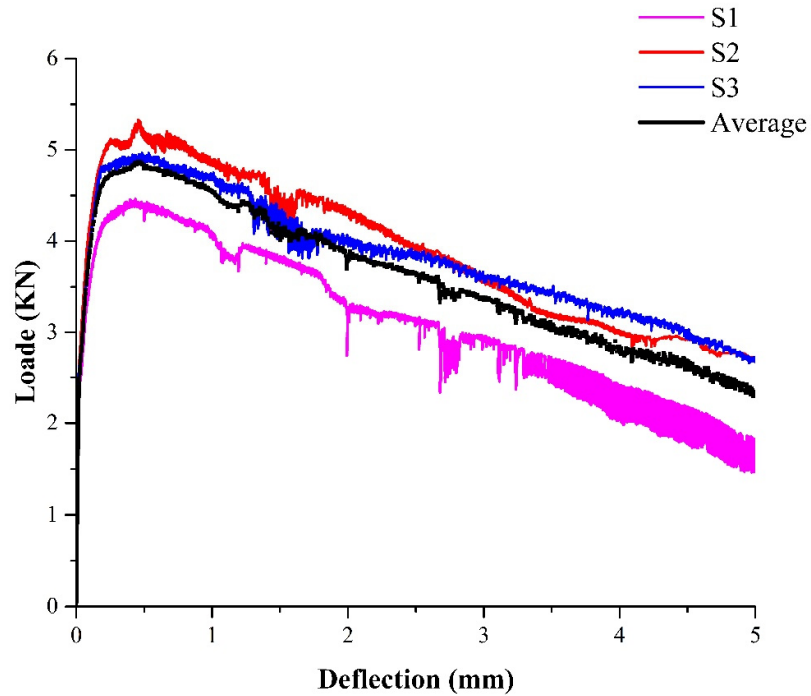
Figure 5.15: Load-Deflection curves and their average for 3-point flexural test of EEUHPC.

By definition (RILEM TC 162-TDF, 2002), F_L is the maximum load in the interval
of 0.05 mm of deflection or CMOD. The objective of determination of this value and
its corresponding deflection is to quantify the concrete contribution to energy
absorption of the specimen. Accordingly, the load at the limit of proportionality (F_L) is
equal to 3.053 KN with a deflection of δ= 0.05 mm.
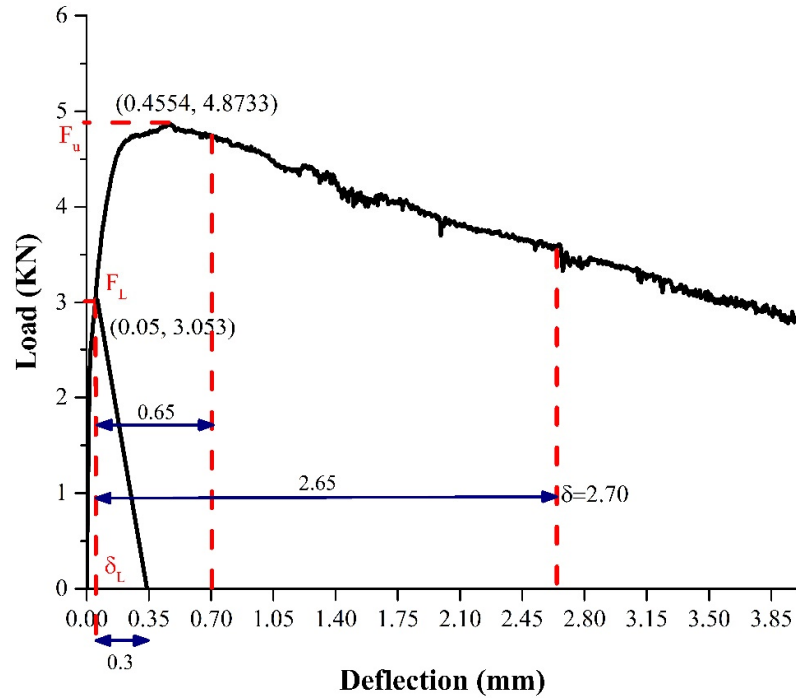
Figure 5.16: Load-deflection curve and corresponding parameters to calculate energy absorption.

As can be seen in **Figure 5.16**, the load-bearing capacity of specimen starts to increase after first crack at the end of elastic phase and the ultimate load, F_u, at $\delta = 0.4554$ mm is equal to 4.873 kN which is almost 1.6 times more than F_L. The corresponding moment of F_L at mid-span of the tested prism (M_L) is determined using **Equation 5.4**:

$$M_L = \frac{F_L}{2} \cdot \frac{L}{2} \qquad \text{(N.mm)} \qquad\qquad \text{Eq.(5.4)}$$

where F_L as explained above is the highest load in the limit of proportionality and L is the span of the specimen between two supports. By assuming a linear elastic stress distribution pattern as shown in **Figure 5.17**, the maximum stress at limit of proportionality $f_{fct,l}$ is calculated using **Equation 5.5**.

$$f_{fct,l} = \frac{3.F_L.L}{2.b.h_{sp}{}^2} \qquad (\text{N/mm}^2) \qquad\qquad \text{Eq.(5.5)}$$

where b is the width of specimen and h_{sp} is the distance between tip of the notch and

top of the cross section all in mm.
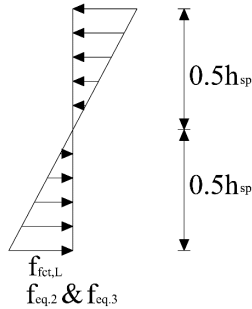
Figure 5.17: Assumed stress distribution (adapted from (RILEM TC 162-TDF, 2002)).

In order to determine the energy-absorption capacity of the specimens, first some

terms should be defined according to **Figure 5.18**.
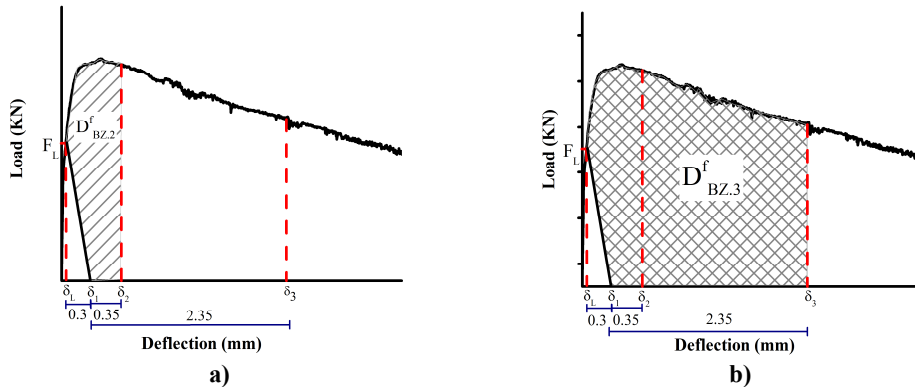
Figure 5.18: 3-point load-deflection curve and corresponding areas for energy-absorption determination (adapted from (RILEM TC 162-TDF, 2002)).

The first term is $D^b{}_{BZ}$ defined as the area under load-deflection curve limited to the

line connecting two points of (δ_L, F_L) to $(\delta_L+0.3, 0)$. This area, shown as a blank area in

Figure 5.18, exhibiting the energy absorption of concrete matrix without considering

fibers' contribution. Two other terms, namely $D^f_{BZ.2}$ and $D^f_{BZ.3}$, represent the fiber

contribution in energy absorption of specimen. With the help of these two parameters,

the equivalent flexural tensile strength can be determined using the following equations:

$$F_2 = \frac{D^f_{BZ.2}}{0.5} \qquad \text{(N)} \qquad \text{Eq.(5.6.a)}$$

$$F_3 = \frac{D^f_{BZ.3}}{2.5} \qquad \text{(N)} \qquad \text{Eq.(5.6.b)}$$

where F_2 and F_3 are mean force corresponding to of $D^f_{BZ.2}$ and $D^f_{BZ.3}$. The moment

resulted from these forces at mid span of the prisms are determined using **Equation

5.7.a** and **Equation 5.7.b** respectively.

$$M_2 = \frac{F_2}{2} \cdot \frac{L}{2} = [\frac{D^f_{BZ.2}}{0.5}]\frac{L}{4} \qquad \text{(N.mm)} \qquad \text{Eq.(5.7.a)}$$

$$M_3 = \frac{F_3}{2} \cdot \frac{L}{2} = [\frac{D^f_{BZ.3}}{2.5}]\frac{L}{4} \qquad \text{(N.mm)} \qquad \text{Eq.(5.7.b)}$$

Finally, the equivalent flexural tensile strength $f_{eq,2}$ and $f_{eq,3}$ are determined using the

following equations:

$$f_{eq,2} = \frac{3}{2} \cdot [\frac{D^f_{BZ.2}}{0.5}]\frac{L}{b.\,h^2_{sp}} \qquad \text{(N/mm}^2\text{)} \qquad \text{Eq.(5.8.a)}$$

$$f_{eq,3} = \frac{3}{2} \cdot [\frac{D^f_{BZ.3}}{2.5}]\frac{L}{b.\,h^2_{sp}} \qquad \text{(N/mm}^2\text{)} \qquad \text{Eq.(5.8.b)}$$

The other four parameters representing the residual flexural tensile strength $f_{R,i}$ at

the beam mid span are determined using following **Equation 5.9**. They are calculated

at deflections of $\delta_{R,i}$ of 0.46 mm, 1.31 mm, 2.15 mm and 3.0 mm. Again, it is assumed

that the stress distribution obeys the pattern shown in **Figure 5.17**. In order to studying

the deflection-CMOD relation, **Figure 5.19** is presented. It can be seen that four values

of $\delta_{R,I}$, correspond to CMOD of 0.39 mm, 1.17 mm, 1.95 mm and 2.72 mm respectively.
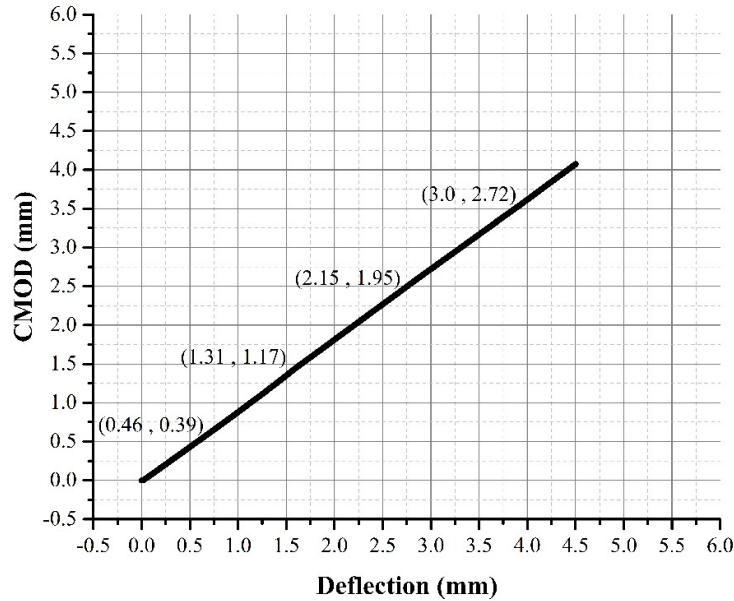
Figure 5.19: Relation between CMOD and Deflection for EEUHPC.

$$f_{R,i} = \frac{3. F_{R,i}. L}{2. b. h_{sp}^{2}} \qquad (\text{N/mm}^2) \qquad \text{Eq.(5.9)}$$

where $F_{R,i}$ is the load corresponding to $\delta_{R,i}$. As stated in (RILEM TC 162-TDF, 2002),

$f_{eq,2}$ or $f_{R,1}$ deal with serviceability state while $f_{eq,3}$ or $f_{R,4}$ are related to ultimate limits.

$D^b{}_{BZ}$, $D^f{}_{BZ.2}$ and $D^f{}_{BZ.3}$ for EEUHPC are 0.5679 kN.mm, 2.54 kN.mm and 10.71

kN.mm respectively. According to all these definitions and equations, the results are

depicted in **Table 5-5**.

Table 5-5: 3-point flexure test results (N/mm^2) for EEUHPC.

$f_{fct,L}$	$f_{eq,2}$	$f_{eq,3}$	$f_{R,1}$	$f_{R,2}$	$f_{R,3}$	$f_{R,4}$
15.3	25.4	21.42	24.4	21.5	18.9	16.8

5.6 Direct tensile test

Three rectangular specimens with dimensions of 5x25 cm^2 and thickness of 2.5 cm were casted and cured based on NC curing method. Two opposite sides of specimens were rectified one day before test until 2 cm of thickness was obtained. After the surface of specimens became dry in laboratory condition, two end plates of 70x50x3 mm^3 were glued to both ends of specimens' tips by means of epoxy resin. Then, they were fixed using a jig until to the next day to avoid any misalignment. Two LVDTs where installed on two opposite sides of the specimens. The test setup is illustrated in **Figure 5.20**. It should be noted that the samples are un-notched in order to evaluate its eventual multi-cracking behavior under tension. The tests were controlled with a displacement rate of 3 μm/s for the machine. The load-displacement and stress-displacement curves are presented in **Figure 5.21**.

Figure 5.20: Direct tensile test setup.

The results demonstrated that just one crack occurred on all three samples which could be the result of the minimum fiber content by 1% (V_f). After finishing the test, the precise dimensions of specimens in cracking section were determined in order to calculate the tensile strength. The load-CMOD and stress-CMOD curves are depicted in **Figure 5.21**. According to this diagrams, the coordinates of average CMODs, loads and strengths corresponding to first cracking and ultimate post-cracking states are (0.019 mm, 4.51 KN, 4.45 MPa), (0.1822 mm, 8.09 KN, 7.94 MPa) respectively.
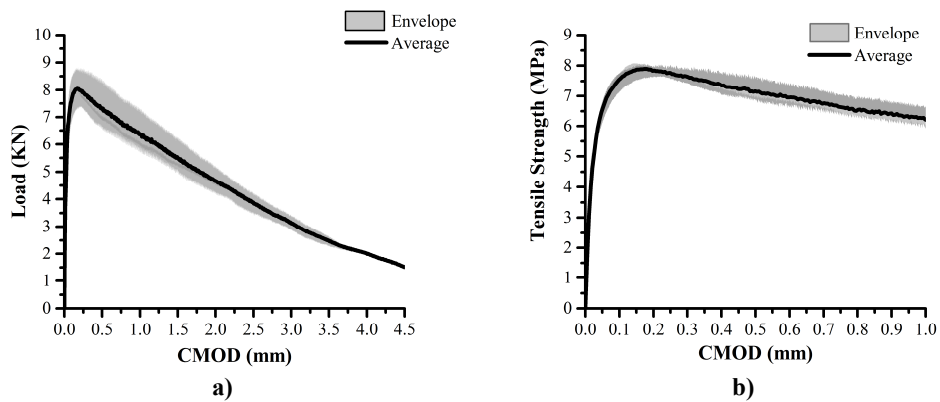
Figure 5.21: Load-CMOD (a) and Tensile strength-CMOD (b) in direct tensile test.

5.7   Chloride ion migration

Beside the test results regarding fresh rheology and mechanical tests, durability-related tests also play a significant role in developing any eco-efficient material. The first test performed in this research to evaluate the durability of EEUHPC, is accelerated non-steady-state chloride migration test to find out its diffusion coefficient based on a Portuguese specification (LNEC E463, 2004), which is based on NT BUILD 492 (1999). Based on definition provided in this standard, migration is related to flow of ions as a result of an external electrical source while diffusion is the action of flow of ions resulted from differences of ion concentration in two opposite sides of a material (NT BUILD 492 , 1999). For this aim, three cylindrical specimens

with dimeter and thickness of 10cm and 5cm respectively were cut from 28-days NC

cylinders having 20cm height and 10cm diameter. Then the surface-dried samples were

placed in a vacuum chamber with a pressure of 1-5 k.Pa for 3 hours. In the following

step, the chamber was filled with a solution of $Ca(OH)_2$ while the vacuum pump was

working. All parts of the samples should be immersed completely in the solution.

Afterwards, the air valve was opened to let the air enter into the chamber. The

specimens were remained in this situation for more 18 ± 2 hours. The next step was to

prepare cathodic solution with a ratio of 100g NaCl in 900 g of water and anode solution

with a ratio of approximately 12 g NaOH in 1 liter of water. The cathode reservoir was

filled with NaCl solution and the specimens were then fixed tightly with two stainless

steel clamps in silicon tubes in order to prevent any leakage of NaOH or NaCl to the

opposite side. The test setup is shown in **Figure 5.22**.
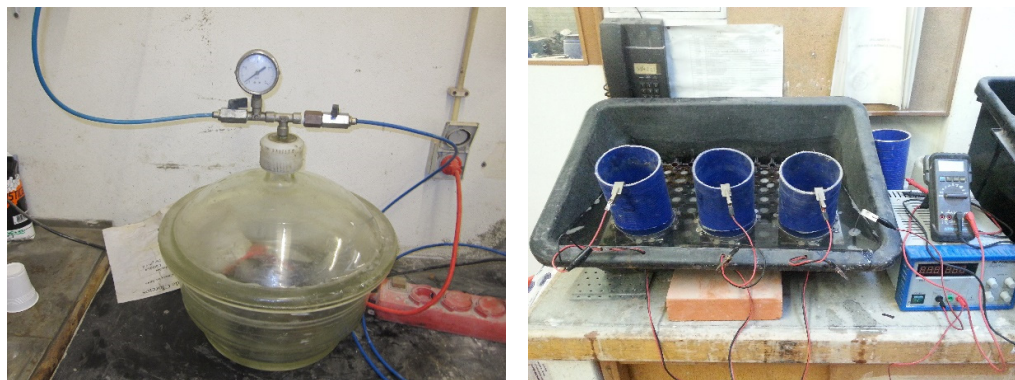
Figure 5.22: Chloride-ion- migration test setup.

After that the specimens were placed in the cathodic reservoir, the anode solution

was poured on the top of silicon tubes and the power supply was connected with a

primary voltage of 30 V. The initial current flow was 264 µA in average which is lower

that 5mA indicating high resistivity of the material to current flow. According to the

Portuguese specification (LNEC E463, 2004) the final voltage as well as test duration

were adjusted to 60 V and 96 hours respectively due to second average initial current

flow of 661 μA which was still lower than 10 mA. After the adjustments, the cathodic container was covered with a plastic sheet in order to prevent fast water lose due to evaporation. After 96 hours one of the samples was washed, dried and splitted into two pieces. The final step was to spray $AgNO_3$ solution to the broken surface of specimen to evaluate the chloride ion penetration depth. According to **Figure 5.25** it was observed that however the steel fibers within UHPC seems to have negative impacts through providing paths to complete an electric circuit, this did not happen and no chloride penetration depth after 96 hours was observed as a result of very dense matrix of EEUHPC. With respect to this result, it was decided to continue the test for more 10 days. After totally 14 days, the two other specimens were divided into two sections and the solution of $AgNO_3$ was sprayed on their surfaces. The results were the same as the previous sample. Not only no penetration depth was observed, but also the corrosion of steel fibers was not a matter of concern since it was detected only in the surface layer of the specimens (see **Figure 5.23**). In addition, the color of cathodic solution in the reservoir had not been changed too much as the result of steel fiber corrosion as shown in **Figure 5.24.**

Figure 5.23: corrosion of specimens' surface.

<div align="center">(a)   (b)</div>

Figure 5.24: The cathodic solution at the beginning (a) and after 14 days in 60 V (b).
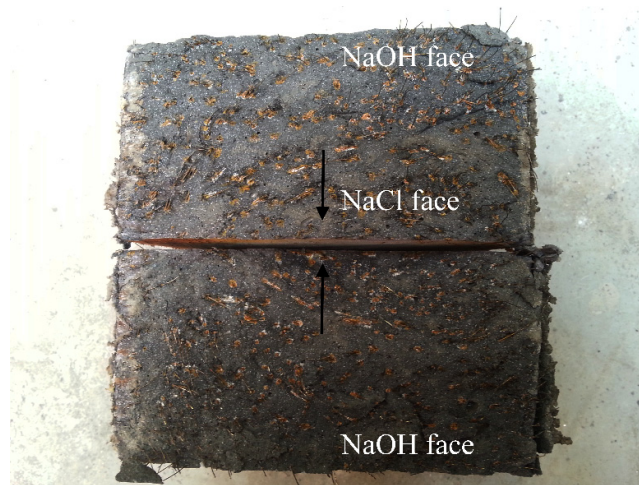
Figure 5.25: A broken and AgNO$_3$-sprayed specimen after 14 days of chloride migration test in 60V.

The diffusion coefficient based on this test method is determined using the following equation:

$$D = \frac{0.0239(273 + T) \times L}{(U - 2) \times t} \cdot \left[x_d - 0.0238\sqrt{\frac{(273 + T) \times L \times x_d}{U - 2}} \right] \qquad \text{Eq.(5.10)}$$

where D is the diffusion coefficient in 10^{-12} m^2/s, T is the average value of initial and final temperature in anolyte in °C, U is the absolute value of the applied voltage in V, L is the thickness of the specimen in mm, x_d is the average of penetration depth in mm and t is the duration of the test in hours. Since just the exterior face of the samples are

contaminated with chloride solution without any penetration depth, the thickness of the surface was measured using ImageJ software (Rasband, 2008) and considered as penetration depth. It should be noted that ImageJ is an image processing and analysis program, which is written in Java. The average of penetration depth in eight measured points was 0.096 mm, which corresponds to a very small diffusion coefficient value extremely close to zero and considered as zero.

5.8 Carbonation

The carbonation test described here is in accordance with European Technical Specification for accelerated carbonation test (FprCEN/TS 12390-12, 2010). The prismatic specimens with dimensions of 4cm x 4cm x 16 cm of 28-days NC were used for this test. After curing period, the samples were conditioned in laboratory (20°C and 55±5 % RH) for 14 days. Then, all faces of the prism except two faces were sealed using melted paraffin and were placed in carbonation chamber with (4±0.5)% CO_2 concentration, temperature of (20±2)°C and (55±5)% RH for at least 70 days. A phenolphthalein solution was used as the PH indicator and was sprayed on the crashed surface of the specimens. The un-carbonated parts of concrete remain in purple color as a measure to determine the depth of carbonation. Since, no carbonation depth was observed as shown in **Figure 5.26**, the test was continued until 77, 103, 144 and 191 days from starting date of placing the specimens in the carbonation chamber. In each test age, a 5 cm-section of the prism was broken and the end surface of the remained prism was sealed again and was returned to the carbonation chamber.
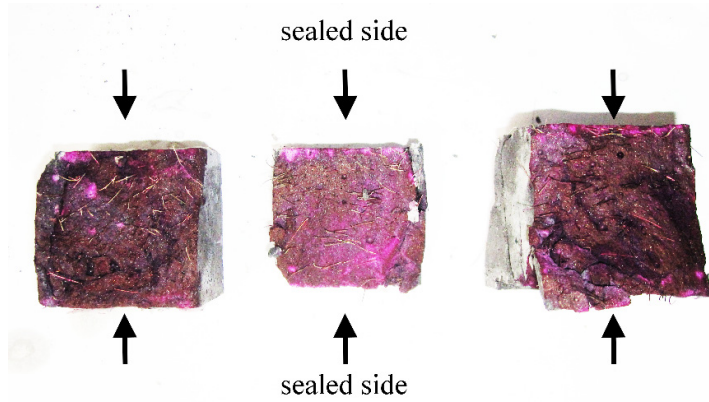
Figure 5.26: carbonated specimens after 70 days.

As can be seen from **Figure 5.26**, a very thin layer on the right and left surface of the samples is carbonated. The other samples with higher exposure time in carbonation chamber also did not demonstrate more carbonation depth as depicted in **Figure 5.27** due to very dense matrix of EEUHPC indicating extremely high durability of the developed material against carbonation action.

a)   b)   c)
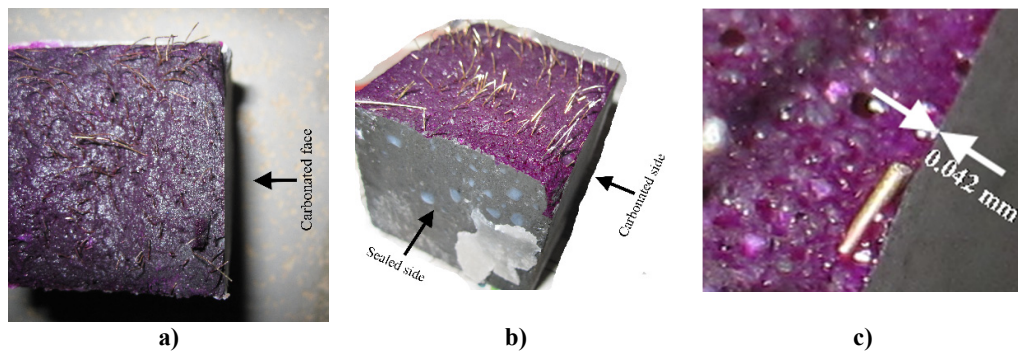
Figure 5.27: Carbonated specimens after 103 days (a) and 144 day (b) and the carbonated surface thickness after 144 days (c).

By measuring the thickness of the carbonated surface by using ImageJ software, it is 42 μm after 191 days of carbonation as shown in **Figure 5.27**.

5.9   Water absorption

5.9.1   Water absorption by immersion

This test was performed according to (ASTM C642 – 97, 1997). Prismatic samples were prepared for optimization with RSM. They were divided into two pieces for water absorption by immersion as well as capillary tests. The reason behind using the RSM was to investigate the effect of different composition on water absorption. First, all the specimens were dried in oven with 100°C. Then they were cooled in dry air and their weight was determined. Again, the samples were returned back to the oven for another 24 hours and they were weighted for the second time. This process was repeated until the difference of two successive values were lower than 0.1% of the previous weight. Afterwards, the final weight was registered as A and the samples were immersed in water (20±2)°C for at least 48 hours when the two consecutive weights of surface-dried samples are less than 0.1% of the lesser one. The saturated-surface-dry (SSD) mass of specimens was recorded as B. After, the samples were placed in boiling water for minimum 5 hours and then conditioned in laboratory condition as cooling period for at least 14 hours. The weight of soaked, boiled, surface-dried mass designated as C. The final step was determining the immersed-apparent mass by suspending the specimens in water through a basket and registering the related mass as D. According to **Equation 5.11**, the following calculations were performed.

$$\text{Absorption after immersion (AAI)}, \% = \frac{B - A}{A} \times 100 \qquad \text{Eq.(5.11.a)}$$

$$\text{Absorption after immersion and boiling (AAIB)}, \%$$
$$= \frac{C - A}{A} \times 100 \qquad \text{Eq.(5.11.b)}$$

$$\text{Bulk density, dry } (g_1) = \frac{A}{C - D} \times \rho \qquad \text{Eq.(5.11.c)}$$

$$\text{Bulk density after immersion (BDAI)} = \frac{B}{C - D} \times \rho \qquad \text{Eq.(5.11.d)}$$

$$Bulk\ density\ after\ immersion\ and\ boiling\ (BDAIB) = \frac{C}{C - D} \times \rho \qquad Eq.(5.11.e)$$

$$Apparent\ density\ (g_2) = \frac{A}{A - D} \times \rho \qquad\qquad\qquad Eq.(5.11.f)$$

$$Volume\ of\ permeable\ pore\ space\ (voids), \% = \frac{g_2 - g_1}{g_2} \times 100 \qquad Eq.(5.11.g)$$

where A is the mass of oven-dried sample in air (g), B is mass of surface-dry sample in air after immersion (g), C is mass of surface-dry sample in air after immersion and boiling (g), D is apparent mass of sample in water after immersion and boiling (g), g_1 is bulk density in dry state, g/cm^3, g_2 is apparent density, g/cm^3 and ρ is density of water (g/cm^3). The calculated results are depicted in **Table 5-6**.

Table 5-6: The test results for water absorption by immersion for different compositions.

	A	B	C	D	AAI	AAIB	g₁	BDAI	BDAIB	g₂	voids
R1	267.09	270.156	270.276	156.72	1.15%	1.193%	2.3521	2.3791	2.3801	2.4200	2.806%
R2	310.12	314.335	314.514	183.89	1.36%	1.417%	2.3741	2.4064	2.4078	2.4568	3.364%
R3	299.258	302.321	302.42	176.21	1.02%	1.057%	2.3711	2.3954	2.3962	2.4320	2.505%
R4	273.968	276.78	276.799	161.74	1.03%	1.033%	2.3811	2.4055	2.4057	2.4412	2.460%
R5	268.167	272.151	272.204	158.23	1.49%	1.505%	2.3529	2.3878	2.3883	2.4393	3.542%
R6	230.634	234.711	234.868	136.63	1.77%	1.836%	2.3477	2.3892	2.3908	2.4534	4.310%
R7	286.591	294.44	294.478	169.95	2.74%	2.752%	2.3014	2.3644	2.3648	2.4570	6.334%
R8	246.105	251.054	251.207	146.51	2.01%	2.073%	2.3506	2.3979	2.3994	2.4711	4.873%
R9	227.051	230.229	230.282	134.18	1.40%	1.423%	2.3626	2.3957	2.3962	2.4448	3.362%
R10	286.898	290.499	290.625	169.31	1.26%	1.299%	2.3649	2.3946	2.3956	2.4399	3.072%
R11	258.744	261.872	262.009	152.32	1.21%	1.262%	2.3589	2.3874	2.3887	2.4313	2.977%
R12	290.357	293.898	294.064	171.24	1.22%	1.277%	2.3640	2.3928	2.3942	2.4376	3.018%
R13	262.692	266.195	266.199	154.24	1.33%	1.335%	2.3463	2.3776	2.3776	2.4222	3.132%
R14	248.307	251.922	252.07	146.74	1.46%	1.515%	2.3574	2.3917	2.3931	2.4448	3.573%
R15	294.246	297.796	297.931	173.82	1.21%	1.252%	2.3708	2.3994	2.4005	2.4434	2.969%
R16	284.045	288.914	289.186	165.85	1.71%	1.810%	2.3030	2.3425	2.3447	2.4032	4.168%
R17	268.602	271.714	271.964	158.54	1.16%	1.252%	2.3681	2.3956	2.3978	2.4405	2.964%
R18	245.053	251.349	251.613	146.78	2.57%	2.677%	2.3376	2.3976	2.4001	2.4936	6.258%
R19	298.353	302.072	302.246	176.34	1.25%	1.305%	2.3696	2.3992	2.4006	2.4453	3.092%
R20	267.065	269.991	270.053	156.53	1.10%	1.119%	2.3525	2.3783	2.3788	2.4161	2.632%
R21	295.22	298.364	298.436	173.5	1.06%	1.089%	2.3630	2.3881	2.3887	2.4254	2.574%
R22	230.539	236.607	236.782	136.83	2.63%	2.708%	2.3065	2.3672	2.3690	2.4602	6.246%
R23	274.4	277.452	277.585	161.83	1.11%	1.161%	2.3705	2.3969	2.3980	2.4376	2.752%
R24	258.403	261.737	261.877	152.64	1.29%	1.344%	2.3655	2.3960	2.3973	2.4432	3.180%
R25	306.968	311.622	311.736	181.12	1.52%	1.553%	2.3502	2.3858	2.3867	2.4392	3.650%
R26	285.877	288.553	288.656	168.54	0.94%	0.972%	2.3800	2.4023	2.4031	2.4364	2.314%

As can be seen the EEUHPC developed in this research, nominated as R_{26} in the table, demonstrates the lowest water absorption in all the cases as well as lowest permeable voids compared to other compositions with values of 0.94%, 0.97% and 2.314% corresponding to AAI, AAIB and voids respectively.

5.9.2   Water absorption by capillarity

As mentioned above, the other half of the prismatic specimens, prepared based on RSM compositions, were utilized here for capillary water absorption. This test was performed in accordance with (LNEC E393, 1993) which is similar to ASTM (ASTM C1585 – 04, 2004). The samples were placed in oven with temperature of (40±5)°C for 14 days. Afterwards four edges of the specimens were sealed using silicon paste to avoid any water absorption from other surfaces of specimens instead of the bottom face. After 24 hours of applying the sealant paste, the mass of specimens were measured and registered as M_0. Then they were placed in a water container in laboratory condition of (20±2)°C and humidity of (65±5) % RH. Their mass were determined according to the **Equation 5.12**.

$$I = \frac{m_t}{a.d} \qquad\qquad\qquad \text{Eq.(5.12)}$$

where I is the absorption in mm, m_t is the change in mass of specimen in different time intervals in gram compared to the initial mass (M_i-M_0), a is the area of exposed cross section of specimen to water in mm^2, and d is density of water in g/mm^3 (0.001 g/mm^3). The results of the test, the corresponding time intervals and the rate of absorption (sorptivity) are presented in **Annex II**. The capillary water absorption trends of all the compositions are also depicted in **Figure 5.28**. The slopes of linear fitted lines to each of these trends, representing their rate of capillary water absorption (ASTM C1585 –

04, 2004), are provided in **Figure 5.29** as well. As can be seen from both figures, R_1,
R_4, R_{11}, R_{24} and R_{26} demonstrate the lowest capillary water absorption after 16 days of
exposure with a quantity of 0.44 mm as well as lowest sorptivity compared to other
compositions with a maximum value of 5E-4 mm/s$^{1/2}$.
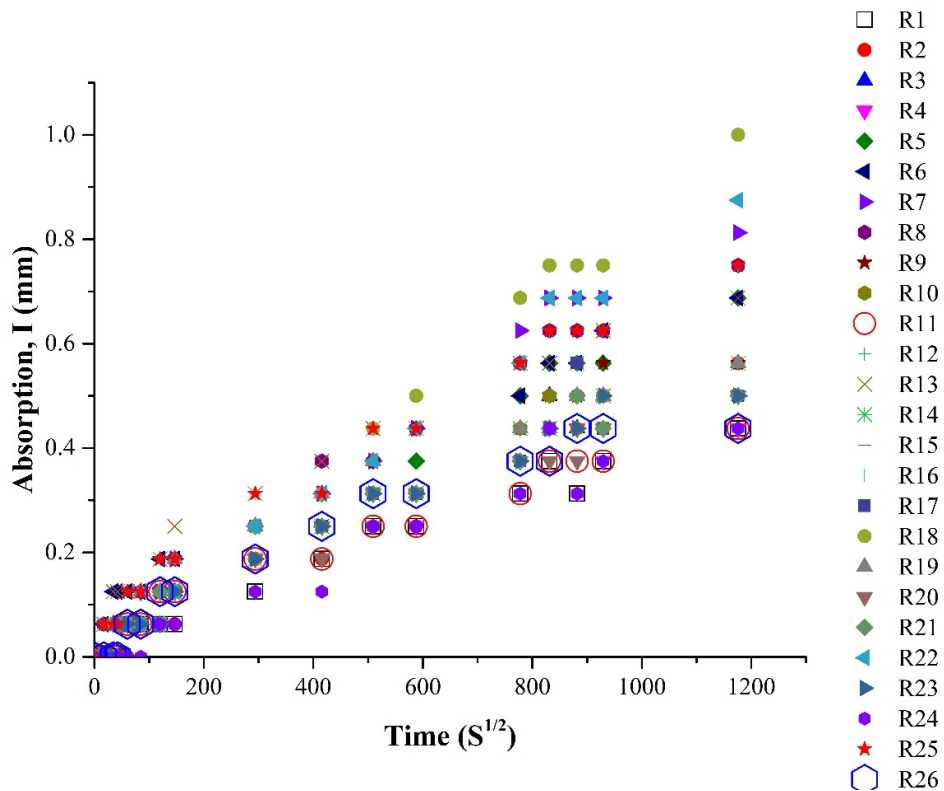
Figure 5.28: Water absorption by capillary (mm) for different compositions of Chapter 4.

By plotting both AAIB and sorptivity in the same graph (see **Figure 5.29**), it can be
observed that both of diagrams follow almost the same trend indicating a good
correlation between capillary and immersed water absorption of the compositions.
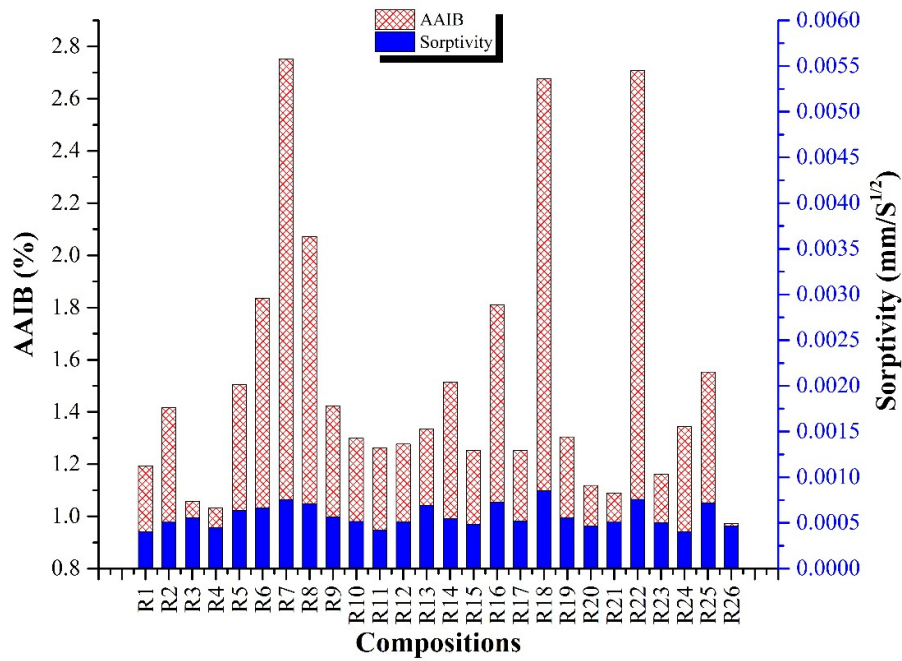
Figure 5.29: AAIB and sorptivity trends for different compositions.

5.9.3   Effect of constituent materials on water absorption

In Chapter 4 the effect of the main ingredients of UHPC, those are SF, UFFA and sand, on the main response variables, namely C.S. and F.D. those have great influence on the other characteristics of the material such as modulus of elasticity or flexural strength, were studied. In fact, the effect of the constituent materials on water-absorption ability of the UHPC is in second order of priority and is beyond the aim of this research, which was just to study the water-absorption behavior of developed EEUHPC, R_{26}, as observed in **Figure 5.29**. Nevertheless, it would be interesting to survey the effect of different constituents on water-absorption characteristics of the concrete developed herein briefly, based on the RSM explained in Chapter 4 through a statistical-based study. In this regard, 26 combinations with their corresponding responses, namely AAIB as well as I after 16 days, (see **Table 5-7**) were

analyzed with the same procedure explained in Chapter 4.

Table 5-7: All variables and their corresponding values for RSM.

Run	A:SF	B:UFFA	C:Sand	AAIB (%)	I (mm)
1	0.100	0.300	1.800	1.193	0.437
2	0.100	0.300	1.300	1.417	0.563
3	0.100	0.650	1.800	1.057	0.562
4	0.100	0.475	1.550	1.033	0.437
5	0.000	0.650	1.800	1.505	0.688
6	0.050	0.300	1.550	1.836	0.687
7	0.000	0.300	1.800	2.752	0.813
8	0.000	0.475	1.550	2.073	0.750
9	0.050	0.475	1.550	1.423	0.562
10	0.050	0.475	1.550	1.299	0.500
11	0.050	0.475	1.800	1.262	0.437
12	0.050	0.475	1.550	1.277	0.500
13	0.050	0.650	1.550	1.335	0.688
14	0.050	0.475	1.300	1.515	0.563
15	0.050	0.475	1.550	1.252	0.500
16	0.000	0.650	1.300	1.810	0.750
17	0.050	0.475	1.550	1.252	0.500
18	0.000	0.300	1.300	2.677	1.000
19	0.050	0.475	1.550	1.305	0.563
20	0.100	0.650	1.300	1.119	0.500
21	0.100	0.650	1.700	1.089	0.500
22	0.000	0.300	1.700	2.708	0.875
23	0.100	0.300	1.700	1.161	0.500
24	0.050	0.470	1.500	1.344	0.438
25	0.000	0.650	1.700	1.553	0.750
26	0.090	0.570	1.760	0.972	0.438

The models for two responses were evaluated. For both responses, a quadratic model was suggested. The summary results of ANOVA analysis after backward insignificant term removal are presented in **Table 5-8** exhibiting a significant model with an insignificant lack-of-fit. In addition, according to diagnostics no transformation was required for both models. Besides that, Pred-R-Squared and Adj-R-Squared are in reasonable agreement to each other (**Table 5-9**).

Table 5-8: Proposed model for AAIB and I by ANOVA.

	AAIB	P-value	I	P-value
Intercept	5.394856	-	+2.83392	-
SF	-29.1067	< 0.0001	-5.58738	< 0.0001
UFFA	-9.12863	< 0.0001	-6.35592	0.0071
Sand	-0.3225	0.0022	-0.53549	0.0075
SF*UFFA	26.34228	< 0.0001	+5.39248	0.0016
SF*Sand	-	-	-	-
UFFA*Sand	-	-	+0.79646	0.0295
SF^2	65.88108	0.0009	-	-
$UFFA^2$	6.3879	0.0002	+4.88639	< 0.0001
$Sand^2$	-	-	-	-

Table 5-9: ANOVA results for full regression models.

Responses	Adj-R^2	Pre-R^2	Model		Lack of fit	
			F-Value	P-Value	F-Value	P-Value
AAIB	0.97702	0.96124	178.1883	< 0.0001	1.651765	0.3028
I	0.9137	0.8839	45.10	< 0.0001	2.25	0.1895

For better understanding of the effect of constituent materials, two perturbation graphs are presented in **Figure 5.30**. As indicated, by increasing the SF content the water-absorption reduces significantly. Sand does not show a considerable influence in water absorption. UFFA up to its middle range which is 0.475 w_t% to cement, improves the material with respect to lower water absorption but in higher contents affects just I to some extent. For more clarification regarding the interaction of SF and UFFA on both responses, **Figure 5.31** is presented. This was the reason that R_7, R_{18} and R_{22} demonstrated the worst behavior regarding water absorption in both tests. In other words, these three compositions with silica fume and UFFA quantities of 0 and 0.3 (w_t% to cement) respectively, which is their minimum level, exhibited the highest water absorption. The next worst compositions as shown in **Figure 5.29** are R_6, R_8 and R_{16} again as the result of minimum level of SF and UFFA. On the other hand, compositions such as R_4 or R_{26} with very high SF and UFFA content revealed very low water absorption in both tests compared to other mixtures. This shows the importance of fine

binders in improvement of durability of materials. In other words, the finer the binder

is, the more durable the concrete would be.

Design-Expert® Software

AAIB

Actual Factors
A: SF = 0.050
B: UFFA = 0.475
C: Sand = 1.550

Perturbation
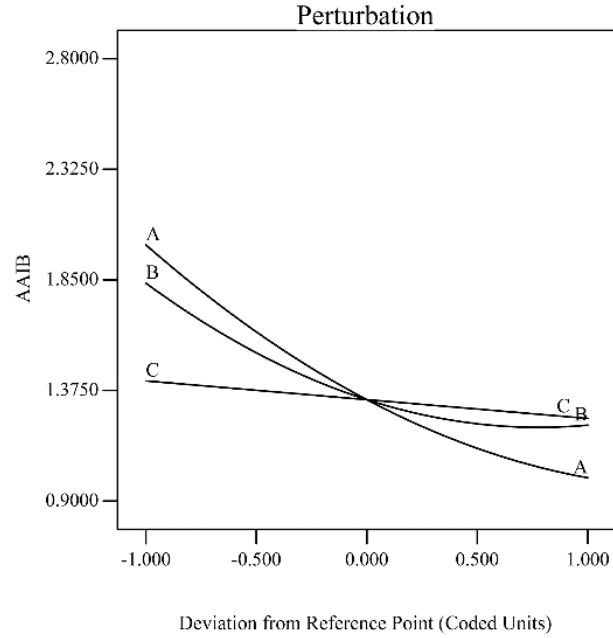
a)

Design-Expert® Software

I

Actual Factors
A: SF = 0.050
B: UFFA = 0.475
C: Sand = 1.550

Perturbation
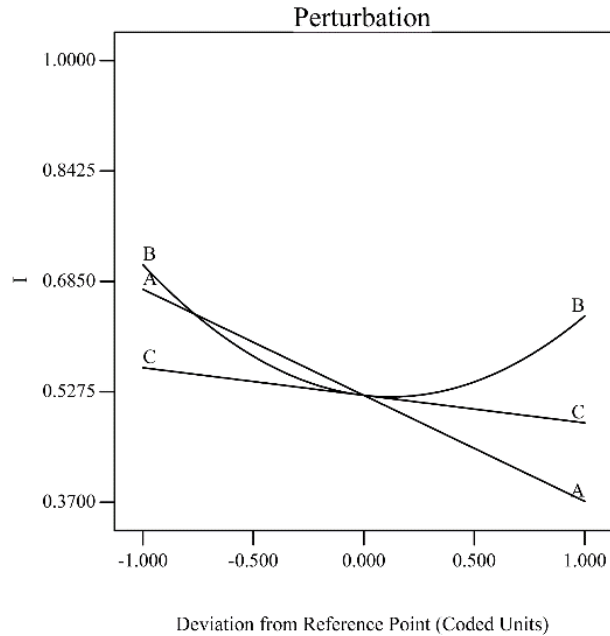
b)

Figure 5.30: Effect of constituent materials on AAIB (a) and I (b).
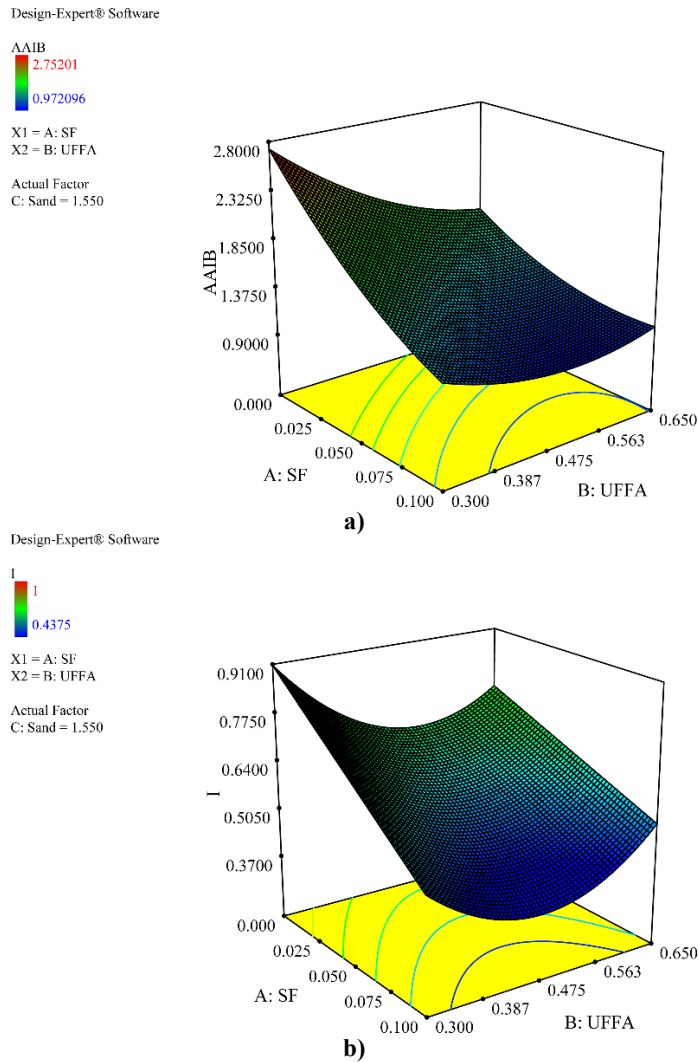
Figure 5.31: 3D representation of SF-UFFA effect on AAIB (a) and I (b).

5.10 Steel fiber distribution

The final stage in material characterization of EEUHPC was to study its fiber

distribution. The main goal is to see if the fibers are distributed uniformly along the

height and the length of the specimens or they have been segregated at the bottom or at

one end. Based on the research performed recently some authors studied the effect of

flow on fiber distribution and orientation in beams (Stähli, et al., 2008). According to

their findings if we can align the fibers in the same direction of applied stress, the

mechanical performance of the concrete could be improved. They also found that the

orientation of fibers was highly influenced by the viscosity of concrete as well as its

flow direction. **Figure 5.32** shows how the authors explained the fibers' alignment along flow direction of fresh concrete as well as the lower speed of flow in vicinity of mold due to friction forces.
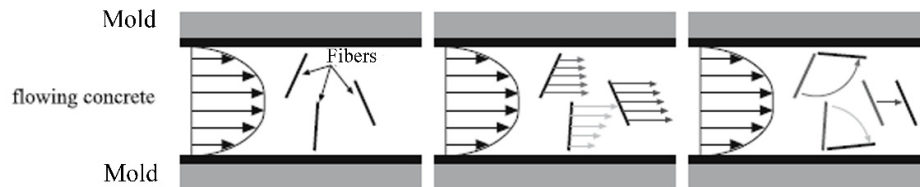
Figure 5.32: Fiber alignment in flow direction of fresh concrete (Stähli, et al., 2008).

Although, there are numerous studies representing different method of assessing fiber orientation, distribution and segregation using advanced theoretical and experimental procedures and their relevant factors (Abrishambaf, 2015), for the aim of this research, image analysis method has been applied (Cunha, 2010). For this aim, three cross sections from each one of 10 prismatic specimen of 4x4x16 cm^3 were splitted. It should be noted that the density of fibers was also studied in three regions of h_1, h_2 and h_3 in each cross section as shown in **Figure 5.33**.
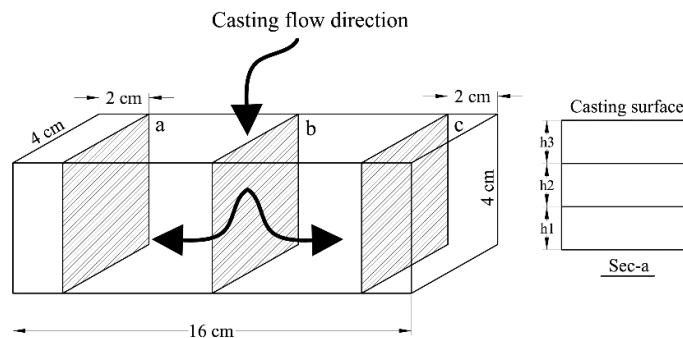
Figure 5.33: Flow direction and places of sections in the prisms.

After cutting the sections, their surfaces were grinded in a grinding machine (see

Figure 5.34) using a very fine sandpaper.

Figure 5.34: Grinding machine before image processing.

Afterwards, the all surfaces were polished and lubricated with vaseline to enhance

the reflective effect of steel fibers and make the concrete surface darker. Later, a color

image was taken from each of sections with a high-resolution digital camera (Canon

Digital IXUS 100 IS, 12.1 M.Pix.) and the images were processed through ImageJ

software (Rasband, 2008). The processing steps include different tasks as shown in

Figure 5.36. First a scale was set to the image. The image was cropped and duplicated.

The fibers were filtered using threshold adjustment in order to filter the fibers from the

concrete matrix. The process was followed by converting the filtered image to a mask.

The next step was to remove any noise due to light reflections from sand particles or

even steel fibers. It was easily performed through a median filter process however, in

some cases it was not applied to keep enough accuracy. Then, in order to separate some

jointed fibers in the image the Watershed command was applied and finally the best

ellipse was fitted on each fiber and the image was analyzed to determine the number of

fibers in three sections along the prism as well as its height. The effect of these steps

can be seen in both **Figure 5.36** and **Figure 5.37**. It should be noted that, during the

analyzing step, the particles with area less than 0.0314 mm², corresponding to area of a

fiber completely perpendicular to the surface, were not taken into consideration. The

other measure, which is useful to understand how the fibers are aligned along the

specimen, is to define their circularity index. By definition, circularity of a fiber is

defined using following equation (Ferreira & Rasband, 2012):

$$Circularity = 4\pi \times \frac{[Area]}{[Perimeter]^2}$$

Eq.(5.13)

In fact, the higher the circularity is, the particles are more perpendicular to the

surface and more horizontally are distributed along the specimens. In this regard, in the

last analyzing step, the number of fibers with circularity between 0.5 and 1.0 were

determined with ImageJ software and the particles with lower circularity were ignored.

For more clarification, two fibers with low and high circularity are shown in

Figure 5.35.
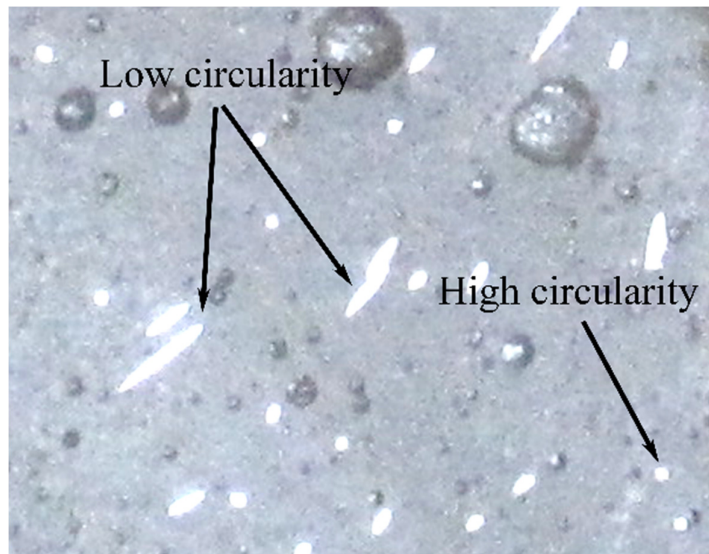
Figure 5.35: Differentiation between fibers' cross sections with low and high circularity.
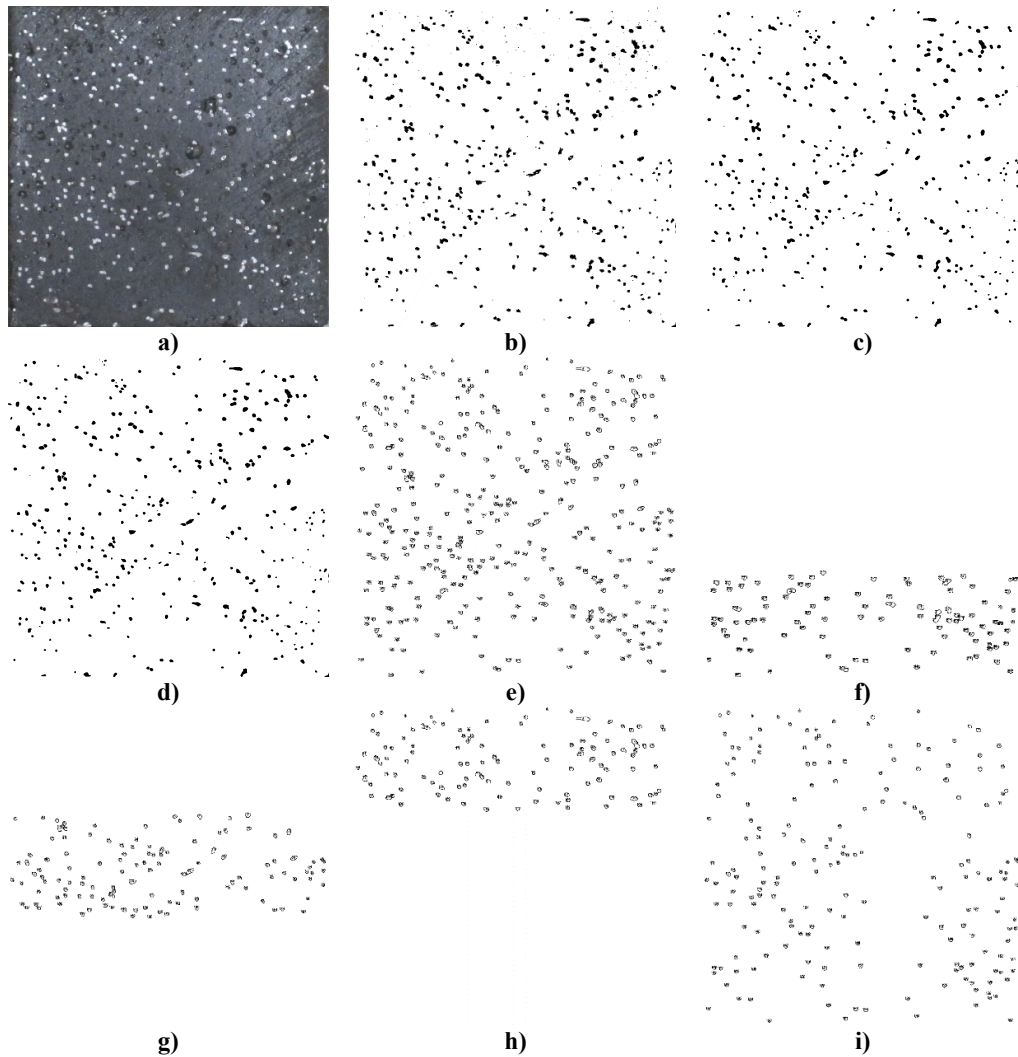
Figure 5.36: Cropped original image (a), Adjusted threshold and converted image to mask (b), median filtered (c), image after watershed (d),   Analyzed particles using fitted ellipses (e), analyzed particles in h_1 (f), Analyzed particles in h_2 (g), Analyzed particles in h_3 (h), analyzed particles with circularity of 0.95 to 1.0 (i).
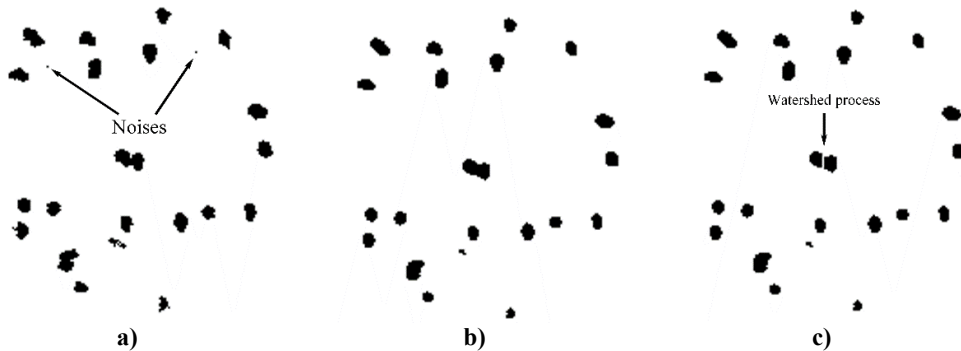
Figure 5.37: 1000X magnified images after threshold adjustment (a), median filtering (b) and watershed processing (c).

Based on the results provided in **Table 5-10**, the fibers are distributed almost equally

along the length of prisms with approximately 300 fiber-cut in each section. In addition,

the fibers are also perfectly distributed along the altitude of the prisms in a range of 90

to 104 fibers in each one-third of the specimens' height in a ratio of 30.1%, 32.8% and

34.5% in h_1, h_2 and h_3 respectively. This shows that the fibers are not segregated and

sediment due to gravity or external vibration. This could be the result of very dense

matrix of the material as well as very small size of the fibers with low weight making

them unwilling for any segregation.

Table 5-10:   Results of fiber distribution along the length and height of samples.

	Fibers in each section	Fibers in Sec-a	Fibers in Sec-c	Fibers in Sec-b	Fibers in h1	Fibers in h2	Fibers in h3
Average	300.3	294.2	294.2	312.4	90.3	98.4	103.6
St.Dev.	36.5	34.4	34.4	39.4	22.2	20.15	19.67
% to 3 sections	33.3%	32.7%	32.7%	34.7%	10%	10.9%	11.5%
% to each section	-	98%	98%	104%	30.1%	32.8%	34.5%

The results from circularity analysis exhibit that the fibers are very well aligned

horizontally along the length of specimens, which would be beneficial for any

load-bearing purposes.
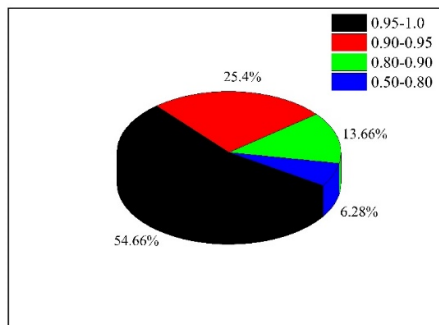
Figure 5.38: The fraction ratio of fibers with different circularity to total number of fibers in each section.

As can be seen in **Figure 5.38**, around 55% of the fibers in each section demonstrate

a circularity factor in a range of 0.95 to 1.0 and 25% between 0.9 to 0.95. In other

words, totally 80% of fibers in each section have a circularity more than 0.9 which

could be a result of horizontal flow-direction as well as external vibration.

5.11 Conclusion

The main characteristics of EEUHPC was discussed in this chapter. The material revealed very good mechanical as well as durability–related characteristics having lower silica fume and steel fiber compared to well-known commercially available products such as Ductal®. The fresh behavior of the material ensured the self-compacting ability of the material. The final compressive strength of normal-cured samples were slightly higher than tempered-water cured samples with a quantity of 172 MPa and 166 MPa respectively nevertheless TWC samples after 48 hours of curing exhibited higher compressive strength of 160 MPa, which is 96% of their final strength, compared to strength of 28-day NC specimens with 152 MPa.

Regarding durability, it was found that the material demonstrates extraordinary resistance against chloride ion penetration and carbonation. Although very low when compared to other types of concrete, showing a completely different order of magnitude, the water-absorption ability of the material was found highly influenced by the silica fume and UFFA content. The more silica fume is consumed the less willingness the concrete shows to water absorption in both capillary and immersion test. On the other hand, sand content does not have any significant effect on water absorption. UFFA in its middle range, around 0.475 to cement weight, causes the lower water absorption. The EEUHPC exhibited 4.69E-04 mm/s$^{1/2}$ of sorptivity and 0.972% of water absorption after immersion and boiling.

Fiber distribution along the length and height of specimens were also studied carefully. They were perfectly distributed and aligned horizontally without any segregation and sedimentation. Almost one third of fibers in each cross section were

distributed in one third of the section altitude. Furthermore, the number of fiber-cuts in three sections along the length were almost equal representing the effective distribution of the fibers as a result of self-flowing of the concrete.

For better comparison of the developed material and the most known commercially available UHPC, Ductal®, their relevant characteristics are presented in **Table 5-11**. The developed composition contains 10% and 76% lower cement and silica fume respectively resulting in 66.1 kg/m^3 and 66.3 €/m^3 lower CO_2 content and cost compared to Ductal®. While, its mechanical and durability-related characteristics, even with half quantity of steel fiber, are very close to Ductal®.

Table 5-11: Comparison between developed EEUHPC and Ductal®.

	Unit	EEUHPC	Ductal® (Graybeal, 2006; Voo & Foster, 2010)
Portland cement	kg/m^3	640	712
Fine sand	kg/m^3	1131.2	1020
Silica fume	kg/m^3	56.3	231
UFFA	kg/m^3	361.1	-
Ground quartz	kg/m^3	-	211
Superplasticizer	kg/m^3	25.61	30.7
Accelerator	kg/m^3	-	30
Steel fiber	kg/m^3	78.7	156
Water	kg/m^3	167.1	109
Compressive strength	MPa	166-172	180-225
Modulus of Elasticity	GPa	50.8-56.5	55-58.5
Flexural strength (4-point)	MPa	22.9	30-35
Toughness indices I$_5$		5.169	5.3-6.2
I$_{10}$		11.41	11.8-14.4
I$_{20}$		26.63	25.9-32.8
Tensile strength	MPa	7.94	6.9-10.3
Chloride ion diffusion coefficient	m^2/s	~0 (after 14 days in 60 V)	1.9×10^{-14}
Carbonation depth	mm	0.042 (after 191 days)	<0.5
Density	kg/m^3	2372-2380	2440-2550
CO_2 content	kg/m^3	594.2	660.3
Cost	€/m^3	126.7	193.0

Chapter 6

Self-healing ability of

EEUHPC

S elf-healing ability of any material, particularly UHPC, is an important issue regarding the life cycle of the material and its capacity for structural recovery. The aim of this part of research is to investigate the autogenic-healing capacity of the material, according to RILEM definition provided in Chapter 2 (RILEM Technical Committee 221-SHC, 2013), with the aim of improving the self-healing ability of the material through autonomic healing as a future research. As reviewed in Chapter 2, one of the shortcomings of the test procedures, those studying the recovery of material against environmental actions, is that they are not capable of structural recovery assessment. In other words, these techniques have not the ability to evaluate cracks in depth precisely. Besides that, they may conclude a material is recovered while it has

been just sealed or clogged due to some chemical reactions in its surface. On the other hand, mechanical test methods evaluate the mechanical properties of material before and after healing process through regain in properties such as strength or stiffness. In general, these type of tests can demonstrate less error in verifying the self-healing ability of material. In this regard, three-point bending test for notched specimens was applied in this research to evaluate the energy-absorption capacity of the notched specimens before and after healing process.

6.1   Sample preparation and test procedure

The specimens used for this study were 4x4x16 cm^3 prisms of EEUHPC composition. In order to study self-healing ability of UHPC in its end life, it is necessary to finalize the hydration process of concrete since the crack propagation generally could occur after the ultimate strength development of concrete. This would be of great importance whether the concrete has ability to be healed spontaneously even after finishing its hydration process. For this aim and before starting the main experiment, two different curing method were applied to investigate the effect of curing on long-term behavior of samples as well as their early age with respect to their strength development. For this aim, two different series of specimens with different curing method were prepared. The first group include the 28-days cured specimens based on NC method as explained in Chapter 5. This group is representative of UHPCs that are cracked at their early age and should be self-healed. The second group are specimens cured based on TWC method but with a treatment period of 6 days (144 h) ensuring final-strength gaining of the material equivalent to its long age. After each curing period, six samples from each series were selected. They were cracked through 3-point bending test with a specific crack-mouth-opening displacement (CMOD). Three

samples of each group of curing method and crack size were immediately tested again in 3-point bending test for evaluating their energy absorption after crack propagation and before healing. The other three samples were transferred to a tempered-water bath with a temperature of 67°C for 48 hours. For more clarification, it should be emphasized that the healing process, after crack generating, is similar for all the specimens with different primary curing methods. The energy-absorption capacity of these specimens were quantified after this healing period. Through this methodology, a comparison between self-healing ability of young and old specimens was applicable beside evaluation of crack-size effect on self-healing behavior of EEUHPC. In addition, this healing method, which is similar to steam curing, was evaluated to see if this procedure could be generally used for *in-situ* healing of cracked members or not.

The reason for adopting 3-point bending test for self-healing assessment of the notched prisms is a) to evaluate the energy-absorption capacity of the specimens before and after healing and b) to determine the relationship between CMOD and degree of healing. In fact, in other test methods, such as 4-point bending test or un-notched prisms, due to multi-cracking phenomena it is not possible to achieve this aims. It should be noticed that the displacement rate of the loading machine was adjusted to 3 μm/s.

6.1.1   Crack generation

In the first step, it was decided to study the CMODs of 10 μm, 30 μm, 50 μm, 100 μm, 200 μm to study their effect on self-healing behavior. In fact, these crack sizes are the remained CMODs after loading, cracking and a relaxation period when no more crack closure is observed. For this aim, it was necessary to perform a cyclic 3-point bending test to investigate the relationship between the different initial CMODs and

their corresponding values after relaxation. To achieve this, the machine was launched

with a CMOD controller to different CMODs. Then the load was released and after a

relaxation period, the test was repeated with a new controlled CMOD. For more

clarification, the results of six loading and relaxing cycles are depicted in **Figure 6.1**.

To draw this diagram, the new initial CMODs and their corresponding relaxed values

were summed with the relaxed CMOD from the previous cycle.
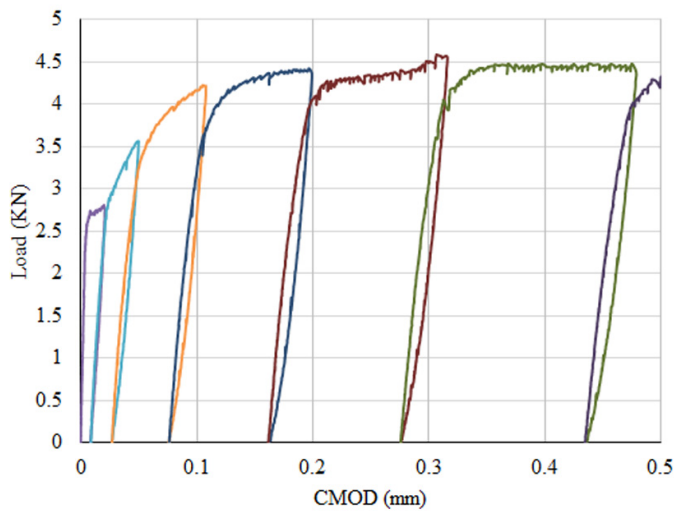
Figure 6.1: Initial and relaxed CMOD in each cycle.

Table 6-1: The relationship between initial and final CMODs after relaxation.

Cycle	Initial CMOD (μm)	Relaxed CMOD (μm)	Relaxation (μm)	Relaxation/ initial CMOD
1	20.8	8.8	12	58%
2	49.9	27	22.9	46%
3	107.8	76.4	31.4	29%
4	199.2	161.7	37.5	19%
5	315.9	275.8	40.1	13%
6	478.8	434.9	43.9	9%
7	839.2	789.3	49.9	6%
8	1589.7	1528.6	61.1	4%
9	2502.6	2432.5	70.1	3%

The results of initial and relaxed CMODs and their corresponding recovered values

are depicted in **Table 6-1**. For better understanding of this relationship, the last column

of the table is presented in **Figure 6.2**.

Figure 6.2:   The percentage of relaxation compared to initial CMOD.

As can be seen, by increasing the size of cracks, their ability to be closed becomes

weaker. In other words, the smaller the crack is, the higher its relaxation would be. For

instance in the first cycle, 58% of the crack was relaxed compared to its initial CMOD

of 20.8 µm while, the crack with initial CMOD of 2502.6 µm could be closed just by

only 3% which is 70.1 µm to a crack size of 2432.5 µm.

Based on this step and to obtain relaxed CMOD of 10 µm, 30 µm, 50 µm, 100 µm

and 200 µm it was decided to stop the test at CMODs of 22 µm, 55 µm, 80 µm, 135 µm

and 237 µm respectively. As mentioned before, for each crack size in each curing

method six prisms were prepared meaning totally 60 prismatic specimens. Three

samples from each six samples were cracked and reloaded immediately. The other three

samples were cracked and transferred to tempered-water bath of 67°C in order to be

healed. After 48 hours of healing they were removed from water bath and were cooled in laboratory condition. Then the second phase of 3-point bending test was performed with the aim of comparing their energy-absorption ability with cracked-non-healed samples.

a)   b)
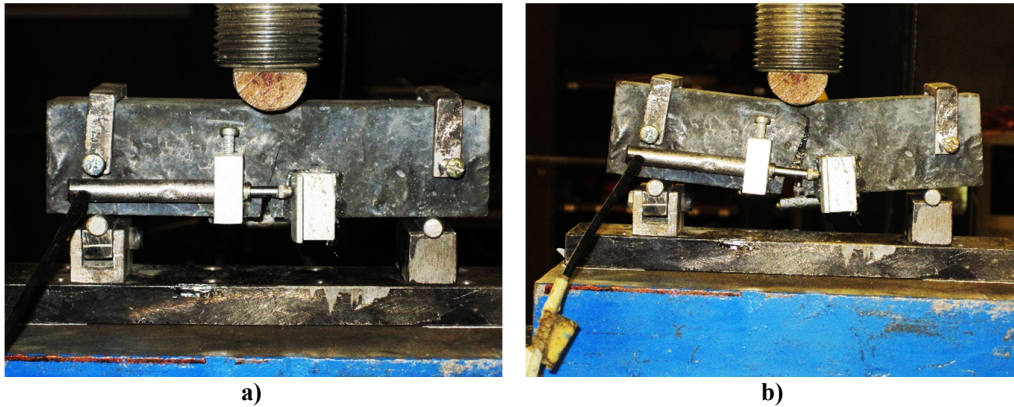
Figure 6.3:   Step 1 crack generation (a) and Step 2 full loading after step 1 with or without healing (b).

6.2   Results and discussion

As explained in the previous section, six samples from each of 6-days cured specimens of TWC and 28-days specimens of NC were cracked in different CMODs. Three samples from six specimens were reloaded immediately after cracking and relaxation and three were transferred to healing tempered-water bath. In order to evaluate the self-healing ability of the specimens, first a visual assessment through optical microscopic observation was performed. In this regard, one of the cracks of 10 μm after healing is depicted in **Figure 6.4**. As can be seen, the crack is almost fully filled with a white color material, which could be $CaCO_3$ precipitations in crack surface or newly formed C-H or C-S-H products, as a result of chemicals' reaction in the concrete and water during 48 hours of healing. It could be also a result of clogging the crack by other fine particles inside concrete and water. This is the main reason that some test methods can evaluate the self-healing against environmental actions but do

not exhibit precise result regarding a real self-healing phenomena. In other words, by saying self-healing we mean a process in which totally the material could be recovered. Nevertheless, through this method, it could be observed that as cracks become wider their ability to be recovered, even on their surfaces, decreases as shown in **Figure 6.5**.

| a) | b) |
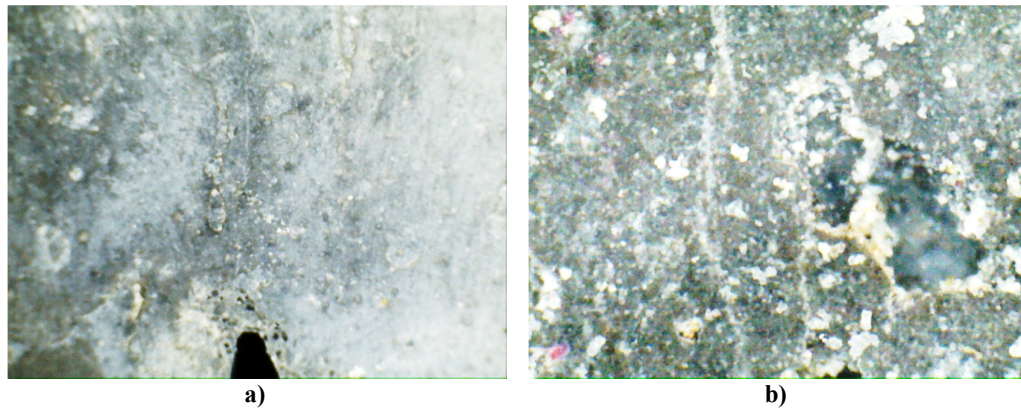
Figure 6.4: 10X magnified (a) and 400X magnified (b) microscope image of 6-day TWC with10 μm crack size after healing.

| 50 μm (B.H.) | 50 μm (A.H.) |
| 100 μm (B.H.) | 100 μm (A.H.) |
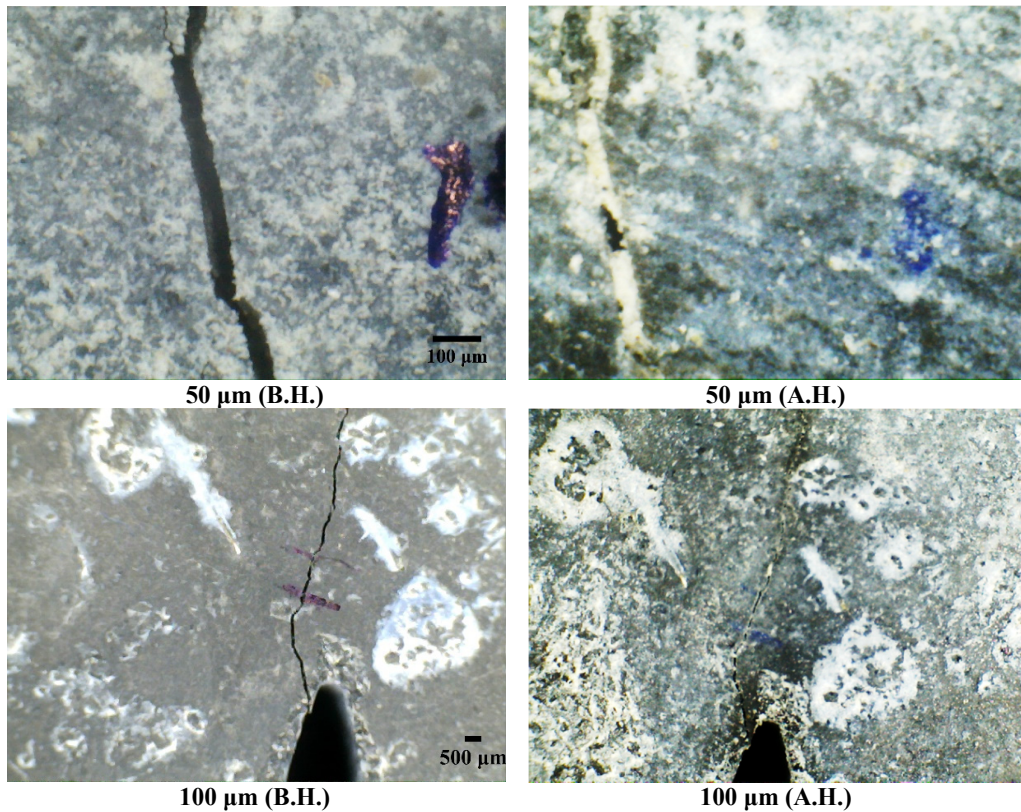
Figure 6.5: Different crack sizes before healing (B.H.) and after healing (A.H.) (to be continued).

| 200 μm (B.H.) | 200 μm (A.H.) |
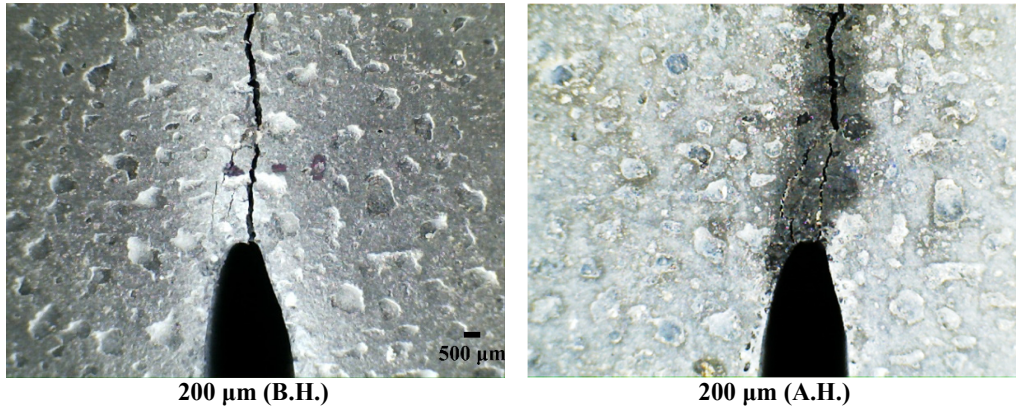
Figure 6.5: Different crack sizes before healing (B.H.) and after healing (A.H.) (continuation).

6.2.1   Self-healing of cementitious matrix of EEUHPC

In the following stage, as mentioned before, the energy absorption of specimens was evaluated. Due to the fact that the post-cracking energy-absorption behavior of specimens is highly dependent on the number, position and angles of fibers at cracking surface and not just on the degree of matrix self-healing, the numerical quantification of energy-absorption capacity is performed before first crack which is around the deflection of 10 μm. To support this, as also depicted in **Figure 6.6 (c&d)**, by passing the linear phase after first cracking, the envelope of three samples (their load-carrying capacity) becomes wider because of variation in number of fibers, their distribution along the height of cracked section and finally their angle with the force direction. For this aim and to consider just the effect of healed matrix on energy absorption of specimens the analysis was performed along the linear part of force-deflection curve.
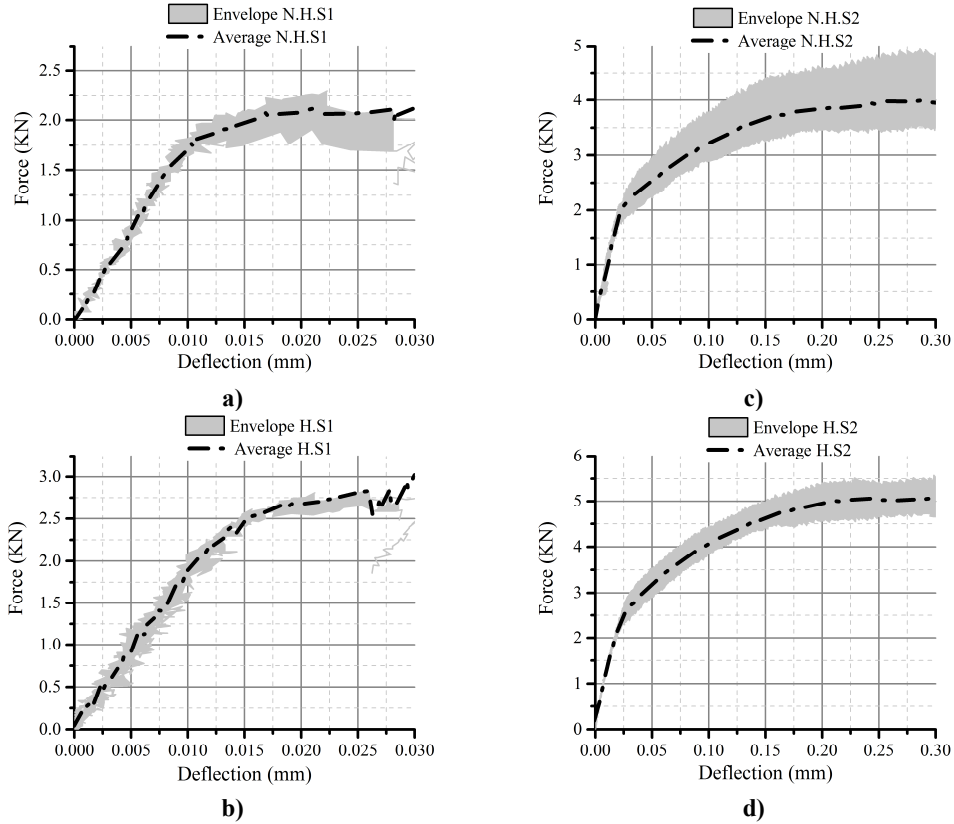
Figure 6.6: Force-deflection curves of TWC specimens up to 22 µm CMOD for non-healed sample step 1 (a), healed samples step 1 (b), and reloading the specimens after first cracking for non-healed specimens step 2 (c) and healed specimens step 2 (d).

The next step is to measure the percentage of structural self-healing through the following formula (**Equation 6.1**) and graphs (**Figure 6.7**).
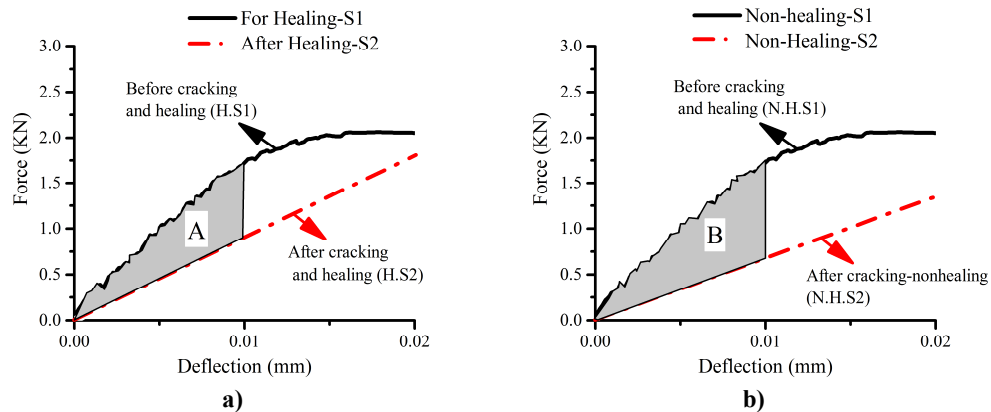
Figure 6.7: Difference of energy-absorption capacity between normal sample and cracked-healed sample (a) and between normal sample and cracked-non-healed sample (b).

$$SH\% = \frac{B - A}{B}$$

<div align="right">Eq.(6.1)</div>

where SH is the self-healing capacity of specimen, B is the difference in energy-absorption between the specimen before cracking and after cracking without healing and A is the difference in energy-absorption between the specimen before cracking and after cracking and healing. According to **Equation 6.1** and based on **Figure 6.7**, the hypothesis is to obtain positive SH which means that the surrounded area between two curves in **Figure 6.7 (a)**, denoted as A, is smaller which means that through healing process the material has regained its primary stiffness and the H.S2 line is closer to H.S1 line. On the other hand, the N.H.S2 demonstrates much lower energy-absorption capacity compared to N.H.S1 leading to a bigger surrounded area in **Figure 6.7 (b)**. The numerator in **Equation 6.1** represents the amount of extra energy, which could be absorbed as the result of self-healing capacity of the material. The results for two series of curing methods, namely NC and TWC, are presented in **Table 6-2**. The corresponding Force-Deflection diagrams are provided in **Annex III**.

Table 6-2: Self-healing capacity of different sizes of CMODs in short and long term for EEUHPC.

Curing series	Relaxed CMOD (μm)	A (Joule)	B (Joule)	SH%
Normal curing (NC)	10	0.00189	0.00291	35.1%
	30	0.00298	0.00398	25.1%
	50	0.00381	0.00512	25.6%
	100	0.00404	0.00543	25.6%
	200	0.00559	0.00672	16.8%
Tempered-water curing (TWC)	10	0.00304	0.00397	23.4%
	30	0.00392	0.0047	16.6%
	50	0.00391	0.00488	19.9%
	100	0.00352	0.00407	13.5%
	200	0.00409	0.00412	0.7%

For more clarification and better comparison between the obtained results, **Figure 6.8** is presented.
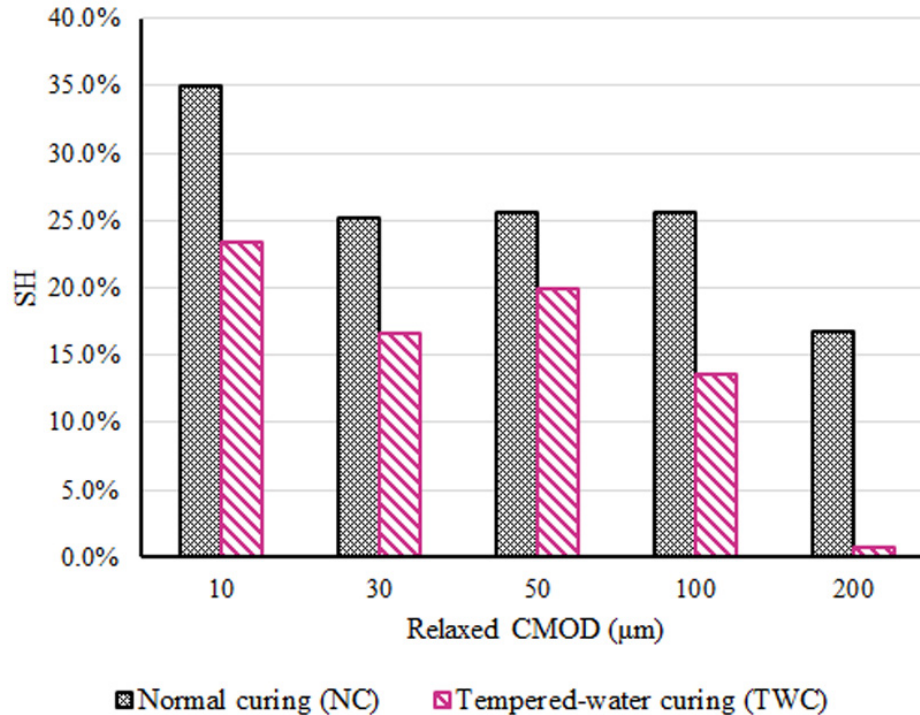
Figure 6.8:   Self-healing ability of specimens with different CMODs and ages.

First, it can be concluded that the healing process of 48 hours in tempered water of 67°C would be an efficient way of healing the material. It gives the opportunity for in-situ repair and strengthening of cracked UHPC with similar procedures such as steam curing methods. NC specimens, representing concrete in early age, exhibited higher self-healing potential by 1.50, 1.51, 1.29, 1.89 and 23.09 times of 6-day TWC specimens, representing the UHPC in its long age. Beside that as the cracks become wider, this difference becomes greater as well. The other significant point which would be of great importance for construction industry is that NC specimens having crack sizes of 200 μm exhibited the potential of 16.8% recovery. Besides that, none of the cracks, even 10 μm relaxed CMOD, could be healed 100%. These findings are different

from the results of some researches. For instance, it has been reported that no

self-healing for cracks greater than 150 μm was observed and on the other hand the

crack sizes less than 50 μm were healed 100% (Li & Yang, 2007; Yang, et al., 2009).

This contradiction could be a result of different assessment method applied by the

authors since they came to these conclusions through permeability test. The TWC

long-aged specimens cured for 6 days demonstrated very negligible self-healing ability

for crack sizes of 200 μm while for crack sizes less than 100 μm a recovery between

13.5% and 23.4% was observed showing the ability of the EEUHPC for self-healing

even in long term, which is of great importance for durability and structural

performance of this material.

6.2.2 Self-healing of EEUHPC as a composite material

Although in the preceding section a comparison was performed to investigate the

degree of self-healing of the cementitious matrix, the role of steel fibers on the total

absorbed energy of the specimens would be of great importance even in post cracking

phase. For this aim, the average of three samples for step 2 of all the healed and

non-healed specimens for two NC and TWC series were compared to study their

energy-absorption capacity in higher deflections. As a basis for this comparison

deflection of 2.5 mm was selected to compare the total energy absorption of plain,

cracked-non-healed and cracked-healed specimens with different crack sizes as well as

different curing methods. The 2.5 mm deflection at mid-span is close to the deflection

for $D^f_{BZ.3}$ calculation, representing the fiber contribution in energy absorption of

specimen as defined by RILEM (RILEM TC 162-TDF, 2002). The energy, determined

here, includes the absorbed energy by the concrete matrix as well as steel fibers. The

aim is to see if the steel fibers are capable, or not, of compensating the loss of

energy-absorption in non-healed specimens even with lower capacity of plain concrete

and generally what is their effect on energy-absorption of the specimens. In this regard,

the force-deflection diagram for 10 μm and 30 μm crack widths of NC specimens after

healing (H.S2) and without healing (N.H.S2) beside the plain specimen is provided in

Figure 6.9. As can be seen, before the first cracking point the curves follow the rule

obtained in the previous part. In other words, before the first-cracking point, the steep

of the curve for plain specimen, representing its stiffness, is greater than curve H.S2

and N.H.S2. In addition H.S2 curve is upper than N.H.S2 also showing its greater

stiffness as a result of self healing. This is in accordance with the absorbed energy by

each group of specimens as the result of the surrounded area under each graph.

Nevertheless, by passing the cracking point, this order is changed randomly. For

example, H.S1 surpasses plain specimen in 10 μm crack-width while in 30 μm it

remains under the plain specimen's curve.

| a) 10 μm | b) 30 μm |
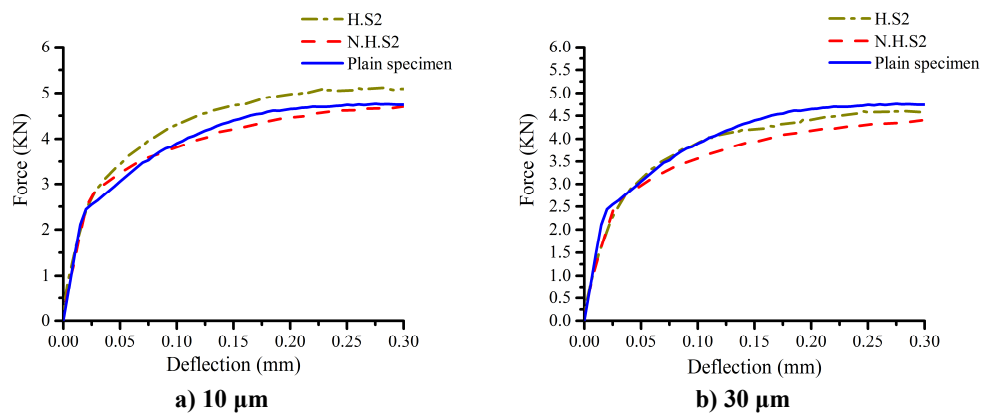
Figure 6.9: Comparison between H.S2 and N.H.S2 specimens having 10 μm and 30 μm crack width and the plain specimen up to deflection of 300 μm.

For more clarification, the force-deflection diagram for 200 μm crack width of NC

specimens after healing (H.S2) and without healing (N.H.S2) beside the plain specimen

is provided in **Figure 6.10** in different deflection scales of 0.3 mm, 1 mm, 1.5 mm and

2.5 mm. These curves demonstrate more fluctuations in different deflections.
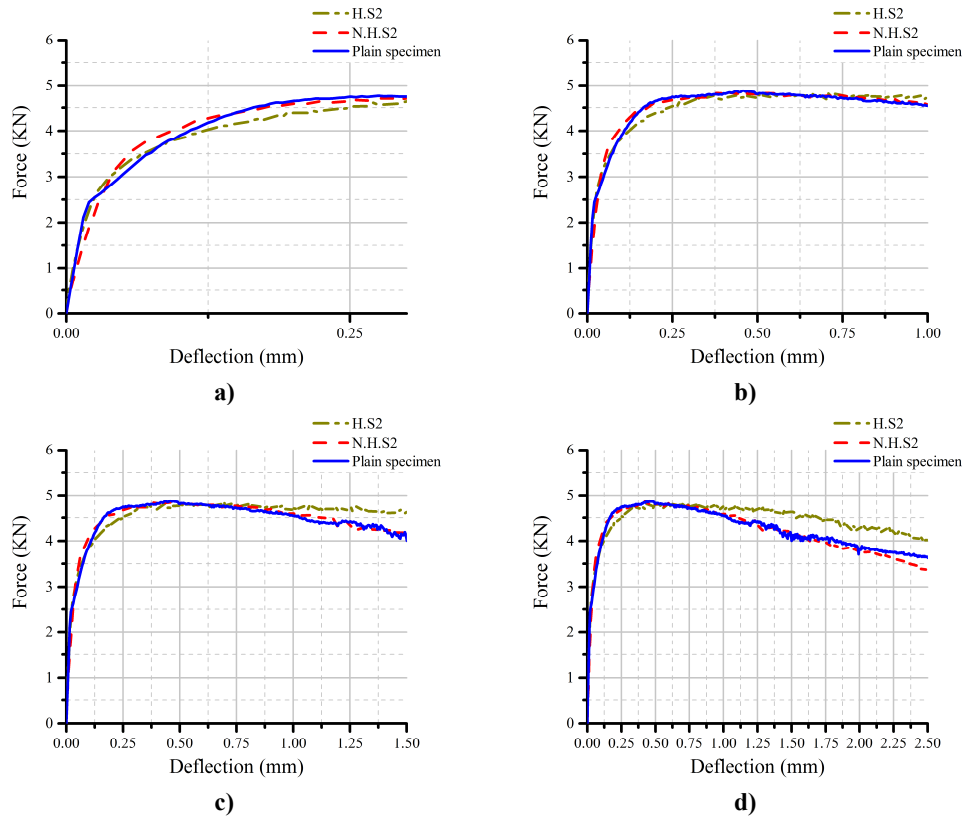
Figure 6.10: Comparison between H.S2 and N.H.S2 specimens having 200 μm crack width and the plain specimen in different deflection scales.

For instance, N.H.S2 overtakes other curves in the interval of around 40 μm to 150 μm while H.S2 falls under two other graphs. Again after this interval the plain sample surpasses up to 0.7 mm and now this is H.S2 which is upper than the others to the end of deflection axes. It is interesting to see that after deflection of around 0.7 mm plain specimen and N.H.S2 exhibit a similar behavior. This phenomenon, as pointed out previously, could be attributed to the different scattering of the steel fibers along the length of prisms, their numbers in the fracture surface, their distribution along the height of section and finally their angles with fracture surface. Therefore, however the self-healing, as studied before, follow a specific trend in lower CMODs as well as lower deflections, depending on different concrete ages and also different crack widths, it is not highly influenced by these factors in higher deflections. In other words, in higher deflections steel fiber placement greatly influences the energy-absorption capacity of

the specimens. In addition, the lower absorbed energy of healed or non-healed cracked specimens in primary phases of deflection or CMOD could be compensated in higher deflections, such as limits of serviceability, when the fibers are distributed more efficiently compared to even non-cracked specimens. This is a great effect of steel fibers, which diminishes the deteriorative effect of cracks on the performance of structural elements. For more clarification, a complete comparison was performed among two curing methods and all the specimens having various crack widths regarding their energy absorption up to 2.5 mm. The results are depicted in **Table 6-3**. The graphical representation of this table is produced in **Figure 6.11**.

Table 6-3: Energy absorption of specimens with different curing methods and crack sizes.

Specimen	NC										TWC									
	10 μm		30 μm		50 μm		100 μm		200 μm		10 μm		30 μm		50 μm		100 μm		200 μm	
	H.S2	N.H.S2	H.S2	N.H.S2	H.S2	N.H.S2	H.S2	N.H.S2	H.S2	N.H.S2	H.S2	N.H.S2	H.S2	N.H.S2	H.S2	N.H.S2	H.S2	N.H.S2	H.S2	N.H.S2
Absorbed energy (J)	11.45	11.54	11.23	10.35	10.93	11.42	12.71	12.09	11.13	10.47	10.84	8.95	9.1	9.22	10.74	9.61	9.58	8.61	9.12	11.28

First of all, it can be clearly seen that generally healed and non-healed specimens of TWC, representing UHPC in long age, demonstrate lower energy-absorption capacity. In other words, without considering the effect of crack sizes, as the material becomes older its ability to absorb energy becomes weaker. The worst difference occurs for 100 μm H.S2 and N.H.S2 specimens with a difference of 25% and 29% respectively compared to their corresponding NC specimens.

Regarding NC samples, however generally H.S2 samples exhibit higher energy-absorption capacity, some exceptions could be observed like the case for 50 μm crack size in which the absorbed energy by N.H.S2 is 4.5% higher than H.S2 specimen.

Similarly, it happened for 10 μm-crack size with just 0.8% higher energy absorption of N.H.S2 sample compared to H.S2. The improvements in energy absorption due to self-healing for crack sizes of 30 μm, 100 μm and 200 μm up to 2.5 mm deflection were 8.5%, 5.1% and 6.3% respectively. By comparing these values with self-healing values of the sole matrix up to deflection of 10 μm, presented in **Table 6-2**, it can be concluded that the gaps between healed and non-healed samples become smaller and in some cases, like 10 μm and 50 μm, alter reversely, meaning non-healed specimen absorbs a little more energy compared to healed sample.
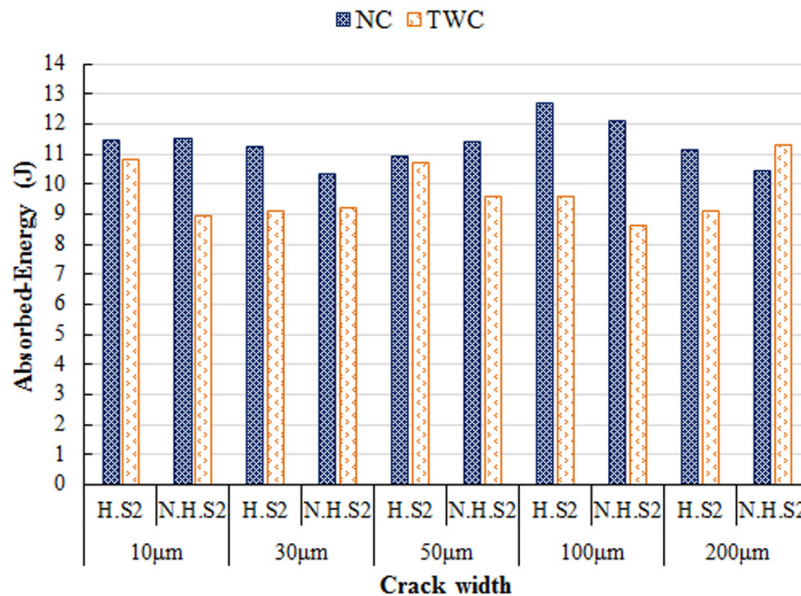
Figure 6.11: Energy-absorption of specimens with different crack sizes and curing methods.

Regarding the TWC specimens, again H.S2 samples demonstrate higher absorbed energy except crack sizes of 30 μm and 200 μm with 1.3% and 19.1% higher energy for N.H.S2 samples. In crack sizes of 10 μm, 50 μm and 100 μm the healed specimens exhibited 21.1%, 11.8% and 11.3% higher capacity for energy absorption compared to non-healed samples. By comparing these values with self-healing values of the sole

matrix up to deflection of 10 μm, presented in **Table 6-2**, it can be concluded that the

gaps between healed and non-healed samples become smaller and even in some cases,

like 30 μm and 200 μm, altered reversely meaning that non-healed specimen absorbs

more energy compared to healed sample. Eventually, it can be concluded that the steel

fiber distribution plays a significant role in energy absorption of specimens in higher

deflections resulting in a random trend and close energy-absorption capacity in healed

and non-healed specimens.

6.3 Conclusion

The self-healing ability of EEUHPC, developed in the first part of this research, was

studied in this chapter. It was investigated that the specimens in their early age

demonstrate higher self-healing capacity compared to old-aged samples due to

availability of more un-reacted cement and pozzolan particles. It also was concluded

that TWC for 48h would be an efficient method for structural recovery of the cracked

samples. This method would be applicable for in-situ self-healing of damaged elements

through a similar process of steam curing for 48 hours at temperature of 67°C. In

addition, self-healing was found highly dependent on the crack width. Through

assessment of energy-absorption capacity of the specimens in their cementitious matrix

and before deflection of 10 μm, it was observed that structural performance of 10 μm

crack width was recovered almost by 35.1% while for 200 μm crack width this recovery

was only around 16.8%. For TWC samples, these values were 23.4% and 0.7%

respectively. These results were different in some aspects with the results by Li & Yang

(2007). Although they also approved the correlation between crack width and the

degree of self healing, they reported that in a high-strength concrete, with compressive

strength of 40-80 MPa, the crack widths of smaller than 50 μm have the ability to be

recovered fully while no recovery could be observed for crack sizes of greater than 150 μm (Li & Yang, 2007). Besides that, findings for conventional concrete, with crack widths of 100 μm and 200 μm and corresponding stiffness recovery around 20% and 10% respectively (Ferrara, et al., 2014), conform to the obtained results in this study demonstrating the higher efficiency of smaller cracks to be healed.

The self-healing of the specimens including their steel fiber interaction was also studied through analyzing the force-deflection diagrams up to deflection of 2.5 mm. it was found that the gaps between healed and non-healed specimens regarding their absorbed energy was lower than their corresponding values in cementitious matrix and in some cases no specific basis could be found. This was an interesting effect of steel fibers on energy absorption of specimens particularly in the post-cracking phase. In fact, depending on the fiber distribution along the length and height of the specimens and their angular alignment to the cross section of the fractured specimens, they exhibited different behavior. This was the main reason of the irregularity of the results in post cracking stage up to deflection of 2.5 mm. In other words, the lack of potentiality for energy absorption of the cracked specimens in lower deflections was found to be compensable by the further behavior of the steel fibers.

Chapter 7

Conclusions and future developments

T he present work mainly aimed at i) developing a type of ultra-high performance concrete with lower environmental impacts compared to already known mixtures and ii) studying its autogenic self-healing ability in its early age as well as long age with having different crack sizes. Nevertheless, it was tried to meet the cost-efficiency of the material as much as possible by appropriate selection of constituent materials particularly cement and silica fume. The methodology applied for the first objective was based on a statistical mixture design procedure known as response surface methodology, which showed its high potential for mixture design of UHPC. The second objective was achieved through mechanical performance assessment of specimens before and after cracking and healing by three-point bending

test by measuring their energy-absorption capacity.

In addition to the main goals presented, a comprehensive review on UHPC was provided in Chapter 2 followed by investigating an effective low-energy mixing procedure. Afterwards, fly ash processing as a prerequisite for applying fly ash in UHPC was explained continued by studying the interaction of superplasticizer on cement and other pozzolanic materials. In chapter 5, the main mechanical and durability characteristics of developed material was analyzed using standard test methods and also response surface methodology regarding water absorption. In addition, steel fiber distribution in the concrete matrix was monitored through image analysis of specimens.

7.1   Concluding remarks

Two compositions regarding cost and environmental efficiency were suggested through response surface methodology. The numerical solutions and their related experimental results demonstrated perfect conformity with high precision representing high efficiency of RSM for UHPC development. The eco-efficient UHPC contains lower quantities of cement and silica fume with 640 kg/m^3 and 56.3 kg/m^3 respectively those are 10% and 76% lower than commercially known UHPCs. This results in 66.1 kg/m^3 and 66.3 €/m^3 lower CO_2 content and cost compared to Ductal®. While, its mechanical and durability-related characteristics, even with half quantity of steel fiber, are very close to Ductal®. Compressive strength and flow diameter of the mixture were 160.3 MPa and 19 cm. The cost efficient mixture includes 658.2 kg/m^3 and 29.6 kg/m^3 cement and silica fume respectively with 19cm of flow diameter and 150.5 MPa compressive strength. In this regard, incorporation of ultra-fine fly ash with average particle size of 4.48 μm was a significant prerequisite in developing UHPC. Otherwise, with applying original fly ash, self-compactness was infeasible. In addition, it was

found that dry processing of FA would be a more effective way of its grinding to finer particle size rather than wet-milling process.

Effect of water and superplasticizer addition time on paste preparation, that is of great importance for developing very low water/binder concretes namely self-compacting UHPC, was studied as well. It was found that the best fluidizing effect could be acquired after adding 70% of mixing water to the cementitious materials. After, the paste must be mixed for 3 minutes followed by adding the optimum dosage of SP and mixing for at least 4 minutes (6 minutes seems preferable based on visual assessment). Finally, the remaining 30% of water must be added and the mixture blended for an extra 6 minutes to reach a steady-state consistency.

The optimum dosage of SP for cement, cement-UFFA and cement-SF blends found to be 1.5%, 2% and 2.3% (W_t.S.SP/V.P) respectively corresponding to 1.61%, 2.3% and 2.74% of W_t.Lq.SP/W_t.P in each slurry. It was investigated that the quantity of SF should be limited as much as possible in UHPC regarding its week interaction with SP as well as its high price while it exhibit positive effect on strength and durability.

The mechanical performance of the material was characterized in detail in chapter 5. The material demonstrated extraordinary resistance against chloride ion penetration and carbonation. Through the response surface methodology it was also found that although all of the tested compositions shows very good performance, the water absorption ability of the material is highly influenced by the silica fume content. The more silica fume is consumed the less willingness the concrete shows to water absorption in both capillary and immersion test. On the other hand, sand content does not have any significant effect on water absorption.

Fiber distribution along the length and height of specimens was also studied carefully. They were perfectly distributed and aligned horizontally without any

segregation and sedimentation. Almost one third of fibers in each cross section were distributed in one third of the section height. Furthermore, the numbers of fiber-cuts in three sections along the length were almost equal representing the effective distribution of the fibers as a result of self-flowing of the concrete.

Regarding self-healing capacity of the developed material, it was investigated that the specimens in their early age demonstrate higher self-healing capacity compared to old-aged samples. It also was concluded that TWC for 48h would be an efficient method for structural recovery of the cracked samples. In addition, self-healing was found highly dependent on the crack width. Through assessment of energy-absorption capacity of the specimens in their cementitious matrix and before deflection of 10 μm, it was observed that structural performance of 10 μm crack width was recovered almost by 35.1% while for 200 μm crack width this recovery was only around 16.8%. For TWC samples, these values were 23.4% and 0.7% respectively. The self-healing of the specimens, including their steel fiber interaction, was also studied through analyzing the force-deflection diagrams up to deflection of 2.5 mm. It was found that the gaps between healed and non-healed specimens regarding their absorbed energy was lower than their corresponding values in cementitious matrix and in some cases no specific regularity could be found. This was due to remarkable effect of steel fibers on load-carrying capacity of specimens particularly in the post-cracking phase. In fact, depending on the fiber distribution along the length and height of the specimens and their angular alignment to the cross section of the fractured specimens, they exhibited different behavior regarding energy absorption in higher deflections. This was the main reason of the irregularity of the results in post-cracking stage up to deflection of 2.5 mm. In other words, the lack of potentiality for energy absorption of the cracked specimens in lower deflections was found to be compensable by the further behavior of

the steel fibers.

7.2   Future research themes

The future step of the current study would be to investigate the autonomic healing of the material. During this work, the potentiality of the material for autogenic self-healing was studied. This step paved the way for a more detailed study on other agents and methods regarding autonomic self-healing.

Based on the fact that EEUHPC developed in this work exhibited excellent mechanical and durability performances beside its capacity for self-healing, a comprehensive life-cycle analysis would be necessary for life-cycle assessment of any construction project developed by this material.

The other significant issue is to investigate the critical minimum steel fiber content in UHPC, which is capable of keeping the energy-absorption capacity of cracked UHPC in a range close to un-cracked specimens in high deflections, and with different crack sizes similar to the situation happened in this research. This point could be defined as optimum steel fiber content for UHPC. It can be predicted that in lower quantities of steel fiber compared to this optimum point, the energy absorption of cracked specimens falls significantly lower than the energy absorption of un-cracked specimens depending on acceptable crack widths in different applications.

Since the material demonstrated very high resistance against chloride ion diffusion and carbonation tests, innovating more time-efficient durability-related tests for UHPC would be of great importance.

Finally, a broader line of future research is to apply the developed material herein in various structural or architectural applications and characterize their behavior in diverse situations.

References

- NT BUILD 492 , 1999. *CHLORIDE MIGRATION COEFFICIENT FROM NON-STEADY-STATE MIGRATION EXPERIMENTS.* FINLAND: NORDTEST.

- Abdel-Jawad, Y. & Dehn, F., 2005. *Self-healing of self-compacting concrete.* s.l., s.n., pp. 1023-1029.

- Abrishambaf, A., 2015. *Creep Behaviour of Cracked Steel Fibre Reinforced Self-Compacting Concrete Laminar Structures.* Portugal: University of Minho.

- ACI, 1992. *ACI 517.2 R-87, Accelerated Curing of Concrete at Atmospheric Pressure-State of the Art, , Revised.* s.l.:s.n.

- Acker, P. & Behloul, M., 2004. *Ductal® Technology: a Large Spectrum of Properties, a Wide Range of Applications.* Kassel, Germany, kassel university press, pp. 11-23.

- AFGC, 2000. *Recommendations for use of Self-Compacting Concrete,* Paris, France: Association Française de Génie Civil (AFGC) Publications.

- AFGC, 2002. *Documents scientifiques et techniques-Ultra High Performance Fibre-Reinforced Concretes-Interim Recommendations,* Paris, France: Association Française de Génie Civil (AFGC) Publications.

- Ahlborn, T. M., Misson, D. L., Peuse, E. J. & Gilbertson, C. G., 2008. *Durability and Strength Characterization of Ultra-High Performance Concrete under Variable Curing Regimes.* Kassel, Germany, Kassel university press.

- Aïtcin, P.-C., 1998. The Art and Science of High-Performance Concrete. *INDUSTRIA ITALIANA DEL CEMENTO,* pp. 350-365.

- Aïtcin, P.-C., 2011. *High Performance Concrete.* s.l.:CRC Press.

- Alarcon-Ruiz, L., Platret, G., Massieu, E. & Ehrlacher, A., 2005. The use of thermal analysis in assessing the effect of temperature on a cement paste. *Cement and Concrete Research,* Volume 35, pp. 609-613.

- Aldea, C.-M., Song, W.-J., Popovics, J. S. & Shah, S. P., 2000. Extent of healing of cracked normal strength concrete. *Journal of materials in civil engineering,* 12(1), pp. 92-96.

- Alexanderson, J., 1972. *STRENGTH LOSSES IN HEAT CURED CONCRETE.* s.l., Swedish Cement Concr Inst Proc.

- Alibaba®, 1999-2016. *Alibaba.* [Online] Available at: http://www.alibaba.com/product-detail/sub-miron-Steam-Jet-Mill-fly_1890878795.html [Accessed 10 6 2015].

- Allena, S. & Newtson, C. M., 2011. Ultra-high strength concrete mixtures using local materials. *Journal of Civil Engineering and Architecture,* 5(4).

- Anderson, M. J. & Whitcomb, P. J., 1998. Find the most favorable formulations.

Chemical Engineering Progress, 94(4), pp. 63-67.

- Andreasen, A. M. & Andersen, J., 1930. Om relationen mellem kornsammansætning og mellemrum i produkter af løse korn med nogle eksperimenter. *Ingeniøren,* 39(9), pp. 99-107.

- ASTM C 230/C 230M – 03, 2007. *Standard Specification for Flow Table for Use in Tests of Hydraulic Cement.* United States.

- ASTM C109/C109M – 05, 2005. *Standard Test Method for Compressive Strength of Hydraulic Cement Mortars (Using 2-in. or [50-mm] Cube Specimens).* ASTM International, West Conshohocken, PA 19428-2959, United States, Patent No. ASTM C109/C109M – 05.

- ASTM C128–04a, 2004. *Standard Test Method for Density, Relative Density (Specific Gravity), and Absorption of Fine Aggregate.* United States: s.n.

- ASTM C1585 – 04, 2004. *Standard Test Method for Measurement of Rate of Absorption of Water by Hydraulic- Cement Concretes.* West Conshohocken, PA 19428-2959, United States: ASTM International.

- ASTM C642 – 97, 1997. *Standard Test Method for Density, Absorption, and Voids in Hardened Concrete.* West Conshohocken, PA 19428-2959, United States: ASTM International.

- ASTM D6910-04, 2004. *Standard Test Method for Marsh Funnel Viscosity of Clay Construction Slurries.* West Conshohocken, PA: ASTM International.

- ASTM, 1995. *Standard Test Method for Density of Hydraulic Cement.* United States, Patent No. C 188 – 95 (Reapproved 2003).

- ASTM-C1018–97, 1998. *Standard Test Method for Flexural Toughness and First-Crack Strength of Fiber-Reinforced Concrete (Using Beam With Third-Point Loading).* West Conshohocken, PA, United States.

- ASTM-C469, 2010. *Standard Test Method for Static Modulus of Elasticity and Poisson's Ratio of Concrete in Compression.* West Conshohocken, PA, Patent No. ASTM Standard C469.

- ASTM-C78–02, 2002. *Standard Test Method for Flexural Strength of Concrete (Using Simple Beam with Third-Point Loading).* West Conshohocken, PA, United States.

- Balogh, A., 1995. *High-reactivity Metakaolin.* s.l.:The AberdeenGroup.

- Bayramov, F., Tasdemir, C. & Tasdemir, M., 2004. Optimisation of steel fibre reinforced concretes by means of statistical response surface method. *Cement & Concrete Composites,* Volume 26, p. 665–675.

- Behloul, M., Causse, G. & Etienne, D., 2002. *Passerelle en Ductal® de Séoul/Ductal® footbridge in Seoul.* Osaka, Japan, Association Française de Génie Civil, fédération internationale du béton (AFGC, FIB), pp. 33-34.

- BEKAERT, 2015. *BEKAERT.* [Online] Available at: http://www.bekaert.com [Accessed 25 6 2015].

- BIBM, et al., 2005. *The European Guidelines for Self Compacting Concrete.* s.l.:s.n.

- Bierwagen, D. & Abu-Hawash, A., 2005. *Ultra High Performance Concrete Highway Bridge.* Ames, IA, Iowa State University.

- Bingöl, A. F. & Tohumcu, I., 2013. Effects of different curing regimes on the compressive strength properties of self compacting concrete incorporating fly ash and silica fume. *Materials and Design,* Volume 51, pp. 12-18.

- Blais, P. Y. & Couture, M., 1999. Precast, Prestressed Pedestrian Bridge — World's First Reactive Powder Concrete Structure. *PCI JOURNAL,* Volume 44, pp. 60-71.

- Box, G. E. & Wilson, K. B., 1951. On the experimental attainment of optimum conditions. *Journal of the Royal Statistical Society, Series B (Methodological),* 13(1), pp. 1-45.

- Brookfield Engineering Laboratories, Inc. , 2015. *BROOKFIELD.* [Online] Available at: http://www.brookfieldengineering.com/education/what-is-viscosity.asp [Accessed 17 11 2015].

- Brouwers, H. J. H., 2006. Particle-size distribution and packing fraction of geometric random packings. *Physical review,* 74(3), p. 031309.

- Brouwers, H. & Radix, H., 2005. Self-Compacting Concrete: Theoretical and experimental study. *Cement and Concrete Research,* Volume 35, p. 2116 – 2136.

- BS EN 1015-3, 2004. *Methods of test for mortar for masonry — Part 3: Determination of consistence of fresh mortar(by flow table).* s.l.

- BS EN 12350-8, 2010. *Testing fresh concrete. Self-compacting concrete. Slump-flow test.* EUROPEAN STANDARD, Brussels, Patent No. BS EN 12350-8:2010.

- BS EN 196-1, 1995. *Methods of testing cement- Part 1: Determination of strength.* Brussels: EUROPEAN COMMITTEE FOR STANDARDIZATION.

- BS EN 197-1, 2000. *Cement - Part 1 Composition,specification and conformity criteria for common cements.* s.l.:s.n.

- BS EN 934-2, 2009. *Admixtures for concrete, mortar and grout . Concrete admixtures. Definitions, requirements, conformity, marking and labelling.* s.l.

- Camões, A., 2002. *Betões de elevado desempenho com incorporação de cinzas volantes, Dissertação para obtenção do grau de doutorado.* Guimaraes, Portugal: Universidade do Minho, Departamento de Engenharia Civil.

- Camões, A., 2005. *Influência do superplastificante nos parâmetros reológicos do betão fresco.* Guimaraes, Portugal: Universidade do Minho, Departamento de Engenharia Civil .

- Cheyrezy, M., Maret, V. & Frouin, L., 1995. MICROSTRUCTURAL ANALYSIS OF RPC (REACTIVE POWDER CONCRETE). *Cement and Concrete Research,* 25(7), pp. 1491-1500.

- Çopuroglu, O. et al., 2013. *Experimental techniques used to verify healing,* s.l.: Springer.

- Çopuroglu, O. et al., 2013. *Self-Healing Phenomena in Cement-Based Materials (RILEM Technical Committee STAR 221-SHC)-Experimental techniques used to verify healing,* s.l.: Springer.

- Cunha, V. M. d. C. F. d., 2010. *Steel Fibre Reinforced Self-Compacting Concrete (from Micro-Mechanics to Composite Behaviour).* Portugal: University of Minho.

- Cwirzen, A., Habemehl-Cwirzen, K. & Penttala, V., 2008. *The effect of heat treatment on the salt freeze-thaw durability of UHSC.* Kassel, Germany, Kassel university press.

- Dallaire, E., Aitcin, P. C. & Lachemi, M., 1998. High-performance powder. *Civil Engineering,* 68(1), p. 48.

- de Larrard, F. & Sedran, T., 1994. Optimization of ultra-high-performance concrete by the use of a packing model. *Cement and Concrete Research,* 24(6), pp. 997-1009.

- de Rooij, M., Van Tittelboom, K., De Belie, N. & Schlangen, E., 2013. *State-of-the-Art Report of RILEM Technical Committee 221-SHC: Self-Healing Phenomena in Cement-Based Materials,* s.l.: Springer .

- Densit, 2016. *Densit.* [Online] Available at: http://www.densit.com/Business_Areas/Renewable_Energy_-_Grouted_Foundation_Solutions/Ducorit%C2%AE.aspx [Accessed 6 4 2016].

- Derringer, G., 1980. Simultaneous optimization of several response variables. *Journal of quality technology,* Volume 12, pp. 214-219.

- Ductal®, 1997. *Ductal.* [Online] Available at: http://www.ductal.com/wps/portal/ductal/2_3_1-Detail?WCM_GLOBAL_CONTEXT=/wps/wcm/connectlib_ductal/Site_ductal/English_version/Page.Navigation.Structural.Footbridges/KeyProjectDuctal%20Page/KeyProjectDuctal_1278712507168 [Accessed 2015].

- Ductal®, 2002. *Ductal.* [Online] Available at: http://www.ductal.com/wps/portal/ductal/fr/2_3_1-Detail?WCM_GLOBAL_CONTEXT=/wps/wcm/connectlib_ductal/Site_ductal/French_version/Page.Navigation.Structural.Footbridges/KeyProjectDuctal%20Page/KeyProjectDuctal_1278713313528 [Accessed 2015].

- Edvardsen, C., 1999. Water permeability and autogenous healing of cracks in concrete. *ACI Materials Journal,* 96(4), pp. 448-454.

- eia, 2015. *U.S. Energy Information Administration.* [Online] Available at: https://www.eia.gov/tools/faqs/faq.cfm?id=74&t=11 [Accessed 4 12 2015].

- El-Dieb, A. S., 2009. Mechanical, durability and microstructural characteristics of ultra-high-strength self-compacting concrete incorporating steel fibers. *Materials and Design,* Volume 30, p. 4286–4292.

- Erdem, T., Turanli, L. & Erdogan, T., 2003. Setting time: An important criterion to determine the length of the delay period before steam curing of concrete. *Cement and Concrete Research,* Volume 33, pp. 741-745.

- Eriksson, L., Johansson, E. & Wikström, C., 1998. Mixture design—design generation, PLS analysis, and model usage. *Chemometrics and Intelligent Laboratory Systems,* 43(1), pp. 1-24.

- Ewert, J., Budelmann, H. & Krauß, M., 2008. *Heat of Hydration and Hardening of Ultra High Performance Concrete (UHPC).* Kassel, Germany, s.n.

- Fayed, M. E. & Otten, L., 1997. *HANDBOOK OF POWDER SCIENCE & TECHNOLOGY.* New York: Chapman & Hall.

- Felekoglu, B., Turkel, S. & Baradan, B., 2007. Effect of water/cement ratio on the fresh and hardened properties of self-compacting concrete. *Building and Environment,* Volume 42, p. 1795–1802.

- Ferdosian, I. & Camões, A., 2016. Effective low-energy mixing procedure to develop high-fluidity cementitious pastes. *Matéria (Rio de Janeiro),* 21(1), pp. 11-17.

- Ferrara, L., Krelani, V. & Carsana, M., 2014. A ''fracture testing'' based approach to assess crack healing of concrete with and without crystalline admixtures. *Construction and Building Materials,* Volume 68, pp. 535-551.

- Ferrara, L., Park, Y.-D. & Shah, S. P., 2007. A method for mix-design of fiber-reinforced self-compacting concrete. *Cement and Concrete Research,* Volume 37, p. 957–971.

- Ferraris, C., Larrard, F. D. & Martys, N., 2001. Fresh concrete rheology: recent developments. *Materials Science of Concrete VI, Amer. Cer. Soc. Ed. S. Mindess, J. Skalny,* pp. 215-241.

- Ferreira, T. & Rasband, W., 2012. *ImageJ User Guide, IJ 1.46r.* [Online] Available at: http://rsbweb.nih.gov/ij/docs/guide/146-30.html#toc-Subsection-30.2 [Accessed 22 1 2016].

- FprCEN/TS 12390-12, 2010. *Testing hardened concrete - Part 12: Determination of the potential carbonation resistance of concrete: Accelerated carbonation method.* Brussels: EUROPEAN COMMITTEE FOR STANDARDIZATION.

- Freytag, B., Juhart, J., Sparowitz, L. & Baumgartner, E., 2004. *The Use of UHPC in Composites - Ideas and Realisations -.* Kassel, Germany, Kassel University Press, pp. 559-571.

- Fuller, W. B. & Thompson, S. E., 1907. The laws of proportioning concrete. *Transactions of the American Society of Civil Engineers,* 59(2), pp. 67-143.

- Funk, J. E. & Dinger, D., 2013. *Predictive process control of crowded particulate suspensions: applied to ceramic manufacturing.* s.l.:Springer Science & Business Media.

- Geisenhanslüke, C. & Schmidt, M., 2004. *Methods for Modelling and Calculation of High Density Packing for Cement and Fillers in UHPC.* Kassel, Germany, Kassel University Press, pp. 303-312.

- Ghafari, E., Costa, H. & Júlio, E., 2014. RSM-based model to predict the performance of self-compacting UHPC reinforced with hybrid steel micro-fibers. *Construction and Building Materials,* Volume 66, pp. 375-383.

- Ghafari, E., Costa, H. & Júlio, E., 2015. Statistical mixture design approach for eco-efficient UHPC. *Cement & Concrete Composites,* Volume 55, pp. 17-25.

- Girard, G., 2011. *Seeking a Safer Future for Electricity's Coal Ash Waste.* [Art] (NATIONAL GEOGRAPHIC).

- Granger, S., Loukili, A., Pijaudier-Cabot, G. & Chanvillard, G., 2005. *Mechanical characterization of the self-healing effect of cracks in Ultra High Performance Concrete (UHPC).* Vancouver, Canada, s.n., pp. 24-25.

- Granger, S., Loukili, A., Pijaudier-Cabot, G. & Chanvillard, G., 2007. Experimental characterization of the self-healing of cracks in an ultra high performance cementitious material: Mechanical tests and acoustic emission analysis. *Cement and Concrete Research,* Volume 37, p. 519–527.

- Granger, S., Loukili, A., Pijaudier-Cabot, G. & Chanvillard, G., 2007. Experimental characterization of the self-healing of cracks in an ultra high performance cementitious material: Mechanical tests and acoustic emission analysis. *Cement and Concrete Research,* Volume 37, pp. 519-527.

- Graybeal, B., 2009. *Structural Behavior of a Prototype Ultra-High Performance Concrete Pi-Girder,* s.l.: FHWA, U.S. .

- Graybeal, B., 2011. *Ultra-High Performance Concrete,* s.l.: Federal Highway Administration(FHWA).

- Graybeal, B. A., 2005. *CHARACTERIZATION OF THE BEHAVIOR OF ULTRA-HIGH PERFORMANCE CONCRETE.* College Park: University of Maryland.

- Graybeal, B. A., 2006. *Material Property Characterization of Ultra-High Performance Concrete,* McLean, VA: FHWA, U.S..

- Groves, G. & Richardson, I., 1994. Microcrystalline Calcium Hydroxide in Pozzolanic Cement Pastes. *Cement and Concrete Research,* 24(6), p. 1191–1196.

- Grupo Parapedra, 2016. *Grupo Parapedra, Sifucel.* [Online] Available at: http://www.parapedra.pt/produtos.php [Accessed 2015].

- Hajar, Z., Lecointre, D., Simon, A. & Petitjean, J., 2004. *Design and Construction of the world first Ultra-High Performance Concrete road bridges.* Kassel, Germany, Kassel University Press, pp. 39-48.

- Hammond, G. & Jones, C., 2011. *Inventory of Carbon & Energy (ICE), Version 2.0.* Department of Mechanical Engineering, University of Bath, UK: University of Bath.

- Hanson, J., 1963. Optimum steam curing in precasting plants. *ACI J.Proc,* Volume 60, pp. 75-100.

- Hanson, J. A., 1963. Optimum Steam Curing Procedure in Precasting Plants. *ACI Journal Proceedings,* 60(1), pp. 75-100.

- Hashimoto, T., Kubo, T., Sannoh, C. & Torii, K., 2011. *A DEVELOPMENT OF ENVIRONMENTALLY-FRIENDLY AND HIGHLY-DURABLE CONCRETE USING CLASSIFIED FLY ASH.* s.l., s.n.

- Hashimoto, T., Kubo, T., Sannoh, C. & Torii, K., n.d. *A DEVELOPMENT OF ENVIRONMENTALLY-FRIENDLY AND HIGHLY-DURABLE CONCRETE USING CLASSIFIED FLY ASH.* s.l., s.n.

- Hassan, A. M. T., Jones, S. W. & Mahmud, &., 2012. Experimental test methods to determine the uniaxial tensile and compressive behaviour of ultra high performance fibre reinforced concrete (UHPFRC). *Construction and Building Materials,* Volume 37, pp. 874-882.

- Heinz, D. & Ludwig, U., 1987. Mechanism of Secondary Ettringite Formation in Mortars and Concretes Subjected to Heat Treatment. *ACI, Special Publication,* Volume 100, pp. 2059-2072.

- HiCON, 2016. *HiCon, High performance Concrete.* [Online] Available at: http://www.hi-con.dk/Default.aspx?ID=1239 [Accessed 30 3 2016].

- Hsu, K.-C., Chiu, J.-J., Chen, S.-D. & Tseng, Y.-C., 1999. Effect of addition time of a superplasticizer on cement adsorption and on concrete workability. *Cement & Concrete Composites,* Volume 21, pp. 425-430.

- Hunger, M. M., 2010. *An integral design concept for ecological self-compacting concrete.* s.l.:Technische Universiteit Eindhoven.

- Hüsken, G. & Brouwers, H. J. H., 2008. A new mix design concept for earth-moist concrete: A theoretical and experimental study. *Cement and Concrete Research,* 38(10), pp. 1246-1259.

- Igarashi, S.-i., Kunieda, M. & Nishiwaki, T., 2009. *Technical Committee on Autogenous Healing in Cementitious Materials,* s.l.: Japan Concrete Institute (JCI).

- Jacobsen, S., Marchand, J. & Hornain, H., 1995. SEM observations of the microstructure of frost deteriorated and self healed concrete. *Cement and Concrete Research,* 28(8), pp. 55-62.

- Jang, S. Y., Kim, B. S. & Oh, B. H., 2011. Effect of crack width on chloride diffusion coefficients of concrete by steady-state migration tests. *Cement and Concrete Research,* Volume 41, pp. 9-19.

- Johnston, C. D. & Zemp, R. W., 1991. Flexural Fatigue Performance of Steel Fiber

Reinforced Concrete--Influence of Fiber Content, Aspect Ratio, and Type. *ACI Materials Journal ,* 88(4), pp. 374-383.

- Jones, R., McCarthy, M. & Newlands, M., 2011. *Fly ash route to low embodied Co2 and implications for concrete construction.* Denver,CO, USA, s.n.

- Jones, R., McCarthy, M. & Newlands, M., 2011. *Fly ash route to low embodied CO2 and implications for concrete construction.* Denver,CO, USA, s.n.

- Karahan, O. et al., 2012. Effect of metakaolin content on the properties self-consolidating lightweight concret. *Construction and Building Materials,* Volume 31, pp. 320-325.

- Kaufman, R., 2011. *Seeking a Safer Future for Electricity's Coal Ash Waste,* s.l.: National Geographic News.

- Khayat, K. H., Ghezal, A. & Hadriche, M. S., 2000. Utility of statistical models in proportioning self-consolidating concrete. *Materials and Structures/Materiaux et Constructions,* Volume 33, pp. 338-344.

- Kibert, C. J., 2012. *Sustainable construction: green building design and delivery.* Third edition ed. s.l.:John Wiley & Sons.

- Kunieda, M., Choonghyun, K., Ueda, N. & Nakamura, H., 2012. Recovery of Protective Performance of Cracked Ultra High Performance-Strain Hardening Cementitious Composites (UHP-SHCC) Due to Autogenous Healing. *Journal of Advanced Concrete Technology,* 10(9), pp. 313-322.

- Lam, L., Wong, Y. & Poon, C., 2000. Degree of hydration and gel/space ratio of high-volume fly ash/cement systems. *Cement and Concrete Research,* Volume 3, pp. 747-756.

- Lee, J. Y., Buxton, G. A. & Balazs, A. C., 2004. Using nanoparticles to create self-healing composites. *The Journal of chemical physics,* 121(11), pp. 5531-5540.

- Lee, N. & Chisholm, D., 2005. *Reactive Powder Concrete,* Judgeford, New Zealand: BRANZ Ltd.

- Leese, R. & Casey, D., 2012. *Embodied CO2e of UK cement, additions and cementitious material,* London: Mineral Products Association (MPA) Cement.

- Leese, R. & Casey, D., 2012. *Embodied CO2e of UK cement, additions and cementitious material,* London: Mineral Products Association (MPA) Cement .

- Lester Lefkowitz, C., 2006. *The High Cost of Cheap Coal.* [Art] (National Geographic).

- Li, F.-X., Chen, Y.-Z., Long, S.-Z. & Yu, Q.-J., 2013. The Retardation Effect of Super-Retarding Polycarboxylate-Type Superplasticizer on Cement Hydration. *Arab J Sci Eng,* Volume 38, p. 571–577.

- Li, V. C. & Yang, E.-H., 2007. Self healing in concrete materials. In: *Self Healing Materials.* Netherlands: Springer, pp. 161-193.

- Li, V. & Yang, E., 2007. Self-healing in concrete materials. In: S. v. d. Zwaag, ed. *Self Healing Materials: An Alternative Approach to 20 Centuries of Materials Science.* Dordrecht, The Netherlands: Springer, pp. 161-193.

- Li, Z. & Ding, Z., 2003. Property improvement of Portland cement by incorporating with metakaolin and slag. *Cement and Concrete Research,* Volume 33, p. 579–584.

- LNEC E393, 1993. *, Concrete. Determination of water absorption by capillarity.* Lisbon: LNEC.

- LNEC E463, 2004. *Determination of diffusion coefficient of chlories from non-steady-state migration test.* s.l.:s.n.

- LNPE,   2014.   *LNPE,.*   [Online]   Available   at: http://www.lnpe.cc/Steam%20Jet%20Mill.html [Accessed 4 12 2015].

- Loeb, A., Ferrara, A. & Ellis, R. S., 2008. *First light in the universe.* Berlin: Springer.

- Lopes, F., 2010. *Central do Pego.* [Art].

- Maeder, U., Lallemant-Gamboa, I., Chaignon, J. & Lombard, J.-P., 2004. *Ceracem, a new high performance concrete: characterisations and applications.* Kassel, Germany, Kassel University Press, pp. 59-68.

- Martirena, J. F. et al., 2004. *Lime-pozzolan binder as a very fine mineral admixture in concrete.* Kassel, Germany, University of Kassel.

- Mazanec, O. & Schießl, P., 2008. *Mixing Time Optimisation for UHPC.* Kassel, Germany, Kassel university press, pp. 401-408.

- Mazanec, O. & Schießl, P., 2008. *Mixing Time Optimisation for UHPC.* Kassel, Germany, Kassel university press, pp. 401-408.

- Mendes, C. S. F., 2013. *Reologia no estado fresco de misturas cimentícias com incorporação de superplastificante.* Guimaraes, Portugal: Universidade do Minho, Escola de Engenharia.

- Mihashi, H., KANEKO, Y., Nishiwaki, T. & Otsuka, K., 2001. Fundamental study on development of intelligent concrete characterized by self-healing capability for strength. *Transactions of the Japan Concrete Institute,* Volume 22, pp. 441-450.

- Mihashi, H., KANEKO, Y., Nishiwaki, T. & Otsuka, K., 2001. Fundamental study on development of intelligent concrete characterized by self-healing capability for strength. *Transactions of the Japan Concrete Institute,* Volume 22, pp. 441-450.

- Mironov, S. A., 1966. *Some generalizations in theory and technology of acceleration,* Washington, DC: Highway Research Board (HRB).

- Müller, U. et al., 2008. *Micro texture and mechanical properties of heat treated and autoclaved Ultra High Performance Concrete (UHPC).* Kassel, Germany, Kassel university press.

- Murthy, A. R., Iyer, N. R. & Prasad, B. R., 2013. Evaluation of mechanical properties for high strength and ultrahigh strength concretes. *Advances in Concrete Construction,* 1(4), pp. 341-358.

- Naghibdehi, M. G., Mastali, M., Sharbatdar, M. K. & Naghibdehi, M. G., 2014. Flexural performance of functionally graded RC cross-section with steel and PP fibres. *Magazine of Concrete Research,* 66(5), pp. 219-233.

- Nematollahi, B., R., R. S. M., Jaafar, M. S. & Voo, Y. L., 2012. A review on ultra high performance 'ductile' concrete (UHPdC) technology. *INTERNATIONAL JOURNAL OF CIVIL AND STRUCTURAL ENGINEERING,* 2(3), pp. 1003-1018.

- Neville, A., 2002. AUTOGENOUS HEALING: A CONCRETE MIRACLE?. *Concrete International,* 24(11), pp. 76-82.

- Ng, K. M., Tam, C. M. & Tam, V. W. Y., 2010. Studying the production process and mechanical properties of reactive powder concrete: a Hong Kong study. *Magazine of Concrete Research,* 62(9), p. 647–654.

- Niu, Q., Feng, N., Yang, J. & Zheng, X., 2002. Effect of superfine slag powder on cement properties. *Cement and Concrete Research,* Volume 32, p. 615–621.

- Pacheco-Torgal, F., Jalali, S., Labrincha, J. & John, V. M., 2013. *Eco-efficient concrete.* s.l.:Elsevier.

- Paya, J. et al., 1995. EARLY-STRENGTH DEVELOPMENT OF PORTLAND CEMENT MORTARS CONTAINING AIR CLASSIFIED FLY ASHES. *Cement and Concrete Research,* 25(2), pp. 449-456.

- Pelletier, M. M., Brown, R., Shukla, A. & Bose, A., 2011. Self-healing concrete with a microencapsulated healing agent. 20(7).

- Perry, V. H. & Seibert, P. J., 2008. *The Use of UHPFRC (Ductal®) for Bridges in North America: The Technology, Applicationsand Challenges Facing Commercialization.* Kassel, Kassel University Press, p. 815–822.

- Perry, V., Scalzo, P. & Weiss, G., 2007. *Innovative Field Cast UHPC Joints for Precast Deck Panel Bridge Superstructures—CN Overhead Bridge at Rainy Lake, Ontario.* Phoenix, AZ, s.n.

- Poon, C., Lam, L. & Wong, Y., 2000. A study on high strength concrete prepared with large volumes of low calcium fly ash. *Cement and Concrete Research,* Volume 30, pp. 447-455.

- Preços de betão pronto, 2016. *Preços de betão pronto.* [Online] Available at: http://orcamentos.eu/precos-de-betao-pronto/ [Accessed 7 4 2016].

- Prisco, M. d., Moro, S., Bayard, O. & Zani, G., 2014. *NEW INDUSTRIAL BUILDING DESIGNED WITH VERY HIGH PERFORMANCE FIBER REINFORCED CONCRETE.* s.l., s.n.

- Ramezanianpour, A., Khazali, M. & Vosoughi, P., 2013. Effect of steam curing cycles on strength and durability of SCC: A case study in precast concrete. *Construction and Building Materials,* Volume 49, p. 807–813.

- Rapoport, J. et al., 2002. Permeability of Cracked Steel Fiber-Reinforced Concrete. *JOURNAL OF MATERIALS IN CIVIL ENGINEERING,* 14(4), p. 355–358.

- Rasband, W., 2008. *ImageJ, Image processing and analysis in Java.* USA: National Institutes of Health.

- Rebentrost, M. & Wight, G., 2008. *Experience and Applications of Ultra-high Performance Concrete in Asia.* Kassel, Germany, kassel university press.

- Reinhardt, H. et al., 2013. *Recovery against environmental action, Self-healing phenomena in cement-based materials, Draft of State-of-the-Art report of RILEM Technical Committee,* s.l.: Springer.

- Reinhardt, H.-W. & Jooss, M., 2003. Permeability and self-healing of cracked concrete as a function of temperature and crack width. *Cement and Concrete Research,* 33(7), pp. 981-985.

- Resplendino, J., 2004. *First recommendations for Ultra-High-Performance Concretes and examples of application.* Kassel, Germany, Kassel University Press, pp. 79-90.

- Richard, P. & Cheyrezy, M., 1995. Composition of Reactive Powder Cconcretes. *Cement and Concrete Research,* 25(7), pp. 1501-1511.

- Richard, P. & Cheyrezy, M., 1995. Composition of Reactive Powder Concretes. *Cement and Concrete Research,* 25(7), pp. 1501-1511.

- Richard, P. & Cheyrezy, M., 1995. COMPOSITION OF REACTIVE POWDER CONCRETES. *Cement and Concrete Research,* 25(7), pp. 1501-1511.

- RILEM TC 162-TDF, 2002. TEST AND DESIGN METHODS FOR STEEL FIBRE,

Bending test, Final Recommendation. *Materials and Structures/Materiaux et Constructions,* Volume 35, pp. 579-582.

- RILEM Technical Committee 221-SHC, 2013. *Self-Healing Phenomena in Cement-Based Materials, STAR 221-SHC,* s.l.: springer.

- Rougeau, P. & Borys, B., 2004. *Ultra High Performance Concrete with ultrafine particles other than silica fume.* kassel, Germany, University of Kassel, pp. 213-225.

- Rouse, J. ". et al., 2011. *Design, Construction, and Field Testing of an Ultra High Performance Concrete Pi-Girder Bridge,* Ames, IA: Iowa State University.

- Russell, H. G. & Graybeal, B. A., 2013. *Ultra-High Performance Concrete: A State-of-the-Art Report for the Bridge Community,* McLean, VA: Federal Highway Administration.

- Saul, A. G. A., 1951 . Principles underlying the steam curing of concrete at atmospheric pressure. *Magazine of Concrete Research,* 2(6), pp. 127-140.

- Schachinger, I., Hilbig, H. & Stengel, T., 2008. *Effect of Curing Temperature at an Early Age on the Long-Term Strength Development of UHPC.* Kassel, Germany, Kassel university press.

- Schachinger, I., Schubert, J. & Mazanec, O., 2004. *Effect of Mixing and Placement Methods on Fresh and Hardened Ultra High Performance Concrete (UHPC).* Kassel, Germany, s.n.

- Scheydt, J. C., Herold, G., Müller, H. S. & Kuhnt, M., 2008. *Development and Application of UHPC Convenience Blends.* Kassel, Germany, Kassel University press.

- Schmets, A. J., 2003. *Self-healing: an emerging property for new materials,* s.l.: Leonardo Times.

- SFA, 2014. *Silica fume Association.* [Online] Available at: http://www.silicafume.org/general-silicafume.html [Accessed 20 10 2015].

- Sharp, S. R. & Clemena, G. G., 2004. *State-of-the-Art Survey of Advanced Materials and Their Potential Application in Highway Infrastructure,* s.l.: Virginia Transportation Research Council.

- Shideler, J. J. & Chamberlin, W. H., 1949. Early Strength of Concrete as Affected by Steam Curing Temperatures. *ACI Journal Proceedings,* 46(12), pp. 273-283.

- Siddique, R., 2007. *Waste Materials and By-Products in Concrete.* Punjab,India: Springer, Science & Business Media.

- Šiler, P. et al., 2014. Influence of superplasticizers on the course of Portland cement hydration. *Chemical Papers,* 68(1), p. 90–97.

- Snoeck, D. & Belie, N. D., 2012. Mechanical and self-healing properties of cementitious composites reinforced with flax and cottonised flax, and compared with polyvinyl alcohol fibres. *Biosystems engineering,* 111(4), pp. 325-335.

- Snoeck, D. et al., 2014. Self-healing cementitious materials by the combination of microfibres and superabsorbent polymers. *Journal of Intelligent Material Systems and Structures,* 25(1), pp. 13-24.

- Soroka, I., Jaegermann, C. H. & Bentur, A., 1978. Short-term steam-curing and concrete later-age strength. *Matériaux et Construction,* 11(2), pp. 93-96.

- Stähli, P., Custer, R. & van Mier, J., 2008. On flow properties, fibre distribution, fibre orientation and flexural behaviour of FRC. *Materials and Structures,* 41(1), pp. 189-196.

- Staquet, S. & Espion, B., 2004. *Early-age autogenous shrinkage of UHPC incorporating very fine fly ash or metakaolin in replacement of silica fume.* Kassel, Germany, Kassel University Press, pp. 587-599.

- Stat-Ease, 2014. *Stat-Ease.* [Online] Available at: http://www.statease.com/pubs/handbk_for_exp_sv.pdf [Accessed 31 3 2015].

- Tam, C.-m. & Tam, V. W.-y., 2012. Microstructural behaviour of reactive powder concrete under different heating regimes. *Magazine of Concrete Research,* 64(3), p. 259–267.

- Tayeh, B. A., Bakar, B. A., Johari, M. M. & Voo, Y. L., 2012. Mechanical and permeability properties of the interface between normal concrete substrate and ultra high performance fiber concrete overlay. *Construction and Building Materials,* Volume 36, p. 538–548.

- Tayeh, B. A., Bakar, B. A., Johari, M. M. & Voo, Y. L., 2013. Utilization of ultra-high performance fibre concrete (UHPFC) for rehabilitation–a review. *Procedia Engineering,* Volume 54, pp. 525-538.

- Taylora, H., Famy, C. & Scrivener, K., 2001. Delayed ettringite formation. *Cement and Concrete Research,* 31(5), p. 683–693.

- Taylor, H., Famy, C. & Scrivener, K., 2001. Delayed Ettringite Formation. *Cement and Concrete Research,* Volume 31, pp. 683-693.

- Teixeira, E. R. et al., 2015. Comparative environmental life-cycle analysis of concretes using biomass and coal fly ashes as partial cement replacement material. *Journal of Cleaner Production,* Volume 112, pp. 2221-2230.

- Terzijski, I., 2004. *Compatibility of Components of High and Ultra High Performance Concrete.* Kassel, Germany, Kassel University Press, pp. 175-186.

- Tittelboom, V., Kim, M. D. & Belie, N. D., 2012. *Durable concrete structures with cracks which heal themselves.* s.l., Woodhead Publishing, pp. 285-294.

- Torrent, R. J., 1992. A two-chamber vacuum cell for measuring the coefficient of permeability to air of the concrete cover on site. *Materials and Structures,* 25(6), pp. 358-365.

- Toutanji, H. A. & El-Korchi, T., 1995. THE INFLUENCE OF SILICA FUME ON THE COMPRESSIVE STRENGTH OF CEMENT PASTE AND MORTAR. *cement and Concrete Research,* 25(7), pp. 1591-1602.

- Tue, N. V., Ma, J. & Orgass, M., 2008. *Influence of addition method of suplerplasticizer on the properties of fresh UHPC.* kassel, Germany, kassel university press.

- Tue, N. V., Ma, J. & Orgass, M., 2008. *Influence of addition method of suplerplasticizer on the properties of fresh UHPC.* kassel, Germany, kassel university press.

- Turkel, S. & Alabas, V., 2005. The effect of excessive steam curing on Portland composite cement concrete. *Cement and Concrete Research,* Volume 35, p. 405– 411.

- Upasani, R. S. & Banga, A. K., 2004. Response Surface Methodology to Investigate the Iontophoretic Delivery of Tacrine Hydrochloride. *Pharmaceutical Research,* 21 (12), pp. 2293-2299.

- Van der Merwe, E., Strydom, C. & Potgieter, J., 1999. Thermogravimetric analysis of the reaction between carbon and $CaSO_4 \cdot 2H_2O$, gypsum and phosphogypsum in an inert atmosphere. *Thermochimica acta,* Volume 340, pp. 431-437.

- Voit, K. & Kirnbauer, J., 2014. Tensile characteristics and fracture energy of fiber reinforced and non-reinforced ultra high performance concrete (UHPC). *International Journal of Fracture,* 188(2), pp. 147-157.

- Voo, Y. L. & Foster, S. J., 2010. Characteristics of ultra-high performance 'ductile' concrete and its impact on sustainable construction. *The IES Journal Part A: Civil & Structural Engineering,* 3(3), pp. 168-187.

- Voo, Y. L., Foster, S. J. & Gilbert, R. I., 2006. Shear strength of fiber reinforced reactive powder concrete prestressed girders without stirrups. *Journal of Advanced Concrete Technology,* 4(1), pp. 123-132.

- Wang, C. et al., 2012. Preparation of Ultra-High Performance Concrete with common technology and materials. *Cement & Concrete Composites,* Volume 34, p. 538–544.

- Wang, K., Jansen, D. C., Shah, S. P. & Karr, A. F., 1997. Permeability study of cracked concrete. *Cement and Concrete Research,* 27(3), pp. 381-393.

- Wang, X.-Y., 2014. Properties prediction of ultra high performance concrete using blended cement hydration model. *Construction and Building Materials,* Volume 64, pp. 1-10.

- Wiktor, V. & Jonkers, H. M., 2011. Quantification of crack-healing in novel bacteria-based self-healing concrete. *Cement and Concrete Composites,* 33(7), pp. 763-770.

- Wille, K., Naaman, A. E., El-Tawil, S. & Parra-Montesinos, G. J., 2012. Ultra-high performance concrete and fiber reinforced concrete: achieving strength and ductility without heat curing. *Materials and Structures,* Volume 45, p. 309–324.

- Wille, K., Naaman, A. E. & El-Tawll, S., 2011. Optimizing ultra-high-performance fiber-reinforced concrete. *Concrete International,* 33(9), pp. 35-41.

- Xiao, R., Deng, Z.-c. & Shen, C., 2014. Properties of Ultra High Performance Concrete Containing Superfine Cement and without Silica Fume. *Journal of Advanced Concrete Technology,* Volume 12, pp. 73-81.

- Yang, Y., Lepech, M. D., Yang, E.-H. & Li, V. C., 2009. Autogenous healing of engineered cementitious composites under wet–dry cycles. *Cement and Concrete Research ,* 39(5), pp. 382-390.

- Yang, Z., Hollar, J., He, X. & Shi, X., 2011. A self-healing cementitious composite using oil core/silica gel shell microcapsules. *Cement and Concrete Composites,* 33(4), pp. 506-512.

- Yang, Z., Hollar, J., X. H. & Shi, X., 2010. Laboratory assessment of a self-healing cementitious composite. *Transportation Research Record: Journal of the Transportation Research Board,* Volume 2142, pp. 9-17.

- Yazici, H., Aydin, S., Yigiter, H. & Baradan, B., 2005. Effect of steam curing on class C high-volume fly ash concrete mixtures. *Cement and Concrete Research,* Volume 35, p. 1122–1127.

- Yiğiter, H., Aydın, S., Yazıcı, H. & Yardımcı., M. Y., 2012. Mechanical performance of low cement reactive powder concrete (LCRPC). *Composites Part B: Engineering,* 43(8), pp. 2907-2914.

- Yoo, D.-Y., Park, J.-J., Kim, S.-W. & Yoon, Y.-S., 2013. Early age setting, shrinkage and tensile characteristics of ultra high performance fiber reinforced concrete. *Construction and Building Materials,* Volume 41, p. 427–438.

- Yu, R., Spiesz, P. & Brouwers, H., 2014. Mix design and properties assessment of Ultra-High Performance Fibre Reinforced Concrete (UHPFRC). *Cement and Concrete*

Research, Volume 56, pp. 29-39.

- Yu, Y. et al., 2013. Interfacial Interaction Between Polycarboxylate-based Superplasticizer and Cement Component Minerals. *Polymers & Polymer Composites,* 21(5), pp. 299-305.

- Zanni, H. et al., 1996. INVESTIGATION OF HYDRATION AND POZZOLANIC REACTION IN REACTIVE POWDER CONCRETE (RPC) USING "Si NMR. *Cement and Concrete Research,* 26(1), pp. 93-100.

- ZDEB, T., 2013. Ultra-high performance concrete – properties and technology. *BULLETIN OF THE POLISH ACADEMY OF SCIENCES: TECHNICAL SCIENCES,* 61(1), pp. 183-193.

- Zhang, M. & Malhotra, V., 1995. Characteristics of a thermally activated alumino-silicate pozzolanic material and its use in concrete. *Cement and Concrete Research,* 25(8), p. 1713–1725.

- Zhou, Q. & Glasser, F., 2001. Thermal stability and decomposition mechanisms of ettringite at< 120 C. *Cement and Concrete Research,* Volume 31, p. 1333–1339.

- Zwaag, S. v. d., 2008. *Self healing materials: an alternative approach to 20 centuries of materials science.* s.l.:Springer.

Annex I

Supplementary

information for Chapter 4

In the first part of this annex, images of flowability test for 28 compositions of RSM are presented. The second subsection includes the supplementary statistical definitions and guidelines for RSM and finally the last section provides a simple estimation on cost and embodied CO_2 for UFFA.
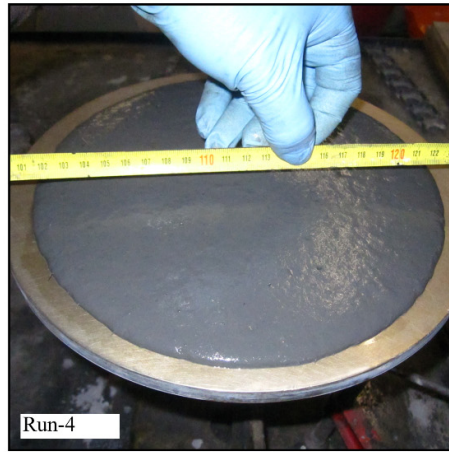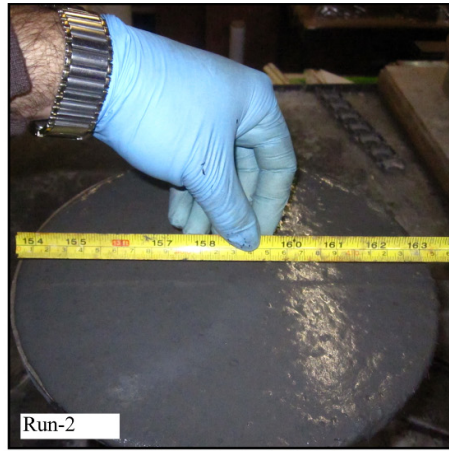
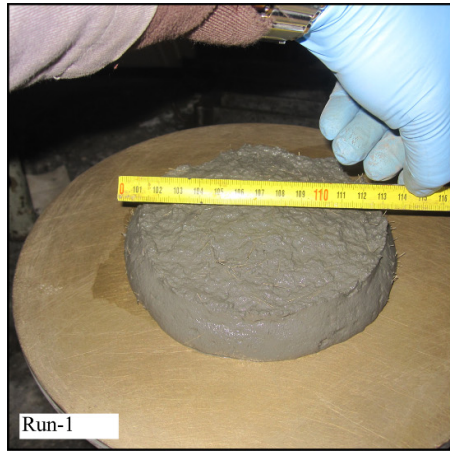## AI.1 Graphical representation of flowability test for RSM

Figure AI. 1: 28 mixtures for RSM (to be continued).

Figure AI. 1: 28 mixtures for RSM (continuation).
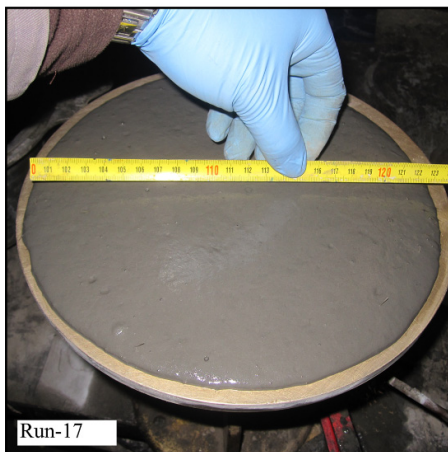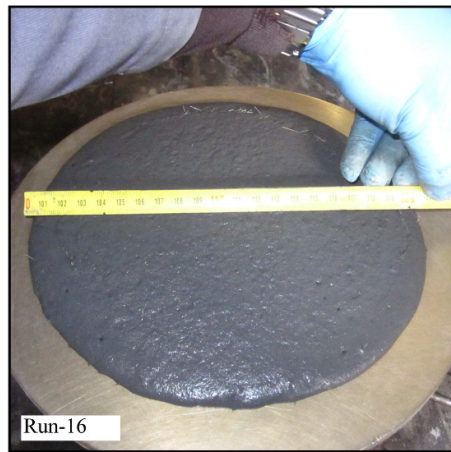
Figure AI. 1: 28 mixtures for RSM (continuation).

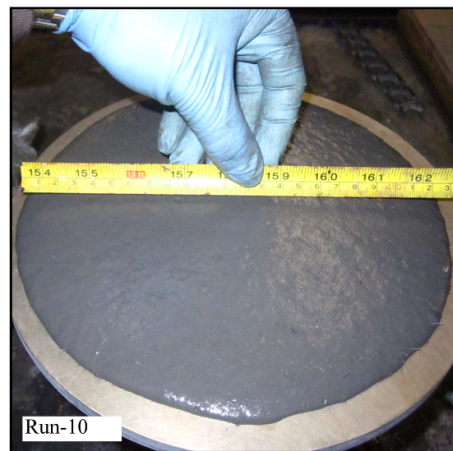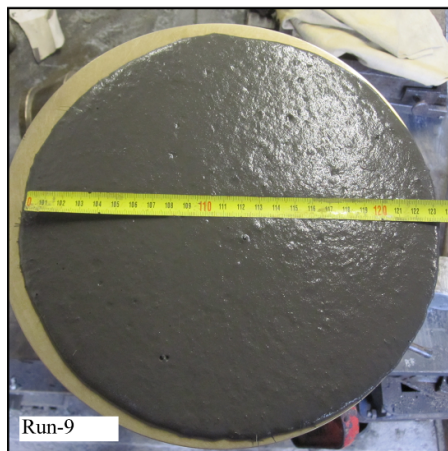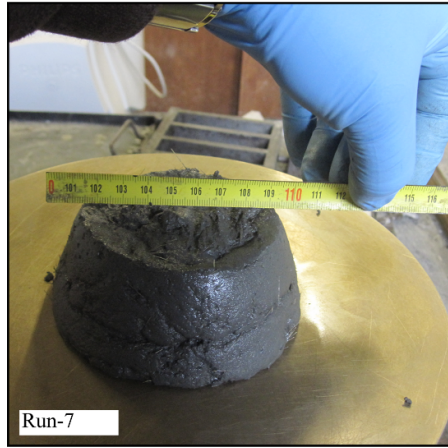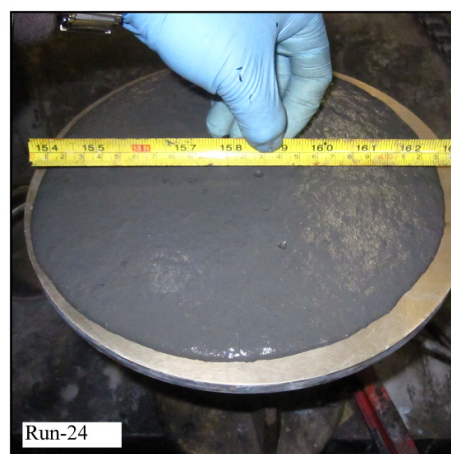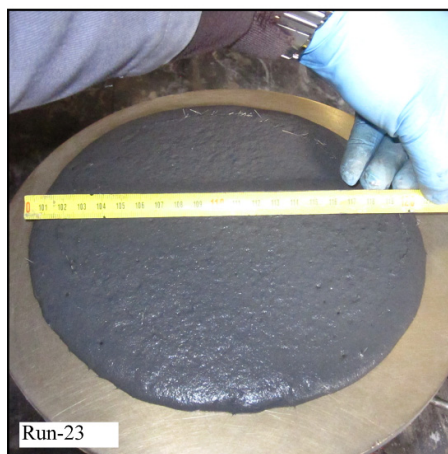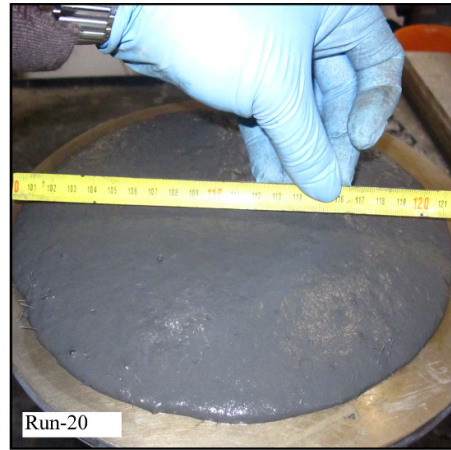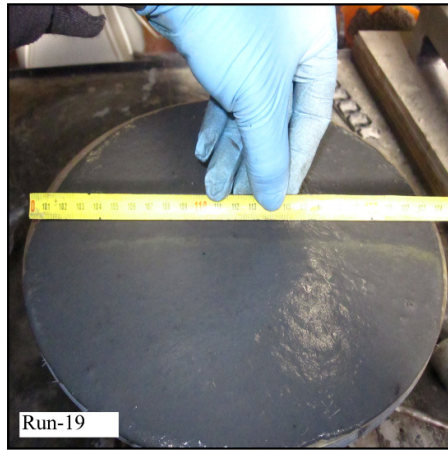**Figure AI. 1:** 28 mixtures for RSM (continuation).
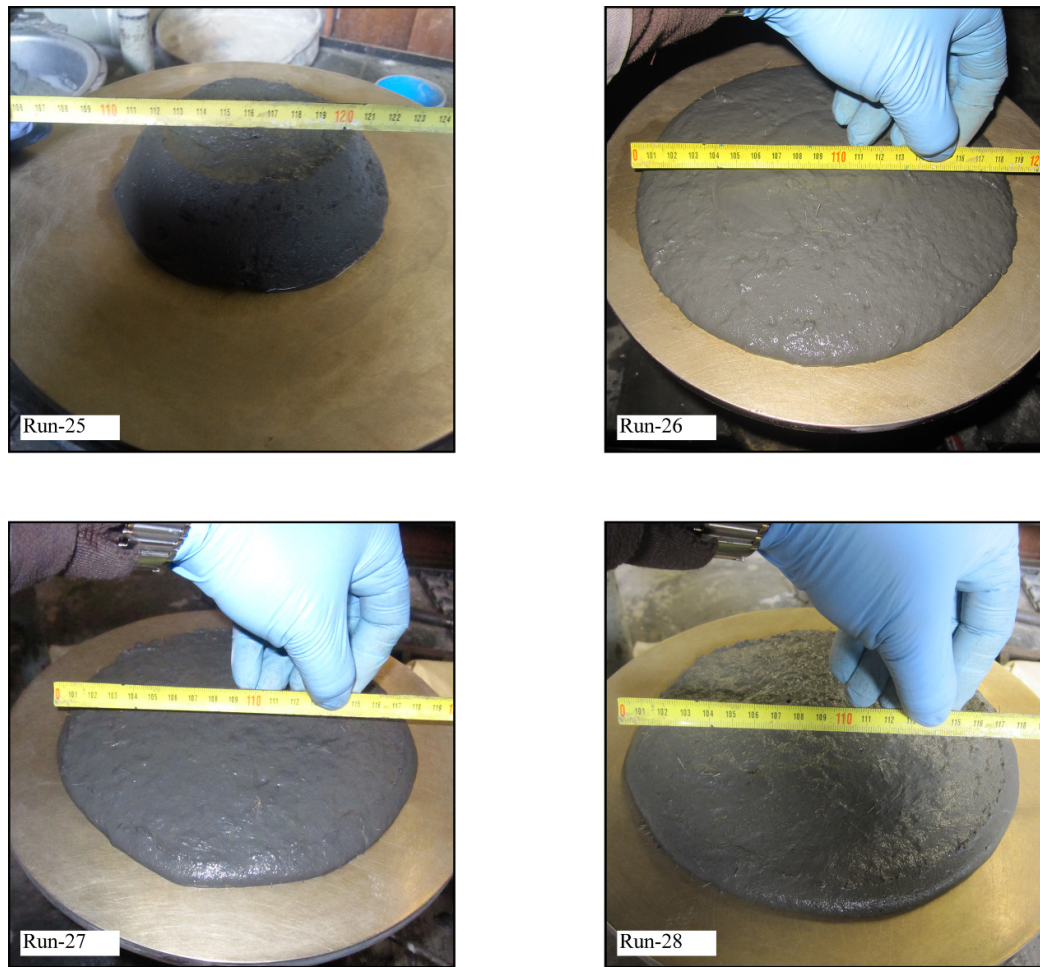
Figure AI. 1: 28 mixtures for RSM (continuation).

AI.2 Statistical Guidelines for RSM

The detailed information and guidelines for Chapter 4 and corresponding statistical terms definitions are provided in this Annex based on Help menu in Desig-Expert® software (© Stat-Ease, Inc. 2016).

AI.2.1   Model evaluation

In the first step and before starting analysis it is necessary to evaluate the design to ensure that the effects we seek can be estimated properly. In this regard, first a quadratic-order polynomial model used to evaluate the design. First, it was observed

that no aliases exist for quadratic Model. Regarding the degree of freedom (df), 3 df for

lack of fit and 4 df for pure error is recommended. Acceptable df for each case are

depicted in **Table AI. 1**. This ensures a valid lack of fit test. Fewer df will lead to a test

that may not detect lack of fit.

Table AI. 1: Degrees of Freedom for Evaluation of cubic model.

Model	**19**
Residuals	8
Lack 0f Fit	3
Pure Error	5
Corr Total	27

To understand if the model is statistically significant, for a fitted line into our design

space, firs a power should be calculated. In other words, power is a quantity indicating

if a study will obtain statistically significant results or not. More specifically, power is

the probability of supporting the hypothesis by the model under study if the research

hypothesis is true and null hypothesis is false. Power is represented as 1-β where β is

risk of error type II. It should be reminded that β is the probability of rejecting a

hypothesis (accepting null hypothesis, H_0) while it should be accepted. On the other

hand, α, is the probability of accepting the main hypothesis while it should be rejected

or probability of rejecting a true null hypothesis when it should not be rejected which

means making error type I. With these definitions, power is the probability of correctly

rejecting H_0 and avoiding a type II error. Anyhow, for instance a power of 30% or 0.3

in a study, which seems a low power, indicates that the study is likely to produces results

30% of them are statistically significant. As we know, power is influenced by some

factors such as sample size, effect size, alpha level (significance level or probability of

error type I, α), test direction (one-tailed or two-tailed) and etc. In other words, a larger

sample size or a higher effect size as well as higher alpha level, all result in increased

power in a study.

P-value is another measure of determining the significance of a test statistically. It is defined as the probability of evidence against the null hypothesis and is calculated from sample data. In other words, the smaller the P-value, the greater the evidence against the null hypothesis. With a given significance level, α, if the P-value is equal or less than α, then the null hypothesis is rejected and the results are statistically significant. On the other hand, if it is greater than α, we do not have significant evidence against null hypothesis. If the null hypothesis is false, then the P-value tends to be close to zero otherwise, it would have a uniform distribution between 0 and 1. P-values less than 0.01 demonstrate very strong evidence against H_0. P-values between 0.01 and 0.05 still show strong evidence against H_0, P-value between 0.05 and 0.1 demonstrates week evidence against H_0 and finally, P-values greater that 0.1 show little or no evidence against H_0.

Significance threshold mentioned in the software is significance level in statistics, which is adjusted to 0.05. The effect size for power calculation is adjusted to 0.5, 1 and 2. In general, power increases when sample size increases. Effect size is the degree to which H_0 is false. It measures how large the effect of one variable on another needs to be. The effect size is a part of power analysis in order to determine how large of a sample is needed to achieve a power greater than or equal to 0.8. If smaller risk of rejecting the null hypothesis is needed, α= 0.01 could also be used. The reason why we do not always use the lowest possible α values is that α and β are inversely related. In other words if we decrease α we will increase β resulting in lower power.

α is determined before study begins while P-value is calculated from the sample data after the study has been completed.

A power analysis is often used to calculate what sample size is needed. Since α is usually 0.05 and power is usually 0.8, most attention should be payed to the effect size

in order to calculate the needed sample size.

The program first determines whether the selected design adequately estimates coefficients for the desired model. If the design provides too few points or picks the wrong points, the estimated model terms will be aliased. First, a cubic-order polynomial model with 5% significance interval and effect sizes of 0.5, 1.0 and 2.0 was selected for evaluation. However no aliases was found, the other design terms show a highly poor model as depicted in **Table AI. 2**.

Table AI. 2: Model terms of a cubic-order polynomial model.

Term	StdErr**	VIF	Ri-Squared	Power at α= 0.05		
				0.5 Std. Dev.	1 Std. Dev.	2 Std. Dev.
A	30.13751	13901.5	0.999928	5.0 %	5.0 %	5.0 %
B	35.08147	18703.93	0.999947	5.0 %	5.0 %	5.0 %
C	1.9172	46.64929	0.978563	5.2 %	5.6 %	7.5 %
AB	0.296053	1.100855	0.091615	11.6 %	31.9 %	84.0 %
AC	0.353416	1.286456	0.222671	9.6 %	23.9 %	69.9 %
BC	0.353428	1.264659	0.209273	9.6 %	23.9 %	69.9 %
A^2	0.602975	2.258183	0.557166	11.4 %	31.0 %	82.7 %
B^2	0.603022	2.302834	0.565753	11.4 %	31.0 %	82.7 %
C^2	0.602651	1.976483	0.494051	11.4 %	31.0 %	82.7 %
ABC	0.334029	1.089567	0.082204	10.2 %	26.2 %	74.6 %
A^2B	1.119307	15.37712	0.934968	5.5 %	6.8 %	12.4 %
A^2C	17.03837	2751.386	0.999637	5.0 %	5.0 %	5.0 %
AB^2	1.117752	15.36691	0.934925	5.5 %	6.8 %	12.4 %
AC^2	1.005627	9.222738	0.891572	5.6 %	7.3 %	14.2 %
B^2C	17.15535	2764.892	0.999638	5.0 %	5.0 %	5.0 %
BC^2	1.006035	9.059788	0.889622	5.6 %	7.2 %	14.2 %
A^3	30.14803	13054.7	0.999923	5.0 %	5.0 %	5.0 %
B^3	35.07789	17755	0.999944	5.0 %	5.0 %	5.0 %
C^3	1.776288	34.65447	0.971144	5.2 %	5.7 %	7.9 %

**Basis Std. Dev. = 1.0

Although, standard errors (StdErr) should be similar within type of coefficient with preferred small values, they do not satisfy these requirements. In addition, ideal VIF is 1.0. VIF's above 10 are cause for alarm, indicating coefficients are poorly estimated

due to multicollinearity. Ideal R_i-squared is 0.0. High R_i-squared, such as ones shown in the table, means terms are correlated with each other, possibly leading to poor models. As a rule of thumb, Power, as explained before, should be approximately 80% for the effect we want to detect however, they are mostly lower than 80% showing very high risk of error type II. With respect to insignificant estimation of model terms, in the second step a quadratic-order polynomial model with the same adjustment for significance level and effect sizes was selected. As can be seen in **Table AI. 4**, all the model terms are in a satisfactory level and so the model is accepted for further analysis.

Table AI. 3: Degrees of Freedom for Evaluation of quadratic model.

Model	9
Residuals	18
Lack of Fit	13
Pure Error	5
Corr Total	27

Table AI. 4: Model terms of a quadratic model.

Term	StdErr**	VIF	Ri-Squared	Power at α= 0.05		
				0.5 Std. Dev.	1 Std. Dev.	2 Std. Dev.
A	0.267637	1.096324	0.087861	14.3 %	42.4 %	94.2 %
B	0.26761	1.088383	0.081206	14.3 %	42.4 %	94.2 %
C	0.287039	1.045662	0.043668	13.1 %	37.8 %	90.9 %
AB	0.284002	1.013051	0.012882	13.3 %	38.5 %	91.4 %
AC	0.326293	1.096575	0.08807	11.2 %	30.6 %	82.6 %
BC	0.32774	1.087499	0.080459	11.2 %	30.3 %	82.3 %
A²	0.562514	1.965293	0.49117	13.4 %	39.1 %	91.9 %
B²	0.546381	1.89055	0.471053	14.0 %	41.0 %	93.3 %
C²	0.51524	1.444707	0.307818	15.1 %	45.1 %	95.6 %

**Basis Std. Dev. = 1.0

From **Table AI. 3** it can be seen that at least 3 lack-of-fit degrees of freedom and 4 pure error degrees of freedom is available meeting the first prerequisite for a good design.

The second and third columns of **Table AI. 4** represent standard error (StdErr) and Variance Inflation Factors (VIF). VIF verifies how much the variance of the model coefficient increases due to the lack of orthogonality in the design. The standard error (StdErr) of a model coefficient increases in proportion to the square root of the VIF. If a coefficient is orthogonal or statistically independent to the remaining model terms, its VIF is one. One or more large VIFs indicate multicollinearity. VIFs exceeding ten indicate problems due to multicollinearity. As an example, if a coefficient has a VIF of 9, its StdErr is 3 times as large as it would be in an orthogonal design. The VIF is also related to R_i-squared, in forth column, through following equation:

$$VIF = 1.0/(1-R_i squared) \qquad\qquad Eq. (AI.1)$$

R_i-squared is the multiple correlation coefficient (also known as the coefficient of determination). It is calculated by regressing one of the factors on all other factors.

$$R_i^2 = (S_{YY} - R_{SS})/S_{YY} \qquad\qquad Eq. (AI.2)$$

where R_i^2 is R_i-squared, S_{YY} is the sum of squares corrected for the mean of X_i and R_{SS} is the sum of squares residuals regressing X_i on all other factors. If the design is orthogonal these two sums of squares are equal and R_i^2 is zero. Since the VIF = $1/(1-R_i^2)$, when R_i^2 is zero, the VIF is one. If the design terms are not orthogonal or they are statistically dependent, the quantity ($S_{YY} - R_{SS}$) is not zero and represents the variation in X_i that can be explained by the settings of the other factors. On the other hand if the design terms are statistically independent or orthogonal, R_i-squared is close to zero. In fact, R_i-squared is a measure of the collinearity of X_i with the other X's. According to these statistical definitions, **Table AI. 2** shows multicollinearity and strong dependency among the cubic-model terms considering the R_i-squared values close to 1 and VIF greater than 10 respectively while the quadratic model demonstrates acceptable ranges for all its terms. The last measure of model evaluation is its power as

depicted in last three columns in both tables. As defined previously, power is the probability of finding an effect of a specific size. More clearly, the power of a design is the ability of the design to detect which specific terms are statistically significant or the ability to find the significant effects. The size of the effect, as shown in both tables, is relative to the standard deviation (Std. Dev.) of the process namely 0.5, 1 and 2.0. It can be seen that the power for almost all the effects in **Table AI. 2** are lower than 80% representing a poor fitted model while in quadratic model for effect of 2 Std. Dev. All the terms show a power of more than 80% for quadratic model. For more clarification, term A in **Table AI. 4** is explained here. The output exhibits that this design term has a 94.2% chance to be statistically significant if the effect is the size of 2*(process standard deviation). If the effect is only as large as 1*(std. dev.) then the chance of finding it, would be only 42.4%. There is a 5% risk (α=0.05) that a term that appears to be statistically significant is not in fact significant, and the effect occurred only due to random chance.

After reviewing the relevant statistical outputs for design evaluation, studying the plots of standard error over the design space is of great importance. Obviously, the shape of the standard error plot depends only on the design points and the polynomial model fitted to those points. An ideal design exhibits a symmetrical shape as well as relatively low and flat error surface around the centroid. As explained before, the actual magnitude of StdErrs and their corresponding plots, is a function of standard deviation. A base standard deviation of 1.0 is used to generate the standard error plot for design evaluation in **Figure AI. 2**.
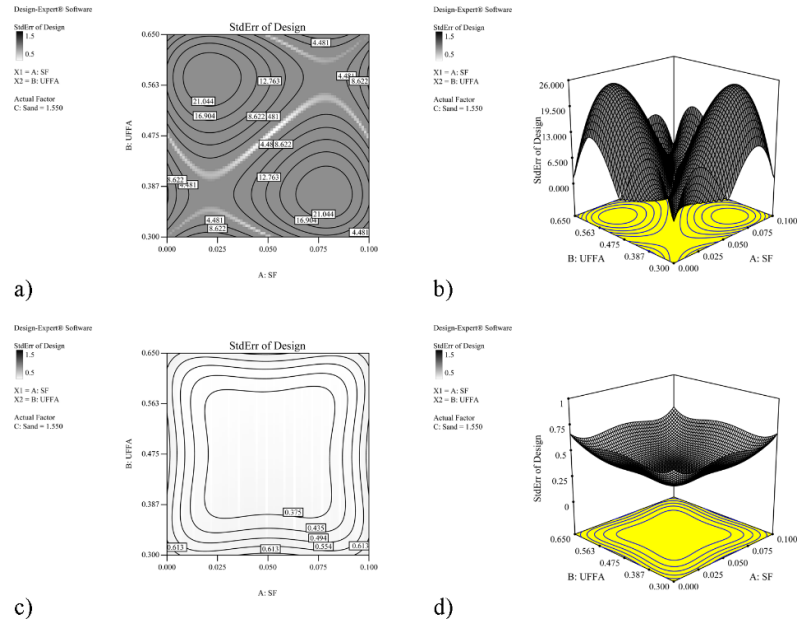
Figure AI. 2:   Standard error of design contour plots for SF-UFFA in cubic model (a&b) and quadratic model (c&d)

As indicated in **Figure AI. 2** and according to the above description, the standard

error plot of the design for cubic model demonstrate no symmetric shape. In addition,

it shows very large values compared to standard deviation of 1.0. On the other hand,

the quadratic model exhibit a symmetrical diagram with values less than standard

deviation of 1.0 verifying the priority of quadratic model over cubic one.

AI.2.2   Model analysis

The analysis of responses includes the following steps:

1. For each response, before any transformation, a regression calculation is
    carried out to fit a model to that specific response. The relevant statistics
    including p-value, lack-of-fit and R-squared results and other adequacy
    measures are compared for choosing the best-fitted model.

2. Analysis of variance (ANOVA) is performed and post-ANOVA analysis of
    individual model coefficients and case statistics for analysis of residuals and

outlier is detected.

3. Various diagnostic plots are inspected in order to validate the model statistically.

4. If the model needs any transformation, it is performed in this stage and again all the steps from 1 to 3 will be repeated again.

5. If the model looks good, model graphs, including contour and 3D graphs, for interpretation are generated.

6. After that all the response are analyzed, multiple response optimization will be carried out.

AI.2.2.1   Flowability

Based on the aforementioned steps, flow diameter (F.D.) as the first response was analyzed through measuring flow diameter of mixtures.

AI.2.2.1.1 Fit summery

In the first step, no transformation was selected and the Fit summery was studied. According to **Table AI. 5**, different models were compared among them quadratic model was suggested. The reason for this selection is that this model is the highest order polynomial model having a big F value and a P-value less than $\alpha=0.05$ and even $\alpha=0.01$ which means rejecting the null hypothesis and accepting the model fitted to this response as a statistically significant model. However generally, models with $P<0.1$ are considered for inclusion.

Table AI. 5: Model fit summery for F.D.

Source	Sum of Squares	df	Mean Square	F Value	p-value Prob > F	
	Response 1 F.D.			Transform: None		
	Sequential Model Sum of Squares [Type I]					
Mean vs Total	11090.27	1	11090.27			
Linear vs Mean	430.7523	3	143.5841	17.55575	< 0.0001	
2FI vs Linear	47.66107	3	15.88702	2.2447	0.1129	
Quadratic vs 2FI	127.3082	3	42.43608	35.82655	< 0.0001	Suggested
Cubic vs Quadratic	14.98162	10	1.498162	1.89068	0.1893	
Residual	6.339145	8	0.792393			
Total	11717.31	28	418.4754			

The next output of the fit-summary is Lack-of-fit test table that diagnoses how well each of the full models fits the data. This table is displayed when extra design points beyond what is needed for the model such as some replicated points, providing an estimate of pure error, are available. In general, Lack-of-fit test is an undesirable characteristic of a model. It compares the residual error (MEAN SQUARE) to the pure error (MEAN SQUARE). In this regard, a small F value and a P-value (prob>F) greater than 0.1 is desirable. If a model shows lack of fit, it should not be used to predict the response. As can be seen from **Table AI. 6**, the quadratic model shows the smallest F-value as well as highest P-value demonstrating desirability for the proposed models.

Table AI. 6: Lack of Fit Tests for quadratic model before transformation.

Source	Sum of Squares	df	Mean Square	F Value	p-value Prob > F	
Linear	195.4151	19	10.285	58.77145	0.0001	
2FI	147.754	16	9.234625	52.76929	0.0002	
Quadratic	20.44576	13	1.572751	8.987149	0.0122	Suggested
Cubic	5.464145	3	1.821382	10.40789	0.0137	
Pure Error	0.875	5	0.175			

The last table in Fit summary menu is Model Summary Statistics as shown in **Table**

AI. 7. Based on definition, R-Squared here is the correlation coefficient for the model. Adjusted R-Squared represents the amount of variation that can be explained by the model. This is the R-Squared value after adjusting for the number of terms in the model relative to the number of design points. Finally, calculated from the PRESS statistic, Model Predicted R-Squared represents the amount of variation in new data explained by the model. A negative Predicted R-Squared means that the overall mean is a better predictor than this model. The Predicted Residual Sum of Squares (PRESS) is a measure of how a particular model fits each design point. The coefficients for the model are calculated without the first design point. This model is used to predict the first point and then the new residual is calculated for this point. This is done for each data point and then the squared residuals are summed.

Table AI. 7: Model Summary Statistics for F.D.

Source	Std. Dev.	R-Squared	Adjusted R-Squared	Predicted R-Squared	PRESS	
Linear	2.859852	0.686959	0.647829	0.532659	293.0424	
2FI	2.660371	0.762968	0.695245	0.300111	438.8598	
Quadratic	1.088341	0.965998	0.948997	0.892958	67.11989	Suggested
Cubic	0.890165	0.98989	0.96588	-0.31971	827.5136	

Finally based on the results, a highest order significant model, in this case a quadratic model, having small P-value, insignificant lack of fit and very close adjusted/predicted R-squared, within 20% of each other and with the maximum values as well was selected.

AI.2.2.1.2 Analysis of variance (ANOVA)

In the next step based on suggestion a quadratic-order model analysis of variance (ANOVA) was performed. For better understanding the outputs, provided by software, first some terms are defined here.

- Model P-value: It should be less than 0.05 to be strongly significant. Between 0.05 and 0.10 is marginally significant.

- Term p-values: Confirm that each of the terms has a p-value less than 0.05 or at least less than 0.10. If a term is not significant, then it should be removed from the model unless it is needed to satisfy hierarchy.

- R-squared values: regarding adjusted and predicted R-squared values, if this is a response surface design for modeling the design space, then the R-squared values should be rather high (perhaps above 0.60, but this is not a "set in stone" rule.)

- Curvature: If you have a curvature term and it is significant, then the middle of the design space is not linear. Predictions in the middle of the design space will not be correct. You may consider augmenting this design to estimate higher-order terms such as quadratic.

- Lack of fit: If you have a lack of fit term and it is significant, this means that the polynomial model is not fitting all of the design points well. You may need a higher order model, or perhaps a transformation since sometimes a polynomial just cannot describe the system very well.

According to above explanations and as depicted in **Table AI. 8**, the Model F-value of 56.82 implies the model is strongly significant. There is only 0.01% chance that a "Model F-Value" this large could occur due to noise. In addition, model terms having P-value higher than 0.1 should be removed from the model while values of "Prob > F" less than 0.05 indicate model terms are significant. In this case A, B, C, AC, BC, A^2, B^2 are significant model terms. If there are many insignificant model terms (not counting those required to support hierarchy), model reduction may improve the model. Furthermore, lack-of-fit has a P-value less than 0.05 showing that it is statistically

significant which is undesirable. In other words, the "Lack of Fit F-value" of 8.99

implies the Lack of Fit is significant. There is only 1.22% chance that a "Lack of Fit F-

value" this large could occur due to noise. As mentioned before, it means that a higher

order model or a transformation is required depending on the results from diagnostics

in the following steps.

Table AI. 8: ANOVA results for F.D. before transformation and insignificant terms removal.

Source	Sum of Squares	df	Mean Square	F Value	p-value Prob > F	
Response 1 F.D.						
ANOVA for Response Surface Quadratic Model						
Analysis of variance table [Partial sum of squares - Type III]						
Model	605.7216	9	67.30241	56.81988	< 0.0001	significant
A-SF	43.49129	1	43.49129	36.7174	< 0.0001	
B-UFFA	31.04247	1	31.04247	26.20753	< 0.0001	
C-Sand	326.1871	1	326.1871	275.3826	< 0.0001	
AB	1.174872	1	1.174872	0.991883	0.3325	
AC	15.75239	1	15.75239	13.29891	0.0018	
BC	24.79729	1	24.79729	20.93505	0.0002	
A^2	6.853035	1	6.853035	5.785657	0.0271	
B^2	28.01943	1	28.01943	23.65533	0.0001	
C^2	3.041749	1	3.041749	2.567989	0.1264	
Residual	21.32076	18	1.184487			
Lack of Fit	20.44576	13	1.572751	8.987149	0.0122	significant
Pure Error	0.875	5	0.175			
Cor Total	627.0424	27				

The next part of the ANOVA outputs is presented in **Table AI. 9**. The "Pred

R-Squared" of 0.8929 is in reasonable agreement with the "Adj R-Squared" of 0.9489.

"Adeq Precision" measures the signal to noise ratio. A ratio greater than 4 is desirable.

The ratio of 27.613 indicates an adequate signal. This model can be used to navigate

the design space.

Table AI. 9: R-squares table for F.D. before transformation and insignificant terms removal.

Std. Dev.	Mean	C.V. %	PRESS	R-Squared	Adj-R-Squared	Pred-R-Squared	Adeq Precision
1.0883	19.90	5.4685	67.119	0.9659	0.9489	0.8929	27.6131

The final estimate of coefficients is provided in **Table AI. 10**. The variance inflation factor (VIF), in the last column, measures how much the variance of the model is inflated by the lack of orthogonality in the design. If the factor is orthogonal to all the other factors in the model or significantly independent to other factors, the VIF is 1.0. The final proposed model in terms of coded and actual values is presented in **Table AI. 11**.

Table AI. 10: Estimate of coefficients for F.D. before transformation and insignificant terms removal.

Factor	Coefficient Estimate	df	Standard Error	95% CI Low	95% CI High	VIF
Intercept	23.37347	1	0.348950208	22.64035	24.10658	
A-SF	1.76501	1	0.291280291	1.153052	2.376967	1.096324
B-UFFA	-1.49101	1	0.291250947	-2.1029	-0.87911	1.088383
C-Sand	-5.18411	1	0.312396243	-5.84043	-4.52779	1.045662
AB	0.307834	1	0.309090605	-0.34154	0.957209	1.013051
AC	1.295033	1	0.355118139	0.548958	2.041109	1.096575
BC	1.632041	1	0.356692573	0.882658	2.381424	1.087499
A²	-1.47257	1	0.612207431	-2.75877	-0.18637	1.965293
B²	-2.89218	1	0.594649312	-4.14149	-1.64287	1.89055
C²	-0.89861	1	0.560756993	-2.07672	0.279497	1.444707

Table AI. 11: Proposed model for F.D. before transformation and insignificant terms removal.

Coded values	Actual values
F.D. =	**F.D. =**
23.37347	36.80379
1.76501 * A	-83.0922 * SF
-1.49101 * B	21.61664 * UFFA
-5.18411 * C	0.935189 * Sand
0.307834 * A * B	35.18098 * SF * UFFA
1.295033 * A * C	103.6027 * SF * Sand

1.632041 * B * C	37.30379 * UFFA * Sand
-1.47257 * A^2	-589.027 * SF^2
-2.89218 * B^2	-94.4386 * $UFFA^2$
-0.89861 * C^2	-14.3778 * $Sand^2$

AI.2.2.1.3 Insignificant terms removal

Through a backward process, the insignificant model terms having P-value greater than 0.1 and not supporting the hierarchy (AB and C^2), were eliminated from the model. Then again, it is necessary to run the ANOVA in order to obtain the new results. The new ANOVA results can be seen in **Table AI. 12** to

Table AI. 15.

Table AI. 12: ANOVA results for F.D. before transformation and after insignificant terms removal.

ANOVA for Response Surface Reduced Quadratic Model						
Analysis of variance table [Partial sum of squares - Type III]						
Source	Sum of Squares	df	Mean Square	F Value	p-value Prob > F	
Model	601.6068	7	85.94383067	67.5776	< 0.0001	significant
A-SF	43.17807	1	43.17806819	33.9509	< 0.0001	
B-UFFA	31.24782	1	31.24782213	24.57015	< 0.0001	
C-Sand	322.6738	1	322.6738056	253.7183	< 0.0001	
AC	15.38784	1	15.38783895	12.09945	0.0024	
BC	24.54496	1	24.54496156	19.29969	0.0003	
A^2	10.79129	1	10.791293	8.48519	0.0086	
B^2	34.31658	1	34.31658151	26.98312	< 0.0001	
Residual	25.4356	20	1.271779802			
Lack of Fit	24.5606	15	1.63737307	9.356418	0.0109	significant
Pure Error	0.875	5	0.175			
Cor Total	627.0424	27				

Table AI. 13: R-squares table for F.D. before transformation and after insignificant terms removal.

Std. Dev.	Mean	C.V. %	PRESS	R-Squared	Adj-R-Squared	Pred-R-Squared	Adeq Precision
1.13	19.9	5.67	52.77	0.9594	0.9452	0.9158	30.398

Table AI. 14: Estimate of coefficients for F.D. before transformation and after insignificant terms removal.

Factor	Coefficient Estimate	df	Standard Error	95% CI Low	95% CI High	VIF
Intercept	23.23549	1	0.348036801	22.5095	23.96148	
A-SF	1.755831	1	0.301340185	1.127246	2.384416	1.092822
B-UFFA	-1.49419	1	0.301440723	-2.12298	-0.8654	1.085848
C-Sand	-5.14147	1	0.322783262	-5.81478	-4.46815	1.039729
AC	1.277564	1	0.367282148	0.511427	2.043701	1.092473
BC	1.621754	1	0.369155782	0.851708	2.391799	1.084872
A²	-1.76593	1	0.606237164	-3.03052	-0.50134	1.794872
B²	-3.11415	1	0.59950544	-4.36469	-1.8636	1.789661

Table AI. 15: Proposed model for F.D. before transformation and after insignificant terms removal.

Coded values	Actual values
F.D. =	**F.D. =**
23.23549	67.91616373
1.755831 * A	-52.66414457 * SF
-1.49419 * B	30.60748107 * UFFA
-5.14147 * C	-43.28372819 * Sand
1.277564 * A * C	102.2051219 * SF * Sand
1.621754 * B * C	37.06865547 * UFFA * Sand
-1.76593 * A2	-706.3717602 * SF2
-3.11415 * B2	-101.6864483 * UFFA2

The results show that, the Model F-value of 67.58 implies the model is significant. There is only 0.01% chance that a "Model F-Value" this large could occur due to noise. In spite of removing the insignificant terms, yet the lack-of-fit is significant clarifying that a transformation is necessary.

AI.2.2.1.4 Diagnostics

In the next step, to find out which kind of transformation is required, a diagnostic study should be carried out. Most of the plots, provided in the diagnostics, display residuals, which show how well the model satisfies the assumptions of the analysis of

variance. Some of the most important diagnostic plots are described as follows:

- Normal Probability: The normal probability plot indicates whether the residuals follow a normal distribution, in which case the points will follow a straight line. Definite patterns like an "S-shaped" curve, indicates that a transformation of the response may provide a better analysis.

- Residuals vs Predicted: This is a plot of the residuals versus the ascending predicted response values. It tests the assumption of constant variance. The plot should be a random scatter (constant range of residuals across the graph.) Expanding variance, having a megaphone pattern (<) in this plot indicates the need for a transformation.

- Residuals vs Run: This is a plot of the residuals versus the experimental run order. It checks for lurking variables that may have influenced the response during the experiment. The plot should show a random scatter. Trends indicate a time-related variable lurking in the background. Blocking and randomization provide insurance against trends ruining the analysis.

- Actual vs Predicted: A graph of the actual response values versus the predicted response values. It helps to detect a value or group of values that are not easily predicted by the model.

- Box Cox Plot for Power Transforms: This plot provides a guideline for selecting the correct power law transformation. A recommended transformation is listed, based on the best lambda value, which is found at the minimum point of the curve generated by the natural log of the sum of squares of the residuals. If the 95% confidence interval around this lambda includes 1 then the software does not recommend a specific transformation. This plot is not displayed when either the logit or the arcsine square root transformation has been applied.

According to above definitions, first the normal plot was studied. As can be seen in

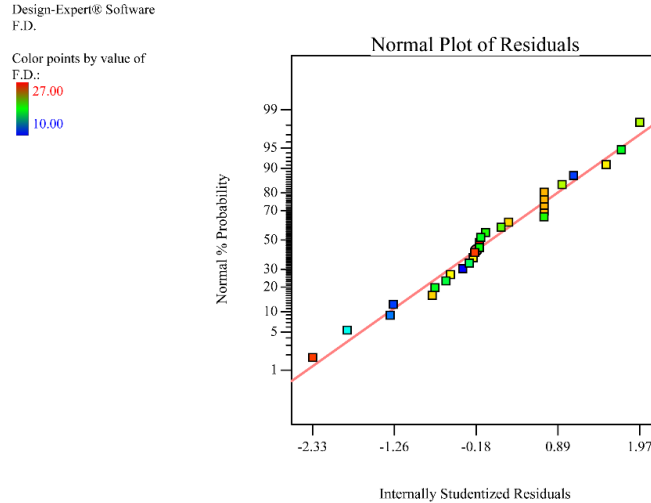**Figure AI. 3**, all residuals follow a normal distribution by following the straight line.

Figure AI. 3: Normal plot of residuals for F.D. after insignificant terms removal and before transformation.

The next diagnostic plot is Residuals vs Predicted as plotted in **Figure AI. 4**. The

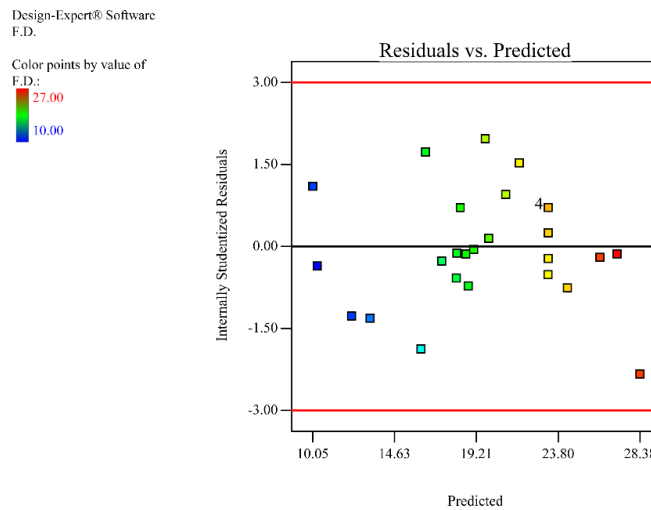points are scattered randomly and no expanding variance like a megaphone pattern (<)

is observed.

Figure AI. 4: Residual vs. predicted diagnostic plot for F.D. after insignificant terms removal and before transformation.

The other graph is the Residuals vs Run. The plot shows a random scatter providing insurance against trends ruining the analysis (**Figure AI. 5**).
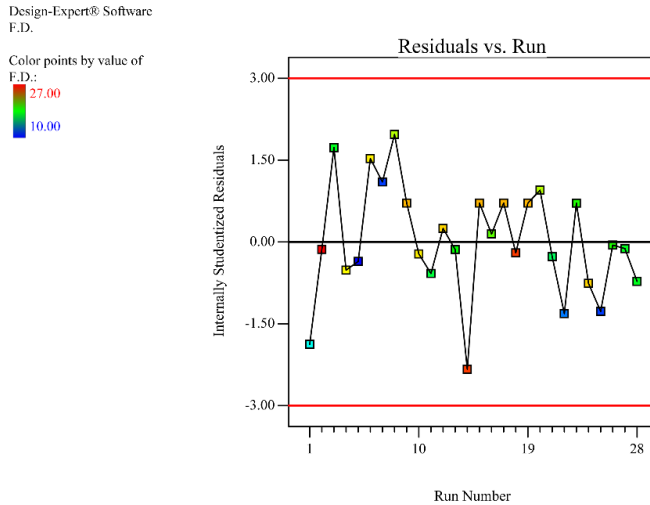

Figure AI. 5: Residual vs. Run diagnostic plot for F.D. after insignificant terms removal and before transformation.

The next figure, **Figure AI. 6**, represents Predicted vs Actual values. It shows that all values can be easily predicted by the model.
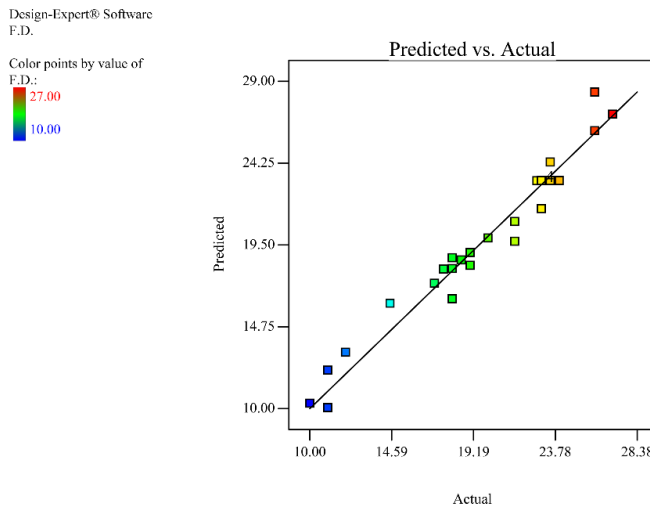

Figure AI. 6: Predicted vs. Actual diagnostic plot for F.D. after insignificant terms removal and before transformation.

The next diagnostic plot is Box-Cox Plot for Power Transforms. As can be seen from

Figure AI. 7, Lambda= 2.74 is recommended for Power transformation for F.D. response.
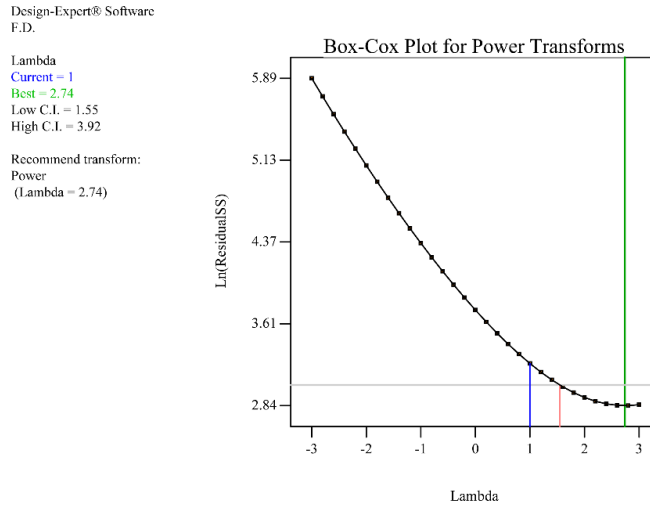

Figure AI. 7: Box-Cox diagnostic plot for F.D. after insignificant terms removal and before transformation.

Based on this, a transformation was carried out and again all the steps was performed from the first step which was Fit summary. It should be noted that henceforth the insignificant terms removal and ANOVA will be done simultaneously for more time efficiency. The Fit summary results after power transformation are plotted in **Table AI. 16** to **Table AI. 18**.

Table AI. 16: Model fit summery for F.D. after power transformation and before insignificant terms removal.

Response1 F.D.			Transform:Power		Lambda:2.74	
Sequential Model Sum of Squares [Type I]						
Source	Sum of Squares	df	Mean Square	F Value	p-value Prob > F	
Mean vs Total	4.69E+08	1	468737230.1			
Linear vs Mean	95532409	3	31844136.18	20.18361	< 0.0001	
2FI vs Linear	12095030	3	4031676.659	3.285379	0.0409	
Quadratic vs 2FI	22067790	3	7355930.028	35.76129	< 0.0001	Suggested
Cubic vs Quadratic	1723040	10	172304.0409	0.696362	0.7095	
Residual	1979476	8	247434.4557			
Total	6.02E+08	28	21504820.53			

Table AI. 17: Lack-of-fit test summery for F.D. after transformation and before insignificant terms removal.

	Lack of Fit Tests					
Source	Sum of Squares	df	Mean Square	F Value	p-value Prob > F	
Linear	37475183	19	1972378.031	25.27695	0.0010	
2FI	25380153	16	1586259.538	20.32866	0.0018	
Quadratic	3312363	13	254797.1174	3.265344	0.0995	Suggested
Cubic	1589322	3	529774.0391	6.789302	0.0326	
Pure Error	390153.5	5	78030.70563			

Table AI. 18: Model Summary Statistics for F.D. after transformation and before insignificant terms removal.

	Model Summary Statistics					
Source	Std. Dev.	R-Squared	Adjusted R-Squared	Predicted R-Squared	PRESS	
Linear	1256.074	0.716147	0.680665492	0.570942	57235383	
2FI	1107.771	0.806816	0.751620608	0.440971	74573221	
Quadratic	453.5365	0.972245	0.958366807	0.929368	9422142	Suggested
Cubic	497.4278	0.985161	0.949918716	-1.1208	2.83E+08	

Again, it can be observed that the quadratic model is statistically significant with almost insignificant lack-of-fit and highest Adjusted R-Squared of 0.9584. As noticed before, in the next step the ANOVA, with a quadratic model and simultaneous backward non-significant terms removal was performed. The removed terms as can be seen in **Table AI. 19**, are AB, C^2 and AC. The model is also significant. It is worthy to notice that after transformation the Lack-of-fit is not significant anymore compared to the results before transformation. The "Pred R-Squared" of 0.9444 is in reasonable agreement with the "Adj R-Squared" of 0.9596 (**Table AI. 20**). **Table** AI. 21 also demonstrates that A^2 and B^2 are not perfectly independent from other model terms.

Table AI. 19: ANOVA results for F.D. after transformation and after insignificant terms removal.

Source	Sum of Squares	df	Mean Square	F Value	p-value Prob > F	
Response 1: F.D.			**Transform: Power**			**Lambda: 2.74**
ANOVA for Response Surface Reduced Quadratic Model						
Analysis of variance table [Partial sum of squares - Type III]						
Model	1.29E+08	6	21533564.16	107.7612	< 0.0001	significant
A-SF	6209422	1	6209422.304	31.07404	< 0.0001	
B-UFFA	12104251	1	12104251.4	60.57376	< 0.0001	
C-Sand	73431870	1	73431869.63	367.4779	< 0.0001	
BC	10833761	1	10833760.75	54.21579	< 0.0001	
A²	1618614	1	1618613.855	8.10009	0.0097	
B²	6611865	1	6611864.597	33.088	< 0.0001	
Residual	4196360	21	199826.6517			
Lack of Fit	3806206	16	237887.8849	3.048645	0.1113	not significant
Pure Error	390153.5	5	78030.70563			
Cor Total	1.33E+08	27				

Table AI. 20: R-squares table for F.D. after transformation and after insignificant terms removal.

Std. Dev.	Mean	C.V. %	PRESS	R-Squared	Adj-R-Squared	Pred-R-Squared	Adeq Precision
447.02	4091.53	10.93	7415391	0.9685	0.9596	0.9444	37.281

Table AI. 21: Estimate of coefficients for F.D. after transformation and after insignificant terms removal.

Factor	Coefficient Estimate	df	Standard Error	95% CI Low	95% CI High	VIF
Intercept	5577.4281	1	137.7843985	5290.89	5863.966	
A-SF	642.593053	1	115.2755315	402.8645	882.3216	1.017813
B-UFFA	-929.289309	1	119.4011965	-1177.6	-680.981	1.08428
C-Sand	-2447.02473	1	127.6505737	-2712.49	-2181.56	1.034909
BC	1076.71376	1	146.2302924	772.6112	1380.816	1.083409
A²	-683.913471	1	240.3013645	-1183.65	-184.179	1.794814
B²	-1366.48716	1	237.5583415	-1860.52	-872.458	1.788478

The final model equations in terms of coded and actual factors are depicted in **Table AI. 22**. Finally, the diagnostic plots are presented in **Figure AI. 8** to **Figure AI. 12**.

They all verify the significance of proposed model for fluidity.

Table AI. 22: Proposed model for F.D. after transformation and after insignificant terms removal.

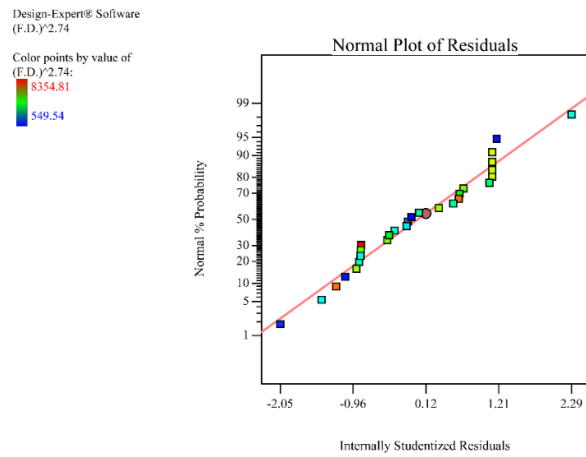| Coded values	Actual values
$(F.D.)^{2.74} =$	$(F.D.)^{2.74} =$
5577.428102	29997.00103
642.5930531 * A	40208.39989 * SF
-929.2893091 * B	-1067.665582 * UFFA
-2447.024729 * C	-21478.13402 * Sand
1076.713759 * B * C	24610.60021 * UFFA * Sand
$-683.9134706 * A^2$	$-273565.3882 * SF^2$
$-1366.487157 * B^2$	$-44619.98881 * UFFA^2$

Figure AI. 8: Normal plot of residuals for F.D. after transformation and after insignificant terms removal.
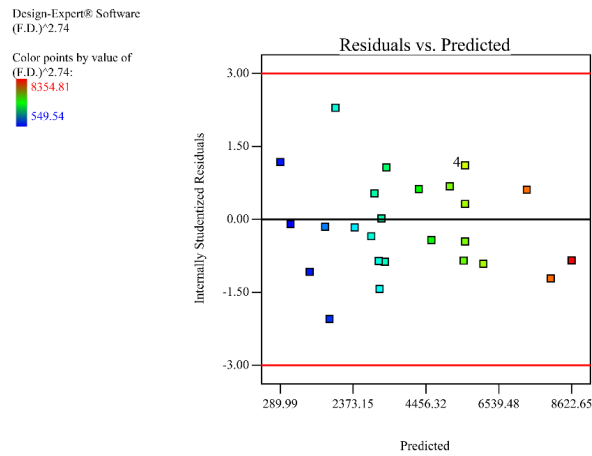

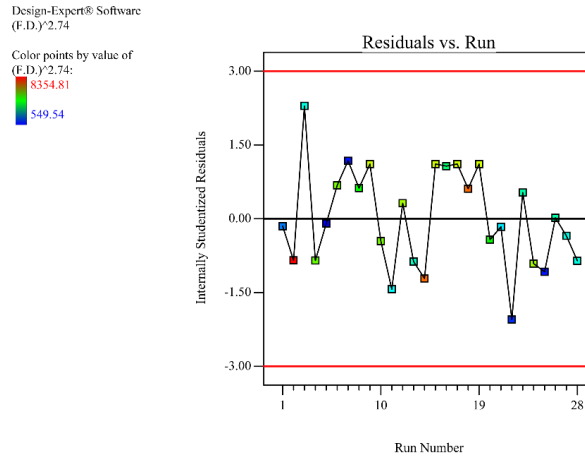**Figure AI. 9:** Residual vs. predicted diagnostic plot for F.D. after transformation and after insignificant terms removal.

Figure AI. 10: Residual vs. Run diagnostic plot for F.D. after transformation and after insignificant terms removal.
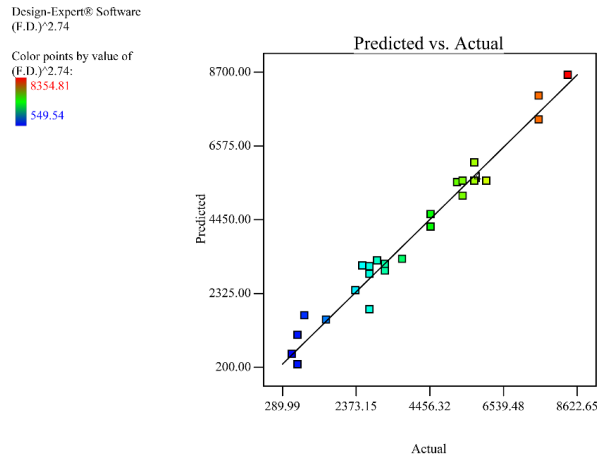

Figure AI. 11: Predicted vs. Actual diagnostic plot for F.D. after transformation and after insignificant terms removal.
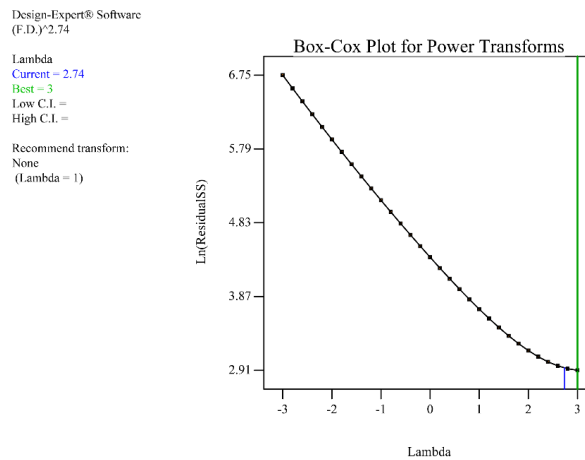

Figure AI. 12: Box-Cox diagnostic plot for F.D. after transformation and after insignificant terms removal.

AI.2.2.1.5 Model Graphs

In this section various graphs are provided for the aim of interpreting the selected model. The first type of model graphs are Perturbations. The perturbation plot helps to compare the effect of all the factors at a particular point in the design space. The response is plotted by changing only one factor over its range while holding of the other factors constant. By default, Design-Expert® sets the reference point at the midpoint (coded 0) of all the factors. A steep slope or curvature in a factor shows that the response is sensitive to that factor. A relatively flat line shows insensitivity to change in that particular factor. If there are more than two factors, the perturbation plot could be used to find those factors that exhibit most effect on the response. These influential factors are good choices for the axes on the contour plots. One of the perturbation plots, also provided in Chapter 4, is explained here.
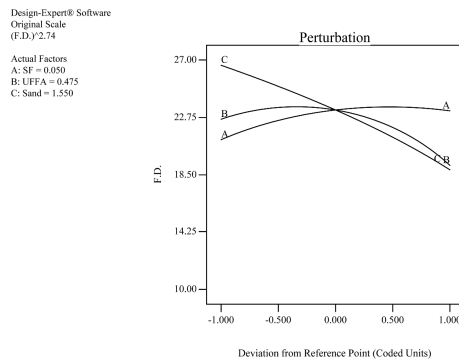

Figure AI. 13: F.D. perturbation plot.

As can be seen from **Figure AI. 13**, the curves display the sensitivity of the models to any variations of the variables those are SF, UFFA and sand. As can be seen, flowability is highly affected by sand content. In other words, flow diameter decreases significantly with incensement of sand content. On the other hand, SF does not have any negative impact on F.D. up to around 90% of its lower boundary. UFFA in a content

above its reference point, which is 50% of its minimum or maximum level, affects F.D. strongly.

The next important type of graphs are contour plots. A contour plot is a two-dimensional or three-dimensional representation of the response for selected factors. As UFFA and sand were recognized as two influential factors, from Perturbation plot, their corresponding 3D contour plots were presented in Chapter 4. Other 2D and 3D contour plots for F.D. are available in **Figure AI. 14**. It should be noticed that however the main F.D. model is in transformed state, the plots are showed in original scale.
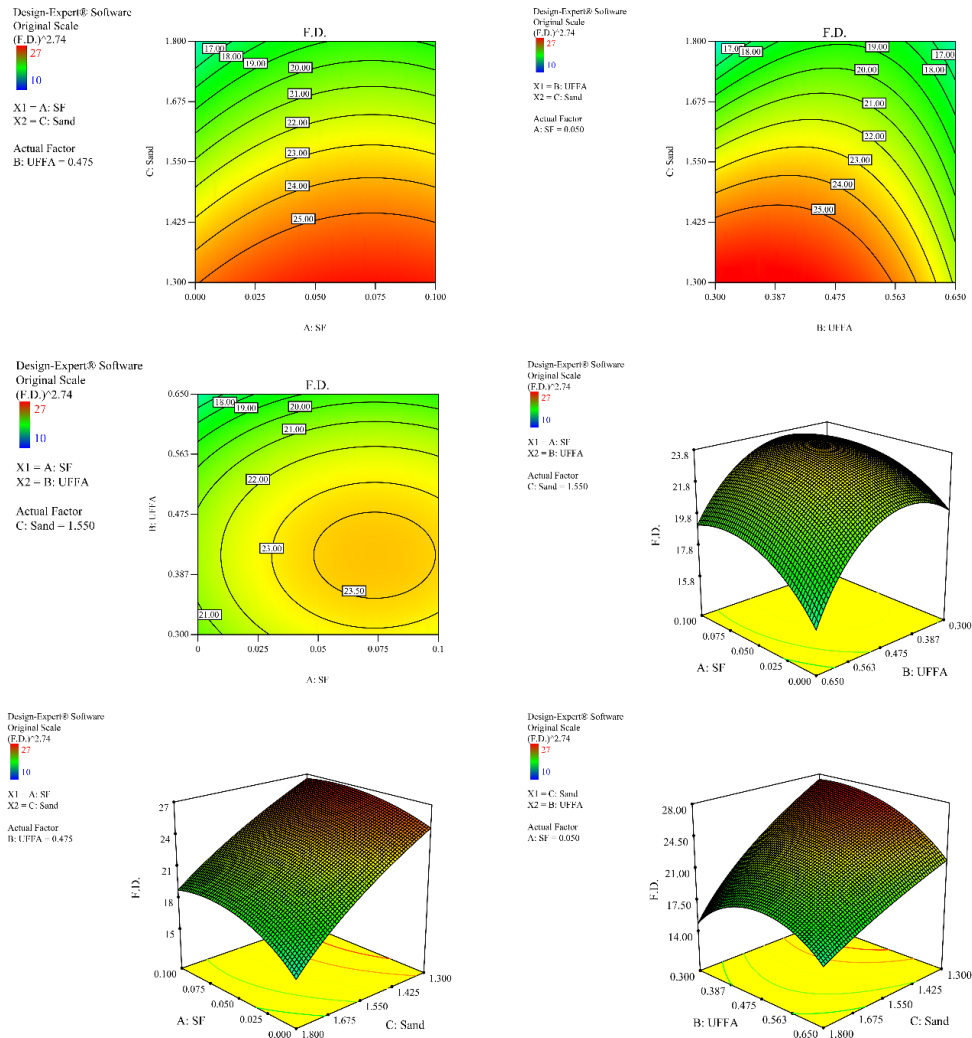

Figure AI. 14: 2D and 3D model graphs after transformation and insignificant terms removal representing interaction of SF, UFFA and sand on F.D.

AI.2.2.2 Compressive strength

The same procedure regarding model analysis for compressive strength is required.

AI.2.2.2.1 Fit summary

First without any transformation the Fit summary was studied. Based on the guidelines provided in last section for Fit summary of F.D., a quadratic model was suggested for C.S. as well. The quadratic model is statistically significant. However, it should be considered that the insignificant terms yet exist in the model. The results for Fit summary are depicted in **Table AI. 23** to **Table AI. 25**.

Table AI. 23: Model fit summery for C.S.

Response 2 C.S.			Transform: None			
Sequential Model Sum of Squares [Type I]						
Source	Sum of Squares	df	Mean Square	F Value	p-value Prob > F	
Mean vs Total	647654	1	647654			
Linear vs Mean	2745.322	3	915.1073	60.09785	< 0.0001	
2FI vs Linear	8.972259	3	2.990753	0.176186	0.9113	
Quadratic vs 2FI	256.6863	3	85.56209	15.43383	< 0.0001	Suggested
Cubic vs Quadratic	69.18801	10	6.918801	1.808811	0.2064	
Residual	30.60043	8	3.825054			
Total	650764.7	28	23241.6			

Table AI. 24: Lack of Fit Tests for quadratic model for C.S.

Lack of Fit Tests						
Source	Sum of Squares	df	Mean Square	F Value	p-value Prob > F	
Linear	355.7786	19	18.72519	9.683774	0.0098	
2FI	346.8064	16	21.6754	11.20948	0.0072	
Quadratic	90.1201	13	6.932316	3.585062	0.0835	Suggested
Cubic	20.9321	3	6.977366	3.60836	0.1005	
Pure Error	9.668333	5	1.933667			

Table AI. 25: Model Summary Statistics for C.S.

	Std.		Adjusted	Predicted		
Source	Dev.	R-Squared	R-Squared	R-Squared	PRESS	
Linear	3.902173	0.882522	0.867837	0.819155	562.5674	
2FI	4.120071	0.885406	0.852665	0.559427	1370.52	
Quadratic	2.354528	0.967922	0.951882	0.827558	536.4287	Suggested
Cubic	1.955775	0.990163	0.9668	-0.3503	4200.468	

AI.2.2.2.2   Analysis of variance (ANOVA)

For more time efficiency, in the next step quadratic model was selected with backward step for non-significant terms removal simultaneously. Then the ANOVA was carried out. The results show that in this case A^2, B, AC, BC and AB were insignificant terms and were removed from the model. As can be seen from **Table AI. 26**, the model is significant and the Lack-of-fit is insignificant.

Table AI. 26: ANOVA results for C.S. after insignificant terms removal.

			ANOVA for Response Surface Reduced Quadratic Model			
		Analysis of variance table [Partial sum of squares - Type III]				
Source	Sum of Squares	df	Mean Square	F Value	p-value Prob > F	
Model	3001.379	5	600.2758	120.7249	< 0.0001	significant
A-SF	2623.699	1	2623.699	527.667	< 0.0001	
B-UFFA	0.007139	1	0.007139	0.001436	0.9701	
C-Sand	191.4923	1	191.4923	38.5121	< 0.0001	
B^2	55.41787	1	55.41787	11.1454	0.0030	
C^2	76.73698	1	76.73698	15.43301	0.0007	
Residual	109.3898	22	4.972263			
Lack of Fit	99.72146	17	5.865968	3.033598	0.1119	not significant
Pure Error	9.668333	5	1.933667			
Cor Total	3110.769	27				

Table AI. 27: R-squares table for C.S. after insignificant terms removal.

Std. Dev.	Mean	C.V. %	PRESS	R-Squared	Adj-R-Squared	Pred-R-Squared	Adeq Precision
2.23	152.09	1.47	205.91	0.9648	0.9568	0.9338	36.905

Table AI. 28: Estimate of coefficients for C.S. after insignificant terms removal.

Factor	Coefficient Estimate	df	Standard Error	95% CI Low	95% CI High	VIF
Intercept	155.6823	1	0.695636	154.2396	157.1249	
A-SF	13.21468	1	0.575277	12.02163	14.40774	1.018701
B-UFFA	0.021828	1	0.57606	-1.17285	1.216504	1.014282
C-Sand	-3.93592	1	0.634231	-5.25123	-2.6206	1.026718
B^2	-3.40354	1	1.019489	-5.51783	-1.28925	1.323756
C^2	-4.30373	1	1.09552	-6.5757	-2.03177	1.313551

Table AI. 29: Proposed model for C.S. after insignificant terms removal.

Coded values	Actual values
C.S. =	C.S. =
155.6823	-23.6995
13.21468* A	264.2937* SF
0.021828 * B	105.7039 * UFFA
-3.93592 * C	197.7216 * Sand
-3.40354 * B^2	-111.136 * $UFFA^2$
-4.30373 *C^2	-68.8598 * $Sand^2$

In addition, the "Pred-R-Squared" value for proposed models is in reasonable agreement with the "Adj-R-Squared" values according to **Table AI. 27**. The VIFs, shown in **Table AI. 28**, verify that all the significant terms are also perfectly orthogonal to other model terms. The final proposed model is provided in **Table AI. 29.**

AI.2.2.2.3   Diagnostics

In this part, the diagnostics for C.S. model was studied. The Normal Probability plot verifies that the residuals follow a normal distribution. The Residuals vs Predicted plot also shows a random scattered plot for the points not having a megaphone pattern. In addition, Residuals vs Run shows totally a random scatter. Regarding Actual vs Predicted, the points are perfectly scattered around the line. The Box-Cox Plot verifies that no transformation is required. The graphs related to diagnostics are available in
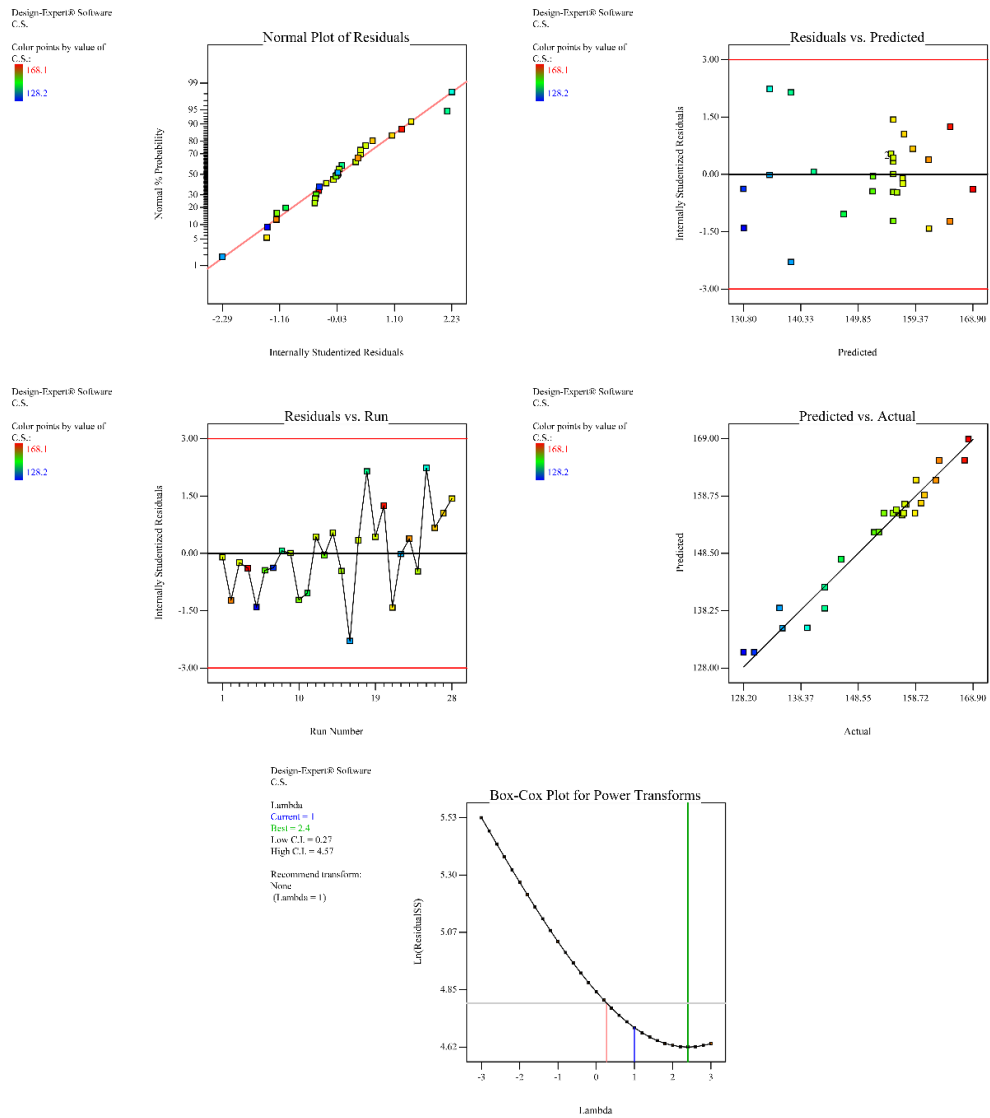
Figure AI. 15.

Figure AI. 15: Diagnostic plots for C.S.

AI.2.2.2.4 Model Graphs

In this section, the model graphs are discussed. The same as last section the first graph deals with influence of all constituents on compressive strength.
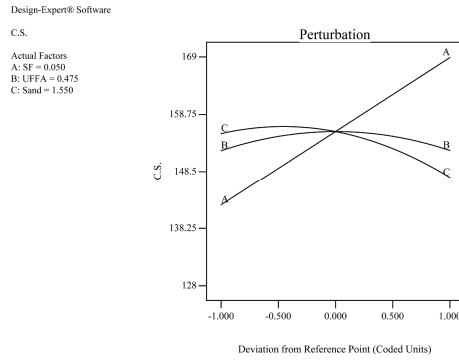
Figure AI. 16: The effect of constituents' variations on C.S.

As indicated, the curves in **Figure AI. 16** display the sensitivity of the models to any variations of the variables those are SF, UFFA and Sand. C.S. shows a reduction when the sand content overpass its 50% of its lower defined boundary. On the other hand, SF showed its ability to improve the compressive strength. FA in a content above its reference point, which is 50% of its minimum or maximum level, affected strength. All the 2D and 3D graphs representing the effect of constituents on C.S. are presented in **Figure AI. 17**.
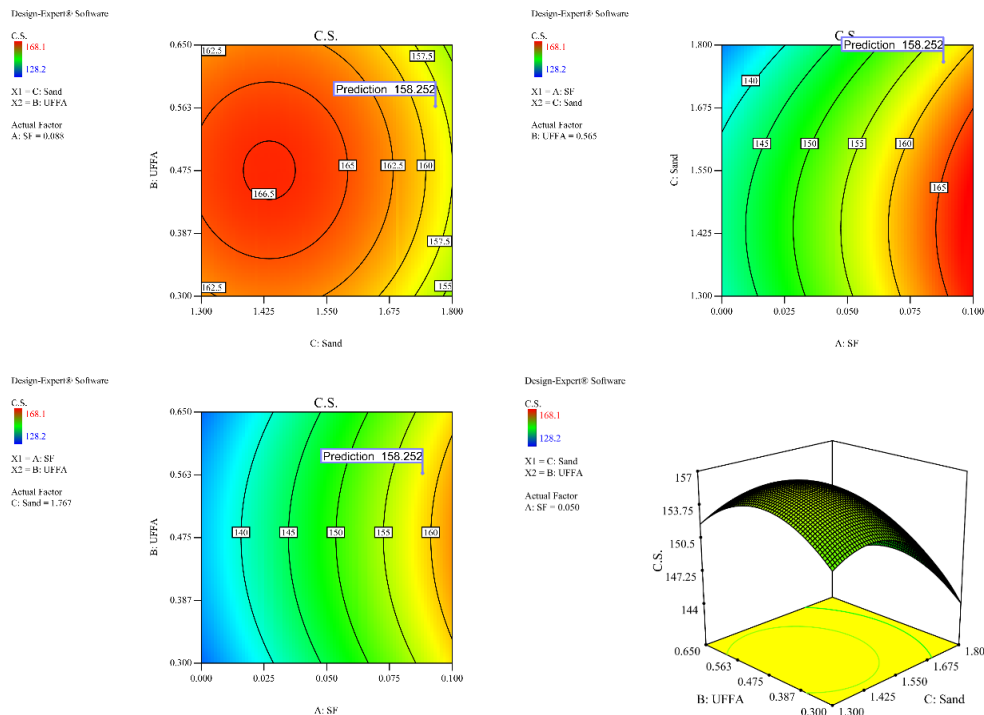

Figure AI. 17: 2D and 3D model graphs after insignificant terms removal representing interaction of SF, UFFA and sand on C.S. (to be continued).
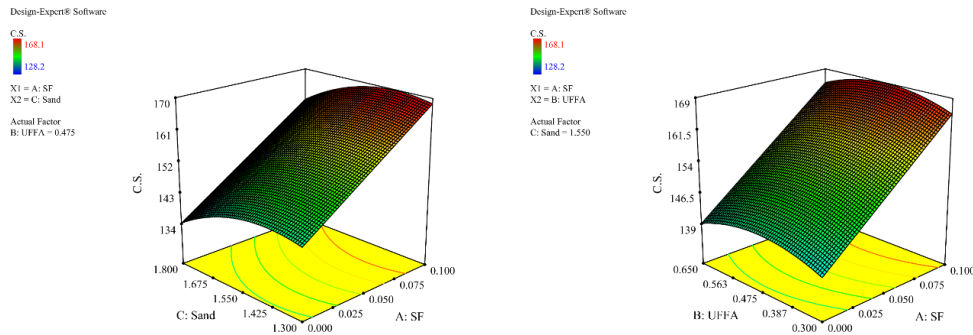
Figure AI. 17: 2D and 3D model graphs after insignificant terms removal representing interaction of SF, UFFA and sand on C.S. (continuation).

AI.3 CO2 content and price of UFFA

Although some detailed studies regarding quantifying produced CO_2 during FA processing to obtain UFFA is required, for the aim of this research it was supposed that FA in high quantities is grinded to smaller particles, namely UFFA in our case, through steam jet-mill fly ash-micronizer technology such as one invented by LNPE company (LNPE, 2014) and shown in **Figure AI. 18**. In this technology, superheated steam causes a high-velocity airflow, which accelerates the particle collision. After that, a turbo air classifier will classify the ground material. Then, the accepted particles, depending on pre-defined average size, will be packed and the coarser particles will be returned to milling machine again. This new superfine pulverizing device has some advantages over other methods such as lower energy consumption, larger capacity, dry-function processing and obtaining higher fineness even in nanometer range. Typical materials could be processed by this technique are fly ash, titanium dioxide, coal powder, petroleum coke, carbon black, graphite etc.

Figure AI. 18: A type of Jet mill machine.

However depending on various type of fuels, the quantity of produced CO_2 would be different (eia, 2015), the maximum generated CO_2 for every kw.h of energy is almost 1 kg. According to the technical parameters reported by factory (**Table AI. 30**), for capacities greater that 30 ton/h, such as LNGS-20T, LNGS-40T or LNGS-40T, and also using their full capacity, almost 5 kw.h energy for production of 1 ton of ground powder with average particle size of 1-45 μm, is consumed corresponding to producing 5 kg CO_2. With respect to this simple calculation, the whole embodied CO_2 for 1 kg of UFFA, including transportation, could have a value around 0.009 kg.

Table AI. 30: Technical information of different models of Steam-jet mills (LNPE, 2014).

Model	Steam consumption	Max Feed Size	Product Size	Capacity	Powder Consumption
LNGS-150	150kg/h	< 3mm	d50=1-45um	50-500kg/h	6-12kw.h
LNGS-1000	1t/h	< 3mm	d50=1-45um	0.2-3t/h	15-30kw.h
LNGS-3000	3t/h	< 3mm	d50=1-45um	0.8-10t/h	45-65kw.h
LNGS-10T	10t/h	< 5mm	d50=1-45um	4-30t/h	125-160kw.h
LNGS-20T	20t/h	< 5mm	d50=1-45um	8-60t/h	250-300kw.h
LNGS-40T	40t/h	< 5mm	d50=1-45um	16-120t/h	500-580kw.h

To calculate the price of UFFA, the following assumptions were considered:

- A factory with a medium capacity (LNGS-10T) with maximum installation price of 200,000 US$ (Alibaba®, 1999-2016) corresponding to 179,000 €;

- A piece of land with cost of 50,000 €/10,000 m^2 with a building of 200,000

€/300 m^2;

- Two 24-hour working days per week for 5 years;

- Four part-time operators for 24 working hours per two days with payment of 700 €/month per person;

- Investment return after 5 years;

- Running the factory with capacity of 8 t/h during first 5 years;

- Original fly ash with cost of 20 €/ton;

- Consumed electricity with price of 0.1587 €/kw.h.

Based on the above assumptions, the final price of UFFA would be 30 €/ton. By adding transportation and other side expenditures, the maximum price would be around 40 €/ton as shown in Chapter 4 **Table 4-6**.

Annex II

Experimental results of

Chapter 5

In this Annex the extra information regarding Modulus of Elasticity of NC and TWC samples beside the results of capillary water absorption test are provided.
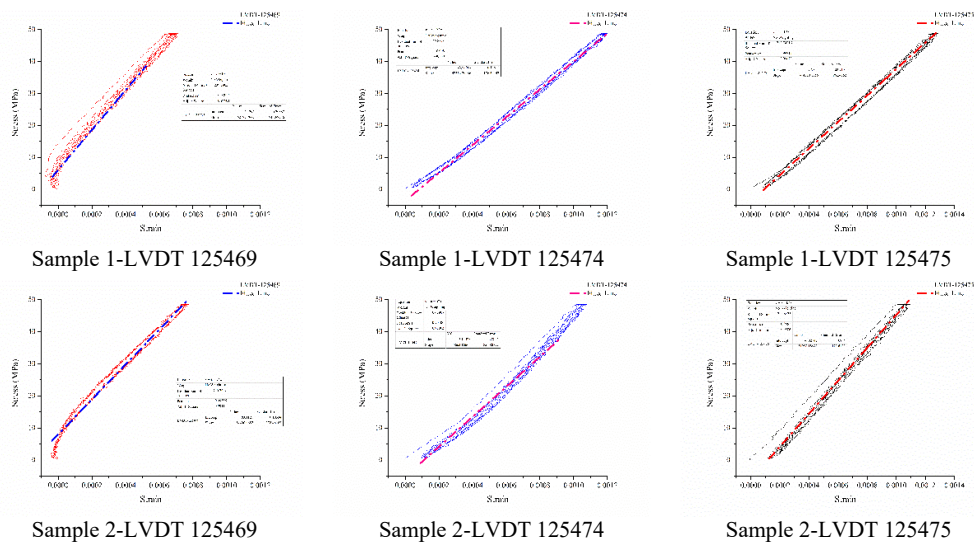

| Sample 1-LVDT 125469 | Sample 1-LVDT 125474 | Sample 1-LVDT 125475 |
| Sample 2-LVDT 125469 | Sample 2-LVDT 125474 | Sample 2-LVDT 125475 |

Figure AII. 1: Axial Stress-Strain diagrams for Modulus of Elasticity of NC samples (to be continued).

| Sample 3-LVDT 125469 | Sample 3-LVDT 125474 | Sample 3-LVDT 125475 |
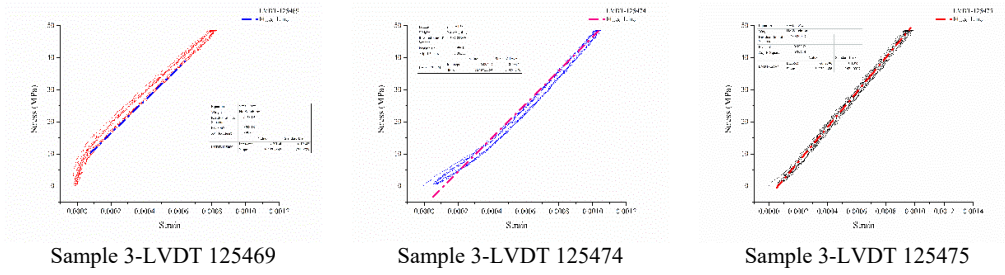
Figure AII. 1: Axial Stress-Strain diagrams for Modulus of Elasticity of NC samples (continuation).

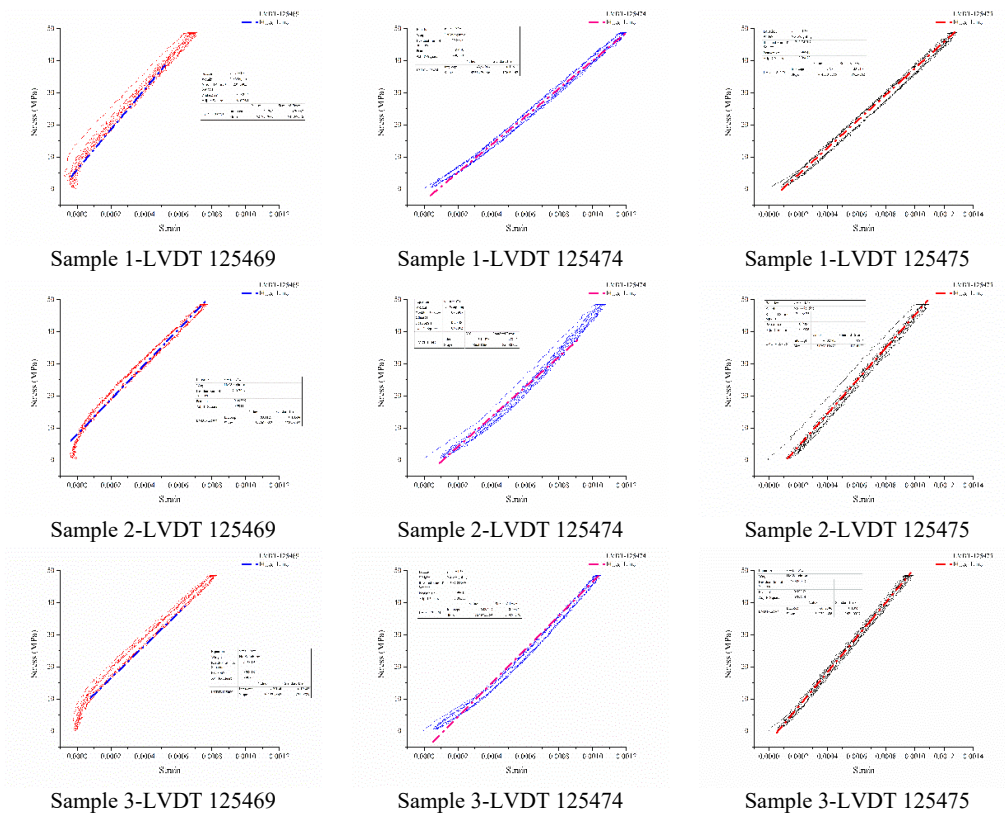| Sample 1-LVDT 125469 | Sample 1-LVDT 125474 | Sample 1-LVDT 125475 |
| Sample 2-LVDT 125469 | Sample 2-LVDT 125474 | Sample 2-LVDT 125475 |
| Sample 3-LVDT 125469 | Sample 3-LVDT 125474 | Sample 3-LVDT 125475 |

Figure AII. 2: Axial Stress-Strain diagrams for Modulus of Elasticity of TWC samples.

Table AII. 1: Results of capillary water absorption test.

Time	0.0	5min±10s	20min±2min	30min±2min	60min±2min	2H±5min	4H±5min	6H±5min	1D±2H	2D±2H	3D±2H	4D±2H	7D±2H	8D±2H	9D±2H	10D±2H	16D±2H
s	0.0	300.0	1200.0	1800.0	3600.0	7200.0	14400.0	21600.0	86400.0	172800.0	259200.0	345600.0	604800.0	691200.0	777600.0	864000.0	1382400.0
$\sqrt{s}$	0.0	17.3	34.6	42.4	60.0	84.9	120.0	147.0	293.9	415.7	509.1	587.9	777.7	831.4	881.8	929.5	1175.8
R1	255.0	255.0	255.0	255.0	255.1	255.1	255.1	255.1	255.2	255.3	255.4	255.4	255.5	255.6	255.5	255.6	255.7
R2	286.9	286.9	286.9	286.9	286.9	287.0	287.1	287.0	287.2	287.2	287.3	287.3	287.5	287.6	287.7	287.7	287.8
R3	295.3	295.3	295.4	295.4	295.4	295.4	295.5	295.5	295.7	295.8	295.9	295.8	296.0	296.1	296.0	296.1	296.2
R4	236.9	236.9	236.9	237.0	237.0	237.1	237.1	237.1	237.2	237.3	237.3	237.3	237.5	237.5	237.6	237.5	237.6
R5	260.4	260.4	260.4	260.4	260.4	260.5	260.5	260.6	260.8	260.9	261.0	261.0	261.2	261.3	261.3	261.3	261.5
R6	277.8	277.9	278.0	278.0	278.0	278.0	278.1	278.1	278.2	278.3	278.4	278.5	278.6	278.7	278.7	278.8	278.9
R7	262.8	262.8	262.8	262.8	262.8	262.9	263.0	263.1	263.1	263.3	263.4	263.5	263.8	263.9	263.9	263.9	264.1
R8	287.1	287.2	287.2	287.2	287.2	287.3	287.3	287.4	287.5	287.7	287.7	287.8	288.0	288.1	288.1	288.1	288.3
R9	281.6	281.6	281.6	281.7	281.7	281.7	281.8	281.8	282.0	282.0	282.2	282.1	282.3	282.4	282.4	282.5	282.5
R10	292.0	292.0	292.0	292.0	292.1	292.1	292.1	292.2	292.3	292.4	292.4	292.5	292.7	292.8	292.7	292.8	292.8
R11	271.1	271.1	271.1	271.1	271.2	271.2	271.3	271.3	271.4	271.4	271.5	271.5	271.6	271.7	271.7	271.7	271.8
R12	257.1	257.2	257.2	257.2	257.3	257.3	257.4	257.3	257.4	257.6	257.6	257.6	257.8	257.8	257.8	257.8	257.9
R13	300.2	300.3	300.4	300.4	300.4	300.4	300.5	300.6	300.7	300.8	300.9	300.9	301.1	301.1	301.1	301.2	301.3
R14	288.7	288.8	288.8	288.8	288.8	288.8	288.8	288.9	289.0	289.1	289.2	289.2	289.4	289.4	289.6	289.5	289.6
R15	244.1	244.2	244.2	244.2	244.2	244.2	244.3	244.3	244.3	244.5	244.5	244.6	244.7	244.8	244.8	244.8	244.9
R16	287.1	287.1	287.2	287.2	287.2	287.2	287.4	287.4	287.6	287.6	287.8	287.8	288.0	288.1	288.2	288.1	288.3
R17	283.3	283.3	283.3	283.3	283.4	283.4	283.5	283.5	283.7	283.7	283.8	283.8	283.9	284.0	284.2	284.0	284.1
R18	282.1	282.1	282.1	282.2	282.2	282.2	282.2	282.3	282.5	282.6	282.8	282.9	283.2	283.3	283.3	283.3	283.7
R19	245.1	245.1	245.1	245.2	245.2	245.3	245.3	245.4	245.5	245.6	245.7	245.6	245.8	245.8	245.9	245.9	246.0
R20	267.7	267.7	267.7	267.7	267.8	267.8	267.8	267.9	268.0	268.0	268.2	268.2	268.3	268.3	268.3	268.4	268.5
R21	247.1	247.1	247.2	247.2	247.2	247.2	247.3	247.3	247.5	247.5	247.6	247.6	247.7	247.8	247.9	247.8	247.9
R22	274.6	274.6	274.6	274.7	274.7	274.7	274.7	274.8	275.0	275.1	275.2	275.3	275.5	275.7	275.7	275.7	276.0
R23	304.7	304.7	304.7	304.8	304.8	304.8	304.8	304.9	305.0	305.1	305.2	305.2	305.3	305.4	305.4	305.5	305.5
R24	265.4	265.4	265.3	265.4	265.4	265.4	265.5	265.5	265.6	265.6	265.8	265.8	265.9	266.1	265.9	266.0	266.1
R25	250.3	250.4	250.4	250.4	250.5	250.5	250.6	250.6	250.8	250.8	251.0	251.0	251.2	251.3	251.3	251.3	251.5
R26	312.4	312.4	312.4	312.4	312.5	312.5	312.6	312.6	312.7	312.8	312.9	312.9	313.0	313.0	313.1	313.1	313.1

Table AII. 2: Rate of water absorption (sorptivity) for all the compositions.

	Slope of fitted line (Sorptivity), mm/s$^{1/2}$	Adjusted R^2
R1	4.03E-04	0.98715
R2	5.08E-04	0.98742
R3	5.53E-04	0.97067
R4	4.46E-04	0.96109
R5	6.36E-04	0.99076
R6	6.63E-04	0.96795
R7	7.53E-04	0.99161
R8	7.09E-04	0.98547
R9	5.69E-04	0.97795
R10	5.16E-04	0.9806
R11	4.20E-04	0.97511
R12	5.11E-04	0.9495
R13	6.89E-04	0.95373
R14	5.48E-04	0.98318
R15	4.84E-04	0.9784
R16	7.24E-04	0.98097
R17	5.17E-04	0.96512
R18	8.50E-04	0.99735
R19	5.56E-04	0.96468
R20	4.66E-04	0.98224
R21	5.08E-04	0.96902
R22	7.59E-04	0.99686
R23	5.03E-04	0.98193
R24	4.06E-04	0.96908
R25	7.16E-04	0.97668
R26	4.69E-04	0.96738

Annex III

Experimental results of

Chapter 6

I n this Annex the extra information regarding Self-healing test for 28-days normal cured (NC) and 6-days TWC specimens are presented.
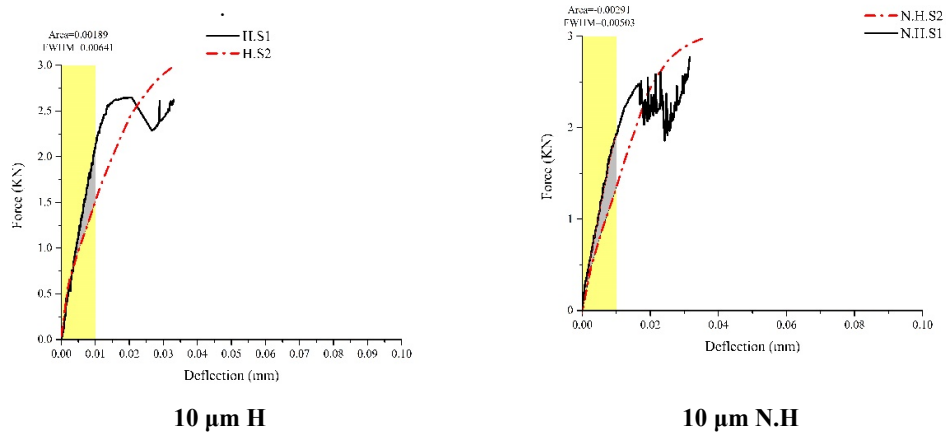

10 µm H   10 µm N.H

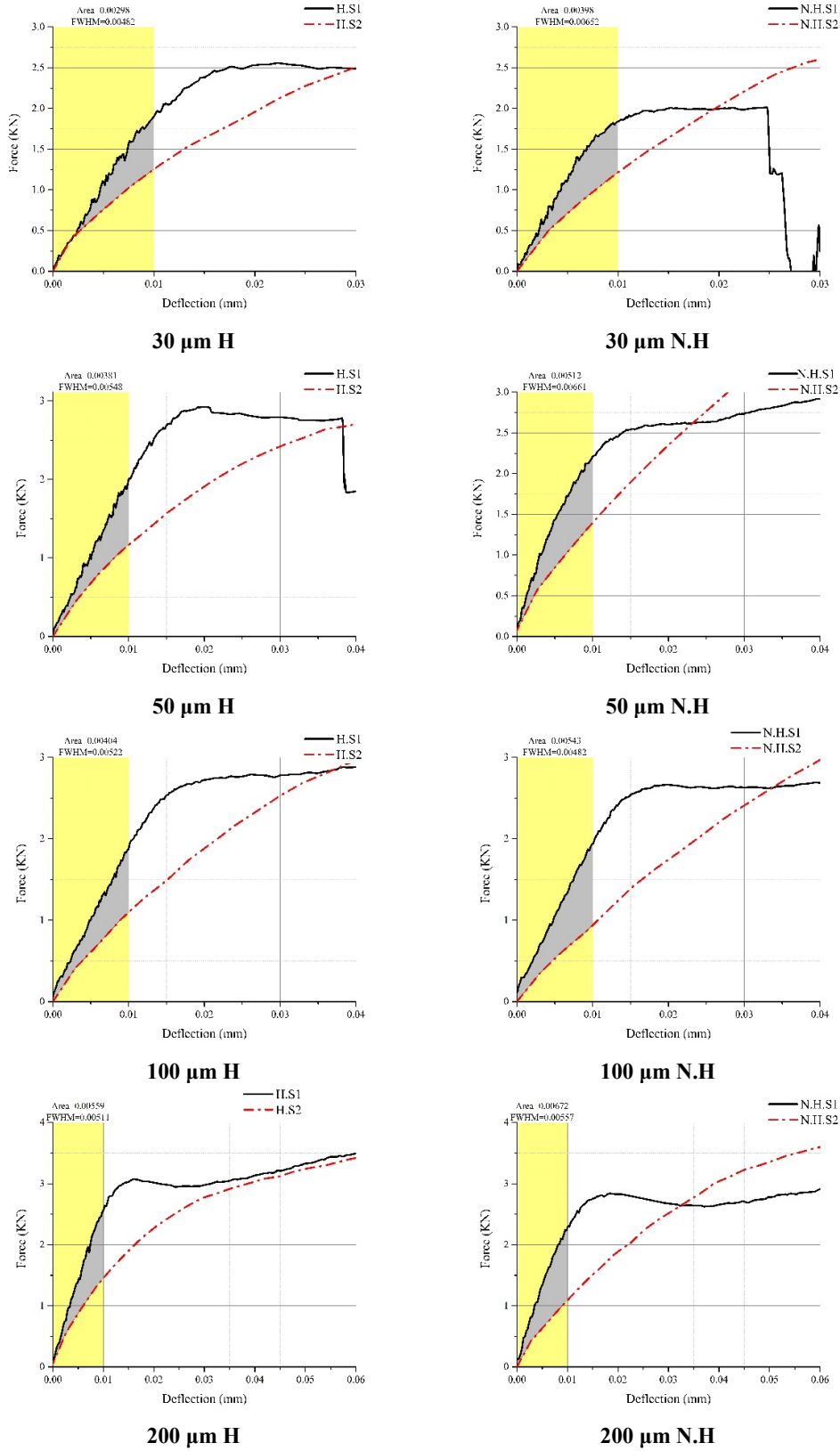**Figure AIII. 1:** Self-healing test for 28-days normal cured (NC) specimens (to be continued).

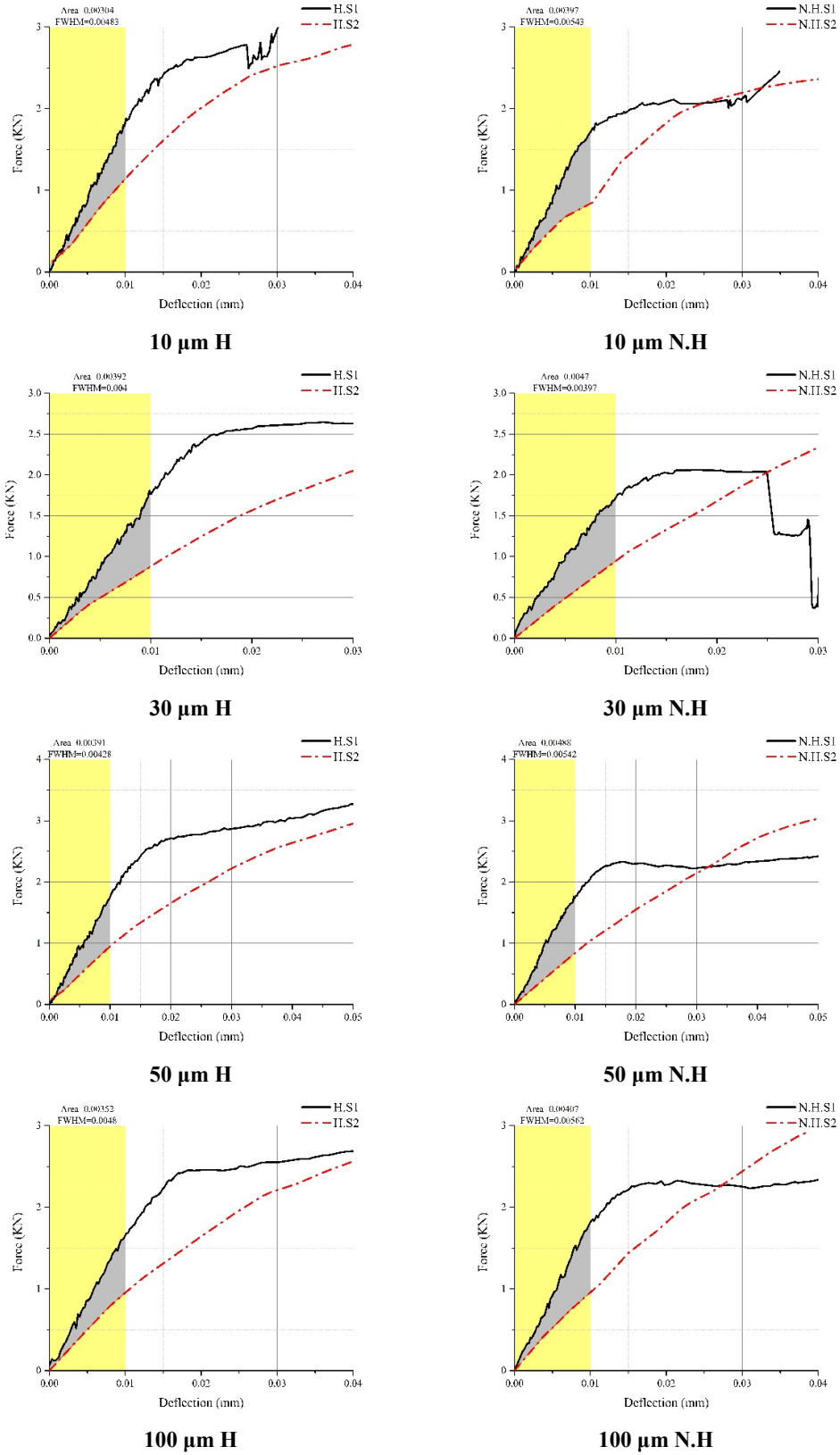**Figure AIII. 1:** Self-healing test for 28-days normal cured (NC) specimens (continuation).

Figure AIII. 2: Self-healing test for 6-days TWC specimens (to be continued).
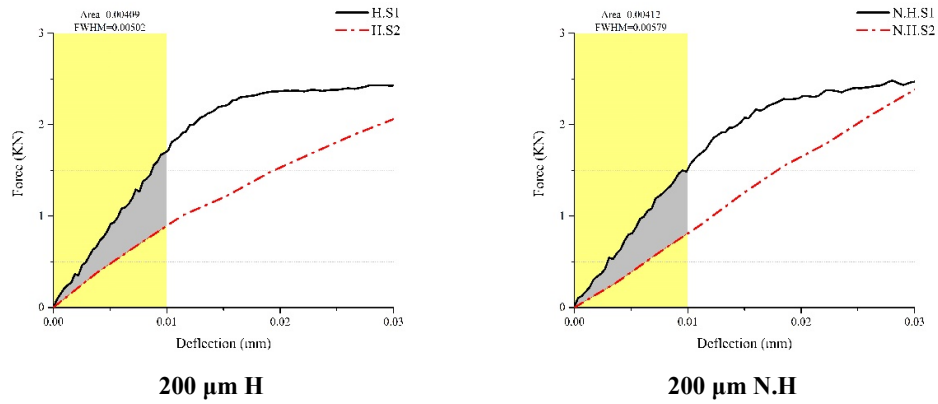
200 μm H   **200 μm N.H**

Figure AIII. 2: Self-healing test for 6-days TWC specimens (continuation).